1D morphodynamical modelling of swash zone beachface evolution

Fangfang Zhu

Thesis submitted to The University of Nottingham

for the degree of Doctor of Philosophy

September 2012

Abstract

The beachface evolution in the swash zone under different single swash events is investigated by fully coupled simulations. Two fully coupled models (bed-load-only and combined load models) comprising the one dimensional shallow water equations and bed evolution equation are developed. The two coupled systems are solved by the specified time interval method of characteristics (STI MOC) (Kelly and Dodd, 2009, 2010), which can resolve shocks very accurately. The fully coupled bed-load-only simulations with six different sediment transport formulae for a single Peregrine and Williams (2001) (PW01) swash over an erodible plane beach all yield net erosion all over the swash zone. Consistent with Kelly and Dodd (2010), however, full coupling yields significantly less erosion for all the $\widehat{q} = \widehat{q}(\widehat{u})$ ($\widehat{q}$ instantaneous sediment flux and $\widehat{u}$ water velocity) formulae compared to the equivalent uncoupled results. It is also shown that including a dependence on $\widehat{h}$ (water depth) in $\widehat{q}$ can result in net deposition in the upper swash, and that with such a formula $\widehat{q}$ the shoreline motion over a plane mobile beach is ballistic in the uprush. Bed shear stress described by the Chezy law is further included in fully coupled simulations, and much reduced maximum inundation and net offshore sediment transport are predicted both

for $\widehat{q} = \widehat{q}(\widehat{u})$ and $\widehat{q} = \widehat{q}(\widehat{h}, \widehat{u})$. Although the net sediment flux at $\widehat{x} = 0$ under one PW01 event is still offshore, deposition in the middle or upper swash may be predicted when bed shear stress is included.

The fully coupled bed-load-only simulation with $\widehat{q} = A\widehat{u}^3$ (A dimensional bed mobility) for a single Hibberd and Peregrine (1979) (HP79) swash event predicts considerable deposition in the swash zone. A backwash bore develops, associated with which a bed step forms when the shoreline catches up with the backwash bore. The subsequent shoreline movement is obtained by the Riemann solution for a wet-dry dam-break problem with a bed step. A bed step also occurs under a solitary wave simulation; its height is much larger than that under the HP79 simulation. Bed step height is found to depend largely on the water depth on the seaward side of the step, which is related to the swash event and the step position.

The PW01 and HP79 swash events are also examined by the combined load model. Results show that suspended load results in deposition in the upper swash and erosion in the lower swash. However, pre-suspended sediment results in deposition in the lower swash, implying that net bed change due to suspended load in the lower swash could be depositional. The inclusion of suspended load has much smaller effect on the maximum inundation and swash hydrodynamics than bed load. The inclusion of bed load reduces the maximum inundation significantly; importantly, bed load results in the formation of a bed step and dominates the beach change near the bed step even when suspended load is dominant in the overall beach change.

Acknowledgements

First of all, I am extremely grateful to my supervisor Professor Nicholas Dodd for providing me the opportunity to undertake this work. I wish to thank him for all his guidance and dedicated support over the past three years. I also wish to acknowledge the help and useful ideas from my secondary supervisor Dr. Matthew Scase. I would also like to thank Dr. David Matthew Kelly and for his kind and helpful suggestions and encouragement.

Secondly, I would like to thank The China Scholarship Council and the International Office of The University of Nottingham for generously funding my Ph.D. research project.

I would also like to thank my colleagues in Infrastructure and Geomatics Division: Anurak, Meinard, Diego, Riccardo, Ben and Hannah. Thank you for all your great help and support. I also wish to thank my other officemates both past and present: Julia, Dave, Bruce, Karwan, Yv, Paloma, Evgenia, Jeff, Athina, Andy, Tom, Nick and John for making the office a pleasant place. Special thanks to Paloma and Diego for helping me through tough times, and also to Julia for playing squash with me. Additionally, I would also like to thank all my other friends in Nottingham, in particular: Wenjuan (Yuan and Deng), Ye, Juan, Hao,

Haowen and Huanlai.

Lastly, I wish to thank my family as well as my boyfriend Xiang Sun. Thank you very much for all your support and encouragement during all these years.

Contents

List of Figures

List of Tables

Nomenclature

[*] Denotes units of the parameter or variable

A [$\mathrm{s^2 m^{-1}}$]	Sediment mobility parameter for bed load ($q = u^3$)
A **[-]**	Coefficient matrix
α [-]	Beach slope
$\widehat{B}$ [m]	Bed elevation
B [-]	Dimensionless bed elevation
$\widehat{c}$ [-]	Volume concentration of suspended sediment
c [-]	Scaled volume concentration of suspended sediment
c_0 [-]	Reference concentration used for scaling
C_D [-]	Drag coefficient applicable to depth-averaged flow
$\widehat{D}$ [$\mathrm{ms^{-1}}$]	Deposition rate of suspended sediment
D [-]	Quantity in the solution of characteristic polynomial
$\Delta\widehat{t}$ [s]	Time interval
Δt [-]	Dimensionless time interval
$\Delta\widehat{x}$ [m]	Space interval in $\widehat{x}$ direction
Δx [-]	Dimensionless space interval in x direction
$\Delta\widehat{y}$ [m]	Space interval in $\widehat{y}$ direction

$\Delta\widehat{z}$ [m]	Space interval in $\widehat{z}$ direction
$\widehat{E}$ [ms^{-1}]	Erosion rate as suspended sediment
E_{in} [-]	Dimensionless energy inside the water column
E_{ex} [-]	Dimensionless energy due to external forces on the water column
$\widehat{\eta}$ [m]	Free surface elevation
F_{bed} [-]	Dimensionless force due to bed step
g [ms^{-2}]	Acceleration due to gravity
$\widehat{h}$ [m]	Water depth
h [-]	Dimensionless water depth
h_{st} [-]	Dimensionless still water depth
h_w [-]	Dimensionless wave height
λ_1, λ_{1h} [-]	Dimensionless purely hydrodynamic backward characteristic
λ_2, λ_{2h} [-]	Dimensionless purely hydrodynamic forward characteristic
$\lambda_{1,2,3}$ [-]	Dimensionless characteristics of the morphodynamic system excluding $\lambda = u$
λ_4 [-]	Wave speed associated with the transport of suspended load
m [-]	Dimensionless water mass
m_s [-]	Dimensionless water mass across a shock
$\widehat{m}_e$ [ms^{-1}]	Parameter of sediment entrainment as suspended load
m_e [-]	Dimensionless parameter of sediment entrainment as suspended load
μ [-]	Constant used to perform characteristic decomposition

ω [-]	Constant used to perform characteristic decomposition
$\widehat{p}$ [Nm^{-2}]	Pressure
p [-]	Bed porosity
$\widehat{q}$[$\mathrm{m}^2\mathrm{s}^{-1}$]	Instantaneous sediment flux
q [-]	Dimensionless instantaneous sediment flux
Q [-]	Dimensionless net sediment flux
σ [-]	Dimensionless bed mobility parameter
R [-]	Right eigenvector matrix
$\Re$ [-]	Dimensionless morphodynamic Riemann invariants
ρ [kgm^{-3}]	Water density
$\overrightarrow{S}$ [-]	Source term vector
$\widehat{t}$ [s]	Time
t [-]	Dimensionless time
t_i [-]	Dimensionless inundation time
t_d [-]	Dimensionless denudation time
$\widehat{\tau}$ [Nm^{-2}]	Bed shear stress
τ [-]	Dimensionless bed shear stress
$\widehat{\tau}_{crb}$ [Nm^{-2}]	Threshold shear stress for sediment movement as bed load
$\widehat{\tau}_{crs}$ [Nm^{-2}]	Threshold bed shear stress for sediment entrainment as suspended load
$\widehat{\tau}_0$ [Nm^{-2}]	Reference bed shear stress
Θ [-]	Quantity in the solution of characteristic polynomial

$\widehat{u}$ [ms^{-1}]	Water velocity in $\widehat{x}$ direction
$\bar{\widehat{u}}$ [ms^{-1}]	Depth-averaged water velocity in $\widehat{x}$ direction
u [-]	Dimensionless depth-averaged water velocity in x direction
$\overrightarrow{U}$ [-]	Vector of dependent variables
$\widehat{u}_{crb}$ [ms^{-1}]	Threshold velocity for sediment movement as bed load
u_{crb} [-]	Dimensionless threshold velocity for sediment movement as bed load
$\widehat{u}_{crs}$ [ms^{-1}]	Threshold velocity for sediment entrainment as suspended load
u_{crs} [-]	Dimensionless threshold velocity for sediment entrainment as suspended load
$\widehat{u}_0$ [ms^{-1}]	Reference velocity corresponding to reference bed shear stress
u_0 [-]	Dimensionless reference velocity corresponding to reference bed shear stress
$\widehat{v}$ [ms^{-1}]	Water velocity in $\widehat{y}$ direction
Γ [-]	Quantity in the solution of characteristic polynomial
$\widehat{w}$ [ms^{-1}]	Water velocity in $\widehat{z}$ direction
W [-]	Dimensionless bore (shock) velocity
$\widehat{w}_s$ [ms^{-1}]	Settling velocity of suspended sediment
w_s [-]	Dimensionless settling velocity of suspended sediment
$\widehat{x}$ [m]	Cross-shore distance

x [-]	Dimensionless cross-shore distance
x_s [-]	Dimensionless shoreline position or tip position
ξ [-]	Bed porosity parameter $\frac{1}{1-p}$
ξ_b [-]	Iribarren number
$\widehat{y}$ [m]	Long-shore distance
$\widehat{z}$ [m]	Vertical abscissa
z [-]	Dimensionless vertical abscissa
ζ [-]	Bore (shock) position

Subscripts:

l	Left constant region of the initial conditions in a Riemann problem
r	Right constant region of the initial conditions in a Riemann problem
L	Left side of a wave
R	Right side of a wave
i	Number of grid point in x direction
p	Point p

Superscripts:

j	Time level

Abbreviations:

STI	Specified time interval
MOC	Method of characteristics
NSWEs	Nonlinear shallow water equations

CHAPTER 1

Introduction

1.1 The swash zone

Coastal zones are the interfaces between the ocean and the land, and are continually changing because of the dynamic interaction between the ocean and the land. The boundary between the ocean and the land is known as the shoreline (zero water depth). The nearshore region is one of the coastal zones; it begins with the surf zone from seawards and ends at the shoreline (Masselink and Hughes, 2003; Kelly, 2009), see Figure 1.1. It is a highly dynamic region where waves, currents, and sediment interact through complex feedback mechanisms. Waves and currents are eroding and depositing sediment on a continuous basis, and the rates of erosion and deposition vary considerably in time.

As waves travel from deep water into intermediate and shallow water, a number of wave processes, e.g., wave shoaling, development of wave asymmetry and wave refraction, take place (Masselink and Hughes, 2003). During wave shoaling, a wave will break when the horizontal velocity of the water particle

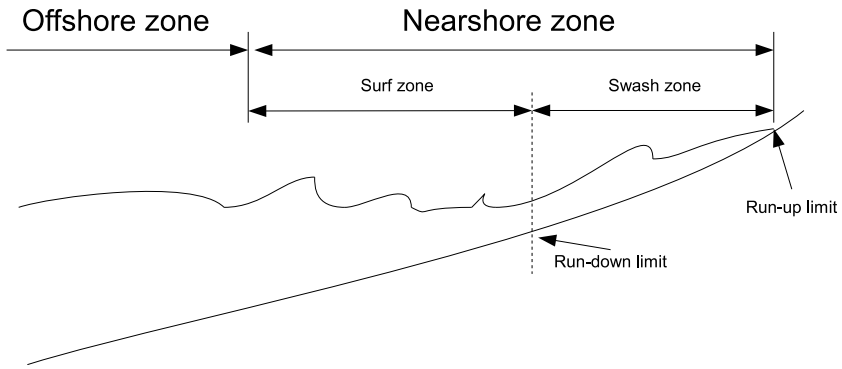

Figure 1.1: Definition of the nearshore region.

at the wave crest exceeds the wave velocity. The zone from the starting point of wave breaking to the run down limit of the moving shoreline is called the surf zone. When a wave reaches the shore, it still has a shoreward velocity and runs up and down the beach. The region successively covered and uncovered by the flow is called the swash zone, extending from the limit of run-down to the limit of run-up. The swash zone contains complex dynamic fluid motion and great energy dissipation, resulting in a considerable amount of sediment transport, as both bed- and suspended load, and therefore the beach elevation changes rapidly in this region.

As a wave runs up the beach and decelerates, onshore sediment transport occurs in the uprush; conversely offshore sediment transport occurs in much of the backwash. These phases both involve large amounts of sediment movement, but the net effect can be either erosion or deposition, depending on which large quantity prevails. Understanding the sediment dynamics of this region is very important as it can result, over many waves, in significant beach changes as well as very substantial erosion/deposition during just one event in the case

of a tsunami.

The beach change prediction is important for the human race in hazard prevention, coastal protection, etc. For instance, severe erosion can affect properties of the inhabitants, while increased deposition can cause obstruction to the ship ways or ports. Therefore, this work focuses on the beachface evolution in the swash zone.

1.2 1D swash zone hydrodynamics

The dynamics of nearshore flows are commonly described approximately by depth-averaged models, which often give the best balance between accuracy of resolution of the flow and numerical cost (Brocchini and Dodd, 2008). The depth-averaged models can be further divided into two general classes: models based on the nonlinear shallow water equations (NSWEs) and Boussinesq models. Brocchini and Dodd (2008) suggest that NSWE models are more suitable for the region from the midsurf to inner surf zone shorewards where water is very shallow and nonlinearity predominates, while Boussinesq models should be used before wave breaking where nonlinearity and dispersion are both significant. Thus, the NSWEs have been commonly used to describe the fluid motion in the swash zone (Whitham, 1958; Keller et al., 1960; Ho and Meyer, 1962; Shen and Meyer, 1963a,b; Hibberd and Peregrine, 1979), where the water is very shallow.

When a wave travels shorewards, sometimes it breaks and sometimes it does not; this depends on its own properties, such as the initial shape and velocity

distribution of the wave, as well as the beach over which it climbs. The type of wave breaking on a beach is dictated by the Iribarren number at breaking ξ_b (Mei, 1990), with medium to larger values ($0.4 < \xi_b < 3$) being typical of steeper slopes, smaller wave heights and / or larger periods. In such conditions waves frequently plunge or "collapse" on the beach as a bore nears or reaches the shoreline, leading to a swash event (uprush and backwash), with associated sediment movement.

Carrier and Greenspan (1958) have examined non-breaking (reflective) waves by analytical solutions. However, most real waves break when they travel shorewards, and considerable efforts have been made to understand the hydrodynamics of the swash associated with a breaking wave or a bore, namely bore-driven swash. There are some analytical solutions or approximations for the behaviour of a bore travelling to the shore and climbing up the beach.

Before a bore reaches the shore, it advances into water of non-uniform depth, and this is essentially a shock wave propagating into a non-uniform flow. Whitham (1958) discovered that the results of the work of Moeckel (1952) and Chisnell (1957) on the propagation of a shock wave into a non-uniform region were described very well by a simple rule. This rule is to apply the Riemann equation which is satisfied by the flow quantities along the advancing characteristic lines to the flow immediately behind the bore; therefore the rule is called the characteristic rule. It is straightforward to apply the characteristic rule to the propagation of a bore towards the shore over a uniformly sloping beach; this rule together with the shock relations can give rise to an approximate solution

for the bore motion. The results show that when a bore approaches the shore, the bore height may increase and then decrease, or decrease all the way to the shore, depending on the initial conditions of the bore; however, for all bores, the bore height approaches 0 at the shoreline and the velocity approaches a finite value. The finding of zero bore height and a finite velocity at the shoreline was further confirmed by the numerical results in Keller et al. (1960).

The work of Whitham (1958) and Keller et al. (1960) shows that the behaviour of different bores travelling shorewards into water on a beach of uniform slope converges as they approach the shore, and are largely independent of the initial conditions that give rise to them. This feature of "forgetting" the initial conditions is analogous to the behaviour of gas under some initial conditions. Ho and Meyer (1962) claimed that the "forgetfulness" was determined by the singularity of the governing differential equations at the initial shoreline position. However, it was pointed out that it was only the quantitative details of boundary conditions that it "forgot", and the velocity value at bore collapse was still determined by the initial and seaward boundary conditions. A detailed derivation of the asymptotic bore path solution for a bore advancing into still water on a beach of uniform slope before it arrives at the shore was also presented by Ho and Meyer (1962). Shen and Meyer (1963a) further extended the shoreward travel of a bore into still water to beaches of non-uniform slope.

The work on how the bore moves after it collapses at the shore was carried out by Shen and Meyer (1963b), henceforth SM63, in which the shoreline motion was interpreted as a singular characteristic boundary-value problem. Based

upon the particular properties of singular characteristics, SM63 derived an analytical solution for the shoreline motion, and an approximate solution for the flow close to the shoreline in the entire run-up and backwash. Furthermore, a new bore, associated with the limit characteristic line, was found possibly to develop both in the uprush and backwash. However, SM63 noted that the secondary bore was more likely to be observed in the backwash.

Peregrine and Williams (2001), henceforth PW01, generalised the SM63 approximate solution for the flow close to the shoreline to the whole swash, and the solution is identical to that of a dam-break problem on a sloping fixed beach (Watson et al., 1992). This exact PW01 solution for the flow in the whole swash zone provides a useful analytical model for the swash hydrodynamics (Pritchard and Hogg, 2005) and also verification data for numerical models (Briganti and Dodd, 2009; Kelly and Dodd, 2010; Zhu et al., 2012). Note that the work of Zhu et al. (2012) is part of the work in Chapter 6 in the present thesis. Moreover, the initial conditions of the dam-break description in PW01 can be utilised as the initial conditions of a swash event (Kelly and Dodd, 2010), to examine the morphodynamics in the swash zone.

More recently, Guard and Baldock (2007), henceforth GB07, pointed out that the PW01 swash event was only a special case of the SM63 swash, and that it neglected the momentum behind the bore and therefore underestimated the water depth in the lower and middle swash compared to experimental and other numerical results. Moreover, it is also pointed out by Antuono (2010) that this dam-break description for a swash event is not realistic as there is no water

in front of the dam, while in reality there is usually water in front of the bore. Pritchard et al. (2008) developed an analytical solution by the hodograph transformation technique and a boundary integral method, which could be applied to various boundary conditions. Moreover, the GB07 swash events were reproduced analytically by the method developed in Pritchard et al. (2008), and the results were in good agreement with those in GB07. Furthermore, the model predicted a secondary bore in both backwash and the uprush in long surf for swash events with different boundary conditions, which was previously predicted by SM63. The formation of a backwash bore in Pritchard et al. (2008) is shown to be closely related to the boundary conditions.

A great advance in the numerical simulation of bore-driven swash was made by Hibberd and Peregrine (1979), henceforth HP79, who investigated a uniform bore advancing into still water and then climbing over a sloping beach. A Lax Wendroff finite difference scheme, including a term to minimize numerical oscillations, was utilised to discretize the flux-conservative form of the NSWEs, and thus this numerical solution could generally be used to compute flows with shocks. In contrast to the PW01 swash event, there is continuously incoming water in the HP79 swash, and the beach comprises a flat part and a sloping part; therefore the solution predicts considerably deeper swash flow than the PW01 solution. Moreover, the continuously incoming water retards the rapidly receding backwash flow, resulting in a backwash bore. This finding confirmed the earlier prediction of the occurrence of a backwash bore in some swash events by SM63.

As previously mentioned, GB07 noticed that the PW01 swash event underestimated the mass and momentum behind the dam, therefore, they investigated several swash events, in which the boundary conditions vary with time, using the floating grid of characteristics method. The swash event with water coming in behind the dam gives considerably deeper swash flow than that in the PW01 swash event. The results also show that the PW01 solution provides a good description of the flow velocity in the upper swash. The appropriate boundary conditions for real swash were further suggested by GB07.

The existing bore-driven swash descriptions may be roughly divided into two classes: first essentially a dam-break problem (see e.g. Peregrine and Williams, 2001; Guard and Baldock, 2007; Pritchard et al., 2008), and secondly a bore propagating into still water, (see e.g. Hibberd and Peregrine, 1979; Antuono, 2010). Both of them are special cases of the SM63 swash, and the SM63 solution can be applied to the shoreline and its near region.

1.3 1D swash zone morphodynamics

Sediment transport is usually categorized into two modes: bed load and suspended load (Masselink and Hughes, 2003; Soulsby, 1997; Van Rijn, 2007a,b). The bed load maintains either continuous or intermittent contact with the bed (Masselink and Hughes, 2003), and it responds to change in flow instantaneously as therefore does the beach itself. Suspended load is transported by the flow at the flow velocity. Since it takes time for sediment to entrain into the water column and also to settle down onto the bed, both suspended sedi-

ment concentration in the water column and bed change caused by suspended load cannot in general adjust immediately to changes in the flow (Pritchard and Hogg, 2005).

Soulsby (1997) has pointed out that bed load is the dominant mode of sediment transport for low flow rates and / or sands of large grains, while when current speeds or wave conditions significantly exceed the threshold of sediment motion, sediment is entrained off the bed and into the flow. It was further pointed out by Soulsby (1997) that when the threshold of sediment motion was significantly exceeded, the proportion of sediment carried in suspension was generally much larger than that carried as bed load.

Beachface evolution in the swash zone is also associated with sediment transport in the form of both bed- and suspended load, depending on the sediment particle size and flow conditions (Elfrink and Baldock, 2002). Field measurements by Horn and Mason (1994) show that bed load dominates the backwash and the proportion of bed load and suspended load depends also on tidal conditions. Meanwhile, suspended load has been recognised as an important form of sediment transport in the swash zone by many researchers (Jackson et al., 2004; Masselink et al., 2005; Blenkinsopp et al., 2011; Pritchard and Hogg, 2005). The suspended sediment concentration and transport rate in the swash zone are about one order of magnitude greater than those in the surf zone (see Masselink et al., 2005). However, the lack of field data causes uncertainty in the predominant mode of sediment transport under the swash flow.

The models for simulating the transport of bed- and suspended load in the

swash zone can generally be divided into two classes: first, those in which the bed change is assumed to have no feedback on the flow, so called decoupled models; secondly, those in which the shallow water equations and the bed evolution equation are solved simultaneously, namely fully coupled models.

Kobayashi and Johnson (2001) developed a decoupled suspended sediment transport model for the surf and swash zone, in which the sediment suspension was associated with turbulence generated by wave breaking and bottom friction. The hydrodynamic input was based on the NSWEs including bottom friction. The sediment storage and advection terms cause the local sediment concentration not to be instantaneously related to the local turbulence, and results in a settling lag.

Pritchard and Hogg (2005), henceforth PH05, also presented an uncoupled analytical solution for suspended sediment transport under the PW01 swash flow. The sediment entrainment rate was assumed only to be related to bed shear stress, essentially the water velocity. The sediment transport was divided into two states for investigation in PH05: steady-state, i.e., $\widehat{c} = \widehat{c}_{eq}$, where $\widehat{c}$ is suspended sediment concentration and $\widehat{c}_{eq}$ is that in equilibrium state, and non-steady-state, i.e., $\widehat{c} \neq \widehat{c}_{eq}$. The steady-state transport in unsteady flows usually occurs only when sediment is very coarse or the water is very shallow, and it is assumed that the sediment entrained into the water is instantaneously balanced by deposition at each point in the swash zone. As the sediment flux caused by steady-state suspended load is $\widehat{q} = \widehat{h}\widehat{c}_{eq}$, where $\widehat{q}$ is sediment flux and $\widehat{h}$ is water depth, and because $\widehat{c}_{eq}$ is a fuction of velocity $\widehat{u}$, the suspended

sediment flux in the steady-state is essentially a total load or bed load description, i.e., $\widehat{q} = \widehat{q}(\widehat{h}, \widehat{u})$. However, the commonly used sediment flux for total load or bed load, e.g., the Bailard formula (Bailard and Inman, 1981), is independent of $\widehat{h}$, so a range of sediment flux formulae $\widehat{q} = \widehat{q}(\widehat{h}, \widehat{u})$ or $\widehat{q} = \widehat{q}(\widehat{u})$ were examined to investigate steady state sediment transport in the PW01 swash. The results show that the intrinsic asymmetry between uprush and backwash velocities in the PW01 swash tends to encourage offshore sediment transport for all the examined sediment transport formulae $\widehat{q}(\widehat{h}, \widehat{u})$ and $\widehat{q}(\widehat{u})$. In the non-steady state, as $\widehat{c} \neq \widehat{c}_{eq}$, the amount of sediment entrained into the water is not equal to the amount of sediment deposited, and the remaining suspended sediment is transported along with the flow, resulting in a settling lag. In non-steady-state transport, suspended sediment was further categorized into sediment entrained within the swash zone and sediment pre-suspended by the bore and input into the swash zone along the seaward boundary, to examine the roles of settling lag and pre-suspended sediment. It was found that the pre-suspended load seemed to be more effective in sediment onshore movement than the settling lag, and was a great contributor for sediment onshore transport. Although the intrinsic asymmetry between uprush and backwash velocities tends to encourage offshore sediment transport, a large concentration of pre-suspended sediment may lead to net deposition. Therefore, PH05 suggested that suspended sediment should be considered in the swash morphodynamic simulations to give more realistic results.

As sediment movement is determined by the hydrodynamic conditions, Pritchard

(2009) investigated further the transport of suspended sediment under the GB07 swash events, which predict deeper swash flow in the lower and middle swash than the PW01 swash. The hydrodynamics in the uncoupled simulations in Pritchard (2009) is obtained by the analytical model in Pritchard et al. (2008), and the suspended sediment transport simulation is based on the same suspended sediment transport model as that in PH05. However, the overall pattern of the sediment transport under different hydrodynamics is qualitatively unchanged, and remains offshore if there is no pre-suspended sediment. Net erosion or deposition in the swash zone still largely depends on the amount of sediment suspended by the incoming bore and advected into the swash zone.

Kelly and Dodd (2010), hereinafter KD10, developed a fully coupled morphodynamic model, which couples the shallow water equations with a sediment conservation equation. In the sediment conservation equation, only bed load is considered, and the sediment flux for bed load is $\widehat{q} = A\widehat{u}^3$, where A is a dimensional bed mobility parameter. In KD10, the specified time interval (STI) method of characteristics (MOC) was used to solve the governing equations simultaneously, and the shock is solved by the shock fitting technique (Moretti, 1987). Moreover, the solutions for embedded shocks belonging to different characteristics were presented. This model was then utilised to simulate one single PW01 swash event to examine the beachface evolution. It was found that a morphodynamic shock formed shoreward of the initial shoreline position when the local flow reversed, and gradually developed into a strong shock. Additionally, net erosion was observed all over the whole swash zone, consis-

tently with the equivalent uncoupled simulation in PH05. However, the comparison between the results in KD10 and PH05 shows that the net erosion and maximum inundation in the fully coupled simulation are considerably reduced from the uncoupled ones.

To conclude, the beachface evolution caused by bed load or total load has been examined by many researchers (Pritchard and Hogg, 2005; Kelly and Dodd, 2010; Zhu et al., 2012). However, it was pointed out by Masselink et al. (2009) according to field measurements that velocity-based models, i.e. total load or bed load only model, were more problematic, particularly lower in the swash zone where swash interactions were more prevalent. Under steady or quasi-steady flows, suspended load is usually in an equilibrium state, and bed- and suspended load can be approximately described as total load (Soulsby, 1997); however, for unsteady swash flows bed load (total load) and suspended load are likely to result in different bed patterns due to the different transport mechanism of bed- and suspended load (Pritchard and Hogg, 2005).

Simulations of Kobayashi and Johnson (2001) and Pritchard and Hogg (2005) model the transport of suspended load but do not include bed load, and do not couple the swash flow with the beach change caused by sediment transport, neglecting the effects of sediment transport and beachface evolution on the hydrodynamics. Note that a bed step occurs associated with a shock in the swash flow when bed load is included (Kelly and Dodd, 2010; Zhu et al., 2012), which might be important for the development of bars in the swash zone. Furthermore, the fully coupled simulation by KD10 shows the great effect of bed load

on the swash hydrodynamics. Due to the uncertainty of the relative proportion of bed- and suspended load in the swash zone, both loads are of possible great importance for the swash simulation. Moreover, the comparison of the results in KD10 and PH05 shows the importance of fully coupling water flow and bed evolution. Thus, the development of a fully coupled model including both bed- and suspended load is a logical next step.

1.4 1D dam-break problem

From the review of the swash zone dynamics research progress, it is noticed that the swash simulation is closely related to the dam-break problem. In fact, the dam-break problem provides the simplest available model for a number of important phenomena (Pritchard and Hogg, 2002). Therefore, dam-break problems on both fixed and mobile beds are one of the focuses of this work and in this section we will look at the progress in this area, and in particular, at a generalised dam-break problem with water (not necessary still) on both sides of the dam.

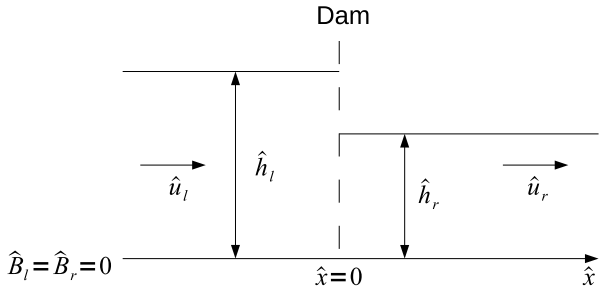

Figure 1.2: Initial conditions of a general dam-break problem.

The initial conditions of a dam-break problem with constant water depth and velocity on both sides are shown in Figure 1.2. Assume that a horizontal channel is separated by a dam into two parts at $\widehat{x} = 0$, and the water depth upstream ($\widehat{x} \leq 0$) is $\widehat{h}_l$ and that downstream ($\widehat{x} \geq 0$) is $\widehat{h}_r$, with $\widehat{h}_r < \widehat{h}_l$. The water velocities on the left and right sides of the dam are denoted as $\widehat{u}_l$ and $\widehat{u}_r$. The dam is assumed to collapse at $\widehat{t} = 0$. The dam-break problem with $\widehat{h}_l > \widehat{h}_r > 0$ is here called the wet-wet dam-break problem, and that with $\widehat{h}_l > \widehat{h}_r = 0$ is called the wet-dry dam-break problem.

1.4.1 Fixed bed dam-break problem

The 1D dam-break flow on a fixed bed can be modelled using the NSWEs (Stoker, 1957; Toro, 2001), if the dam collapses in a sufficiently small time. The NSWEs constitute a hyperbolic system, and therefore the generalization of such a dam-break problem with constant water depth and velocity on a fixed bed is a Riemann problem (Toro, 1997).

There are a variety of analytical solutions for dam-break problems on a fixed bed when the bed friction is not taken into account. Stoker (1957) investigated a dam-break problem, in which there was still water on both sides of the dam, over a fixed bed by the method of characteristics. In this case, the wave has two dominant features: a right-facing wave travels into shallow water, raising the depth immediately and a left-facing wave travels into deep water and reduces the water depth of the left side. To be more accurate, the wave structure is of three constant regions connected by a rarefaction fan and a shock. Moreover,

a dam-break problem over a dry flat bed (Ritter, 1892) was also examined, and the corresponding wave structure is a rarefaction fan connecting the original constant region and the dry bed. Toro (2001), also based on the method of characteristics, investigated dam-break problems of various initial conditions, e.g. different initial velocity or depth; possible wave structures as well as the determining criteria were concluded. Once the wave structure is determined, the waves can subsequently be solved. The rarefaction wave is solved using the Riemann invariants along characteristic lines, while the shock is solved by Rankine-Hugoniot shock conditions (Stoker, 1957; Toro, 2001). It was pointed out by Toro (2001) that a dry bed can only be adjacent to a rarefaction wave.

Note that in the above analytical solutions for dam-break problems, bed friction has been neglected for simplicity. However, bed friction exists, and it may become significant at the wave tip in the wet-dry dam-break flows, and therefore has considerable effect on the flow. Dam-break problems with bottom friction has also been addressed by some researchers (Dressler, 1952; Whitham, 1955; Hogg and Pritchard, 2004).

Dressler (1952) examined the effects of bed friction on a dam-break problem over a fixed flat bed, by introducing a friction term into the NSWEs, and the governing equations comprise a nonhomogeneous system. In order to get some quantitative understanding, perturbations were introduced to the Ritter solution (Stoker, 1957; Ritter, 1892), by imposing on it an asymptotic expression related to bed friction. The Ritter solution with a first-order asymptotic expression related to the resistance effect was presented. However, the pertur-

bation term becomes singular near the tip, therefore it was pointed out that a boundary-layer was necessary to account for this tip.

Whitham (1955) also examined the hydraulic effects of bed friction in the dam-break problem; it was assumed that the resistance only existed in the tip region near the wave front, and the main flow was solved by the Ritter solution (Ritter, 1892). In the tip region, the water velocity was assumed to vary very little in the direction $\widehat{x}$ and to be a function only of time $\widehat{t}$. The Pohlhausen method, which is often used in conventional boundary-layer problems, was applied to the boundary layer near the wave front. The water depth and velocity in the tip region were then solved; close agreement was found with those in Dressler (1952).

The wet-wet dam-break problem on a fixed flat bed, but with a discontinuity in bed level at $\widehat{x} = 0$, was examined by Bernetti et al. (2008). A stationary shock develops at the position of the bed step, i.e., $\widehat{x} = 0$, and possible wave structures were analysed and presented. The results show that the newly formed constant region in Toro (2001) is separated into two constant regions by the stationary shock at $\widehat{x} = 0$, when a bed step is present. Note that in the dam-break problem with $\widehat{h}_l > \widehat{h}_r > 0$, there is no rarefaction wave on the right side of the stationary shock. However, in the wet-dry dam-break problem over a discontinuous bed, the dry bed on the right side can only be adjacent to a rarefaction wave (Toro, 2001). Therefore the wave structure for the wet-dry dam-break problem over a fixed bed with a discontinuity in bed level might be quite different from those for the equivalent wet-wet dam-break problems in Bernetti et al. (2008).

Considering the great significance of the fixed bed dam-break problem for the corresponding mobile bed dam-break problem, and the emergence of a discontinuity in the beach profile in the swash zone (see Kelly and Dodd, 2010; Zhu et al., 2012), it seems desirable to examine the wet-dry dam-break problem over a fixed bed with a bed step. Note that the NSWEs are usually not valid near discontinuities, because the assumption of gradual variation in the x direction no longer applies. However, the NSWEs are used to model shocks and discontinuities in the present work in order to achieve a balance between the accuracy of resolution of the flow and numerical cost.

1.4.2 Mobile bed dam-break problem

The fully coupled systems for the dam-break problem over a flat mobile bed usually comprise three or more equations, constituting a hyperbolic system. It was pointed out by Jeffrey (1976) that a direct extension of the existence of a Riemann invariant along a characteristic line for the system which contains more than two equations was not possible. However, generalised Riemann invariants have been introduced to solve this kind of hyperbolic system, see Jeffrey (1976) for further details.

Capart and Young (1998) examined a wet-dry dam-break problem over a granular bed by numerical method and experiment, and it was found that near the wave centre the free surface broke backwards and a hydraulic jump formed. It was bed friction and bed deformation that caused the characteristics of the same family to converge and form a shock wave, and the numerical results

also confirmed this. Fraccarollo and Capart (2002) also examined the sudden erosional flow initiated by the release of a dam-break over a dry loose sediment bed. Three sharp interfaces (air-water boundary, water-liquid-granular boundary and liquid-granular-bed boundary) were introduced to describe the vertical flow structure. The Riemann solution was used to determine the wave structure when bed friction was not included. There is one constant state, two smoothly varied simple waves and a morphodynamic shock at the flow tip. Moreover, two sets of experiments, which differ primarily in the sediment material used and one of which is the experiment in Capart and Young (1998), were also conducted. The numerical predictions compare favourably with the experimental results for loose sediment. The main difference between the two sets of experimental results is the hydraulic jump near the wave centre, and this was suggested to be caused by the different bed material used.

Kelly and Dodd (2009), henceforth KD09, also investigated a wet-dry dam-break problem over a mobile flat bed; the Riemann solution for the fully coupled system with the NSWEs and a bed evolution formula was presented. The flow structure in KD09 is similar to that of Fraccarollo and Capart (2002), but slightly different at the tip. This might be caused by different assumptions of vertical flow structure in the above two studies. The solution over a flat mobile bed in KD09 is successfully used as initial data for the swash simulation based on a dam-break problem over a sloping mobile bed, i.e., PW01 swash.

In the wet-dry dam-break problem in both Fraccarollo and Capart (2002) and KD09 (see also Kelly, 2009), the water is motionless and the bed is continuous at

the initial time. However, a generalised wet-dry dam-break problem on a mobile bed, in which the water may have an initial velocity and the initial bed may have a discontinuity, is of great interest, both from the theoretical and practical point of view. For instance, in some morphodynamic swash simulations, the retreating shoreline sometimes catches up with the backwash bore (Zhu et al., 2012; Erikson et al., 2005), and there is a dry bed on the right side of the new shoreline but water on the left side, and there is a bed step at the shoreline. The Riemann solution of a wet-dry dam-break problem over a flat mobile bed with a bed step could provide a technique to analyse the subsequent movement of the new shoreline in such swash simulations.

The wet-dry dam-break problem can be considered as a special case of a family of wet-wet dam-break problems, in which there is water on both sides of the dam. The Riemann solution for a wet-wet dam-break problem could be utilised for analysing the wave structure after a shock-shock collision. Moreover, dams with water on both sides are often observed across rivers, therefore it is worth examining the analytical solution for the wet-wet dam-break problem.

1.5 Motivation and objectives of this work

In recent years, the desire for developing fully coupled models to solve the swash flow and beachface evolution simultaneously has been increasing. Although there are no analytical solutions describing fully coupled swash flow and bed change, a number of numerical fully coupled models have been developed. What should be emphasised is the need for accuracy in the prediction

of the sediment transport in swash zones; during a single swash event, the net sediment transport, depending on the swash flow and beach conditions, will be the difference between two large quantities of sediment transport in the uprush and backwash, and therefore in general is a small quantity. Therefore, relatively small inaccuracies in either phase can result in completely wrong net predictions (e.g., deposition instead of erosion). Furthermore, after many swash events even a small net transport will be magnified. Consequently, a small inaccuracy in the prediction of the net sediment transport can be magnified as time increases, which can cause failure in the beachface prediction. Thus, the present work aims to develop relatively accurate and fully coupled solutions for the beachface evolution in a single swash event, which could provide some guidance for more complicated numerical simulations.

To achieve high accuracy, we need to choose the numerical scheme for the model very carefully. Since shocks have been recognised as common in the swash zone, shock solutions are aimed to be included in the fully coupled model. There are two main kinds of shock solution techniques for unsteady flows: shock capturing and shock fitting.

In shock capturing schemes discontinuities are represented by a steep gradient over a few mesh points, whereas they are treated as moving internal boundaries in shock fitting schemes (Moretti, 1987; Kelly, 2009). Moretti (1987) has pointed out that the purpose of shock capturing was to provide a mathematical foundation for simple general-purpose codes for simplicity, whereas the purpose of shock fitting is physical justification of codes around a shock. In most numeri-

cal models the shock capturing technique is utilised, which could suffer from a large amount of numerical diffusion or spurious numerical oscillation around the bores (Kelly, 2009). Many kinds of filters are introduced to stabilize the numerical scheme, which do help, however they sometimes make the numerical method complicated, which violates the principal purpose of the shock capturing scheme. However, it should be noted that the shock capturing scheme also has advantages. Under the shock capturing scheme, discontinuities do not have to be treated explicitly as moving boundaries, and the numerical code is much simpler if an appropriate filter is used; the 1D code can be extended to 2D more easily.

Since the shock fitting technique deals with the shock from a physical standpoint, it is suggested as the most reliable, accurate technique in fluid dynamics (Moretti, 2002). Considering the advantages of the shock fitting technique, in the present work we choose to utilise the method of characteristics (MOC), which can implement the shock fitting technique easily, to develop fully coupled models. Moreover, because of the advantages of the specified time interval (STI) scheme in time saving over the grid of characteristics (GC) scheme (Kelly, 2009; Kelly and Dodd, 2009), as well as its quite good accuracy, the STI MOC scheme is used in the swash simulations in this work.

From the review of modelling beachface evolution in the swash zone, there are few fully coupled models for both bed- and suspended load, thus in this work we aim to include both loads in the fully coupled model. However, we start with the development of a fully coupled morphodynamic model includ-

ing only bed load. There are several empirical formulae for the transport of bed load (Soulsby, 1997); we therefore extend the solution in KD10 for $\widehat{q} = A\widehat{u}^3$ to a more general formula $\widehat{q} = \widehat{q}(\widehat{h}, \widehat{u})$, and the model including only bed load is called a bed-load-only model. The developed bed-load-only model is then used to examine the qualitative differences in the beachface evolution with the same series of sediment transport formulae as those in PH05 under the PW01 swash event and, importantly, whether the same swash event can yield net sediment movement of opposing signs depending on which sediment transport formula is used. The results of the fully coupled simulations are also compared with the equivalent uncoupled simulations in PH05. Furthermore, bed shear stress described by the Chezy law is included in the bed-load-only PW01 swash simulation to examine the effects of bed shear stress on swash flow and beachface evolution.

It has been pointed out that the PW01 swash event is not realistic, underestimating the swash flow in the lower and middle swash; therefore we also examine beachface evolution under the HP79 swash event by the bed-load-only model in § 6. However, the PW01 and HP79 swash events are more likely to be appropriate for describing extreme waves, so the swash event driven by a solitary wave is also examined by the bed-load-only model in § 6 to get further understanding of beachface evolution under a single wave impinging on a natural beach and also the difference between different swash events.

Starting from the developed bed-load-only model, we further include suspended load, and develop a fully coupled model including both bed- and suspended

load, referred to as a combined load model. The PW01 and HP79 swash events are simulated by the combined load model in § 7, and the results in the bed-load-only and combined load simulations are compared. The roles of bed- and suspended load are identified.

The previous review of the swash dynamics research progress shows that the swash simulation is closely related to a dam-break problem, and the Riemann solutions of dam-break problems could provide theoretical tools for wave interactions in the swash simulation. Therefore, a generalised wet-dry dam-break problem on a fixed / mobile bed, in which the water has an initial velocity and in which a discontinuity in the initial bed level exists, is examined in § 3. Moreover, the Riemann solution of a wet-wet dam-break problem over a flat erodible bed, which could be utilised for analysing the wave structure after a shock-shock collision, is also investigated in this work. However, the water on both sides of the dam is motionless.

CHAPTER 2

1D mathematical model

In this chapter, the governing equations for water flows and bed evolution on an erodible beach are presented. Due to the shallow water depth in the swash zone, it has been widely accepted that the flow in this zone is well described by the NSWEs. Thus, the 1D NSWEs, in which bed friction is excluded for simplification, are used to describe the water motion. Here the 1D NSWEs are derived from Euler equations, in which the effects of viscosity, and compressibility are assumed to be negligible. During the derivation, the long wave assumption, that is the depth of water is very small compared with a wavelength, and zero vorticity assumption are used. The bed evolution due to sediment transport is described by a bed evolution equation including bed- and suspended load.

Firstly, the governing equations for the bed-load-only model are presented. Thereafter, the coupled equations are characteristically decomposed. Then the bed evolution equation, comprising both bed- and suspended load, is fully coupled with the NSWEs in the combined load model. In the combined load system, there is also another equation describing the transport of suspended load.

Therefore, there are four equations in the combined load system, and four Riemann equations are obtained by characteristic decomposition. Since the governing equations and the corresponding solutions for bed-load-only and combined load models are different, they are given in two separate sections.

2.1 1D nonlinear shallow water equations (NSWEs)

In this section we derive the 1D NSWEs from the Euler equations.

The three-dimensional (3D) equation of continuity, representing the conservation of mass, is (Stoker, 1957, p. 3-15)

$$\widehat{u}_{\widehat{x}} + \widehat{v}_{\widehat{y}} + \widehat{w}_{\widehat{z}} = 0, \tag{2.1}$$

where the positive $\widehat{z}$-axis is vertically upward, and the $\widehat{x}$, $\widehat{y}$ plane is horizontal. $(\widehat{u}, \widehat{v}, \widehat{w})$ are the components of the dimensional particle velocity $\overrightarrow{\widehat{u}}$ along $\widehat{x}$, $\widehat{y}$ and $\widehat{z}$ directions. The subscripts $\widehat{x}$, $\widehat{y}$ and $\widehat{z}$ represent partial derivatives with respect to $\widehat{x}$, $\widehat{y}$ and $\widehat{z}$ directions, e.g., $\widehat{u}_{\widehat{x}} = \dfrac{\partial \widehat{u}}{\partial \widehat{x}}$. Note that variables with a hat are dimensional.

The 3D equations of fluid motion in terms of the Euler variables are (Stoker, 1957, p. 3-15)

$$\widehat{u}_{\widehat{t}} + \widehat{u}\widehat{u}_{\widehat{x}} + \widehat{v}\widehat{u}_{\widehat{y}} + \widehat{w}\widehat{u}_{\widehat{z}} = -\frac{1}{\rho}\widehat{p}_{\widehat{x}}, \tag{2.2}$$

$$\widehat{v}_{\widehat{t}} + \widehat{u}\widehat{v}_{\widehat{x}} + \widehat{v}\widehat{v}_{\widehat{y}} + \widehat{w}\widehat{v}_{\widehat{z}} = -\frac{1}{\rho}\widehat{p}_{\widehat{y}}, \tag{2.3}$$

$$\widehat{w}_{\widehat{t}} + \widehat{u}\widehat{w}_{\widehat{x}} + \widehat{v}\widehat{w}_{\widehat{y}} + \widehat{w}\widehat{w}_{\widehat{z}} = -\frac{1}{\rho}\widehat{p}_{\widehat{z}} - g, \tag{2.4}$$

where $\widehat{t}$ is dimensional time, ρ is the density of fluid, $\widehat{p}$ is pressure, and g rep-

resents the acceleration due to gravity. Since the fluid is assumed to be incompressible, the density ρ is taken as a constant.

Assume that there is no velocity component along the $\widehat{y}$-direction, i.e., $\widehat{v}(\widehat{x},\widehat{y},\widehat{z},\widehat{t}) = 0$, therefore (2.3) disappears and the 3D equations of continuity and fluid motion become two dimensional ($\widehat{x}$, $\widehat{z}$ plane)

$$\widehat{u}_{\widehat{x}} + \widehat{w}_{\widehat{z}} = 0, \tag{2.5}$$

$$\widehat{u}_{\widehat{t}} + \widehat{u}\widehat{u}_{\widehat{x}} + \widehat{w}\widehat{u}_{\widehat{z}} = -\frac{1}{\rho}\widehat{p}_{\widehat{x}}, \tag{2.6}$$

$$\widehat{w}_{\widehat{t}} + \widehat{u}\widehat{w}_{\widehat{x}} + \widehat{w}\widehat{w}_{\widehat{z}} = -\frac{1}{\rho}\widehat{p}_{\widehat{z}} - g. \tag{2.7}$$

The kinematic condition at the free surface is

$$(\widehat{\eta}_{\widehat{t}} + \widehat{u}\widehat{\eta}_{\widehat{x}} - \widehat{w})|_{\widehat{\eta}} = 0 \Rightarrow \widehat{w}|_{\widehat{\eta}} = \widehat{\eta}_{\widehat{t}} + \widehat{u}|_{\widehat{\eta}}\widehat{\eta}_{\widehat{x}}, \tag{2.8}$$

where $\widehat{\eta}$ is the elevation of the free surface.

At the bottom, the boundary condition is

$$(\widehat{B}_{\widehat{t}} + \widehat{u}\widehat{B}_{\widehat{x}} - \widehat{w})|_{\widehat{B}} = 0 \Rightarrow \widehat{w}|_{\widehat{B}} = \widehat{B}_{\widehat{t}} + \widehat{u}|_{\widehat{B}}\widehat{B}_{\widehat{x}}, \tag{2.9}$$

where $\widehat{B}$ is bed level.

Integrating (2.5) from $\widehat{B}$ to $\widehat{\eta}$ with respect to $\widehat{z}$, and replacing $\widehat{w}|_{\widehat{\eta}}$ and $\widehat{w}|_{\widehat{B}}$ from (2.8) and (2.9) gives

$$\int_{\widehat{B}}^{\widehat{\eta}} \widehat{u}_{\widehat{x}} d\widehat{z} + \widehat{w}|_{\widehat{B}}^{\widehat{\eta}} = 0 \Rightarrow \int_{\widehat{B}}^{\widehat{\eta}} \widehat{u}_{\widehat{x}} d\widehat{z} + \widehat{\eta}_{\widehat{t}} + \widehat{u}|_{\widehat{\eta}}\widehat{\eta}_{\widehat{x}} - \widehat{B}_{\widehat{t}} - \widehat{u}|_{\widehat{B}}\widehat{B}_{\widehat{x}} = 0. \tag{2.10}$$

From the Leibniz law, we have

$$\begin{aligned} \frac{\partial}{\partial \widehat{x}} \int_{\widehat{B}}^{\widehat{\eta}} \widehat{u} d\widehat{z} &= \widehat{u}|_{\widehat{\eta}}\widehat{\eta}_{\widehat{x}} - \widehat{u}|_{\widehat{B}}\widehat{B}_{\widehat{x}} + \int_{\widehat{B}}^{\widehat{\eta}} \widehat{u}_{\widehat{x}} d\widehat{z} \\ \Rightarrow \int_{\widehat{B}}^{\widehat{\eta}} \widehat{u}_{\widehat{x}} d\widehat{z} &= \frac{\partial}{\partial \widehat{x}} \int_{\widehat{B}}^{\widehat{\eta}} \widehat{u} d\widehat{z} - \widehat{u}|_{\widehat{\eta}}\widehat{\eta}_{\widehat{x}} + \widehat{u}|_{\widehat{B}}\widehat{B}_{\widehat{x}}. \end{aligned} \tag{2.11}$$

Substituting (2.11) into (2.10) gives

$$\frac{\partial}{\partial \widehat{x}} \int_{\widehat{B}}^{\widehat{\eta}} \widehat{u} d\widehat{z} + (\widehat{\eta} - \widehat{B})_{\widehat{t}} = 0. \tag{2.12}$$

We can write $\int_{\widehat{B}}^{\widehat{\eta}} \widehat{u} d\widehat{z} = \widehat{h}\bar{\widehat{u}}$, where $\widehat{h} = \widehat{\eta} - \widehat{B}$ is water depth and $\bar{\widehat{u}}$ is depth-averaged velocity. Therefore (2.12) becomes

$$\widehat{h}_{\widehat{t}} + (\widehat{h}\bar{\widehat{u}})_{\widehat{x}} = 0. \tag{2.13}$$

The Lagrangian form of (2.7) is

$$\frac{D\widehat{w}}{D\widehat{t}} = -\frac{1}{\rho}\widehat{p}_{\widehat{z}} - g, \tag{2.14}$$

where $\dfrac{D\widehat{w}}{D\widehat{t}}$ is the particle derivative of $\widehat{w}$, and it represents the acceleration of a water particle along $\widehat{z}$-direction. Based on the long wave assumption, there is no vertical acceleration, i.e., $\dfrac{D\widehat{w}}{D\widehat{t}} = 0$, which gives $\widehat{p}_{\widehat{z}} = -\rho g$. As the pressure at the free surface $\widehat{z} = \widehat{\eta}$ is Pa (constant), since $\widehat{\eta} = \widehat{\eta}(\widehat{x}, \widehat{t})$,

$$\widehat{p}(\widehat{x}, \widehat{z}, \widehat{t}) = \rho g(\widehat{\eta} - \widehat{z}) + Pa \tag{2.15}$$

is obtained.

Multiplying (2.5) by $\widehat{u}$ and combining with (2.6) gives

$$\widehat{u}_{\widehat{t}} + (\widehat{u}\widehat{u})_{\widehat{x}} + (\widehat{u}\widehat{w})_{\widehat{z}} = -\frac{1}{\rho}\widehat{p}_{\widehat{x}}. \tag{2.16}$$

Integrating (2.16) from $\widehat{B}$ to $\widehat{\eta}$ with respect to $\widehat{z}$ gives

$$\int_{\widehat{B}}^{\widehat{\eta}} \widehat{u}_{\widehat{t}} d\widehat{z} + \int_{\widehat{B}}^{\widehat{\eta}} (\widehat{u}^2)_{\widehat{x}} d\widehat{z} + [\widehat{u}\widehat{w}]_{\widehat{B}}^{\widehat{\eta}} = -\frac{1}{\rho}\int_{\widehat{B}}^{\widehat{\eta}} \widehat{p}_{\widehat{x}} d\widehat{z}. \tag{2.17}$$

From (2.15), $\widehat{p}_{\widehat{x}} = \rho g \widehat{\eta}_{\widehat{x}}$ is obtained; substituting $\widehat{p}_{\widehat{x}}$ into (2.17) and applying the Leibniz law gives

$$\begin{aligned} &\frac{\partial}{\partial \widehat{t}} \int_{\widehat{B}}^{\widehat{\eta}} \widehat{u} d\widehat{z} - \widehat{\eta}_{\widehat{t}}\widehat{u}|_{\widehat{\eta}} + \widehat{B}_{\widehat{t}}\widehat{u}|_{\widehat{B}} + \frac{\partial}{\partial \widehat{x}} \int_{\widehat{B}}^{\widehat{\eta}} \widehat{u}^2 d\widehat{z} - \widehat{\eta}_{\widehat{x}}(\widehat{u}^2)|_{\widehat{\eta}} \\ &+ \widehat{B}_{\widehat{x}}(\widehat{u}^2)|_{\widehat{B}} + (\widehat{u}\widehat{w})|_{\widehat{B}}^{\widehat{\eta}} = -\frac{1}{\rho}\frac{\partial}{\partial \widehat{x}} \int_{\widehat{B}}^{\widehat{\eta}} \rho g \widehat{\eta} d\widehat{z} + g\widehat{\eta}_{\widehat{x}}\widehat{\eta} - g\widehat{B}_{\widehat{x}}\widehat{\eta}. \end{aligned} \tag{2.18}$$

From (2.8) and (2.9), we have $(\widehat{u}\widehat{w})|_{\widehat{B}}^{\widehat{\eta}} = \widehat{u}|_{\widehat{\eta}}(\widehat{\eta}_{\widehat{t}} + \widehat{u}|_{\widehat{\eta}}\widehat{\eta}_{\widehat{x}}) - \widehat{u}|_{\widehat{B}}(\widehat{B}_{\widehat{t}} + \widehat{u}|_{\widehat{B}}\widehat{B}_{\widehat{x}})$, and (2.18) is reduced to

$$\begin{aligned}
\frac{\partial}{\partial \widehat{t}}\int_{\widehat{B}}^{\widehat{\eta}} \widehat{u}d\widehat{z} + \frac{\partial}{\partial \widehat{x}}\int_{\widehat{B}}^{\widehat{\eta}} \widehat{u}^2 d\widehat{z} &= -g\frac{\partial(\widehat{\eta}(\widehat{\eta}-\widehat{B}))}{\partial \widehat{x}} + g(\widehat{\eta}-\widehat{B})_{\widehat{x}}\widehat{\eta} \\
&= -g\widehat{\eta}_{\widehat{x}}(\widehat{\eta}-\widehat{B}) \\
&= -g(\widehat{\eta}-\widehat{B})_{\widehat{x}}(\widehat{\eta}-\widehat{B}) - g\widehat{B}_{\widehat{x}}(\widehat{\eta}-\widehat{B}) \\
&= -\frac{1}{2}g((\widehat{\eta}-\widehat{B})^2)_{\widehat{x}} - g\widehat{B}_{\widehat{x}}(\widehat{\eta}-\widehat{B}). \qquad (2.19)
\end{aligned}$$

Based on the assumption of no vorticity, $\int_{\widehat{B}}^{\widehat{\eta}} \widehat{u}^2 d\widehat{z} = \widehat{h}\bar{\widehat{u}}^2$, and with $\int_{\widehat{B}}^{\widehat{\eta}} \widehat{u}d\widehat{z} = \widehat{h}\bar{\widehat{u}}$ (2.19) becomes

$$(\widehat{h}\bar{\widehat{u}})_{\widehat{t}} + (\widehat{h}\bar{\widehat{u}}^2)_{\widehat{x}} + \frac{1}{2}g(\widehat{h}^2)_{\widehat{x}} + g\widehat{h}\widehat{B}_{\widehat{x}} = 0. \qquad (2.20)$$

(2.13) and (2.20) represent, respectively, mass conservation and the momentum change law, and constitute the 1D NSWEs.

2.2 Bed-load-only system

2.2.1 Governing equations

Henceforth, $\widehat{u}$ instead of $\bar{\widehat{u}}$ is used to denote the depth-averaged velocity along the $\widehat{x}$ direction, for simplification. For characteristic decomposition purposes, $\widehat{h}$ and $\widehat{u}$ in (2.20) can be disentangled using (2.20) and also (2.13) as

$$\widehat{u}_{\widehat{t}} + \widehat{u}\widehat{u}_{\widehat{x}} + g\widehat{h}_{\widehat{x}} + g\widehat{B}_{\widehat{x}} = 0. \qquad (2.21)$$

In the bed evolution process, if only bed load is considered the rate of bed change in a fixed domain $[\widehat{x}_1, \widehat{x}_2]$ is equal to the net sediment mass flux into

(out of) the region, i.e:

$$\frac{d}{d\widehat{t}}\int_{\widehat{x}_1}^{\widehat{x}_2}\widehat{B}d\widehat{x}+\xi[\widehat{q}]_{\widehat{x}_1}^{\widehat{x}_2}=0, \tag{2.22}$$

where $\widehat{q}$ is sediment flux caused by bed load, which is, in general, a function of $\widehat{h}$ and $\widehat{u}$, and $\xi=\dfrac{1}{1-p}$ with p being bed porosity.

As x_1 and x_2 are fixed and independent from time $\widehat{t}$, their derivatives with respect to $\widehat{t}$ are 0. When the bed is continuous, applying the Leibniz law, (2.22) becomes

$$\int_{\widehat{x}_1}^{\widehat{x}_2}\widehat{B}_{\widehat{t}}d\widehat{x}+\int_{\widehat{x}_1}^{\widehat{x}_2}\xi\widehat{q}_{\widehat{x}}d\widehat{x}=0\Rightarrow\int_{\widehat{x}_1}^{\widehat{x}_2}(\widehat{B}_{\widehat{t}}+\xi\widehat{q}_{\widehat{x}})d\widehat{x}=0. \tag{2.23}$$

Since this [$\widehat{x}_1$, $\widehat{x}_2$] domain could be any arbitrary fixed and continuous region, (2.23) is valid only when

$$\widehat{B}_{\widehat{t}}+\xi\widehat{q}_{\widehat{x}}=0, \tag{2.24}$$

and this is the Exner (bed evolution) equation when only bed load is taken into account.

Equations (2.13), (2.21) and (2.24) form a set of three governing equations of the bed-load-only system.

2.2.2 Non-dimensionalization

To make the results more intercomparable, we non-dimensionalize all variables. Dimensionless variables are:

$$x=\frac{\widehat{x}}{h_0},t=\frac{\widehat{t}}{h_0^{1/2}g^{-1/2}},h=\frac{\widehat{h}}{h_0},u=\frac{\widehat{u}}{(gh_0)^{1/2}},B=\frac{\widehat{B}}{h_0}\text{ and }q=\frac{\widehat{q}}{q_0}, \tag{2.25}$$

where h_0 is a vertical length scale, and q_0 represents a sediment flux scale.

Substituting (2.25) into the governing equations (2.13) and (2.21) gives

$$h_t + uh_x + hu_x = 0, \tag{2.26}$$

$$u_t + uu_x + h_x + B_x = 0. \tag{2.27}$$

Assuming $q = q(h, u)$ and substituting (2.25) into (2.24) gives

$$B_t + \sigma q_h h_x + \sigma q_u u_x = 0, \tag{2.28}$$

where $\sigma = \dfrac{\xi q_0}{g^{1/2} h_0^{3/2}}$ represents the non-dimensional bed mobility. Note that for different sediment transport formulae, the expressions for q_0 and therefore σ in terms of dimensional bed mobility A are different; see § 5.1.

The equations (2.26), (2.27) and (2.28) can be written in the vector form:

$$\overrightarrow{U}_t + \mathbf{A}(\overrightarrow{U})\overrightarrow{U}_x = 0 \tag{2.29}$$

with

$$\overrightarrow{U} = \begin{bmatrix} h \\ u \\ B \end{bmatrix}, \mathbf{A}(\overrightarrow{U}) = \begin{bmatrix} u & h & 0 \\ 1 & u & 1 \\ \sigma q_h & \sigma q_u & 0 \end{bmatrix}.$$

The eigenvalues of **A** are the roots of the equation,

$$\lambda^3 - 2u\lambda^2 + (u^2 - \sigma q_u - h)\lambda + \sigma(uq_u - hq_h) = 0. \tag{2.30}$$

As (2.29) is a hyperbolic system (Kelly, 2009), there are three real roots for the polynomial equation (2.30). Here the three roots are denoted λ_1, λ_2 and λ_3, such that $\lambda_1 \leq \lambda_3 \leq \lambda_2$. When $\sigma \to 0$, one root $\to 0$, and the other two approach the corresponding hydrodynamic characteristic speeds (Stoker, 1957; Kelly, 2009).

The cubic equation (2.30) can be solved directly using Cardano's formula (Kelly and Dodd, 2009), and the solutions are as follows:

$$\lambda_1 = 2(-D)^{\frac{1}{2}} \cos\left(\frac{\Theta + 2\pi}{3}\right) - \frac{a_2}{3}, \tag{2.31}$$

$$\lambda_2 = 2(-D)^{\frac{1}{2}} \cos\left(\frac{\Theta}{3}\right) - \frac{a_2}{3}, \tag{2.32}$$

$$\lambda_3 = 2(-D)^{\frac{1}{2}} \cos\left(\frac{\Theta + 4\pi}{3}\right) - \frac{a_2}{3}, \tag{2.33}$$

where

$$D = \frac{3a_1 - a_2^2}{9}, \tag{2.34}$$

$$\Gamma = \frac{1}{54}(9a_1a_2 - 27a_0 - 2a_2^3), \tag{2.35}$$

$$\Theta = \cos^{-1}\left(\frac{\Gamma}{(-D)^{\frac{3}{2}}}\right). \tag{2.36}$$

In (2.36), $|\Gamma/(-D)^{3/2}| \leq 1$ when $h \geq 0$, and this ensures three real roots for (2.30). In (2.31)-(2.36), a_0, a_1 and a_2 are the coefficient terms of the cubic polynomial (2.30),

$$a_0 = \sigma(uq_u - hq_h),\ a_1 = u^2 - \sigma q_u - h,\ a_2 = -2u. \tag{2.37}$$

From $\mathbf{A}(\overrightarrow{U})\mathbf{R}^{(k)} = \lambda_k \mathbf{R}^{(k)}$, the kth right eigenvector of $\mathbf{A}$ corresponding to λ_k is:

$$\mathbf{R}^{(k)} = \begin{bmatrix} r_1^{(k)} \\ r_2^{(k)} \\ r_3^{(k)} \end{bmatrix} = \begin{bmatrix} 1 \\ \dfrac{\lambda_k - u}{h} \\ \dfrac{(\lambda_k - u)^2}{h} - 1 \end{bmatrix} \text{ for } k = 1, 2, 3. \tag{2.38}$$

The characteristic $\dfrac{dx}{dt} = \lambda_k$ defines a characteristic field, the λ_k field, which is also called the $\mathbf{R}^{(k)}$ field.

2.2.3 Characteristic decomposition

The method of characteristics aims to find the relationship between the variables at two points located on the same characteristic line, therefore the governing equations are required to be written in the form of the total derivative of each variable with respect to time along three characteristic lines. To obtain the total derivatives of h, u and B, two combination factors μ and ω are introduced to combine equations (2.26), (2.27) and (2.28):

$$\begin{aligned}
\Re &= \mu(2.26) + \omega(2.27) + (2.28) \\
&= \mu h_t + \mu u h_x + \mu h u_x + \omega u_t + \omega u u_x + \omega h_x + \omega B_x + B_t + \sigma q_h h_x + \sigma q_u u_x \\
&= \mu h_t + (\mu u + \omega + \sigma q_h) h_x + \omega u_t + (\mu h + \omega u + \sigma q_u) u_x + B_t + \omega B_x \\
&= 0. \qquad (2.39)
\end{aligned}$$

Introducing the total derivatives, (2.39) reduces to

$$\Re = \mu \frac{dh}{dt} + \omega \frac{du}{dt} + \frac{dB}{dt} \qquad (2.40)$$

with

$$\lambda = \frac{dx}{dt} = \frac{\mu u + \omega + \sigma q_h}{\mu} = \frac{\mu h + \omega u + \sigma q_u}{\omega} = \omega, \qquad (2.41)$$

where λ is the characteristic velocity. From (2.41), μ and ω are represented by λ,

$$\mu = \frac{\lambda + \sigma q_h}{\lambda - u} \text{ and } w = \lambda. \qquad (2.42)$$

The solution for λ can be also obtained from (2.41),

$$\lambda = \frac{\mu h + \omega u + \sigma q_u}{\omega}, \qquad (2.43)$$

and substituting (2.42) into (2.43) gives

$$\lambda^3 - 2u\lambda^2 + (u^2 - \sigma q_u - h)\lambda + \sigma(u q_u - h q_h) = 0, \qquad (2.44)$$

which is identical to (2.30).

Replacing μ and ω in (2.40) with (2.42), and as there are three characteristics, it gives three Riemann equations

$$\Re^{(k)} = \lambda_k \frac{du}{dt} + \frac{\lambda_k + \sigma q_h}{\lambda_k - u}\frac{dh}{dt} + \frac{dB}{dt} = 0 \quad \text{along} \quad \frac{dx}{dt} = \lambda_k, \quad k = 1, 2, 3. \tag{2.45}$$

These three equations (2.45) are solved numerically to get h, u and B in the bed-load-only system.

From (2.30), it can be shown that when $h \neq 0$, $\lambda_{1,2} - u \neq 0$. However, $\lambda_3 - u = 0$ when $u = 0$. The Riemann equation (2.45) is investigated when $u = 0$ in Appendix B.1.

2.2.4 Shock conditions

We assume a shock with its position ζ located between x_1 and x_2, i.e., $x_1 < \zeta < x_2$, see Figure 2.1. The shock position ζ is assumed to vary in time such that $\zeta = \zeta(t)$ and $\frac{d\zeta}{dt} = W$. Here x_1 and x_2 are fixed , so $\frac{\partial x_1}{\partial t} = \frac{\partial x_2}{\partial t} = 0$.

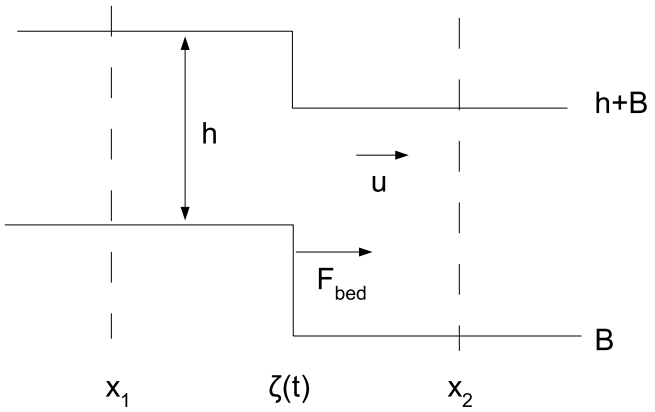

Figure 2.1: Schematic diagram of a morphodynamic shock.

From the mass conservation law, the rate of change of the total amount of water mass in $[x_1, x_2]$ is equal to the net water flux into (out of) the domain, i.e:

$$\frac{d}{dt}\int_{x_1}^{x_2} h dx + [hu]_{x_1}^{x_2} = 0. \tag{2.46}$$

As there is a shock inside $[x_1, x_2]$, we split the integration domain $[x_1, x_2]$ into two parts: $[x_1, \zeta^-]$ and $[\zeta^+, x_2]$. Here ζ^- and ζ^+ are the left and right limits of the shock position, respectively. Also applying the Leibniz law (2.46) becomes

$$\begin{aligned} &\frac{d}{dt}\int_{x_1}^{\zeta^-} h dx + \frac{d}{dt}\int_{\zeta^+}^{x_2} h dx + [hu]_{x_1}^{x_2} = 0 \\ \Rightarrow &\int_{x_1}^{\zeta^-} h_t dx + h|_{\zeta^-}\frac{\partial \zeta^-}{\partial t} + \int_{\zeta^+}^{x_2} h_t dx - h|_{\zeta^+}\frac{\partial \zeta^+}{\partial t} + [hu]_{x_1}^{x_2} = 0. \end{aligned} \tag{2.47}$$

If we let the spatial extent of the domain of integration become very small so that $x_1 \to \zeta^-$ and $x_2 \to \zeta^+$, then we find

$$\int_{x_1}^{\zeta^-} (\cdot)\, dx \to 0, \quad \int_{\zeta^+}^{x_2} (\cdot)\, dx \to 0 \tag{2.48}$$

$$\text{and} \quad (\cdot)\,|_{\zeta^-} \to (\cdot)\,|_{x_1}, \quad (\cdot)\,|_{\zeta^+} \to (\cdot)\,|_{x_2}. \tag{2.49}$$

Therefore (2.47) becomes

$$\begin{aligned} h|_{x_1}W - h|_{x_2}W + [hu]_{x_1}^{x_2} &= 0 \\ \Rightarrow \quad -W[h]_{x_1}^{x_2} + [hu]_{x_1}^{x_2} &= 0. \end{aligned} \tag{2.50}$$

For the momentum, the change of momentum of the water in $[x_1, x_2]$, is caused by the momentum fluxes across x_1 and x_2 sections, and the external forces. The external forces include the hydrostatic pressure on the x_1 and x_2 sections of the water element, and the force due to the bed. When the bed is continuous, the dimensionless force due to bed is $\int hB_x dx$; while when the bed is discontinuous

there is a horizontal force caused by the vertical bed step, and the dimensionless form of the force is denoted F_{bed}, see Figure 2.1. F_{bed} is positive when the bed level on the left side of the bed step is higher than that on the right side. Therefore, the conservation law of momentum is

$$\begin{aligned}
&\frac{d}{dt}\int_{x_1}^{x_2}\rho hudx + [\rho hu^2]_{x_1}^{x_2} + \frac{1}{2}\rho[h^2]_{x_1}^{x_2} + \int_{x_1}^{\zeta^-}\rho hB_x dx + \int_{\zeta^+}^{x_2}\rho hB_x dx - \rho F_{bed} = 0 \\
&\Rightarrow \frac{d}{dt}\int_{x_1}^{\zeta^-} hudx + \frac{d}{dt}\int_{\zeta^+}^{x_2} hudx + \left[hu^2 + \frac{1}{2}h^2\right]_{x_1}^{x_2} + \int_{x_1}^{\zeta^-} hB_x dx + \int_{\zeta^+}^{x_2} hB_x dx \\
&\qquad\qquad -F_{bed} = 0 \\
&\Rightarrow \int_{x_1}^{\zeta^-}(hu)_t dx + [hu]|_{\zeta^-}\frac{\partial\zeta^-}{\partial t} + \int_{\zeta^+}^{x_2}(hu)_t dx - [hu]|_{\zeta^+}\frac{\partial\zeta^+}{\partial t} + \left[hu^2 + \frac{1}{2}h^2\right]_{x_1}^{x_2} + \\
&\qquad\qquad + \int_{x_1}^{\zeta^-} hB_x dx + \int_{\zeta^+}^{x_2} hB_x dx - F_{bed} = 0. \qquad (2.51)
\end{aligned}$$

And in the limit $x_1 \to \zeta^-$ and $x_2 \to \zeta^+$, (2.51) becomes

$$\begin{aligned}
&[hu]|_{x_1}W - [hu]|_{x_2}W + \left[hu^2 + \frac{1}{2}h^2\right]_{x_1}^{x_2} - F_{bed} &&= 0 \\
\Rightarrow \quad &-W[hu]_{x_1}^{x_2} + \left[hu^2 + \frac{1}{2}h^2\right]_{x_1}^{x_2} - F_{bed} &&= 0. \qquad (2.52)
\end{aligned}$$

For the sediment conservation, the rate of bed change in the domain is equal to the net sediment mass flux into (out of) the region, i.e:

$$\begin{aligned}
&\frac{d}{dt}\int_{x_1}^{x_2} Bdx + \sigma[q]_{x_1}^{x_2} &&= 0 \\
\Rightarrow \quad &\frac{d}{dt}\int_{x_1}^{\zeta^-} Bdx + \frac{d}{dt}\int_{\zeta^+}^{x_2} Bdx + \sigma[q]_{x_1}^{x_2} &&= 0 \\
\Rightarrow \quad &\int_{x_1}^{\zeta^-} B_t dx + B|_{\zeta^-}W + \int_{\zeta^+}^{x_2} B_t dx - B|_{\zeta^+}W + \sigma[q]_{x_1}^{x_2} &&= 0. \qquad (2.53)
\end{aligned}$$

In the limit $x_1 \to \zeta^-$ and $x_2 \to \zeta^+$, (2.53) becomes

$$-W[B]_{x_1}^{x_2} + \sigma[q]_{x_1}^{x_2} = 0. \qquad (2.54)$$

Assume x_1 and x_2 represent the left and right side of a shock, respectively, and the variables on the two sides are denoted by subscripts L and R. Note that the term F_{bed} is usually related to dynamic pressure, and is not represented and cannot be resolved in the shallow water framework due to undefinedness of h and B at a discontinuity. Here, the integration method for a discontinuous bed in alluvial river flow presented by Needham and Hey (1991), which has also been successfully used in KD10 is employed to approximate the force F_{bed}

$$F_{bed} = -\int_{x_L}^{x_R} hB_x dx = -\frac{1}{2}(B(x_R)-B(x_L))(h(x_L)+h(x_R)) = -\frac{1}{2}(B_R-B_L)(h_L+h_R). \tag{2.55}$$

The three shock conditions (2.50), (2.52) and (2.54) therefore become

$$h_R u_R - h_L u_L - (h_R - h_L)W = 0, \tag{2.56}$$

$$W(h_R u_R - h_L u_L) - \left(h_R u_R^2 + \frac{h_R^2}{2} - h_L u_L^2 - \frac{h_L^2}{2}\right) - \frac{1}{2}(B_R - B_L)(h_R + h_L) = 0, \tag{2.57}$$

$$(B_R - B_L)W - \sigma(q_R - q_L) = 0. \tag{2.58}$$

2.3 Combined load system

2.3.1 Governing equations

Including both bed- and suspended load, the rate of bed change in the fixed domain [x_1, x_2] is equal to the total amount of net sediment flux into (out of) the region at the end sections plus the sediment settled down onto (entrained

off) the bed (Soulsby, 1997)

$$\frac{d}{d\widehat{t}}\int_{\widehat{x}_1}^{\widehat{x}_2}\widehat{B}d\widehat{x}+\xi[\widehat{q}]_{\widehat{x}_1}^{\widehat{x}_2}-\int_{\widehat{x}_1}^{\widehat{x}_2}\xi(\widehat{D}-\widehat{E})d\widehat{x}=0, \tag{2.59}$$

where $\widehat{D}$ is the dimensional deposition rate, expressed as the volume of sediment grains settling from suspension per unit area of bed per unit time. $\widehat{E}$ is the dimensional erosion rate, expressed as the volume of sediment grains eroded into suspension per unit area of bed per unit time.

When the bed across [x_1, x_2] is continuous and fixed, the Leibniz law is applied for (2.59) and gives

$$\begin{aligned}\int_{\widehat{x}_1}^{\widehat{x}_2}\widehat{B}_{\widehat{t}}d\widehat{x}+\int_{\widehat{x}_1}^{\widehat{x}_2}\xi\widehat{q}_{\widehat{x}}d\widehat{x}-\int_{\widehat{x}_1}^{\widehat{x}_2}\xi(\widehat{D}-\widehat{E})d\widehat{x} &= 0\\ \Rightarrow\qquad \int_{\widehat{x}_1}^{\widehat{x}_2}\left(\widehat{B}_{\widehat{t}}+\xi\widehat{q}_{\widehat{x}}-\xi(\widehat{D}-\widehat{E})\right)d\widehat{x} &= 0.\end{aligned} \tag{2.60}$$

Therefore, the sediment conservation equation including both bed- and suspended load is

$$\widehat{B}_{\widehat{t}}+\xi\widehat{q}_{\widehat{x}}=\xi(\widehat{D}-\widehat{E}). \tag{2.61}$$

The rate of change of the amount of suspended sediment in the water column in a fixed domain [x_1, x_2] is equal to the total amount of net suspended sediment flux into (out of) the region and the net sediment entrained into (settled from) the water column, i.e:

$$\begin{aligned}\frac{d}{d\widehat{t}}\int_{\widehat{x}_1}^{\widehat{x}_2}\widehat{h}\widehat{c}d\widehat{x}+[\widehat{h}\widehat{u}\widehat{c}]_{\widehat{x}_1}^{\widehat{x}_2}-\int_{\widehat{x}_1}^{\widehat{x}_2}(\widehat{E}-\widehat{D})dx &= 0\\ \Rightarrow\quad \int_{\widehat{x}_1}^{\widehat{x}_2}(\widehat{h}\widehat{c})_{\widehat{t}}d\widehat{x}+\int_{\widehat{x}_1}^{\widehat{x}_2}(\widehat{h}\widehat{u}\widehat{c})_{\widehat{x}}d\widehat{x}-\int_{\widehat{x}_1}^{\widehat{x}_2}(\widehat{E}-\widehat{D})dx &= 0\\ \Rightarrow\qquad \int_{\widehat{x}_1}^{\widehat{x}_2}\left((\widehat{h}\widehat{c})_{\widehat{t}}+(\widehat{h}\widehat{u}\widehat{c})_{\widehat{x}}-(\widehat{E}-\widehat{D})\right)d\widehat{x} &= 0,\end{aligned} \tag{2.62}$$

where $\widehat{c}$ is the depth-averaged concentration of suspended sediment.

Therefore the conservative form of the transport of suspended load is

$$(\widehat{h}\widehat{c})_{\widehat{t}} + (\widehat{h}\widehat{u}\widehat{c})_{\widehat{x}} = \widehat{E} - \widehat{D}. \tag{2.63}$$

Disentangling $\widehat{h}$ and $\widehat{c}$ by combining (2.13) and (2.63) gives

$$\widehat{c}_{\widehat{t}} + \widehat{u}\widehat{c}_{\widehat{x}} = \frac{1}{h}(\widehat{E} - \widehat{D}). \tag{2.64}$$

The Meyer-Peter Müller formula (see Yalin, 1977; Soulsby, 1997; Briganti et al., 2012), which is commonly used, is employed in the combined load simulation

$$\widehat{q} = A(\widehat{u}^2 - \widehat{u}_{crb}^2)^{3/2}, \tag{2.65}$$

where A is dimensional bed mobility parameter with unit $\mathrm{s}^2\mathrm{m}^{-1}$ and $\widehat{u}_{crb}$ is the velocity at threshold of sediment motion as bed load.

We employ the entrainment model in Pritchard and Hogg (2003) and PH05, taking the entrainment rate $\widehat{E} = \widehat{m}_e \left(\dfrac{\widehat{\tau} - \widehat{\tau}_{crs}}{\widehat{\tau}_0} \right)$, where $\widehat{\tau}$ bed shear stress, $\widehat{\tau}_{crs}$ the threshold stress of erosion as suspended load, and $\widehat{\tau}_0$ a reference bed shear stress. $\widehat{m}_e$ is the parameter of sediment entrainment rate as suspended load. The effective bed shear stress is calculated by the Chezy law $\widehat{\tau} = \rho C_D \widehat{u}^2$ (Soulsby, 1997) with C_D drag coefficient, therefore $\widehat{E} = \widehat{m}_e \left(\dfrac{\widehat{u}^2 - \widehat{u}_{crs}^2}{\widehat{u}_0^2} \right)$, where $\widehat{u}_{crs}$ is the velocity at threshold of sediment motion as suspended load and $\widehat{u}_0$ a reference velocity corresponding to $\widehat{\tau}_0$.

The deposition rate of suspended load also follows PH05; $\widehat{D} = \widehat{w}_s \widehat{c}$ with $\widehat{w}_s$ the effective settling velocity of the suspended sediment.

Therefore, (2.61) and (2.65) become

$$\widehat{B}_{\widehat{t}} + 3\xi A|\widehat{u}|(\widehat{u}^2 - \widehat{u}_{crb}^2)^{1/2}\widehat{u}_{\widehat{x}} = \xi \left(\widehat{w}_s \widehat{c} - \widehat{m}_e \left(\frac{\widehat{u}^2 - \widehat{u}_{crs}^2}{\widehat{u}_0^2} \right) \right), \tag{2.66}$$

$$\widehat{c}_{\widehat{t}} + \widehat{u}\widehat{c}_{\widehat{x}} = \frac{1}{\widehat{h}} \left(\widehat{m}_e \left(\frac{\widehat{u}^2 - \widehat{u}_{crs}^2}{\widehat{u}_0^2} \right) - \widehat{w}_s \widehat{c} \right). \tag{2.67}$$

2.3.2 Non-dimensionalization

The scaled form c is set as

$$c = \frac{\widehat{c}}{c_0} \quad \text{with} \quad c_0 = \frac{\widehat{m}_e}{\widehat{w}_s}, \tag{2.68}$$

where c_0 is a reference concentration. The other dimensionless variables are the same as those shown in § 2.2.2.

Substituting the dimensional variables in (2.66) by the corresponding nondimensional forms gives

$$\begin{aligned} & \frac{h_0}{h_0^{1/2} g^{-1/2}} B_t + 3\xi A \frac{(gh_0)^{3/2}}{h_0} |u| (u^2 - u_{crb}^2)^{1/2} u_x = \xi \left(\frac{\widehat{m}_e}{\widehat{w}_s} \widehat{w}_s c - \widehat{m}_e \left(\frac{u^2 - u_{crs}^2}{u_0^2} \right) \right) \\ \Rightarrow \quad & B_t + 3\xi A g |u| (u^2 - u_{crb}^2)^{1/2} u_x = \frac{\xi \widehat{m}_e}{(gh_0)^{1/2}} \left(c - \left(\frac{u^2 - u_{crs}^2}{u_0^2} \right) \right), \end{aligned} \tag{2.69}$$

where u_{crb}, u_{crs} and u_0 are the dimensionless forms of $\widehat{u}_{crb}$, $\widehat{u}_{crs}$ and $\widehat{u}_0$. Note that $u_0 = 1$ is assumed, and the value of u_0 affects the determination of $\widehat{m}_e$ and m_e. Let $\sigma = \xi A g$ and $m_e = \xi \frac{\widehat{m}_e}{(gh_0)^{1/2}}$, (2.69) becomes

$$B_t + 3\sigma |u| (u^2 - u_{crb}^2)^{1/2} u_x = m_e \left(c - (u^2 - u_{crs}^2) \right) \tag{2.70}$$

Substituting (2.25) and (2.68) into the dimensional governing equation of the transport of suspended sediment (2.67), gives

$$\begin{aligned} & \frac{c_0}{h_0^{1/2} g^{-1/2}} c_t + \frac{(gh_0)^{1/2} c_0}{h_0} u c_x = \frac{1}{h_0} \frac{1}{h} \left(\widehat{m}_e (u^2 - u_{crs}^2) - c_0 \widehat{w}_s c \right) \\ \Rightarrow \quad & c_t + u c_x = w_s \frac{1}{h} \left((u^2 - u_{crs}^2) - c \right), \end{aligned} \tag{2.71}$$

where $w_s = \frac{\widehat{w}_s}{(gh_0)^{1/2}}$.

When sediment concentration c is only determined by water velocity, it is denoted c_{eq} to represent suspended sediment concentration in equilibrium state

and we have $c_{eq} = u^2 - u_{crs}^2$. In (2.71), when $w_s/h \to \infty$, the adjustment of c to c_{eq} becomes immediate.

The four non-dimensional governing equations for the combined load system are (2.26), (2.27), (2.70) and (2.71). The vector form of these four equations is

$$\overrightarrow{U}_t + \mathbf{A}(\overrightarrow{U})\overrightarrow{U}_x = \overrightarrow{S} \tag{2.72}$$

with

$$\overrightarrow{U} = \begin{bmatrix} h \\ u \\ B \\ c \end{bmatrix}, \mathbf{A}(\overrightarrow{U}) = \begin{bmatrix} u & h & 0 & 0 \\ 1 & u & 1 & 0 \\ 0 & 3\sigma|u|(u^2 - u_{crb}^2)^{1/2} & 0 & 0 \\ 0 & 0 & 0 & u \end{bmatrix},$$

$$\overrightarrow{S} = \begin{bmatrix} 0 \\ 0 \\ m_e\,(c - (u^2 - u_{crs}^2)) \\ w_s \dfrac{1}{h}\,((u^2 - u_{crs}^2) - c) \end{bmatrix}.$$

The eigenvalues of **A** are the roots of the polynomial,

$$(\lambda - u)(\lambda^3 - 2u\lambda^2 + (u^2 - 3\sigma|u|(u^2 - u_{crb}^2)^{1/2} - h)\lambda + 3\sigma u|u|(u^2 - u_{crb}^2)^{1/2}) = 0. \tag{2.73}$$

The polynomial (2.73) has four roots, one of which is always equal to u, and denoted as λ_4, corresponding to the transport of suspended load. The other three roots of (2.73) are denoted as λ_1, λ_2 and λ_3 such that $\lambda_1 \leq \lambda_3 \leq \lambda_2$. However, λ_4 could be $\geq \lambda_3$ or $\leq \lambda_3$. When $u > 0$, we have $\lambda_3 \leq \lambda_4 \leq \lambda_2$; while when $u > 0$, $\lambda_1 \leq \lambda_4 \leq \lambda_3$. The cubic polynomial in (2.73) for $\lambda_{1,2,3}$ is identical to (2.30) if the Meyer-Peter Müller formula is employed in the bed-load-only system. The solution of $\lambda_{1,2,3}$ we refer to those in § 2.2.3.

From $\mathbf{A}(\overrightarrow{U})\mathbf{R}^{(k)} = \lambda_k \mathbf{R}^{(k)}$, the kth right eigenvector of $\mathbf{A}$ corresponding to λ_k is

$$\mathbf{R}^{(k)} = \begin{bmatrix} r_1^{(k)} \\ r_2^{(k)} \\ r_3^{(k)} \\ r_4^{(k)} \end{bmatrix} = \begin{bmatrix} 1 \\ \dfrac{\lambda_k - u}{h} \\ \dfrac{(\lambda_k - u)^2}{h} - 1 \\ 0 \end{bmatrix} \text{ for } k = 1, 2, 3, \tag{2.74}$$

and

$$\mathbf{R}^{(4)} = \begin{bmatrix} r_1^{(4)} \\ r_2^{(4)} \\ r_3^{(4)} \\ r_4^{(4)} \end{bmatrix} = \begin{bmatrix} 0 \\ 0 \\ 0 \\ 1 \end{bmatrix}. \tag{2.75}$$

It should be noted that the $\lambda_{1,2,3}$ characteristic fields are genuinely nonlinear, while the λ_4 characteristic field is linearly degenerate; see § 3.1.4 (see also Toro, 2001, 2009).

2.3.3 Characteristic decomposition

As the $\lambda_{1,2,3}$ characteristic fields associated with equations (2.26), (2.27) and (2.70) are genuinely nonlinear, and the λ_4 field associated with (2.71) is linearly degenerate, equations (2.26), (2.27) and (2.70) are combined to get the total derivative of h, u and B in time and (2.71) is used to find the total derivative of c in time.

Two combination factors μ and ω are introduced to combine (2.26), (2.27) and

(2.70)

$$\begin{aligned}\Re &= \mu(2.26) + \omega(2.27) + (2.70) \\ &= \mu h_t + \mu u h_x + \mu h u_x + \omega u_t + \omega u u_x + \omega h_x + \omega B_x + B_t + 3\sigma|u|(u^2 - u_{crb}^2)^{1/2} u_x \\ &= \mu h_t + (\mu u + \omega) h_x + \omega u_t + (\mu h + \omega u + 3\sigma|u|(u^2 - u_{crb}^2)^{1/2}) u_x + B_t + \omega B_x \\ &= m_e \left(c - \left(u^2 - u_{crs}^2\right)\right). \qquad (2.76)\end{aligned}$$

Introducing the total derivatives, (2.76) is reduced to

$$\Re = \mu \frac{dh}{dt} + \omega \frac{du}{dt} + \frac{dB}{dt} = m_e \left(c - \left(u^2 - u_{crs}^2\right)\right) \qquad (2.77)$$

with

$$\lambda = \frac{dx}{dt} = \frac{\mu u + \omega}{\mu} = \frac{\mu h + \omega u + 3\sigma|u|(u^2 - u_{crb}^2)^{1/2}}{\omega} = \omega. \qquad (2.78)$$

From (2.78), μ and ω are obtained,

$$\mu = \frac{\lambda}{\lambda - u} \quad \text{and} \quad w = \lambda. \qquad (2.79)$$

The solutions for λ can also be obtained from (2.78),

$$\lambda = \frac{\mu h + \omega u + 3\sigma|u|(u^2 - u_{crb}^2)^{1/2}}{\omega}, \qquad (2.80)$$

and substituting (2.79) into (2.78) gives

$$\lambda^3 - 2u\lambda^2 + (u^2 - 3\sigma|u|(u^2 - u_{crb}^2)^{1/2} - h)\lambda + 3\sigma u|u|(u^2 - u_{crb}^2)^{1/2} = 0, \qquad (2.81)$$

which is identical to the cubic polynomial in (2.73).

Replacing μ and ω in (2.77) with the above solution gives

$$\Re^{(k)} = \lambda_k \frac{du}{dt} + \frac{\lambda_k}{\lambda_k - u} \frac{dh}{dt} + \frac{dB}{dt} = m_e \left(c - \left(u^2 - u_{crs}^2\right)\right) \text{ along } \frac{dx}{dt} = \lambda_k,\ k = 1, 2, 3. \qquad (2.82)$$

Equation (2.71) is written as the total derivative of c with respect to time

$$\frac{dc}{dt} = w_s \frac{1}{h}\left(\left(u^2 - u_{crs}^2\right) - c\right), \text{along } \frac{dx}{dt} = \lambda_4 = u. \tag{2.83}$$

These four equations of (2.82) and (2.83) are solved numerically to get h, u, B and c in the combined load system.

2.3.4 Shock conditions

The shock conditions for mass and momentum equations are the same as those in § 2.2.4, and therefore not derived here.

In the combined load system, the equation governing the bed level change is

$$\frac{d}{dt}\int_{x_1}^{x_2} B dx + [\sigma(u^2 - u_{crb}^2)^{3/2}]_{x_1}^{x_2} = \int_{x_1}^{x_2} m_e \left(c - \left(u^2 - u_{crs}^2\right)\right) dx. \tag{2.84}$$

If a shock is located between x_1 and x_2, i.e., $x_1 < \zeta(t) < x_2$, (2.84) becomes

$$\begin{aligned}
&\frac{d}{dt}\int_{x_1}^{\zeta^-} B dx + \frac{d}{dt}\int_{\zeta^+}^{x_2} B dx + [\sigma(u^2 - u_{crb}^2)^{3/2}]_{x_1}^{x_2} = \\
&\int_{x_1}^{\zeta^-} m_e \left(c - (u^2 - u_{crs}^2)\right) dx + \int_{\zeta^+}^{x_2} m_e \left(c - (u^2 - u_{crs}^2)\right) dx \\
\Rightarrow \quad &\int_{x_1}^{\zeta^-} B_t dx + B|_{\zeta^-} W + \int_{\zeta^+}^{x_2} B_t dx - B|_{\zeta^+} W + [\sigma(u^2 - u_{crb}^2)^{3/2}]_{x_1}^{x_2} = \\
&\int_{x_1}^{\zeta^-} m_e \left(c - (u^2 - u_{crs}^2)\right) dx + \int_{\zeta^+}^{x_2} m_e \left(c - (u^2 - u_{crs}^2)\right) dx.
\end{aligned} \tag{2.85}$$

In the limit $x_1 \to \zeta^-$ and $x_2 \to \zeta^+$, (2.85) becomes

$$-W[B]_{x_1}^{x_2} + [\sigma(u^2 - u_{crb}^2)^{3/2}]_{x_1}^{x_2} = 0. \tag{2.86}$$

The non-dimensional equation for the suspended sediment conservation is

$$\frac{d}{dt}\int_{x_1}^{x_2}(hc)dx + [huc]_{x_1}^{x_2} = \int_{x_1}^{x_2} m_e\left((u^2-u_{crs}^2)-c\right)dx$$

$$\Rightarrow \quad \frac{d}{dt}\int_{x_1}^{\zeta^-}(hc)dx + \frac{d}{dt}\int_{\zeta^+}^{x_2}(hc)dx + [huc]_{x_1}^{x_2} = \int_{x_1}^{\zeta^-} m_e\left((u^2-u_{crs}^2)-c\right)dx + \int_{\zeta^+}^{x_2} m_e\left((u^2-u_{crs}^2)-c\right)dx$$

$$\Rightarrow \quad \int_{x_1}^{\zeta^-}\frac{\partial(hc)}{\partial t}dx + (hc)|_{\zeta^-}W + \int_{\zeta^+}^{x_2}\frac{\partial(hc)}{\partial t}dx - (hc)|_{\zeta^+}W + [huc]_{x_1}^{x_2} = \int_{x_1}^{\zeta^-} m_e\left((u^2-u_{crs}^2)-c\right)dx + \int_{\zeta^-}^{x_2} m_e\left((u^2-u_{crs}^2)-c\right)dx$$

$$\Rightarrow \quad [-hcW+hcu]_{x_1}^{x_2} = 0. \tag{2.87}$$

Again assuming x_1 and x_2 represent the left and the right side of the shock, respectively, and the variables on the two sides are denoted by the subscripts L and R. (2.86) and (2.87) are rearranged and become

$$(B_R - B_L)W - \sigma\left((u_R^2-u_{crb}^2)^{3/2} - (u_L^2-u_{crb}^2)^{3/2}\right) = 0, \tag{2.88}$$

$$h_R c_R(u_R - W) - h_L c_L(u_L - W) = 0. \tag{2.89}$$

It is found that the shock condition of the bed evolution (2.88) in the combined load system is identical to (2.58) in the bed-load-only system if Meyer-Peter Müller formula is employed.

From the shock condition (2.56) for mass conservation, we have

$$h_R(u_R - W) = h_L(u_L - W). \tag{2.90}$$

Replacing (2.89) with (2.90) gives

$$h_L(u_L - W)(c_R - c_L) = 0. \tag{2.91}$$

For a $\lambda_{1,2,3}$ shock, if $h_L \neq 0$ and $h_R \neq 0$, $u_L - W \neq 0$, the shock condition for the transport of suspended load is further simplified as

$$c_R - c_L = 0, \tag{2.92}$$

which implies that the sediment concentration across a $\lambda_{1,2,3}$ shock is continuous, and it is determined by the linearly degenerate characteristic field associated with the transport of suspended sediment.

For a λ_4 discontinuity, which is a contact wave (see § 3.1.4), when $W \neq 0$, we have $h_L = h_R$, $u_L = u_R$, $B_L = B_R$ and $c_L \neq c_R$.

2.4 Entropy condition for a shock with a bed discontinuity

In this section the normal force caused by the bed step is again represented by the general form F_{bed} to investigate the entropy condition.

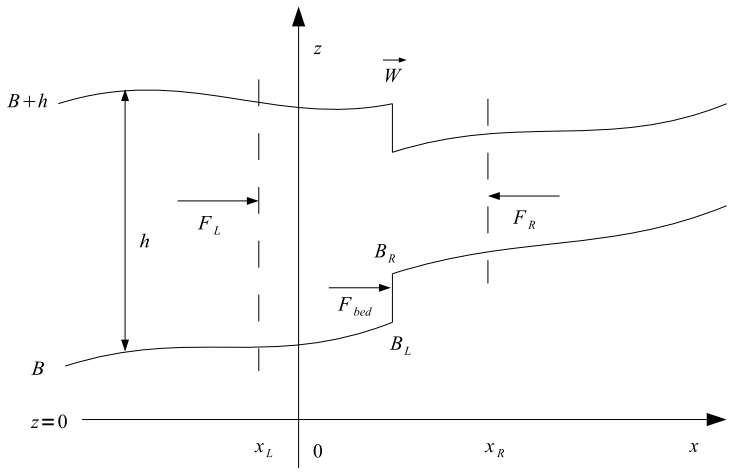

Figure 2.2: Propagation of a morphodynamic shock.

The shock condition (2.57) is written in a general form using F_{bed}

$$W(h_R u_R - h_L u_L) - \left(h_R u_R^2 + \frac{h_R^2}{2} - h_L u_L^2 - \frac{h_L^2}{2} \right) + F_{bed} = 0. \tag{2.93}$$

The dimensionless total energy in a water column, denoted as E_{in}, is a sum of the kinetic and potential energies, i.e:

$$E_{in} = \sum z \Delta m + \sum \frac{1}{2} u^2 \Delta m, \tag{2.94}$$

where Δm is the dimensionless mass of water in a small rectangular element with $\Delta m = \Delta x \Delta y \Delta z$.

We consider the energy change in the domain $[x_L, x_R]$, different from $[x_1, x_2]$, with the shock position $x_L < \zeta < x_R$. The water mass is conserved in the domain $[x_L, x_R]$, therefore x_L and x_R are moving at the speeds of the water particles, i,e., $\frac{dx_L}{dt} = u_L$ and $\frac{dx_R}{dt} = u_R$. Assuming $\Delta y = 1$, then $\Delta m = \Delta x \Delta z$. equation (2.94) becomes

$$\begin{aligned} E_{in} &= \sum \left(z \Delta x \Delta z + \frac{1}{2} u^2 \Delta x \Delta z \right) \\ &= \int_{x_L}^{x_R} \int_{B}^{B+h} \left(z + \frac{1}{2} u^2 \right) dz dx, \text{ as } \Delta x \Delta z \to 0 \\ &= \int_{x_L}^{x_R} \left(\frac{1}{2} h^2 + Bh + \frac{1}{2} h u^2 \right) dx. \end{aligned} \tag{2.95}$$

Energy gained due to external forces during the time interval Δt is

$$E_{ex} = \left(\frac{1}{2} h_L^2 u_L - \frac{1}{2} h_R^2 u_R + F_{bed} W \right) \Delta t. \tag{2.96}$$

We assume that there is energy loss when particles cross a shock front, and it is denoted E_{loss}, such that $\Delta E_{in} - E_{ex} = -E_{loss}$. As the particles do not gain energy upon crossing a shock front (Stoker, 1957, p. 291-341), $E_{loss} \geq 0$ for a

moving water column containing a shock, then $\Delta E_{in} - E_{ex} \leq 0$. When $E_{loss} = 0$ and $\Delta E_{in} - E_{ex} = 0$, the shock is continuous, i.e., there is no shock, or it is a contact shock.

The rate of energy gain in domain $[x_L, x_R]$ during the time interval Δt is

$$\begin{aligned} \frac{\Delta E}{\Delta t} &= -\frac{\Delta E_{loss}}{\Delta t} = \frac{\Delta E_{in}}{\Delta t} - \frac{E_{ex}}{\Delta t} \\ &= \frac{\Delta E_{in}}{\Delta t} - \left(\frac{1}{2}h_L^2 u_L - \frac{1}{2}h_R^2 u_R + F_{bed}W\right). \end{aligned} \tag{2.97}$$

In the limit $\Delta t \to 0$, the rate of energy gain in $[x_L, x_R]$ becomes

$$\begin{aligned} \frac{dE}{dt} &= \frac{dE_{in}}{dt} - \left(\frac{1}{2}h_L^2 u_L - \frac{1}{2}h_R^2 u_R + F_{bed}W\right) \\ &= \frac{d}{dt}\int_{x_L}^{x_R}\left(\frac{1}{2}h^2 + Bh + \frac{1}{2}hu^2\right)dx - \frac{1}{2}h_L^2 u_L + \frac{1}{2}h_R^2 u_R - F_{bed}W \\ &= -\left(\frac{1}{2}h^2 + Bh + \frac{1}{2}hu^2\right)|_{x_L}(u_L - W) + \left(\frac{1}{2}h^2 + Bh + \frac{1}{2}hu^2\right)|_{x_R}(u_R - W) \\ &\quad -\frac{1}{2}h_L^2 u_L + \frac{1}{2}h_R^2 u_R - F_{bed}W. \end{aligned} \tag{2.98}$$

The shock condition (2.56) for mass conservation gives

$$\begin{aligned} h_L(u_L - W) = h_R(u_R - W) = m_s, \\ h_L v_L = h_R v_R = m_s, \end{aligned} \tag{2.99}$$

where $u_L - W = v_L$ and $u_R - W = v_R$. Substituting (2.99) into (2.98) gives

$$\begin{aligned} \frac{dE}{dt} &= \left(\frac{1}{2}h_R^2 + B_R h_R + \frac{1}{2}h_R u_R^2\right)v_R - \left(\frac{1}{2}h_L^2 + B_L h_L + \frac{1}{2}h_L u_L^2\right)v_L \\ &\quad +\frac{1}{2}h_R^2 u_R - \frac{1}{2}h_L^2 u_L - F_{bed}W \\ &= \left(\frac{1}{2}h_R + B_R + \frac{1}{2}u_R^2\right)m_s - \left(\frac{1}{2}h_L + B_L + \frac{1}{2}u_L^2\right)m_s + \\ &\quad \frac{1}{2}h_R^2 u_R - \frac{1}{2}h_L^2 u_L - F_{bed}W. \end{aligned} \tag{2.100}$$

From (2.93), it gives

$$\begin{aligned} F_{bed} &= -W(h_R u_R - h_L u_L) + \left(h_R u_R^2 + \frac{h_R^2}{2} - h_L u_L^2 - \frac{h_L^2}{2} \right) \\ &= m_s(u_R - u_L) + \frac{1}{2}h_R^2 - \frac{1}{2}h_L^2. \end{aligned} \tag{2.101}$$

Substituting (2.101) into (2.100) gives

$$\begin{aligned} \frac{dE}{dt} &= \frac{1}{2}(h_R + 2B_R - h_L - 2B_L + u_R^2 - u_L^2)m_s + \frac{1}{2}h_R^2 u_R - \frac{1}{2}h_L^2 u_L - F_{bed}W \\ &= \frac{1}{2}(h_R + 2B_R - h_L - 2B_L + u_R^2 - u_L^2)m_s + \frac{1}{2}h_R^2 u_R - \frac{1}{2}h_L^2 u_L - \\ &\quad W\left(m_s(u_R - u_L) - \frac{1}{2}h_L^2 + \frac{1}{2}h_R^2 \right) \\ &= \frac{1}{2}(h_R + 2B_R - h_L - 2B_L + u_R^2 - u_L^2)m_s - \\ &\quad W m_s(u_R - u_L) + \frac{1}{2}m_s(h_R - h_L) \\ &= \frac{1}{2}(2h_R + 2B_R - 2h_L - 2B_L)m_s + \frac{1}{2}(u_R^2 - u_L^2 - 2W(u_R - u_L))m_s \\ &= \frac{1}{2}(2h_R + 2B_R - 2h_L - 2B_L)m_s + \frac{1}{2}(v_R^2 - v_L^2)m_s \\ &= \frac{1}{2}(2h_R + 2B_R - 2h_L - 2B_L + v_R^2 - v_L^2)m_s. \end{aligned} \tag{2.102}$$

Due to the uncertainty of the force F_{bed}, the variables on both sides of the shock cannot be exactly calculated, and consequently the term $\frac{dE}{dt}$. Therefore, $\frac{dE}{dt} < 0$ could not be used as a very accurate criterion to check which solution is physical when there is more than one solution for a shock with a bed step.

Another approach to the entropy condition is the convergence of characteristics, i.e. $\lambda_R < W < \lambda_L$ (LeVeque, 1992; Toro, 2001), where λ_L and λ_R are the characteristics on the left and right sides of the shock. It has been further pointed out by LeVeque (1992) that a more general form of the entropy condition $\lambda_R < W < \lambda_L$, which is only applicable when λ is strictly decreasing as x

increases, is $\lambda_R \leq W \leq \lambda_L$. For a morphodynamic system, as not all $\lambda_{1,2,3}$ functions are strictly decreasing as x increases, $\lambda_R \leq W \leq \lambda_L$ is utilised to check whether a shock is physical or not. A shock with $\lambda_R < W = \lambda_L$ or $\lambda_R = W < \lambda_L$ could be physical, and it usually connects a constant region and a rarefaction fan of the same characteristic family. Moreover, $\lambda_R < W = \lambda_L$ or $\lambda_R = W < \lambda_L$ also exists in some limiting cases, e.g., if one side of the shock is a dry bed.

CHAPTER 3

Dam-break problem

1D idealised dam-break problems with variables (h, u and B) in constant states on both sides of the dam, are examined over a mobile bed (and a fixed bed) in this chapter. In all dam-break problems, the bed evolution is assumed to be only due to sediment movement in the form of bed load. Such dam-break problems are generalised Riemann problems. Accordingly, the generalised simple wave theory for the Riemann solution is presented. The Riemann solution, including wave structure and wave pattern determination, is then presented.

Following the generalised simple wave theory, firstly we generalise the Riemann solution in KD09 for a wet-dry dam-break problem over a flat continuous mobile bed with the sediment transport formula $q = u^3$ to a more general sediment flux formula $q = q(h, u)$. The wave structure and solution are similar to those in KD09.

Then, the wet-dry dam break problem on a flat bed with a bed step, i.e., a discontinuity in bed level, is examined, in which both fixed bed and mobile bed are considered. The dam-break problem on a fixed discontinuous bed is examined

first; the corresponding wave structures are analysed in terms of characteristics. Dam-break problems with various initial conditions (different water velocities behind the dam), are solved to illustrate the wave structures.

Based upon the wave structures for the wet-dry dam-break problem on a fixed discontinuous bed, the wave structures for a wet-dry dam-break problem on a mobile discontinuous bed are then deduced. The Riemann solution of the dam-break problem on a mobile bed is thereafter verified by comparing the results of mobile bed cases with the dimensionless bed mobility $\sigma \to 0$ with those of the equivalent fixed bed cases. Additionally, several cases with various initial conditions are solved to illustrate the Riemann solution and wave structures.

Lastly, the dam-break problem on a wet-wet flat mobile bed, which could provide a technique to solve a shock-shock collision problem, is also investigated in this chapter. It should be pointed out that the water on both sides of the dam is initially motionless, which is usually not the case in the shock-shock collision problem. However, this simple wet-wet dam-break problem could give insight into more complex wet-wet dam-break problems.

Note that although we present the Riemann solution for a wet-dry dam-break problem over a continuous mobile bed with a general sediment transport formula $q(h, u)$, the formula utilised to describe the bed evolution in the wet-dry dam-break problem over a discontinuous bed and the wet-wet dam-break problem over a continuous mobile bed is here taken as $q = u^3$.

3.1 Generalised simple wave theory

3.1.1 The Riemann problem

Consider a quasilinear hyperbolic system

$$\overrightarrow{U}_t + \mathbf{A}(\overrightarrow{U})\overrightarrow{U}_x = 0, \tag{3.1}$$

where $\overrightarrow{U}$ is a vector of n dependent variables, given by

$$\overrightarrow{U} = [u_1, u_2, \ldots, u_n]^T. \tag{3.2}$$

If this system has the following initial conditions

$$\overrightarrow{U}(x, t = 0) = \begin{cases} \overrightarrow{U}_l, & \text{if } x \leq 0, \\ \overrightarrow{U}_r, & \text{if } x \geq 0, \end{cases}$$

which means that the two regions on the left and right sides of $x = 0$ are constant state regions, it is called a Riemann problem and the solution for this problem is called the Riemann solution.

The real eigenvalues λ_i $(i = 1, 2, \ldots, n.)$ of (3.1) can be obtained by

$$|\mathbf{A} - \lambda_i \mathbf{I}| = 0, \tag{3.4}$$

where $\mathbf{I}$ is a $n \times n$ unit matrix. The corresponding right eigenvector of λ_i is

$$\mathbf{R}^{(i)} = [r_1^{(i)}, r_2^{(i)}, \ldots, r_n^{(i)}]^T, \tag{3.5}$$

and $\mathbf{R}^{(i)}$ is obtained from $(\mathbf{A} - \lambda_i \mathbf{I})\mathbf{R}^{(i)} = 0$.

3.1.2 Generalised simple wave

Jeffrey (1976) has shown that a direct extension of the concept of a Riemann invariant is not possible when there are more than two equations and variables

in a Riemann problem; the generalised simple wave theory as well as the generalised Riemann invariants are therefore introduced to solve such Riemann problems. In system (3.1), if $\overrightarrow{U} = \overrightarrow{U}(u_1)$ across a wave, which means that there is a functional dependence between u_i and u_1 of the form $u_i = f(u_1)$, the wave is called a generalised simple wave (Jeffrey, 1976).

For a simple wave, equation (3.1) can be written as,

$$\begin{aligned} & \frac{d\overrightarrow{U}}{du_1}\frac{\partial u_1}{\partial t} + \mathbf{A}(\overrightarrow{U})\frac{d\overrightarrow{U}}{du_1}\frac{\partial u_1}{\partial x} = 0, \\ \Rightarrow \quad & \left(\frac{\partial u_1}{\partial t}\mathbf{I} + \frac{\partial u_1}{\partial x}\mathbf{A}\right)\frac{d\overrightarrow{U}}{du_1} = 0. \end{aligned} \tag{3.6}$$

This system can have a non-trivial solution only if

$$|\mathbf{A} - \lambda\mathbf{I}| = 0, \tag{3.7}$$

where $\lambda = -(\partial u_1/\partial t)/(\partial u_1/\partial x)$. From (3.7), we know that there are n such λ values

$$\begin{aligned} & \frac{dx}{dt} = \lambda_i = -\left(\frac{\partial u_1}{\partial t}\right) / \left(\frac{\partial u_1}{\partial x}\right), i = 1, 2, \ldots, n \\ \Rightarrow \quad & \frac{\partial u_1}{\partial x}dx + \frac{\partial u_1}{\partial t}dt = 0 \text{ along the } \lambda_i \text{ characteristics.} \end{aligned} \tag{3.8}$$

Assuming that $u_1(x,t)$ is constant along a curve, we have $\frac{du_1}{dt} = \frac{\partial u_1}{\partial x}dx + \frac{\partial u_1}{\partial t}dt = 0$ along this curve, and this curve is a λ_i characteristic according to (3.8). Furthermore, $\overrightarrow{U}$ and $A(\overrightarrow{U})$ are also constant along this λ_i characteristic, which results in the eigenvalues of $A(\overrightarrow{U})$, i.e., λ, being constant along this characteristic line. Consequently, the characteristic associated with λ_i is a straight line. The wave, across which the λ_i characteristics are all straight lines, is called a generalised λ_i simple wave.

From equation (3.6), when $\lambda = \lambda_i$ the vector $\dfrac{d\overrightarrow{U}}{du_1}$ must be proportional to the right eigenvector $\mathbf{R}^{(i)}$ of $\mathbf{A}$, which gives a set of n differential equations (Jeffrey, 1976),

$$\frac{du_1}{r_1^{(i)}} = \frac{du_2}{r_2^{(i)}} = \ldots = \frac{du_n}{r_n^{(i)}} = d\varepsilon, \tag{3.9}$$

where $\varepsilon_0 d\varepsilon = du_1$, with ε_0 being a constant. Equation (3.9) gives

$$du_j = \frac{r_j^{(i)}}{r_1^{(i)}} du_1, j = 2, \ldots, n. \tag{3.10}$$

Integrating (3.10) yields the generalised Riemann invariants

$$u_j - \int \frac{r_j^{(i)}}{r_1^{(i)}} du_1 = K_j, j = 2, \ldots, n. \tag{3.11}$$

where K_j is the generalised Riemann invariant associated with the λ_i simple wave. Further details of the simple wave theory can be found in Jeffrey (1976).

3.1.3 Wave structure for a Riemann problem

In terms of the solution for the Riemann problem (3.1), it has been pointed out that there are n waves associated with the n characteristic families in a Riemann problem of n equations (Toro, 2009; Lax, 1957; Fraccarollo and Capart, 2002). These n waves are separated by $n - 1$ newly formed constant regions (Toro, 2009; Lax, 1957; Fraccarollo and Capart, 2002), see Figure 3.1.

We will introduce the definitions of a linearly degenerate field and a genuinely nonlinear field to explain the wave types. The gradient of an eigenvalue λ_i is given by Toro (2001) as

$$\nabla_{\vec{U}} \lambda_i = \left[\frac{\partial}{\partial u_1} \lambda_i, \frac{\partial}{\partial u_2} \lambda_i, \ldots, \frac{\partial}{\partial u_n} \lambda_i \right]^T. \tag{3.12}$$

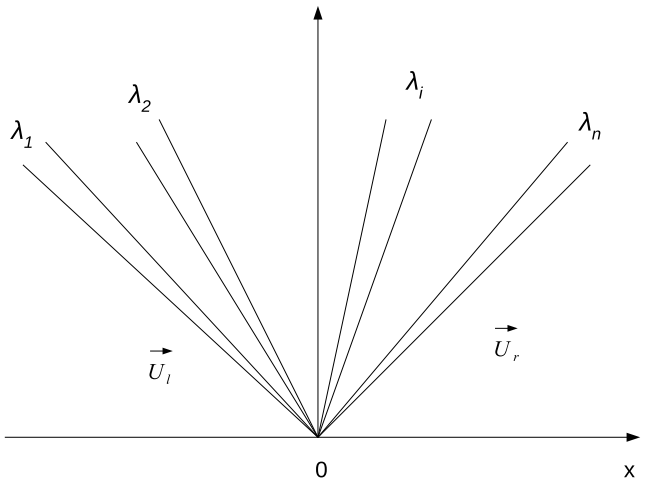

Figure 3.1: Structure of the wave solution for a Riemann problem with n characteristic families.

A λ_i characteristic field is defined to be linearly degenerate if

$$\nabla_{\overrightarrow{U}} \lambda_i \cdot R^{(i)} = 0; \tag{3.13}$$

conversely, it is said to be a genuinely nonlinear field if

$$\nabla_{\overrightarrow{U}} \lambda_i \cdot R^{(i)} \neq 0. \tag{3.14}$$

For a λ_i wave,

$$d\lambda_i = \frac{\partial \lambda_i}{\partial u_1} du_1 + \frac{\partial \lambda_i}{\partial u_2} du_2 + \ldots + \frac{\partial \lambda_i}{\partial u_n} du_n. \tag{3.15}$$

If the λ_i wave is further assumed to be a simple wave, then from equation (3.9) we have $du_1 = r_1^{(i)} d\varepsilon$, $du_2 = r_2^{(i)} d\varepsilon$, …, $du_n = r_n^{(i)} d\varepsilon$, and equation (3.15) becomes

$$d\lambda_i = \frac{\partial \lambda_i}{\partial u_1} r_1^{(i)} d\varepsilon + \frac{\partial \lambda_i}{\partial u_2} r_2^{(i)} d\varepsilon + \ldots + \frac{\partial \lambda_i}{\partial u_n} r_1^{(n)} d\varepsilon = \nabla_{\overrightarrow{U}} \lambda_i \cdot R^{(i)} d\varepsilon. \tag{3.16}$$

If the λ_i characteristic field is linearly degenerate, i.e., $\nabla_{\overrightarrow{U}} \lambda_i \cdot R^{(i)} = 0$, then $d\lambda_i = 0$, i.e., $\lambda_i(\overrightarrow{U}_L) = \lambda_i(\overrightarrow{U}_R)$ across the λ_i simple wave, where $\overrightarrow{U}_L$ and $\overrightarrow{U}_R$

are vectors of variables on the left and right side of the λ_i wave. This implies that although some variables of $\overrightarrow{U}$ are changed across the λ_i wave, the λ_i value remains unchanged; this wave is called a contact wave (shock), see Figure 3.2.

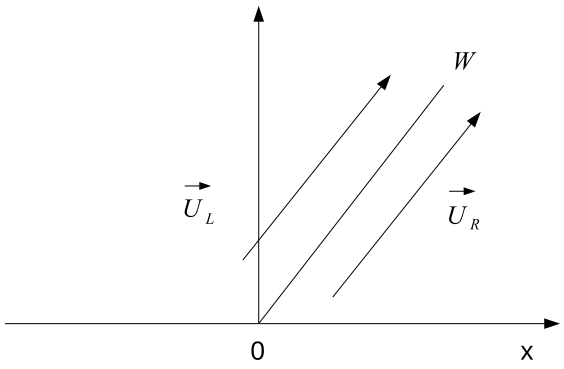

Figure 3.2: Schematic diagram for a contact wave.

When the λ_i characteristic field is genuinely nonlinear, then $d\lambda_i \neq 0$ across the λ_i simple wave, that is $\lambda_i(\overrightarrow{U}_L) \neq \lambda_i(\overrightarrow{U}_R)$. The value of λ_i may increase or decrease across the wave. When $d\lambda_i < 0$, i.e., $\lambda_i(\overrightarrow{U}_L) < \lambda_i(\overrightarrow{U}_R)$, the λ_i wave is a smooth transition wave, where all quantities vary continuously across the λ_i wave, and it is called a rarefaction wave, see Figure 3.3. When $\lambda_i(\overrightarrow{U}_L) > \lambda_i(\overrightarrow{U}_R)$, $\overrightarrow{U}_L$ and $\overrightarrow{U}_R$ are connected through a jump discontinuity, and the wave is called a shock (see Figure 3.4); equation (3.16) cannot be used across a shock.

3.1.4 Wave pattern determination

Toro (2001) presented the conditions to determine the wave patterns.

1) A rarefaction wave is associated with a genuinely nonlinear field, see Figure 3.3, and the following two conditions apply.

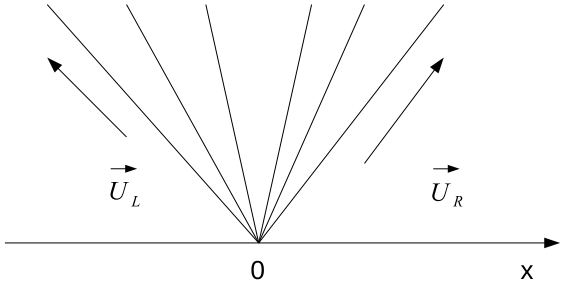

Figure 3.3: Schematic diagram for a rarefaction wave.

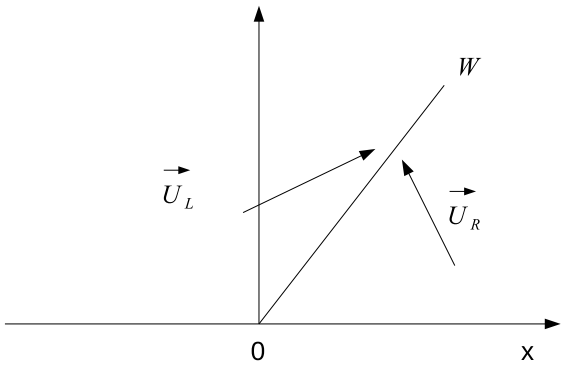

Figure 3.4: Schematic diagram for a shock wave.

- Constancy of generalised Riemann invariants across the wave, i.e., equation (3.9) should be satisfied.

- Divergence of characteristics

$$\lambda_i(\overrightarrow{U}_L) < \lambda_i(\overrightarrow{U}_R). \tag{3.17}$$

2) A contact wave is a discontinuous wave in a linearly degenerate field, see Figure 3.2, and the following conditions apply.

- The shock conditions.

- Constancy of generalised Riemann invariants across the wave, satisfying

equation (3.9).

- The parallel characteristic condition

$$\lambda_i(\overrightarrow{U}_L) = \lambda_i(\overrightarrow{U}_R) = W. \tag{3.18}$$

3) A shock wave is a discontinuous wave in a genuinely nonlinear field, see Figure 3.4, and the following conditions apply.

- The shock conditions.

- The entropy condition and here the more general entropy condition, see § 2.4, is imposed

$$\lambda_i(\overrightarrow{U}_L) \geq W \geq \lambda_i(\overrightarrow{U}_R). \tag{3.19}$$

3.2 Wet-dry dam-break problem over a continuous mobile bed with a general sediment transport formula $q = q(h, u)$

The wet-dry dam-break problem, with motionless water of constant depth on one side and none on the other side, over a flat mobile bed can be solved by simple wave theory (Jeffrey, 1976; Fraccarollo and Capart, 2002; Kelly and Dodd, 2009). The initial conditions are shown in Figure 3.5. As there are three characteristics in the fully coupled bed-load-only system (2.29), there are three waves and four regions of constant state separated by these three waves (Lax, 1957; Toro, 1997; Fraccarollo and Capart, 2002). However, in the wet-dry dam-break

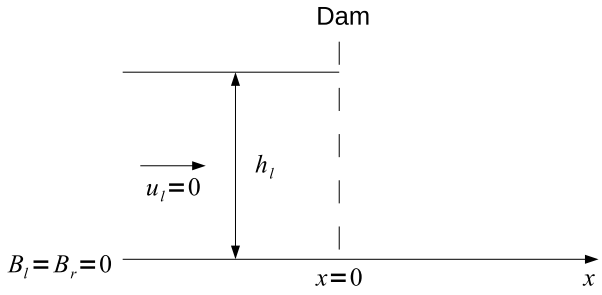

Figure 3.5: Initial conditions for a wet-dry dam-break problem over a continuous bed.

problem one wave and two regions of constant state vanish due to the dry bed, and the other two waves are λ_1 and λ_3 centred simple waves (rarefaction fans) (KD09). There is a newly formed constant region with constant $h = h_*$, $u = u_*$ and $B = B_*$, separating these two waves.

3.2.1 Rarefaction solution

We apply the generalised Riemann invariants to solve for the variables across the rarefaction waves. Replacing u_1, u_2 and u_3 in (3.9) by h, u and B gives

$$\frac{dh}{r_1^{(k)}} = \frac{du}{r_2^{(k)}} = \frac{dB}{r_3^{(k)}} = d\varepsilon, k = 1, 3 \tag{3.20}$$

Eliminating $d\varepsilon$ and substituting (2.75) into (3.20) gives

$$du = \left(\frac{\lambda_k - u}{h}\right) dh, \tag{3.21}$$

$$dB = \left(\frac{(\lambda_k - u)^2}{h} - 1\right) dh, \quad k = 1, 3. \tag{3.22}$$

The above equations are used to solve the rarefaction waves.

3.2.2 Solution algorithm for a rarefaction wave

If the variation of h across a λ_k rarefaction fan is known, u and B across the rarefaction wave are solved by integrating (3.21) and (3.22) in small decrements of h. Assuming that the water depths h_l and h_* on the two sides of the λ_1 rarefaction wave are known, the water depth variation range in this fan is from h_l to h_*, with $h_l \geq h_*$. Moreover, the velocity and bed level at the left boundary of the λ_1 rarefaction are also known (u_l and B_l). We integrate from h_l to h_* in steps of Δh, for $h_l \geq h_i \geq h_*$, $h_i = h_l + (i-1)\Delta h$, where Δh is a negative value. The Runge-Kutta method is used to integrate (3.21) and (3.22) to obtain u_i and B_i. As the λ_1 rarefaction is a centred simple wave it thus follows that $\lambda_{1_i} = \frac{x_i}{t}$, and x_i is therefore calculated from λ_{1_i}, where λ_{1_i} is the λ_1 characteristic for the ith computational cell with h_i, u_i and B_i.

Therefore the solution proceeds as

$$u_{i+1} = u_i + \frac{\lambda_{1_i} - u_i}{h_i}(h_{i+1} - h_i), \tag{3.23}$$

$$B_{i+1} = B_i + \left(\frac{(\lambda_{1_i} - u_i)^2}{h_i} - 1\right)(h_{i+1} - h_i), \tag{3.24}$$

$$x_{i+1} = \lambda_{1_{i+1}} t. \tag{3.25}$$

Here $u_1 = u_l$ and $B_1 = B_l$, and λ_{1_1} is calculated when h_1 and u_1 are known.

3.2.3 Computation procedure

The procedure for the Riemann solution of the wet-dry dam-break problem is:

1. Give an initial guess value to the water depth in the newly formed constant region: $h_* = h_*^{(1)}$.

2. Solve the left λ_1 rarefaction wave. The variables across the λ_1 rarefaction are obtained by the rarefaction solution.

3. Solve for the variables across the λ_3 rarefaction.

4. Refine h_*. According to the results of wave solutions, we check whether the sediment volume is conserved within the required accuracy, if it is conserved, the updated h_* is assumed to be correct and the updated wave solutions are the correct solution for the dam-break problem; if not, h_* is changed (i.e. $h_*^{(2)}$) and repeat Steps 2-4 until the desired accuracy is achieved. Note that the desired accuracy of sediment conservation depends largely on the numerical decrement in h for integration to calculate u and B values.

The Riemann solutions for wet-dry dam-break problems over a mobile continuous bed with different sediment transport formulae q have been tested by nearly fixed bed cases ($\sigma = 1 \times 10^{-8}$), and the results are compared with the equivalent fixed bed dam-break solutions (Toro, 2001) (not shown).

3.3 Wet-dry dam-break problem over a discontinuous fixed bed

3.3.1 Initial conditions

The initial conditions for a wet-dry dam-break problem over a fixed discontinuous bed are shown in Figure 3.6. There is a dam located at $x = 0$, where there

is also a discontinuity in the bed level. The bed level on the left side of the dam is B_l, and B_r on the right side; values of $B_r > B_l$ are considered here. The region on the left side of the dam, i.e. $x \leq 0$, is of water of constant depth h_l and velocity u_l, while there is no water on the right side. The dam is assumed to collapse at $t = 0$.

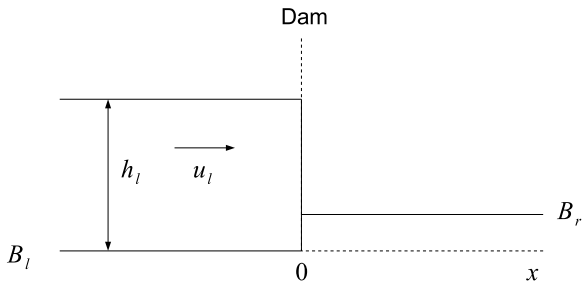

Figure 3.6: Initial conditions for a wet-dry dam-break problem with a bed step.

3.3.2 Wave profile analysis

In the initial conditions of this dam-break problem, the two regions separated by the dam are constant regions; it is therefore a Riemann problem (Toro, 2009). In the fixed bed system, there are two governing equations (the 1D NSWE) for the water flow; two characteristics are $\lambda_1 = u - \sqrt{h}$ and $\lambda_2 = u + \sqrt{h}$. Therefore, there are two waves associated with two characteristic families; however, one wave vanishes in the wet-dry dam-break problem due to the dry bed (Toro, 2001; Stoker, 1957, p. 291-341).

The wave structure of the equivalent wet-dry dam-break problem on a fixed continuous bed is a λ_1 rarefaction wave (Toro, 2001; Stoker, 1957, p. 291-341). However, this λ_1 rarefaction wave is sometimes confined to the region $x < 0$,

and could also flow to the region $x > 0$, depending on the initial conditions of the water behind the dam. When there is a discontinuity in the bed, this λ_1 rarefaction wave cannot be developed smoothly, because it is affected by the bed step. When the height of the bed step, i.e., $B_r - B_l$, is relatively small, the water can overtop the bed step and flow into the region $x \geq 0$. When the bed step is higher than a critical value, the dam-break flow cannot overtop the high bed, and is confined to the region $x \leq 0$. Note that the variables on the left and right side of the bed step are represented by subscripts L and R, see Figure 3.7, and we could have the solution of $h_L = h_l$ and $u_L = u_l$ or that of $h_L \neq h_l$ and $u_L \neq u_l$.

3.3.3 Wave overtopping check

When solving a wet-dry dam-break problem with a bed step, it is important to know whether the water can overtop the bed on the right side or not due to the different wave structures for these two cases. Here, we discuss the process of checking it.

When the water behind the dam is motionless, i.e., $u_l = 0$, if $h_l > B_r - B_l$, then the water can overtop the bed step; conversely if $h_l \leq B_r - B_l$, then the water cannot overtop. However, when $u_l \neq 0$, the water depth and velocity on the left side of the bed step $h_L \neq h_l$ and $u_L \neq u_l$, therefore h_L and u_L are solved first to determine whether the water can overtop.

When $u_l \neq 0$, it is initially assumed that the water cannot overtop, and the bed step is adjacent to a newly formed constant region, in which $u_L = 0$. There is a

λ_1 wave connecting the original constant region and the newly formed constant region, and this λ_1 wave could be a rarefaction fan or a shock. The water depth in the newly formed constant region h_L is subsequently solved by the λ_1 rarefaction / shock wave. If $u_l > 0$, then the left wave is a shock and h_L is solved using the hydrodynamic shock conditions (2.56) and (2.57); if $u_l \leq 0$ then it is a λ_1 rarefaction wave, and h_L is solved by the Riemann invariant along the λ_2 characteristic (Toro, 2001; Stoker, 1957, p. 291-341). If $h_L > B_r - B_l$, the water can overtop the bed step, while if $h_L \leq B_r - B_l$, the water cannot overtop.

3.3.4 Wave structure for the case when the water cannot overtop the bed step

The wave structure for the case when the water cannot overtop the high bed comprises the left original constant region, a λ_1 wave and a newly formed constant region.

3.3.5 Wave structure for the case when the water can overtop the bed step

When the water overtops the bed on the right, the immobile bed step results in a stationary shock at $x = 0$. The right wave in the $x > 0$ region is deduced to be a rarefaction wave, as a dry bed can only be adjacent to a rarefaction fan (Toro, 2001). Moreover, this rarefaction wave is a λ_1 wave, since λ_2 decreases as h decreases in this region which will result in a shock and the dry bed cannot be

adjacent to a shock. By analogy with the wave structure of the equivalent continuous fixed bed dam-break flow (see Stoker, 1957, p. 291-341), the left wave is deduced to be a λ_1 wave; however, this λ_1 wave could be a shock or a rarefaction wave depending on the initial conditions.

The general wave structure is shown in Figure 3.7: the original constant region (a), a λ_1 fan (b), a new formed constant region (c), a stationary shock at $x = 0$, a new formed constant region (d) and a λ_1 rarefaction wave (e). Here constant regions are assumed to connect every two waves. Note that the λ_1 wave (b) in Figure 3.7 could be a λ_1 shock; however, it is shown as a rarefaction wave in all the schematic diagrams for wave structures.

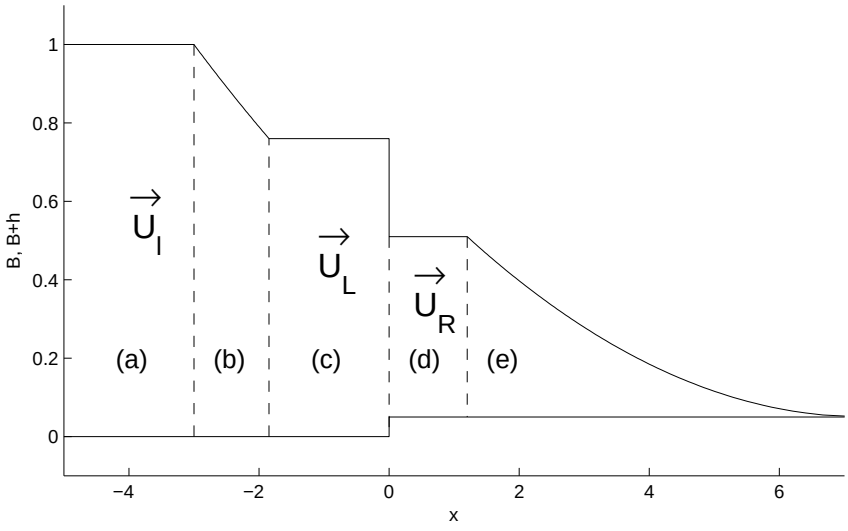

Figure 3.7: Schematic general wave structure for a wet-dry dam-break problem on a fixed discontinuous bed ($B_r > B_l$).

As $h_L > 0$ and $h_R > 0$, then $\lambda_{2L} > \lambda_{1L}$ and $\lambda_{2R} > \lambda_{1R}$. As the right λ_1 rarefaction wave is located in $x \geq 0$, $\lambda_1 \geq 0$ in the whole rarefaction region (e), consequently $\lambda_1 \geq 0$ in the constant region (d) and on the right side of the stationary

shock, i.e., $\lambda_{1R} \geq 0$. However, λ_1 on the left side of the discontinuity, i.e. λ_{1L}, could be less or greater than or equal to 0.

There are four unknowns (h_L, u_L, h_R and u_R) for a stationary shock, and four governing equations are required to solve this shock: whether or not four equations can be found is utilised as a criterion to determine which wave solution is physical. All possible solutions are listed and discussed below.

1) $\lambda_{1L} < 0$ **and** $\lambda_{1R} = 0$

As $\lambda_{1R} = 0$, the region (d) in Figure 3.7 does not exist, and the corresponding wave structure is shown in Figure 3.8.

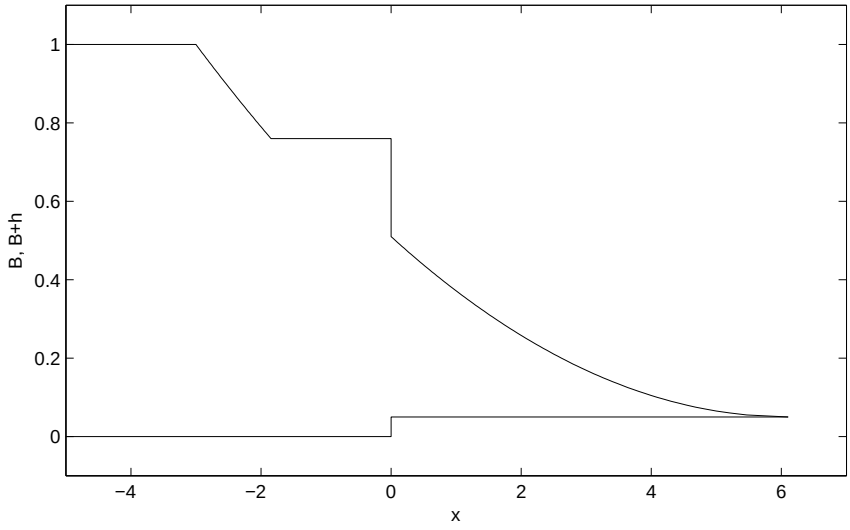

Figure 3.8: Schematic wave structure for the solution of $\lambda_{1L} < 0$ and $\lambda_{1R} = 0$.

In this case, it could be that $\lambda_{2L} < 0$ or ≥ 0, while we must always have $\lambda_{2R} > 0$. If $\lambda_{2L} < 0$ and $\lambda_{2R} > 0$, there is one equation of $\lambda_{1R} = 0$ on the right side of the shock. Along with the two shock conditions for the stationary shock, there are three equations; however, there are four unknowns, and this system

is therefore not determined. Therefore $\lambda_{1L} < 0$, $\lambda_{1R} = 0$, $\lambda_{2L} < 0$ and $\lambda_{2R} > 0$ is not a solution to this shock.

When $\lambda_{2L} \geq 0$ and $\lambda_{2R} > 0$, there is one Riemann invariant along λ_{2L} on the left side and one equation of $\lambda_{1R} = 0$ on the right side. Along with the two shock conditions, there are four equations and four unknowns, and therefore $\lambda_{1L} < 0$, $\lambda_{1R} = 0$, $\lambda_{2L} \geq 0$ and $\lambda_{2R} > 0$ is a possible solution to the shock.

2) $\lambda_{1L} < 0$ **and** $\lambda_{1R} > 0$

In this case, the wave structure is the same as that shown in Figure 3.7.

As with the preceding case, we could have $\lambda_{2L} < 0$ or ≥ 0, while $\lambda_{2R} > 0$ always.

When $\lambda_{2L} < 0$ and $\lambda_{2R} > 0$, there are no Riemann equations on both sides of the stationary shock. There are only two shock conditions but four unknowns, and this system is not determined. Therefore, $\lambda_{1L} < 0$, $\lambda_{1R} > 0$, $\lambda_{2L} < 0$ and $\lambda_{2R} > 0$ is not a solution to the shock.

When $\lambda_{2L} \geq 0$ and $\lambda_{2R} > 0$, there is one Riemann invariant equation along λ_{2L} on the left side and none on the right. Along with the two shock conditions, there are three equations but four unknowns, and $\lambda_{1L} < 0$, $\lambda_{1R} > 0$, $\lambda_{2L} \geq 0$ and $\lambda_{2R} > 0$ is not a solution to the shock.

3) $\lambda_{1L} \geq 0$ **and** $\lambda_{1R} = 0$

When $\lambda_{1L} \geq 0$ and $\lambda_{1R} = 0$, there are two possible wave structures, see Figure 3.9. The structure in Figure 3.9(a) is for the case when λ_1 in the original

constant region is less than 0, i.e. $\lambda_{1l} = u_l - \sqrt{h_l} < 0$; there is still a rarefaction fan on the left side of the shock, and as $\lambda_{1l} = 0$ this fan forms up to $x = 0$. The wave structure in Figure 3.9(b) is for the case when $\lambda_{1l} \geq 0$ and we must have $\lambda_{1L} = \lambda_{1l} > 0$, as a result there is no λ_1 wave on the left side of the stationary shock.

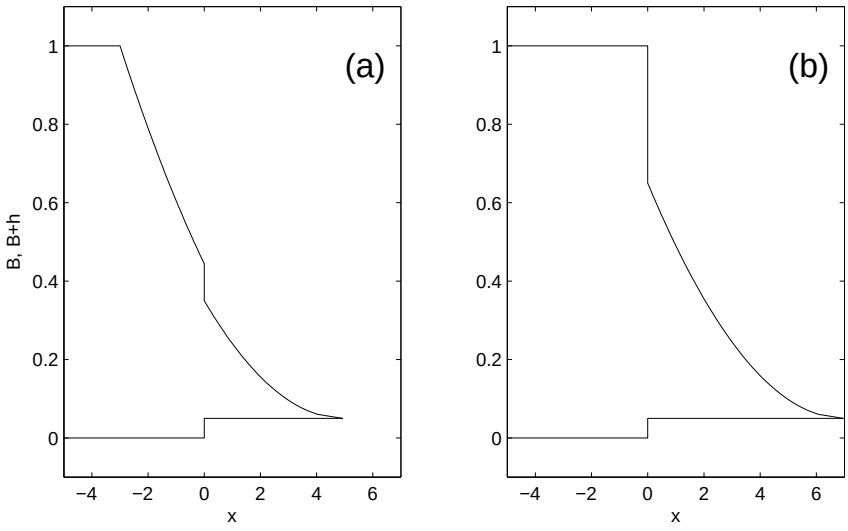

Figure 3.9: Schematic wave structures for $\lambda_{1L} \geq 0$ and $\lambda_{1R} = 0$. (a) for case of $\lambda_{1l} < 0$, $\lambda_{1L} = 0$ and $\lambda_{1R} = 0$; (b) for case of $\lambda_{1l} \geq 0$, $\lambda_{1L} = \lambda_{1l} \geq 0$ and $\lambda_{1R} = 0$.

When $\lambda_{1L} \geq 0$ and $\lambda_{1R} = 0$, we have $\lambda_{2L} > 0$ and $\lambda_{2R} > 0$. There are two Riemann equations (along λ_{1L} and λ_{2L}) and one equation of $\lambda_{1R} = 0$. Together with the two shock conditions, there are five equations but four unknowns, therefore $\lambda_{1L} \geq 0$, $\lambda_{1R} = 0$, $\lambda_{2L} > 0$ and $\lambda_{2R} > 0$ is not a solution to the shock.

4) $\lambda_{1L} \geq 0$ **and** $\lambda_{1R} > 0$

In this case, the new formed constant region (d) in Figure 3.7 exists and the possible wave structures are shown in Figure 3.10.

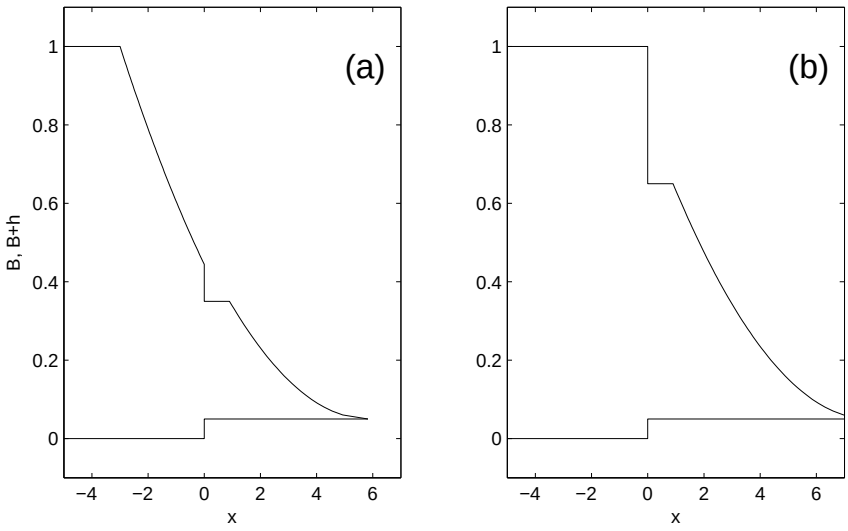

Figure 3.10: Schematic wave structures for the solution of $\lambda_{1L} \geq 0$ and $\lambda_{1R} > 0$. (a) for case of $\lambda_{1l} < 0$, $\lambda_{1L} = 0$ and $\lambda_{1R} = 0$; (b) for case of $\lambda_{1l} \geq 0$, $\lambda_{1L} = \lambda_{1l} \geq 0$ and $\lambda_{1R} > 0$.

When $\lambda_{1L} \geq 0$ and $\lambda_{1R} > 0$, we have $\lambda_{2L} > 0$ and $\lambda_{2R} > 0$. There are two Riemann equations (along λ_{1L} and λ_{2L}) on the two sides of the shock. Thus together with the two shock conditions, there are four equations and four unknowns, therefore $\lambda_{1L} \geq 0$, $\lambda_{1R} > 0$, $\lambda_{2L} > 0$ and $\lambda_{2R} > 0$ is a possible solution to the shock.

Summary of the wave solutions

All the possible solutions discussed above are shown in Table 3.1.

In summary, there are two possible solutions for the shock, with Solution i):

Case	λ_2	Number of equations	Possible solution	Figure
1) $\lambda_{1L} < 0$ and $\lambda_{1R} = 0$	$\lambda_{2L} < 0$ and $\lambda_{2R} > 0$	3		Figure 3.8
	$\lambda_{2L} \geq 0$ and $\lambda_{2R} > 0$	4	Solution i)	
2) $\lambda_{1L} < 0$ and $\lambda_{1R} > 0$	$\lambda_{2L} < 0$ and $\lambda_{2R} > 0$	2		Figure 3.7
	$\lambda_{2L} \geq 0$ and $\lambda_{2R} > 0$	3		
3) $\lambda_{1L} \geq 0$ and $\lambda_{1R} = 0$	$\lambda_{2L} > 0$ and $\lambda_{2R} > 0$	5		Figure 3.9
4) $\lambda_{1L} \geq 0$ and $\lambda_{1R} > 0$	$\lambda_{2L} > 0$ and $\lambda_{2R} > 0$	4	Solution ii)	Figure 3.10

Table 3.1: Summary of all possible wave solutions for a wet-dry dam-break problem over a fixed discontinuous bed.

$\lambda_{1L} < 0$, $\lambda_{1R} = 0$, $\lambda_{2L} \geq 0$ and $\lambda_{2R} > 0$ (Figure 3.8) and Solution ii): $\lambda_{1L} \geq 0$, $\lambda_{1R} > 0$, $\lambda_{2L} > 0$ and $\lambda_{2R} > 0$ (Figure 3.9).

Solution i) is a possible solution for the case in which the water flow is subcritical, i.e. $\lambda_{1l} = u_l - \sqrt{h_l} < 0$. However, in Solution ii), $\lambda_{1L} = 0$ and $\lambda_{1R} > 0$ could also be a solution to the dam-break problem with initial conditions of $\lambda_{1l} < 0$. Furthermore, in Solution ii), $\lambda_{1L} > 0$ and $\lambda_{1R} > 0$ might be a solution describing supercritical dam-break flow. In the following, we here prove that Solution ii) is not a solution to the wet-dry dam-break problem with $B_r > B_l$.

For the stationary shock, $W = 0$, the shock conditions (2.56) and (2.57) become

$$h_R u_R - h_L u_L = 0, \tag{3.26}$$

$$h_R u_R^2 + \frac{h_R^2}{2} - h_L u_L^2 - \frac{h_L^2}{2} + \frac{1}{2}(B_R - B_L)(h_L + h_R) = 0. \tag{3.27}$$

In Solution ii), as $\lambda_{1L} = u_L - \sqrt{h_L} \geq 0$, we have $u_L \geq \sqrt{h_L} \Rightarrow (h_L u_L)^2 \geq h_L^3$.

Therefore

$$h_R u_R^2 + \frac{h_R^2}{2} - h_L u_L^2 - \frac{h_L^2}{2} = \frac{(h_L u_L)^2}{h_R} + \frac{h_R^2}{2} - \frac{(h_L u_L)^2}{h_L} - \frac{h_L^2}{2}$$
$$= (h_L u_L)^2 \left(\frac{1}{h_R} - \frac{1}{h_L}\right) + \frac{h_R^2}{2} - \frac{h_L^2}{2}. \tag{3.28}$$

Furthermore, from Bernetti et al. (2008), it is shown that when $h_L u_L > 0$, $h_R + B_R - h_L - B_L < 0$, and it gives $h_R < h_L$. Therefore we have $\frac{1}{h_R} - \frac{1}{h_L} > 0$, and from (3.28), we have

$$\begin{aligned} h_R u_R^2 + \frac{h_R^2}{2} - h_L u_L^2 - \frac{h_L^2}{2} &\geq h_L^3 \left(\frac{1}{h_R} - \frac{1}{h_L}\right) + \frac{h_R^2}{2} - \frac{h_L^2}{2} \\ &\geq h_L^2 \left(\frac{h_L}{h_R} - 1 + \frac{1}{2}\frac{h_R^2}{h_L^2} - \frac{1}{2}\right) \\ &\geq h_L^2 \left(\frac{1}{2}\frac{h_L}{h_R} + \frac{1}{2}\frac{h_L}{h_R} + \frac{1}{2}\frac{h_R^2}{h_L^2} - \frac{3}{2}\right) \\ &\geq 0. \end{aligned} \tag{3.29}$$

However, from (3.27) and because $B_L = B_l$ and $B_R = B_r$, $h_R u_R^2 + \frac{h_R^2}{2} - h_L u_L^2 - \frac{h_L^2}{2} = -\frac{1}{2}(B_R - B_L)(h_L + h_R) < 0$ in the case of $B_r - B_l > 0$. This contradicts (3.29), therefore Solution ii) is not a solution. Therefore, Solution i) is the physical solution for the dam-break problem over a discontinuous fixed bed with $B_l < B_r$.

3.3.6 Stationary shock solution

From the wave structure analysis, the left λ_1 wave could be a rarefaction fan or a shock, therefore the solution for the stationary shock is divided into two parts for discussion.

When the left λ_1 wave is a rarefaction, the four governing equations for the shock are a Riemann invariant associated with the left λ_1 rarefaction, two shock

conditions and $\lambda_{1R} = 0$

$$u_l + 2\sqrt{h_l} = u_L + 2\sqrt{h_L}, \tag{3.30}$$

$$h_R u_R - h_L u_L = 0, \tag{3.31}$$

$$h_R u_R^2 + \frac{h_R^2}{2} - h_L u_L^2 - \frac{h_L^2}{2} + \frac{1}{2}(B_R - B_L)(h_L + h_R) = 0, \tag{3.32}$$

$$u_R - \sqrt{h_R} = 0, \tag{3.33}$$

from which the four unknowns h_L, u_L, h_R and u_R are solved.

When the left λ_1 wave is a shock, the solution of the stationary shock is combined with that for the left λ_1 shock, the speed of which is denoted as W_l. There are therefore 5 unknowns, W_l, h_L, u_L, h_R and u_R. The 5 governing equations are two shock conditions for the left λ_1 shock, two shock conditions for the stationary shock and $\lambda_{1R} = 0$

$$h_l u_l - h_L u_L - (h_l - h_L)W_l = 0, \tag{3.34}$$

$$W_l(h_l u_l - h_L u_L) - h_l u_l^2 - \frac{h_l^2}{2} + h_L u_L^2 + \frac{h_L^2}{2} - \frac{1}{2}(B_l - B_L)(h_L + h_l) = 0, \tag{3.35}$$

$$h_R u_R - h_L u_L = 0, \tag{3.36}$$

$$h_R u_R^2 + \frac{h_R^2}{2} - h_L u_L^2 - \frac{h_L^2}{2} + \frac{1}{2}(B_R - B_L)(h_L + h_R) = 0, \tag{3.37}$$

$$u_R - \sqrt{h_R} = 0. \tag{3.38}$$

For the solution for the λ_1 rarefaction wave we refer to Stoker (1957).

3.3.7 Computation procedure

The procedure of the Riemann solution when the water can overtop the bed on the right is:

1. Solve the stationary shock to obtain h_L, u_L, h_R and u_R. Assume that the left λ_1 wave is a rarefaction wave, and the stationary shock is solved by equations (3.30)-(3.33). If $h_L \leq h_l$, the assumption that the left λ_1 wave is a rarefaction is correct, and the stationary shock is solved. If $h_L > h_l$, the λ_1 wave should be a shock, and the stationary shock is solved by equations (3.34)-(3.38).

2. Solve the left λ_1 wave. If $h_L > h_l$, the λ_1 shock has already been solved. If $h_L \leq h_l$, the left λ_1 wave is a rarefaction, and the variables across the λ_1 rarefaction are solved according to the Riemann invariant along the λ_2 characteristic.

3. Solve the λ_1 rarefaction on the right side of the stationary shock by the rarefaction solution.

3.3.8 Test cases and results

The wave solutions for the wet-dry dam-break problems with a discontinuous bed with $h_l = 1, B_l = 0, B_r = 0.2$ and various u_l values are shown in Figure 3.11. It is shown that when $u_l = -1.5$, the water cannot overtop the bed on the right of the dam, and the bed step is adjacent to a newly formed constant region, in which $h_L = 0.0625$ and $u_L = 0$. When $u_l = 0$, the water can overtop the bed step, and the dry bed is adjacent to a rarefaction wave. When u_l increases, $\lambda_{1L} = u_L - \sqrt{h_L}$ and water depth h_L in the newly formed constant region also increase. When $u_l = 0.488$, h_L is increased to h_l and $\lambda_{1L} = \lambda_{1l} = -0.512 < 0$. Further increasing u_l but with $-0.512 < \lambda_{1l} < 0$, results in an increased $h_L > h_l$,

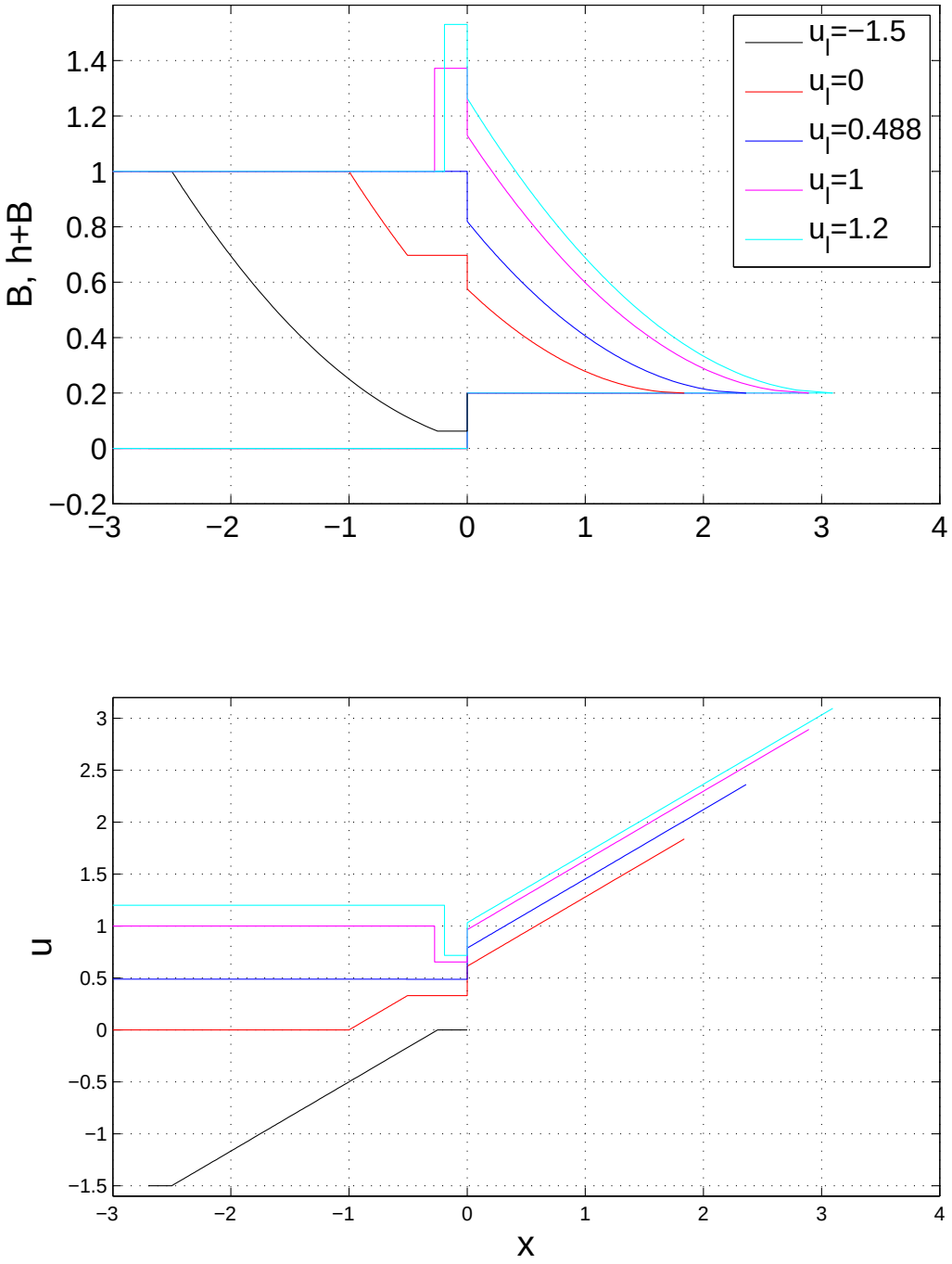

Figure 3.11: Wave solution for wet-dry dam-break problems over a fixed discontinuous bed with various u_l values at $t = 1$.

and the left λ_1 rarefaction wave develops into a λ_1 shock with $W_l < 0$ and $\lambda_{1L} < 0 < \lambda_{1l}$. The corresponding wave structure is the original constant region, a λ_1

shock, a newly formed constant region, a stationary shock and a λ_1 rarefaction wave, see Figure 3.11.

When u_l increases further such that $\lambda_{1l} > 0$, h_L also increases and the left λ_1 wave remains a shock. However, as u_l increases λ_{1L} and W_l increase, but λ_{1L} and W_l remain negative. For instance, when u_l increases from 1 to 1.2, W_l increases from -0.276 to -0.192. Furthermore from § 3.3.5, it is shown that we always have $\lambda_{1L} < 0$, which implies that W_l is always negative. As $\lambda_{1l} \to \infty$, $W_l \to 0$.

The wave solution for the wet-dry dam-break problem with $h_l = 1$, $u_l = 1.2$, $B_l = 0$ and $B_r = 2.6$ is shown in Figure 3.12. As the bed on the right side of the dam is high enough, the water still cannot overtop the bed step even though the water behind the dam is of a large velocity. However, the water depth in the new formed constant region is greater than that in the original constant state, and it results in a λ_1 shock, see Figure 3.12. The water depth in the newly formed constant region is $h_L = 2.428$, and velocity is $u_L = 0$. The speed of the left shock λ_1 is $W_l = -0.84$.

3.4 Wet-dry dam-break problem over a discontinuous mobile bed

3.4.1 Wave profile analysis

The dam-break problem over a mobile discontinuous bed is slightly different from the equivalent fixed bed case. In the fixed bed case, as $\sigma = 0$, whatever

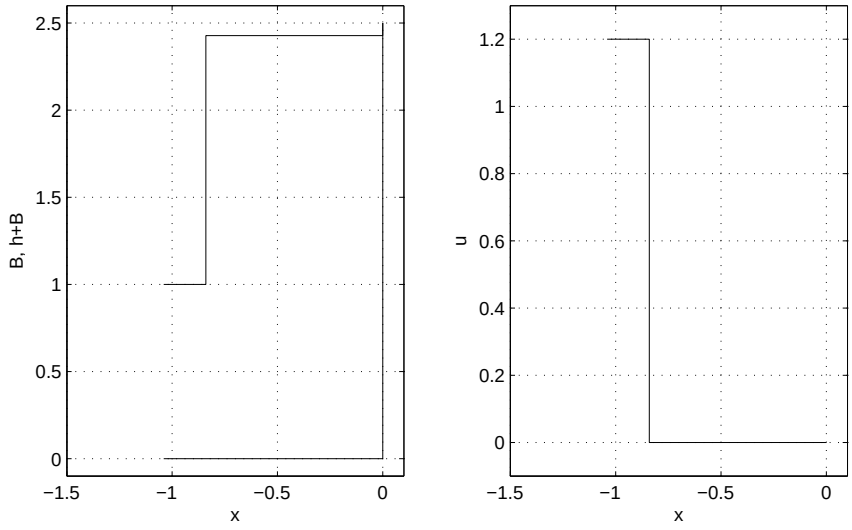

Figure 3.12: Wave solution for the fixed bed wet-dry dam-beak problem with $h_l = 1$, $u_l = 1.2$, $B_l = 0$ and $B_r = 2.6$ at $t = 1$.

the size of the bed step, it forms a stationary shock; however, in the mobile bed case the bed step may disappear and a smooth slope form, which connects two different bed levels, or the bed step may still exist but move at a certain speed. The fixed bed case could be achieved by setting the bed mobility σ in the morphodynamic system to 0. Therefore the Riemann solutions in § 3.3 for wet-dry dam-break problems on a fixed bed are analysed by the morphodynamic theory aiming to provide some guidance for the solution of the wet-dry dam-break problem over a mobile discontinuous bed.

There are three characteristics in a morphodynamic system with $\lambda_1 \leq \lambda_3 \leq \lambda_2$, and when $\sigma = 0$, one of these characteristics $\equiv 0$. Here we introduce λ_{1h} and λ_{2h} to represent the two hydrodynamic characteristics in the fixed bed system. With $\lambda_1 \leq \lambda_3 \leq \lambda_2$ in the morphodynamic system in mind, when $\lambda_{1h} < 0$ and $\lambda_{2h} > 0$ in the hydrodynamic system, we have (for $\sigma = 0$) $\lambda_1 = \lambda_{1h}$, $\lambda_2 = \lambda_{2h}$

and $\lambda_3 = 0$ in the equivalent morphodynamic system. Conversely when $\lambda_{1h} \geq 0$ and $\lambda_{2h} > 0$, then $\lambda_1 = 0$, $\lambda_2 = \lambda_{2h}$ and $\lambda_3 = \lambda_{1h}$, because $\lambda_1 \leq \lambda_3 \leq \lambda_2$.

The wave structure when the water cannot overtop the bed step in the fixed bed case is a λ_{1h} wave and a newly formed constant region, see Figure 3.12. When the λ_{1h} wave is a rarefaction fan, $\lambda_{1h} = u_l - \sqrt{h_l} < 0$ across this fan and therefore it corresponds to the λ_1 rarefaction fan in the equivalent mobile bed case of $\sigma = 0$. When the λ_{1h} wave is a shock with a negative shock speed, it also corresponds to a λ_1 shock in the mobile bed case of $\sigma = 0$. Therefore when the water cannot overtop the bed step, the wave structure for a wet-dry dam-break problem over a discontinuous mobile bed is the original constant region, a λ_1 wave and a new formed constant region, in which the velocity is 0.

In order to know whether the water can overtop the bed step or not in the mobile bed case, we could first assume that the water cannot overtop. In this case, the water velocity in the new constant region adjacent to the bed step is 0, i.e., $u_L = 0$. Based upon $u_L = 0$, the water depth h_L and bed level B_L in this region are obtained by solving the left λ_1 wave. If $u_l \leq 0 = u_L$, the left λ_1 wave is deduced to be a rarefaction and h_L is solved according to the rarefaction solution. While when $u_l > 0 = u_L$, the λ_1 wave is a shock, and h_L is solved by the shock conditions. We then compare the calculated h_L with the bed step height $B_R - B_L$ ($B_R = B_r$) to determine whether the water can overtop the bed step. If $h_L > B_R - B_L$, the water can overtop the bed step; conversely if $h_L \leq B_R - B_L$, the water cannnot overtop the bed step.

When the water can overtop the bed step, the wave structure in a hydrody-

namic system is the original constant region, a λ_{1h} wave, a new formed constant region, a stationary shock and a λ_{1h} rarefaction wave ($\lambda_{1h} \geq 0$), see Figure 3.11. The corresponding morphodynamic wave structure is the original constant region, a λ_1 wave, a new formed constant region, a λ_3 stationary shock and a λ_3 rarefaction wave. It should be noted that the stationary shock and λ_{1h} rarefaction wave on the right of the bed step in the fixed bed case have become a λ_3 stationary shock and a λ_3 wave in a morphodynamic system.

Note that for the stationary shock in the $\sigma = 0$ case, $\lambda_{3L} = W = \lambda_{3R} = 0$, and the shock is a contact wave. By analogy, we introduce a kind of shock for the morphodynamic system ($\sigma \neq 0$), in which the variables on the two sides of the shock are discontinuous but the characteristic on one side is equal to the shock speed, i.e., $\lambda_{kL} \geq W = \lambda_{kR}$ or $\lambda_{kL} = W \geq \lambda_{kR}$ ($k = 1, 2, 3$); see Figure 3.13. It is here called a parallel rarefaction shock, and this shock usually connects a constant region with a rarefaction fan of the same characteristic family of the shock. In the limit case of $\sigma = 0$, $\lambda_{3L} = W = \lambda_{3R}$ for the stationary shock.

Figure 3.13: Schematic diagram for a parallel rarefaction shock. Left: $\lambda_{kL} = W \geq \lambda_{kR}$; right: $\lambda_{kL} \geq W = \lambda_{kR}$.

From another aspect, the flow structure of the wet-dry dam-break problem over a continuous mobile bed with motionless water behind the dam is two rarefaction fans (λ_1 and λ_3) (KD09). When there is a bed step, if the λ_3 wave is only a rarefaction, the λ_3 characteristic increases, decreases and then increases, and as the dry bed can only be adjacent to a λ_3 rarefaction, it is deduced that a λ_3 parallel rarefaction shock also exists. If, in general, we call the combination of the λ_3 stationary shock and λ_3 rarefaction fan a λ_3 wave, the general structure for a wet-dry dam-break problem over a discontinuous mobile bed $\sigma = 0$ is the original constant region, a λ_1 wave, a newly formed constant region and a λ_3 wave, see Figures 3.11-3.12. By analogy, the wave structure for a wet-dry dam-break problem over a discontinuous mobile bed ($\sigma \geq 0$), when the water overtops the bed step, is further deduced to be a λ_1 wave, a new formed constant region and a λ_3 wave, in which the λ_3 wave could be a rarefaction or the combination of a parallel rarefaction shock and a rarefaction, and the left λ_1 could be a rarefaction or a shock, see Figures 3.14-3.15.

3.4.2 Parallel shock solution

There are seven variables for a morphodynamic parallel rarefaction shock (h_L, u_L, B_L, h_R, u_R, B_R and W). We assume the variables on the left side of a parallel rarefaction shock are known, and we need to obtain the other four unknowns by the shock conditions and also the fact that the shock velocity W is equal to the characteristic on the right side.

There are three shock conditions and one equation $\lambda_{3R} = W$. Substituting $\lambda_{3R} =$

W into the λ polynomial equation (2.30), the four equations for the λ_3 parallel rarefaction shock become

$$(h_L - h_R)W - (h_L u_L - h_R u_R) = 0, \tag{3.39}$$

$$W(h_R u_R - h_L u_L) - \left(h_R u_R^2 + \frac{h_R^2}{2} - h_L u_L^2 - \frac{h_L^2}{2}\right) - \frac{1}{2}(B_R - B_L)(h_R + h_L) = 0, \tag{3.40}$$

$$(B_L - B_R)W - \sigma(u_L^3 - u_R^3) = 0, \tag{3.41}$$

$$W^3 - 2u_R W^2 + (u_R^2 - 3\sigma u_R^2 - h_R)W + 3\sigma u_R^3 = 0. \tag{3.42}$$

Note, however, the hypothesis of a parallel rarefaction shock in the wave structure is not confirmed by the numerical solution, i.e: the λ_3 parallel rarefaction shock is not obtained by the numerical solution. This could be because that the hypothesis of the Riemann wave structure with a parallel rarefaction shock is not correct, or that the numerical method used to solve the governing equations cannot find all the possible solutions for the system. In the latter case, an appropriate numerical method is required.

3.4.3 Computation procedure

When the water can overtop the bed step, the procedure of the Riemann solution for a wet-dry dam-break problem over a flat discontinuous mobile bed is:

1. Give an initial estimate for the water depth in the new formed constant region: $h_L = h_L^{(1)}$.

2. Solve the left λ_1 wave.

- If $h_L > h_l$, the left λ_1 wave is a shock, and as the variables on the left side of the λ_1 shock are known, the variables in the newly formed constant region are obtained by the morphodynamic shock conditions.
- If $h_L \leq h_l$, the λ_1 wave is a rarefaction wave, and the variables across the λ_1 rarefaction are obtained by the rarefaction solution.

3. Solve λ_3 wave.
   - Initially assume that the λ_3 wave is the combination of a λ_3 parallel rarefaction shock and a λ_3 rarefaction.
   - As the left λ_1 wave has been solved, h_L, u_L, and B_L are known. Subsequently, solve the λ_3 parallel rarefaction shock to get h_R, u_R and B_R; if $h_R = h_L$, which means that there is no discontinuity, then the λ_3 wave is deduced to be a rarefaction only. If $h_R < h_L$, it is deduced that a λ_3 parallel rarefaction shock is present, and this shock is solved.
   - Solve for the variables across the λ_3 rarefaction wave by the rarefaction solution.
4. Refine h_L. According to the results of wave solutions, we check whether the sediment volume is conserved within the required accuracy. If it is conserved, the updated h_L is assumed to be correct and the updated wave solutions are the correct solution for the dam-break problem; if not, h_L is changed (i.e. $h_L^{(2)}$) and Steps 2-4 are repeated until the desired accuracy is

achieved. Note that the required accuracy of sediment conservation depends largely on the numerical decrement in h for integration to calculate u and B values.

3.4.4 Test cases and results

Dam-break problems with various initial conditions are considered over a mobile bed with $\sigma = 0.0654$ (this value being chosen for consistency with KD10, who determined it by crudely equating it to field measurements of Masselink et al. (2005)). The effects of the initial velocity of the water behind the dam u_l and bed step height B_r on the dam-break flow and bed change profile are investigated.

The wave solutions for wet-dry dam-break problems over a flat discontinuous mobile bed ($\sigma = 0.0654$) with $h_l = 1, B_l = 0, B_r = 0.2$ and various u_l values are shown in Figure 3.14. When $u_l = -1.5$, the water cannot overtop the bed step, and the bed step is adjacent to a newly formed constant region, in which $h_L = 0.083$, $u_L = 0$ and $B_L = -0.118$. In the case of $u_l = 0$, the water can overtop the bed step; the stationary shock in the equivalent fixed bed case disappears as a result of the large bed mobility and a λ_3 rarefaction wave forms. There is a sediment bore with the height of 0.121 at the tip. When u_l increases to 1, h_L increases to nearly h_L, and the width of the left λ_1 rarefaction wave is considerably reduced. When $u_l = 1.5$, the left λ_1 wave becomes a shock. It is found that the bed step in the equivalent fixed bed case does not exist because of the lack of bed mobility.

Further, we alter B_r values to show the effects of the bed step height on the dam-break flow, see Figure 3.15. It is shown that as B_r increases, the starting point of the λ_3 rarefaction wave approaches the position of the initial bed step. When the bed step height is high enough, it has the potential to form a parallel rarefaction shock; however, it is not obtained by the numerical simulation.

3.5 Wet-wet mobile bed dam-break problem over a continuous mobile bed

3.5.1 Initial conditions

The initial conditions for a wet-wet dam-break problem are shown in Figure 1.2. However, all the variables in this section are non-dimensional. There is a dam located at $x = 0$. There is water of constant depth and velocity on each side of the dam with $h_l > h_r$ and $u_l = u_r = 0$. The bed on the two sides is flat and continuous with $B_l = B_r = 0$. Hence, the two regions on the two sides of the dam are in constant state. The dam is assumed to be removed at $t = 0$.

3.5.2 Wave profile analysis

There are two constant regions on the two sides of the dam at the initial time; the wet-wet problem is therefore a Riemann problem. There are three characteristic families in the bed-load-only morphodynamic system, so there are three waves and four constant states separated by the three waves (Toro, 1997;

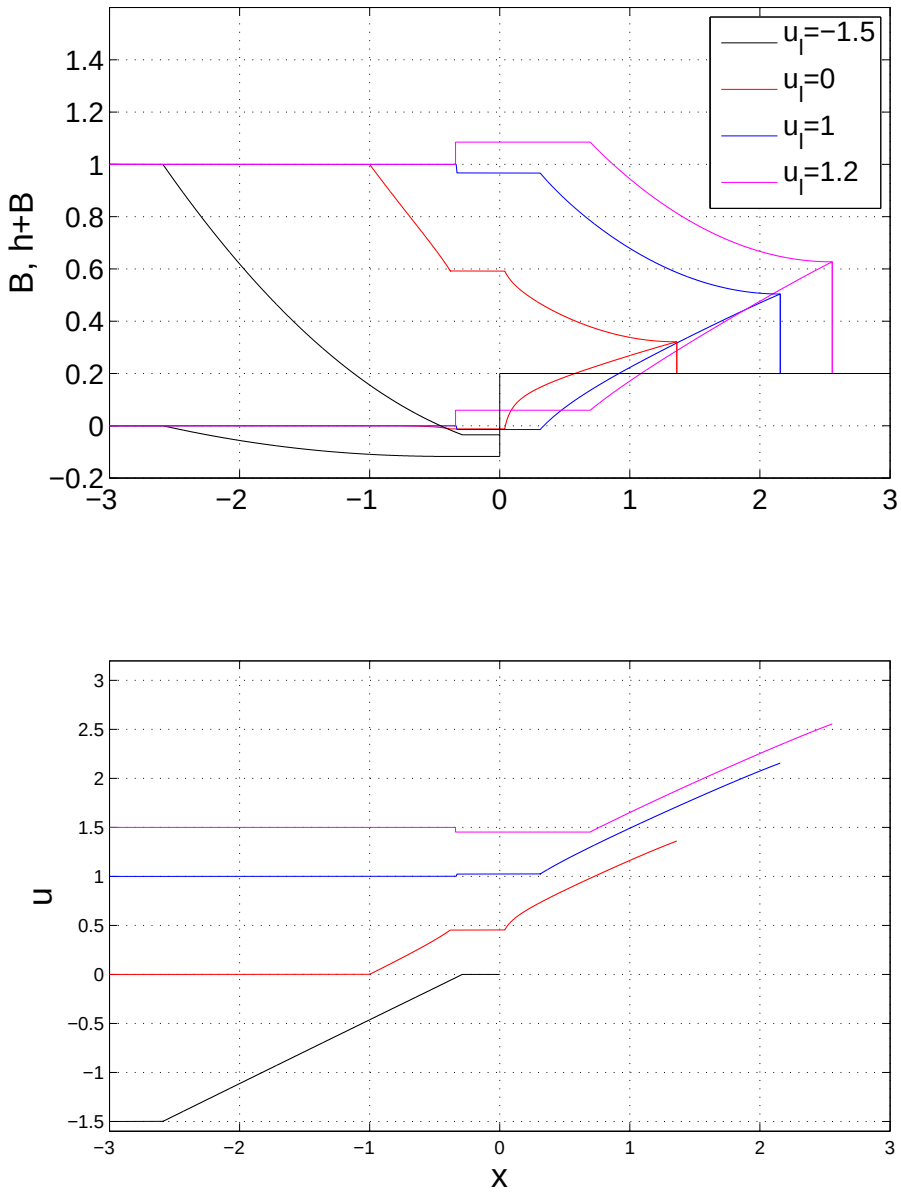

Figure 3.14: Wave solutions for wet-dry dam-break problems over a discontinuous mobile bed with various u_l values ($\sigma = 0.0654$) at $t = 1$.

Fraccarollo and Capart, 2002). The three characteristic fields are genuinely non-linear, so the three waves are rarefaction waves or shock waves.

KD09 have examined the wave structure for a wet-dry dam-break problem on a mobile bed, and in the wet-dry bed case, there are two centred simple waves, a

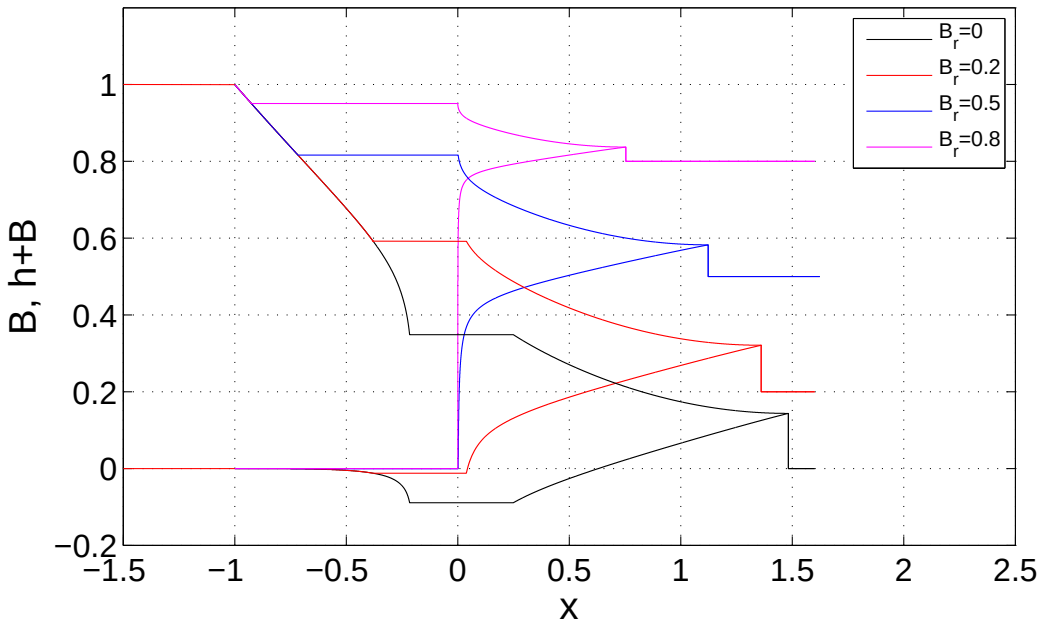

Figure 3.15: Wave solutions for wet-dry dam-break problems over discontinuous mobile beds with various B_r values ($\sigma = 0.0654$) at $t = 1$.

λ_1 simple wave and a λ_3 simple wave. In the region $x < 0$ the λ_1 centered simple wave forms up to the point where the original constant state region ends; this is then followed further downstream by the λ_3 centred simple wave. The λ_2 wave terminates because of the dry bed (h=0). In the wet-wet dam-break problem, the λ_2 wave does not vanish, so there are three waves and two newly formed constant regions.

Using the wet-dry mobile bed dam-break problem in KD09 as a guide, we hypothesize that there is still a λ_1 rarefaction fan and a λ_3 rarefaction fan in the wet-wet bed case. Additionally, in the wet-dry bed case, when sediment mobility $\sigma \to 0$, the width of the newly formed constant region $\to 0$ (KD09), and the λ_1 and λ_3 rarefaction fans merge into a single fan, forming the Ritter solution

(Fraccarollo and Capart, 2002). By analogy, the solutions of the wet-wet mobile bed case should approach the equivalent fixed bed solution in the limiting case of $\sigma = 0$. In the equivalent wet-wet fixed bed case, the wave structure is a left λ_1 rarefaction and a right λ_2 shock (Stoker, 1957, p. 291-341), and as the left λ_1 rarefaction in the fixed bed case corresponds to two (λ_1 and λ_3) rarefactions in the mobile case, the right λ_2 shock in the fixed bed case is deduced to correspond to the third wave in the mobile bed case. That means the third wave in the wet-wet mobile bed case is a λ_2 shock, see Figure 3.16. Furthermore, because the λ_2 field is a genuinely nonlinear field, it is not a contact discontinuity but a shock. The four constant regions are called the left constant region, the left constant star region, the right constant star region and the right constant region. The variables in these four regions are denoted as $\overrightarrow{U}_l$, $\overrightarrow{U}_{l*}$, $\overrightarrow{U}_{r*}$ and $\overrightarrow{U}_r$, respectively, see Figure 3.16. From another point of view, the water velocity increases after traversing the two rarefaction fans such that $u_{r*} > 0 = u_r$; however, if the third wave were a rarefaction fan, the velocity should keep increasing across the third wave, so it must be a λ_2 shock that connects the right constant star region and the original right constant region.

3.5.3 Morphodynamic shock solution

According to the wave structure analysis, the shock is a λ_2 shock, and it is therefore the case of a uniform bore advancing into still water over a mobile bed.

Substituting the variables in the right constant region and right constant star

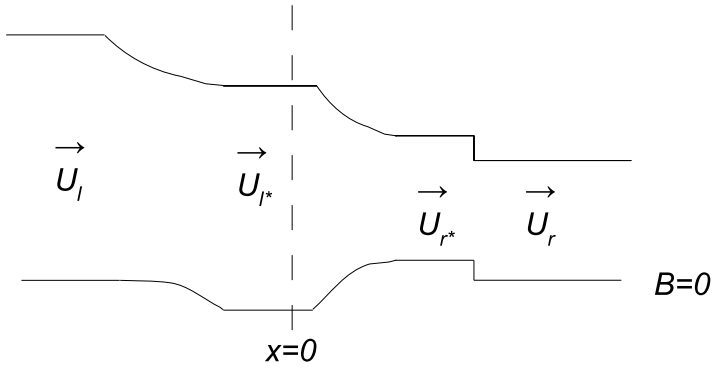

Figure 3.16: Wave structure for a wet-wet dam-break problem over a continuous mobile bed.

region into the shock conditions (2.56), (2.57) and (2.58) gives

$$h_{r*}u_{r*} - h_r u_r - (h_{r*} - h_r)W = 0 \tag{3.43}$$

$$W(u_{r*}h_{r*} - u_r h_r) - \left(h_{r*}u_{r*}^2 + \frac{h_{r*}^2}{2} - h_r u_r^2 - \frac{h_r^2}{2}\right) - \frac{1}{2}(B_{r*} - B_r)(h_{r*} + h_r) = 0 \tag{3.44}$$

$$(B_{r*} - B_r)W - \sigma u_{r*}^3 + \sigma u_r^3 = 0 \tag{3.45}$$

As $u_r = 0$ and $B_r = 0$, u_{r*} and B_{r*} are obtained from (3.43) and (3.45)

$$u_{r*} = \frac{W(h_{r*} - h_r)}{h_{r*}}, \tag{3.46}$$

$$B_{r*} = \frac{\sigma u_{r*}^3}{W}. \tag{3.47}$$

The equation (3.44) associated with the conservation of fluid momentum is simplified, and it gives

$$W u_{r*}h_{r*} - \frac{h_{r*}^2}{2} - u_{r*}^2 h_{r*} + \frac{h_r^2}{2} - \frac{B_{r*}}{2}(h_{r*} + h_r) = 0. \tag{3.48}$$

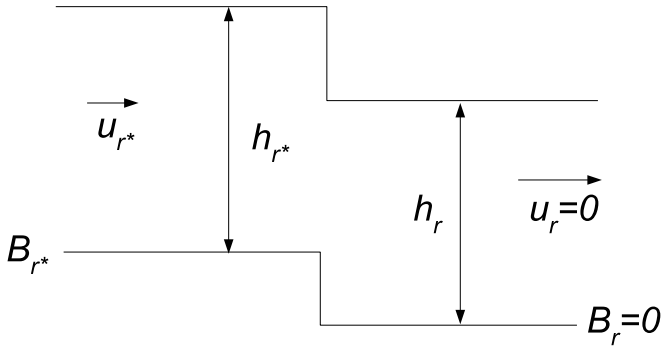

Figure 3.17: Shock relations between the right constant star region and right constant region.

Substituting (3.47) and (3.46) into (3.48) gives

$$\left[h_{r*} - h_r - \frac{(h_{r*}-h_r)^2}{h_{r*}} - \frac{\sigma(h_{r*}-h_r)^3}{2h_{r*}^2}\left(\frac{h_{r*}+h_r}{h_{r*}}\right)\right]W^2 + \frac{(h_r^2 - h_{r*}^2)}{2} = 0. \tag{3.49}$$

Letting

$$\psi = h_{r*} - h_r - \frac{(h_{r*}-h_r)^2}{h_{r*}} - \frac{\sigma(h_{r*}-h_r)^3}{2h_{r*}^2}\left(\frac{h_{r*}+h_r}{h_{r*}}\right) \tag{3.50}$$

gives

$$W = \pm\left(\frac{h_{r*}^2 - h_r^2}{2\psi}\right)^{\frac{1}{2}}. \tag{3.51}$$

Here as it is a λ_2 shock and $\lambda_2 > 0$, the shock velocity W is positive. The value of h_r is known, and if h_{r*} is known as well, W can be solved from (3.51), and u_{r*} and B_{r*} can be obtained from (3.46) and (3.47).

3.5.4 Computation procedure

1. Give initial guess values $h_{l*}^{(1)}$ and $h_{r*}^{(1)}$ to the water depths in the left and right constant star regions h_{l*} and h_{r*}.

2. Wave solutions.

   - Given the water depths in the two star regions, we obtain the variables across the λ_1 and λ_3 rarefaction as well as those in constant star regions by the rarefaction solution.
   - Given the water depth in the right constant star region, the speed of the λ_2 shock and the water velocity in the right constant star region are calculated by the shock solution.

3. Refine h_{r*}. Compare the velocity u_{r*} values calculated from the rarefaction side and the shock side, if the two agree within the desired accuracy, the water depth h_{r*} with the fixed h_{l*} is considered to have been achieved; if they do not, h_{r*} is changed (i.e. $h_{r*}^{(2)}$), the wave solutions and the u_{r*} comparing process are repeated until the desired accuracy is achieved via bisection method. Note that the required accuracy of velocity agreement depends largely on the numerical decrement in h for integration to calculate u and B values.

4. Refine h_{l*}. According to the results of wave solutions, we check whether the sediment volume is conserved within the required accuracy, if it is conserved, the updated values for h_{l*} and h_{r*} are assumed to be correct and the updated variables are correct; if not, change h_{l*} (i.e. $h_{l*}^{(2)}$) and repeat the above steps until the sediment volume is conserved. Also the required accuracy of sediment conservation depends largely on the numerical decrement in h for integration to calculate u and B values.

3.5.5 Test cases and results

In this section, the Riemann solution for the wet-wet dam-break problem is verified by two limiting cases. One limiting case is the nearly fixed bed case ($\sigma = 1 \times 10^{-8}$); the results are compared and those of the equivalent fixed bed case. Another is the nearly dry but mobile bed case ($\sigma = 0.0654$); it is achieved by setting $h_r = 1 \times 10^{-8}$, and the results of this limiting case are compared with the equivalent wet-dry dam-break problem. Lastly, a wet-wet dam-break problem over a mobile bed with finite water depth on both sides is examined.

Nearly fixed bed case

The initial conditions are $h_l = 1$, $u_l = 0$, $B_l = 0$, $h_r = 0.1$, $u_r = 0$, $B_r = 0$ and $\sigma = 1 \times 10^{-8}$. The comparison between the results of this case and those in the equivalent fixed bed case at $t = 1$ is shown in Figure 3.18, which shows very close agreement. There are two rarefaction fans and one shock, and the wave structure is identical to the previous analysis of the wave structure in § 3.5.2.

The left constant star region is barely noticeable, with a width of 2.056×10^{-4}; the λ_1 and λ_3 rarefaction fans are becoming close and merging into the λ_1 rarefaction fan in the equivalent fixed bed case. Furthermore, the two constant star region solutions in the mobile bed case are $h_{l*} = 0.445$, $u_{l*} = 0.667$, $B_{l*} = -6.517 \times 10^{-8}$, $h_{r*} = 0.396$, $u_{r*} = 0.741$ and $B_{r*} = 1.136 \times 10^{-8}$. The speed of the λ_2 shock is 0.991.

In the equivalent hydrodynamic dam-break problem, the water depth and velocity in the newly formed constant region are 0.396 and 0.741, which are very

close to h_{r*} and u_{r*}. The shock speed in the fixed bed case is 0.991, also close to that in the mobile bed case. It should be noted that the comparison for bed level B in Figure 3.18 shows a significant difference between the two sets of results; however, the order of bed change and therefore the difference is extremely small.

Nearly dry bed case

In this case, $\sigma = 0.0654$ is set to represent the mobile bed. The initial conditions in this case are $h_l = 1$, $u_l = 0$, $B_l = 0$, $h_r = 1 \times 10^{-8}$, $u_r = 0$ and $B_r = 0$. The comparison between the results of this case with those of the equivalent wet-dry dam-break problem at $t = 1$ is shown in Figure 3.19, and very close agreement is obtained. The right constant star region tends to vanish: its width is only 0.0486, and its depth is very close to 0.

The variables in the two constant star regions are $h_{l*} = 0.435$, $u_{l*} = 0.739$, $B_{l*} = -0.0917$, $h_{r*} = 3.161 \times 10^{-7}$, $u_{r*} = 1.485$ and $B_{r*} = 0.140$. While in the equivalent wet-dry dam-break problem, the water depth, velocity and bed level in new formed constant region are 0.437, 0.733 and -0.0888, which are close to h_{l*}, u_{l*} and B_{l*} in the wet-wet dam-break problem. Furthermore, the λ_2 shock speed is 1.533, and it is also close to the speed of the sediment bore (1.482) in the equivalent wet-dry dam-break problem. The difference in the speeds of the λ_2 shock and the sediment bore at the tip is due to the small water depth $h_r = 1 \times 10^{-8}$ used to represent a dry bed. The calculations in Pritchard and Hogg (2002) suggest that the perturbation to the shock speed speed scales as $2^{7/4} h_r^{1/4}$,

which with $h_r = 1 \times 10^{-8}$ would be 0.034. Additionally, the bed level at the tip in the wet-dry dam-break problem is 0.144, higher than B_{r*}, but still close.

Wet-wet dam-break problem

The initial conditions are $h_l = 1$, $u_l = 0$, $B_l = 0$, $h_r = 0.1$, $u_r = 0$ and $B_r = 0$, with $\sigma = 0.0654$. The wave solution at $t = 1$ is shown in Figure 3.20.

The constant star region solutions are $h_{l*} = 0.509$, $u_{l*} = 0.597$, $B_{l*} = -0.0378$, $h_{r*} = 0.380$, $u_{r*} = 0.735$ and $B_{r*} = 0.0263$. The speed of the λ_2 shock is 0.998.

3.6 Concluding remarks

The simple wave theory for the Riemann problem are presented; Riemann solutions and wave structures for different dam-break problems are presented. The wave structure for a wet-dry dam-break problem over a mobile continuous bed is a λ_1 and λ_3 rarefaction, and a sediment bore forms at the tip. For a wet-dry dam-break problem over a fixed discontinuous bed, there is a stationary shock separating two rarefactions waves. For the equivalent dam-break problem over a mobile discontinuous bed, the wave structure could be two rarefactions or two rarefactions separated by a special shock with $\lambda_{3L} > W = \lambda_{3R}$. However, the parallel rarefaction shock is not obtained in the numerical solution. Two rarefactions (λ_1 and λ_3) and a λ_2 shock forms under a wet-wet dam-break problem with still water on both sides over a continuous mobile bed.

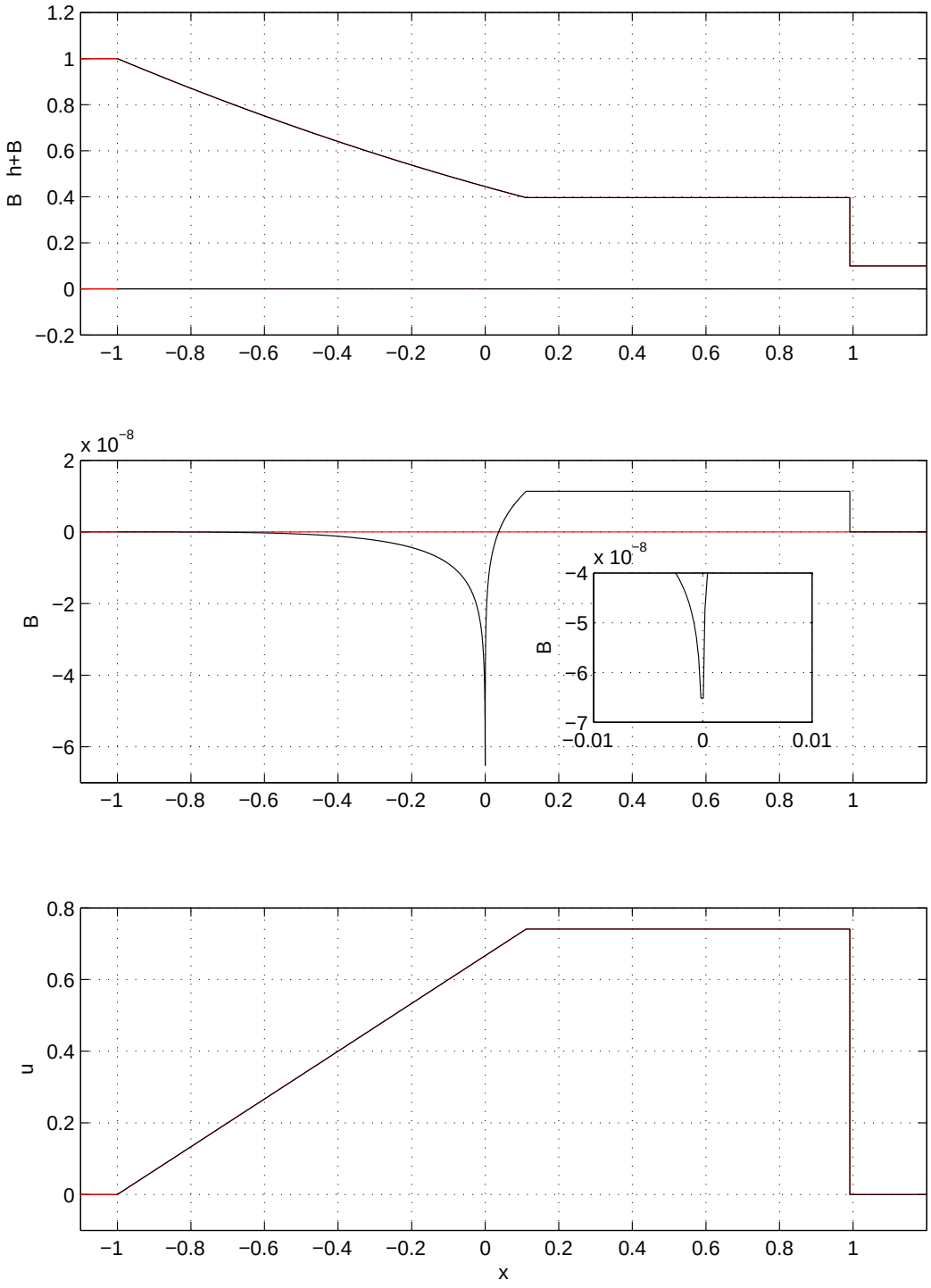

Figure 3.18: Comparison between the results of the nearly fixed bed case and those of the equivalent fixed dam-break problem at $t = 1$. Black: present model; red: equivalent fixed bed dam-break solution.

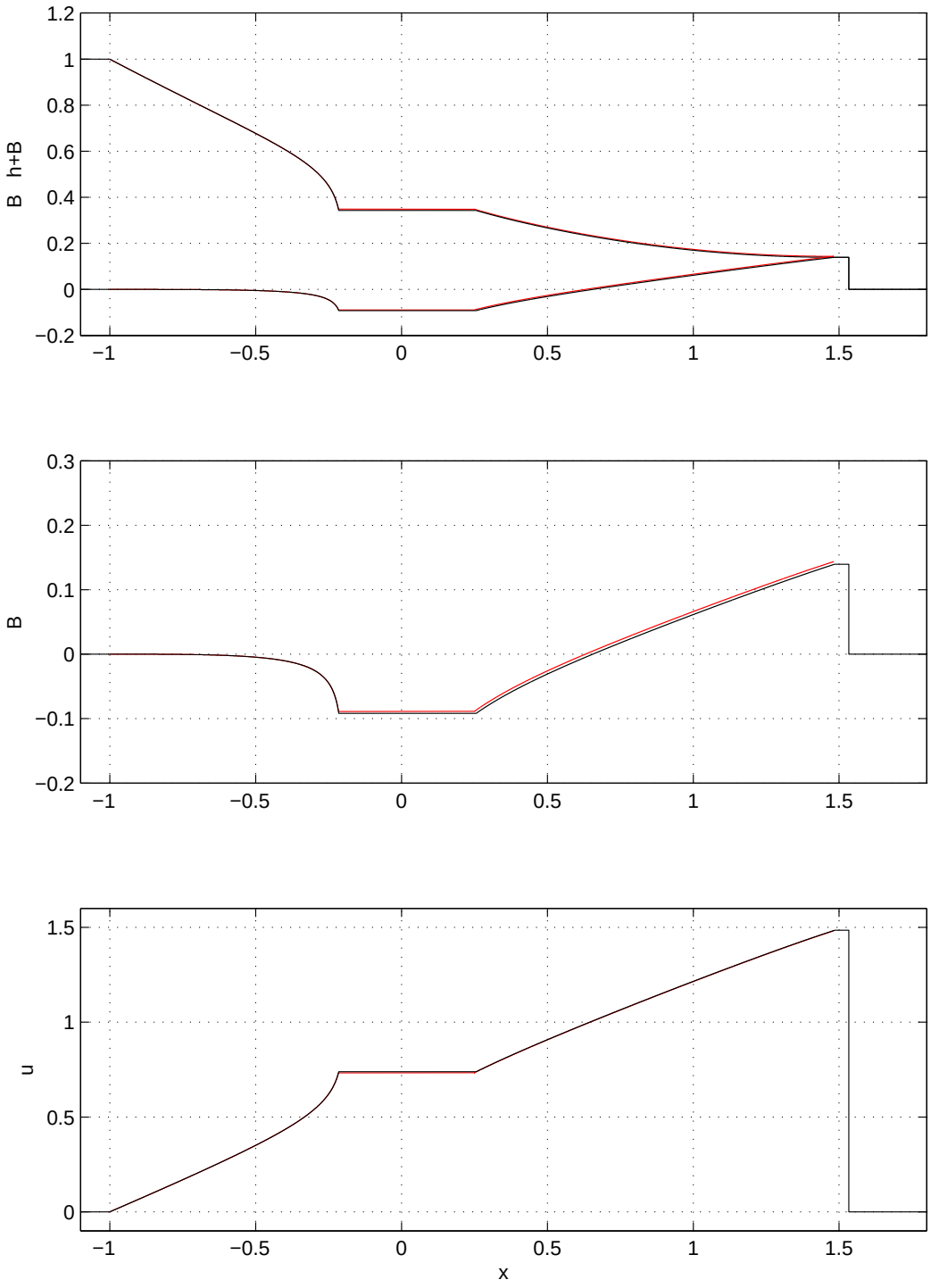

Figure 3.19: Comparison between the results of the nearly wet-dry dam-break problem and those of the equivalent wet-dry dam-break problem at $t = 1$. Black: present model; red: equivalent wet-dry dam-break solution.

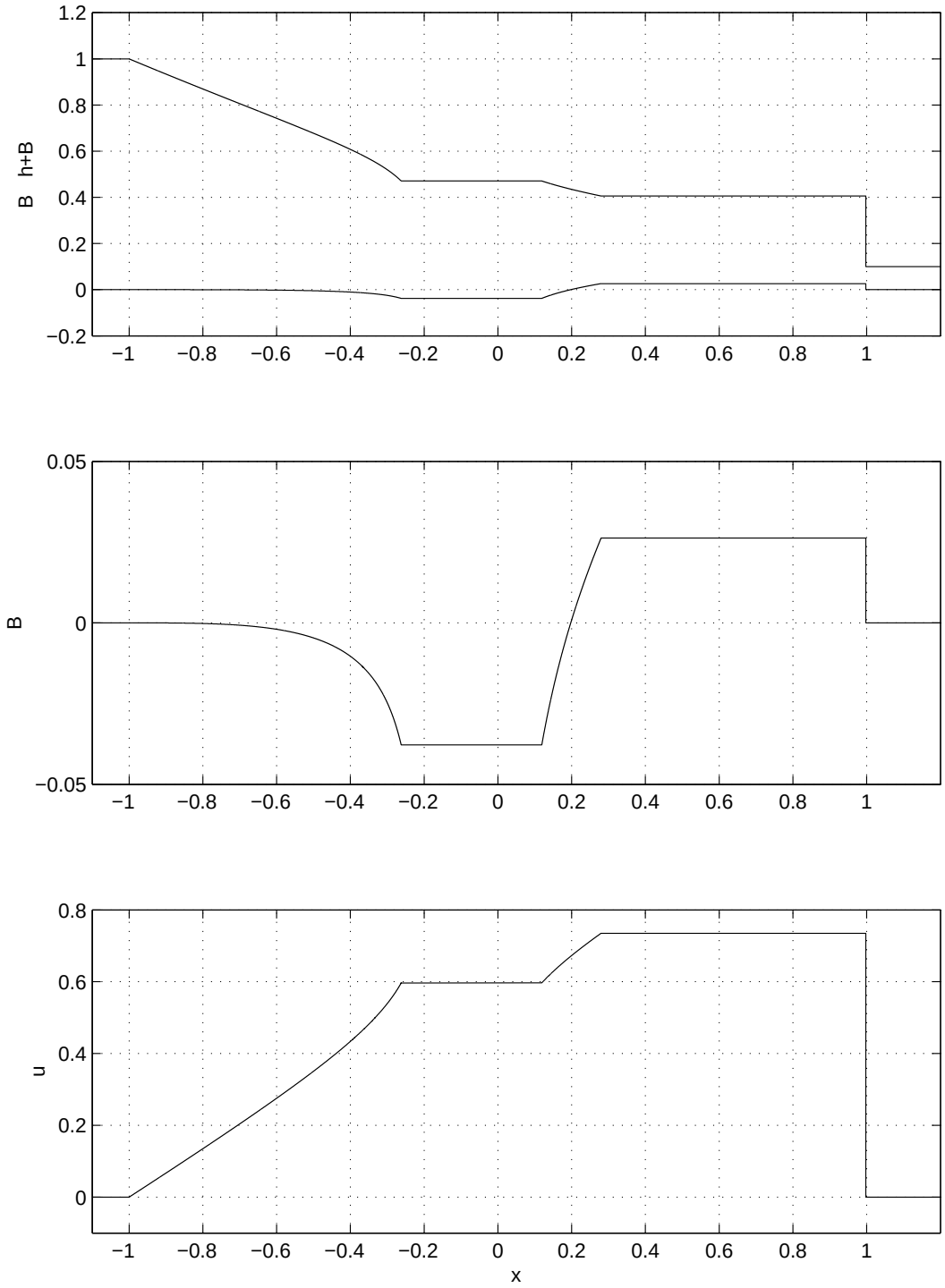

Figure 3.20: Wet-wet dam-break solution over a continuous mobile bed at $t = 1$ ($\sigma = 0.0654$).

CHAPTER 4

Numerical method

The numerical construction including the boundary treatment for the STI MOC solver for the bed-load-only and combined load systems is presented in this chapter. The shock inception and solution for unsteady flows on a fixed grid are also explained. The convergence of results is also checked by varying the space interval Δx and time interval Δt.

4.1 STI MOC numerical construction

4.1.1 Bed-load-only system

The schematic grid and characteristic configuration based on the STI MOC scheme for the bed-load-only system are shown in Figure 4.1.

First-order accuracy scheme

To obtain the h, u and B values at the (i) grid at time step (j+1), i.e., point p in Figure 4.1, we put the Riemann equation for the bed-load-only system (2.45)

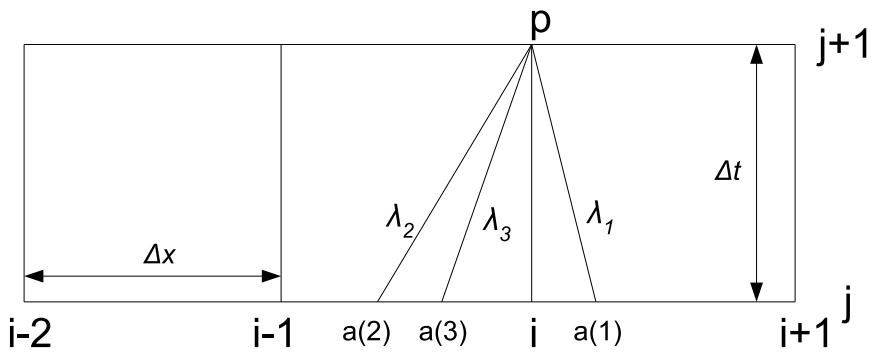

Figure 4.1: Grid and characteristic configuration based on STI MOC scheme for the bed-load-only system.

into Euler difference form. If the Euler difference is of first-order accuracy in time and space, it gives:

$$\Re^{(k)} = \lambda_k \frac{u_p - u_{a(k)}}{\Delta t} + \frac{\lambda_k + \sigma q_h}{\lambda_k - u_{a(k)}} \frac{h_p - h_{a(k)}}{\Delta t} + \frac{B_p - B_{a(k)}}{\Delta t} = 0, k = 1, 2, 3, \quad (4.1)$$

where $u_{a(k)} \equiv u(a(k))$ etc., and $\lambda_k \equiv \lambda_k(a(k))$ refer to values of dependent variables at the time $(j\Delta t)$ along the k^{th} characteristic at point $a(k)$; see Figure 4.1. Here, point p is the point at which the dependent variables are unknown and at which we need to solve the equation (4.1). $\dfrac{\Delta x}{\Delta t} \geq \lambda_{max}$ is required to satisfy the Courant-Friedrichs-Lewy (CFL) condition, where λ_{max} is the maximum absolute value of all characteristics.

In (4.1), if the values of variables at points $a(1)$, $a(2)$ and $a(3)$ are all known, then there are three unknowns: h_p, u_p and B_p. Putting the known variables on the right side, (4.1) is rearranged as:

$$\lambda_k u_p + \frac{\lambda_k + \sigma q_h}{\lambda_k - u_{a(k)}} h_p + B_p = L_k, \; k = 1, 2, 3, \quad (4.2)$$

with

$$L_k = \lambda_k u_{a(k)} + \frac{\lambda_k + \sigma q_h}{\lambda_k - u_{a(k)}} h_{a(k)} + B_{a(k)}. \tag{4.3}$$

Equation (4.2) forms a set of three linear equations with three unknowns, and h_p, u_p and B_p are solved directly from (4.2):

$$u_p = \frac{(L_3 - L_1) - N(L_2 - L_1)}{(\lambda_3 - \lambda_1) - N(\lambda_2 - \lambda_1)}, \tag{4.4}$$

$$h_p = \frac{(\lambda_1 - u_{a(1)})(\lambda_2 - u_{a(2)})(L_2 - L_1 - (\lambda_2 - \lambda_1)u_p)}{(\lambda_1 - u_{a(1)})(\lambda_2 + \sigma q_h) - (\lambda_2 - u_{a(2)})(\lambda_1 + \sigma q_h)}, \tag{4.5}$$

$$B_p = L_1 - \lambda_1 u_p - \frac{\lambda_1 + \sigma q_h}{\lambda_1 - u_{a(1)}} h_p, \tag{4.6}$$

wherein

$$N = \frac{(\lambda_2 - u_{a(2)})((\lambda_1 - u_{a(1)})(\lambda_3 + \sigma q_h) - (\lambda_3 - u_{a(3)})(\lambda_1 + \sigma q_h))}{(\lambda_3 - u_{a(3)})((\lambda_1 - u_{a(1)})(\lambda_2 + \sigma q_h) - (\lambda_2 - u_{a(2)})(\lambda_1 + \sigma q_h))}. \tag{4.7}$$

Second-order accuracy scheme

The Euler difference form of (2.45) of second-order accuracy in time and space is:

$$\Re^{(k)} = \lambda_k^{j+1/2} \frac{u_p - u_{a(k)}}{\Delta t} + \frac{\lambda_k^{j+1/2} + \sigma q_h}{\lambda_k^{j+1/2} - u_k^{j+1/2}} \frac{h_p - h_{a(k)}}{\Delta t} + \frac{B_p - B_{a(k)}}{\Delta t} = 0$$

$$\lambda_k^{j+1/2}(u_p - u_{a(k)}) + \frac{\lambda_k^{j+1/2} + \sigma q_h}{\lambda_k^{j+1/2} - u_k^{j+1/2}}(h_p - h_{a(k)}) + (B_p - B_{a(k)}) = 0,\ k = 1, 2, 3, \tag{4.8}$$

where $\lambda_k^{j+1/2} = \frac{1}{2}(\lambda_k(a(k)) + \lambda_{kp})$ and $u_k^{j+1/2} = \frac{1}{2}(u_{a(k)} + u_p)$. λ_{kp} represents the value of the kth characteristic at the point p. Equation (4.8) constitutes a system of three nonlinear equations with three unknowns (h_p, u_p and B_p). These three equations cannot be solved directly, and they are solved by a Newton-Raphson method to get h_p, u_p and B_p.

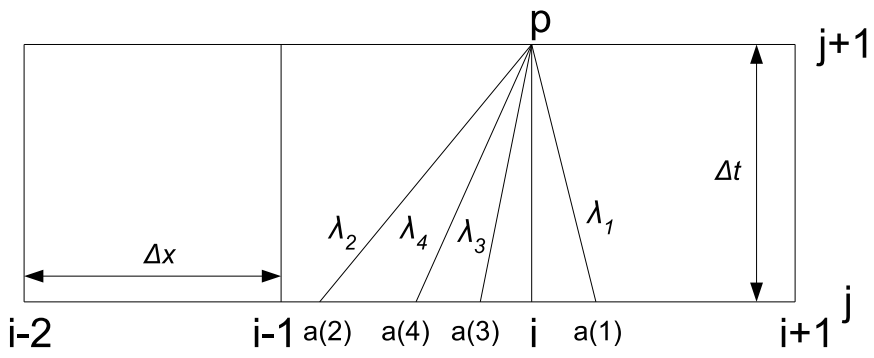

Figure 4.2: Grid and characteristic configuration based on STI MOC scheme for the combined load system.

4.1.2 Combined load system

The schematic grid and characteristic configuration based on the STI MOC scheme for the combined load system is shown in Figure 4.2.

First-order accuracy scheme

Similarly, putting the Riemann equation for the combined load system (2.82) into Euler difference form of first-order accuracy gives

$$\begin{aligned} \Re^{(k)} &= \lambda_k \frac{(u_p - u_{a(k)})}{\Delta t} + \frac{\lambda_k}{(\lambda_k - u_{a(k)})} \frac{h_p - h_{a(k)}}{\Delta t} + \frac{B_p - B_{a(k)}}{\Delta t} \\ &= m_e \left(c_{a(k)} - \left(u_{a(k)}^2 - u_{crs}^2 \right) \right), k = 1, 2, 3. \end{aligned} \tag{4.9}$$

Putting (2.83) into Euler difference form of first-order accuracy gives

$$\frac{c_p - c_{a(4)}}{\Delta t} = \frac{w_s}{h_{a(4)}} ((u_{a(4)}^2 - u_{crs}^2) - c_{a(4)}). \tag{4.10}$$

In (4.9) and (4.10), the values of variables at points $a(1)$, $a(2)$, $a(3)$ and $a(4)$ are all known, and there are four unknowns: h_p, u_p, B_p and c_p. Multiplying Δt and

putting the known variables on the right side, (4.9) and (4.10) can be written as:

$$\lambda_k u_p + \frac{\lambda_k}{\lambda_k - u_{a(k)}} h_p + B_p = L_k,\ k = 1, 2, 3, \tag{4.11}$$

with

$$L_k = \lambda_k u_{a(k)} + \frac{\lambda_k}{\lambda_k - u_{a(k)}} h_{a(k)} + B_{a(k)} + m_e \left(c_{a(k)} - \left(u_{a(k)}^2 - u_{crs}^2 \right) \right) \Delta t, \tag{4.12}$$

and

$$c_p = c_{a(4)} + \frac{w_s}{h_{a(4)}} ((u_{a(4)}^2 - u_{crs}^2) - c_{a(4)}) \Delta t. \tag{4.13}$$

Equation (4.11) forms a set of three linear equations with three unknowns h_p, u_p and B_p; the solution is similar to that for the bed-load-only system, and not presented here. c_p is solved from (4.13).

Second-order accuracy scheme

The Euler difference forms of second-order accuracy for (2.82) and (2.83) are:

$$\begin{aligned} \Re^{(k)} &= \lambda_k^{j+1/2} \frac{(u_p - u_{a(k)})}{\Delta t} + \frac{\lambda_k^{j+1/2}}{\lambda_k^{j+1/2} - u_k^{j+1/2}} \frac{h_p - h_{a(k)}}{\Delta t} + \frac{B_p - B_{a(k)}}{\Delta t} \\ &= m_e \left(c_k^{j+1/2} - \left((u_k^{j+1/2})^2 - u_{crs}^2 \right) \right), k = 1, 2, 3. \end{aligned} \tag{4.14}$$

$$\frac{c_p - c_{a(4)}}{\Delta t} = \frac{w_s}{h_4^{j+1/2}} \left(\left((u_4^{j+1/2})^2 - u_{crs}^2 \right) - c_4^{j+1/2} \right). \tag{4.15}$$

where $h_k^{j+1/2} = \frac{1}{2}(h_{a(k)} + h_p)$ and $c_k^{j+1/2} = \frac{1}{2}(c_{a(k)} + c_p)$, $k = 1, 2, 3, 4$. Equations (4.14) and (4.15) are simplified as:

$$\begin{aligned} \lambda_k^{j+1/2}(u_p - u_{a(k)}) + \frac{\lambda_k^{j+1/2}}{\lambda_k^{j+1/2} - u_k^{j+1/2}} (h_p - h_{a(k)}) + B_p - B_{a(k)} \\ = m_e \left(c_k^{j+1/2} - \left((u_k^{j+1/2})^2 - u_{crs}^2 \right) \right) \Delta t, k = 1, 2, 3. \end{aligned} \tag{4.16}$$

$$c_p - c_{a(4)} = \frac{w_s}{h_4^{j+1/2}} \left(\left((u_4^{j+1/2})^2 - u_{crs}^2 \right) - c_4^{j+1/2} \right) \Delta t. \tag{4.17}$$

Equations (4.16) and (4.17) constitute a system of four nonlinear equations with four unknowns (h_p, u_p, B_p and c_p). These four equations are solved by a Newton-Raphson method to get h_p, u_p, B_p and c_p.

4.2 Procedure of the STI MOC solver

The procedure of implementing the STI MOC scheme of second-order accuracy in both time and space for the bed-load-only system is as follows:

1. Assume that the values of the variables h, u and B at point p in Figure 4.1, i.e., the (i) grid at the ($j+1$) time step, are equal to those at the (i) grid at the (j) time step.

2. Calculate the slope of each characteristic line λ_{kp} (k =1, 2, 3) at point p using the variables at this point.

3. Estimate the locations of $a(1)$, $a(2)$ and $a(3)$ by extrapolation backwards, i.e., $x_{a(k)} = x_p - \lambda_{kp}\Delta t$, see Figure 4.1.

4. The values of variables at the $a(1)$, $a(2)$ and $a(3)$ points are obtained by the second-order interpolation in space from the variables at the neighbouring points.

5. The characteristics $\lambda_k(a(k))$ are calculated at point $a(k)$ ($k = 1, 2, 3$), and the averaged $\lambda_k^{j+1/2} = \frac{1}{2}(\lambda_k(a(k)) + \lambda_{kp})$ and $u_k^{j+1/2} = \frac{1}{2}(u_{a(k)} + u_p)$ are used in equation (4.8) to achieve the second-order accuracy in time.

6. With all the variables known at $a(1)$, $a(2)$ and $a(3)$, the Riemann equation (4.8) is used to calculate the values of variables at p.

7. Check whether the new computed values at point p and the previously calculated ones agree with each other within the required accuracy (10^{-12}). If yes, the variables at point p are deemed to be obtained; if not, repeat Steps 2-7 until the required accuracy is achieved.

The procedure of implementing the STI MOC scheme for combined load system is similar to that for the bed-load-only system, and is not presented here. Note that the procedure of the STI MOC scheme of first-order accuracy for both bed-load-only and combined load systems is also not presented.

4.3 Shock solution under the STI MOC solver

In unsteady flows, a shock may develop during the simulation even when there is no shock at the initial time, therefore we need to identify the occurrence of a shock. In the shock fitting technique, a shock is treated as a moving internal boundary and the shock position should be tracked through the computation time. When a shock is present, it separates the research domain into two regions (or more regions when more than one shock is present) and the computation proceeds in each region. The shock conditions and the information along the characteristic lines are utilised to obtain the variables on both sides of the shock and also the position of the shock. In this section, the shock inception and also the solutions for both bed-load-only and combined load systems under the STI

MOC scheme are presented.

4.3.1 Shock inception

The technique for the detection of embedded shocks on fixed grid developed by Moretti (1971) is employed to find when and where a shock occurs. The main idea of this method is that when the gradient of a dependent variable between two meshes is relatively great and keeps increasing, a shock may occur. This indicates that the shock is most likely to form at the point where the gradient is greatest, if it is also increasing in time at that point. With this in mind, the gradients of a chosen dependent variable between all the mesh intervals are calculated at the end of each time step, and the position $(i, i+1)$ where the greatest gradient is located is identified.

However, the conditions under which the point with the greatest gradient is assumed to have developed into a shock still needs further discussion. There are three conditions that must be satisfied for a shock to be identified in the present work:

- This greatest gradient of a chosen dependent variable increases for several consecutive time steps; the number of the consecutive steps is an empirical parameter, and in this work five is chosen.

- The position of the maximum gradient should be located between the same or adjacent mesh intervals at the two consecutive time steps. For instance, if the maximum gradient is within $(i, i+1)$ at time step (j), the greatest gradient should have been located within $(i-1, i)$, $(i, i+1)$ or

$(i+1, i+2)$ at time step $(j-1)$; this ensures that the greatest gradients at the two time steps are the same one.

- Two characteristic lines from the same family at the points (i) and $(i+1)$ must converge. Thus if the λ_k $(k = 1, 2, 3)$ characteristic lines intersect, it is deduced to be a λ_k shock.

If the above three conditions are satisfied at the same time, then a shock is deemed to be present at the mid-point of the mesh $(i, i+1)$, and $\zeta = \frac{1}{2}(x_i + x_{i+1})$. The initial shock velocity is approximated by the averaged characteristic speeds at the points (i) and $(i+1)$, which is written as follows:

$$W = \frac{1}{2}(\lambda_{k_i} + \lambda_{k_{i+1}}), \tag{4.18}$$

where λ_{k_i} denotes the kth wave speed at node (i).

The initial values of the dependent variables on the left side of the shock are interpolated using the values of variables at three neighbouring points $(i-1)$, (i) and $(i+1)$ (Di Giacinto and Valorani, 1989):

$$\overrightarrow{U}_L = \overrightarrow{U}_i + \frac{\Delta x}{2(1+n)} \left(\frac{\overrightarrow{U}_i - \overrightarrow{U}_{i-1}}{\Delta x} + 2n \frac{\overrightarrow{U}_{i+1} - \overrightarrow{U}_i}{3\Delta x} \right), \tag{4.19}$$

where $\overrightarrow{U}_L = (h_L, u_L, B_L)$ for the bed-load-only system and $\overrightarrow{U}_L = (h_L, u_L, B_L, c_L)$ for the combined load system, and n is an empirical coefficient (typically $n = 5$). Similarly, variables on the right side of the shock are also computed from the values of variables at three neighbouring points (i), $(i+1)$ and $(i+2)$:

$$\overrightarrow{U}_R = \overrightarrow{U}_{i+1} - \frac{\Delta x}{2(1+n)} \left(\frac{\overrightarrow{U}_{i+2} - \overrightarrow{U}_{i+1}}{\Delta x} + 2n \frac{\overrightarrow{U}_{i+1} - \overrightarrow{U}_i}{3\Delta x} \right), \tag{4.20}$$

where $\overrightarrow{U}_R = (h_R, u_R, B_R)$ for the bed-load-only system and $\overrightarrow{U}_R = (h_R, u_R, B_R, c_R)$ for the combined load system.

It should be noted that in the combined load system the sediment concentration c is continuous across λ_1, λ_2 and λ_3 shocks, therefore when $u_L \leq W$, $c_L = c_R$, in which c_R is interpolated by (4.20), while when $u_L > W$, $c_R = c_L$, in which c_L is obtained from (4.19).

4.3.2 Embedded shock solution for bed-load-only system

There are three kinds of shocks: λ_1 shock, λ_2 shock and λ_3 shock. For λ_1 and λ_2 shocks, on one side three characteristics could be extrapolated backwards to the previous time step (see Figure 4.3(a) and (b)) and the three variables on this side can be solved by three Riemann equations along these three characteristics. On the other side, there is one Riemann equation, and together with the three shock conditions, the four unknowns (three variables on this side and the shock velocity) can be solved. For a λ_3 shock, four Riemann equations (two on each side, see Figure 4.3(c)) and three shock conditions are used to solve the seven unknowns (h_L, u_L, B_L, h_R, u_R, B_R and W). The procedures of solution for the three shocks are presented in this section.

λ_1 shock

1. Estimate the approximate shock position at time step $(j+1)$ by the shock position and velocity at time step (j), $\zeta^{j+1^{(1)}} = \zeta^j + W^j \Delta t$.

2. Set the values of variables on both sides of the shock at time step $(j+1)$

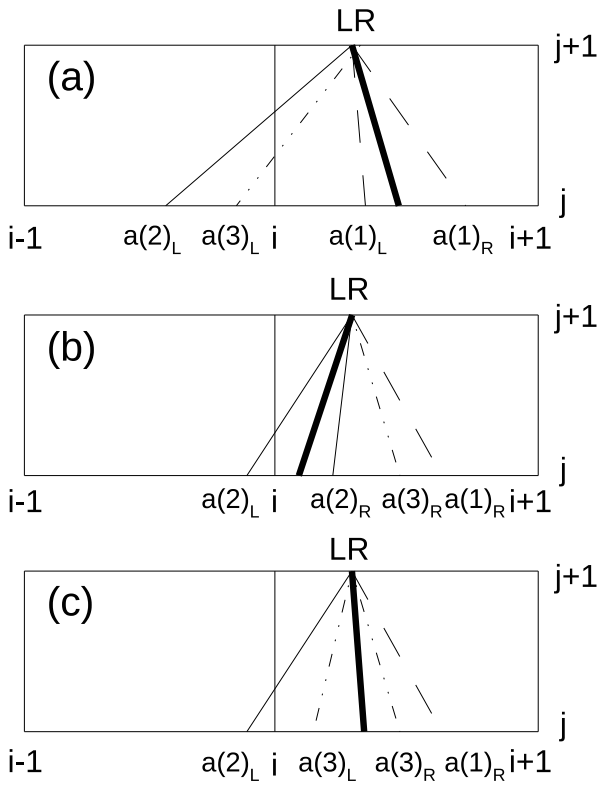

Figure 4.3: Configuration of characteristics in the $x - t$ plane for (a) λ_1 shock, (b) λ_2 shock and (c) λ_3 shock in the bed-load-only system. The shock path is shown by the thick line whereas λ_1, λ_2 and λ_3 characteristics are represented by dashed, thinner solid and dot-dashed lines, respectively.

identical to those at time step (j).

3. Utilising the values of variables on the two sides of the shock to estimate the positions of $a(1)_L$, $a(2)_L$, $a(3)_L$ and $a(1)_R$ by extrapolating backwards, see Figure 4.3(a). The values of variables at $a(1)_L$, $a(2)_L$, $a(3)_L$, $a(1)_R$ are determined by interpolation using the values of variables at the neighbouring points on the left and right sides of the shock.

4. The variables on the left side of the shock (h_L, u_L and B_L) are solved di-

rectly from the three Riemann equations along the three characteristics on the left side.

5. The three shock conditions, together with the Riemann equation along λ_{1R} characteristic comprise a system of four nonlinear equations including four unknowns (h_R, u_R, B_R and W).

6. The variables h_R, u_R, B_R and W are obtained by solving the four nonlinear equations using the Newton-Raphson method. Since h_L, u_L and B_L are known, all the variables of this shock are solved.

7. Estimate the new location of the shock at the $(j+1)$ time step by using $\zeta^{j+1^{(2)}} = \zeta^j + \frac{1}{2}(W^j + W^{j+1})\Delta t$. If $\zeta^{j+1^{(1)}}$ and $\zeta^{j+1^{(2)}}$ do not agree with each other within the desired accuracy (10^{-12}), set $\zeta^{j+1^{(1)}} = \zeta^{j+1^{(2)}}$ and repeat Steps 3-7 to calculate the new $\zeta^{j+1^{(2)}}$ until the desired accuracy is achieved; if the two values agree with each other within the required accuracy, the shock has been solved.

λ_2 shock

The procedure for the λ_2 shock is similar to that for the λ_1 shock, and is not presented here.

λ_3 shock

1. Estimate the approximate shock position at $(j+1)$ step by the shock velocity at (j) time step, $\zeta^{j+1^{(1)}} = \zeta^j + W^j \Delta t$.

2. Set all the variables of the shock at time step $(j+1)$ equal to those at time step (j).

3. Estimate the approximate locations of $a(2)_L$, $a(3)_L$, $a(1)_R$ and $a(3)_R$ by extrapolation backwards, and the values of the variables at these four points are determined by interpolation using the values of variables at the neighbouring points on the left and right sides of the shock.

4. There are two characteristic lines on the left side and also two on the right side of the shock, giving four Riemann equations. Together with the three shock conditions, this system comprises seven nonlinear equations with seven unknowns (h_L, u_L, B_L, h_R, u_R, B_R and W).

5. The Newton-Raphson method is again used to solve the seven nonlinear equations, and seven unknowns are obtained.

6. Estimate the new location $\zeta^{j+1^{(2)}}$ of the shock at time step $(j+1)$ by using $\zeta^{j+1^{(2)}} = \zeta^j + \frac{1}{2}(W^j + W^{j+1})\Delta t$. If $\zeta^{j+1^{(1)}}$ and $\zeta^{j+1^{(2)}}$ do not agree with each other within a desired accuracy (10^{-12}), set $\zeta^{j+1^{(1)}} = \zeta^{j+1^{(2)}}$ and repeat Steps 3-6 to calculate the new $\zeta^{j+1^{(2)}}$ until the desired accuracy is achieved; if the two values agree within the desired accuracy, the shock has been solved.

4.3.3 Embedded shock solution for combined load system

In this combined load system, there is an additional λ_4 characteristic family and there are nine unknowns for a shock (h_L, u_L, B_L, c_L, h_R, u_R, B_R, c_R and W).

When $\lambda_{4L} > W$, the Riemann equation along λ_{4L} can be used to solve the shock; when $\lambda_{4R} < W$, the Riemann equation along λ_{4R} is used to solve the shock. If one of $\lambda_{4L} > W$ and $\lambda_{4R} < W$ applies, there are five Riemann equations for λ_1, λ_2 and λ_3 shocks. Together with the four shock conditions, it forms a system of nine equations and nine unknowns, and the shock can be solved by solving these nine nonlinear equations.

If $\lambda_{4L} > W$ and $\lambda_{4R} < W$ applied at the same time, there would be three Riemann equations on both sides, and the system would be overdetermined with ten equations but nine unknowns. On the other extreme, if $\lambda_{4L} < W$ and $\lambda_{4R} > W$ applied simultaneously, there would be four Riemann equations along the characteristics on both sides, and the system would be undetermined with eight equations while nine unknowns.

As $\lambda_{4L} = u_L$ and $\lambda_{4R} = u_R$, we could write the shock condition for mass (2.56) as:

$$h_R(\lambda_{4R} - W) = h_L(\lambda_{4L} - W). \tag{4.21}$$

From (4.21), if $h_L > 0$ and $h_R > 0$, it is deduced that $\lambda_{4L} > W$ and $\lambda_{4R} < W$ cannot be satisfied at the same time. Similarly, $\lambda_{4L} < W$ and $\lambda_{4R} > W$ also cannot be satisfied simultaneously.

λ_1 shock and λ_2 shock

For a λ_1 shock, as $\lambda_4 > \lambda_1$, we have $\lambda_{4L} > W$, and there is an additional λ_4 characteristic on the left side compared to the λ_1 shock in the bed-load-only system, see Figure 4.4(a). Thus for a λ_1 shock, there are four Riemann equations

on the left side of the shock, and the shock variables on the left side (h_L, u_L, B_L and c_L) are solved by these Riemann equations. On the right side, there is one Riemann equation along λ_{1R}, and four shock conditions, making five equations, so that the other five variables (h_R, u_R, B_R, c_R and W) are solved.

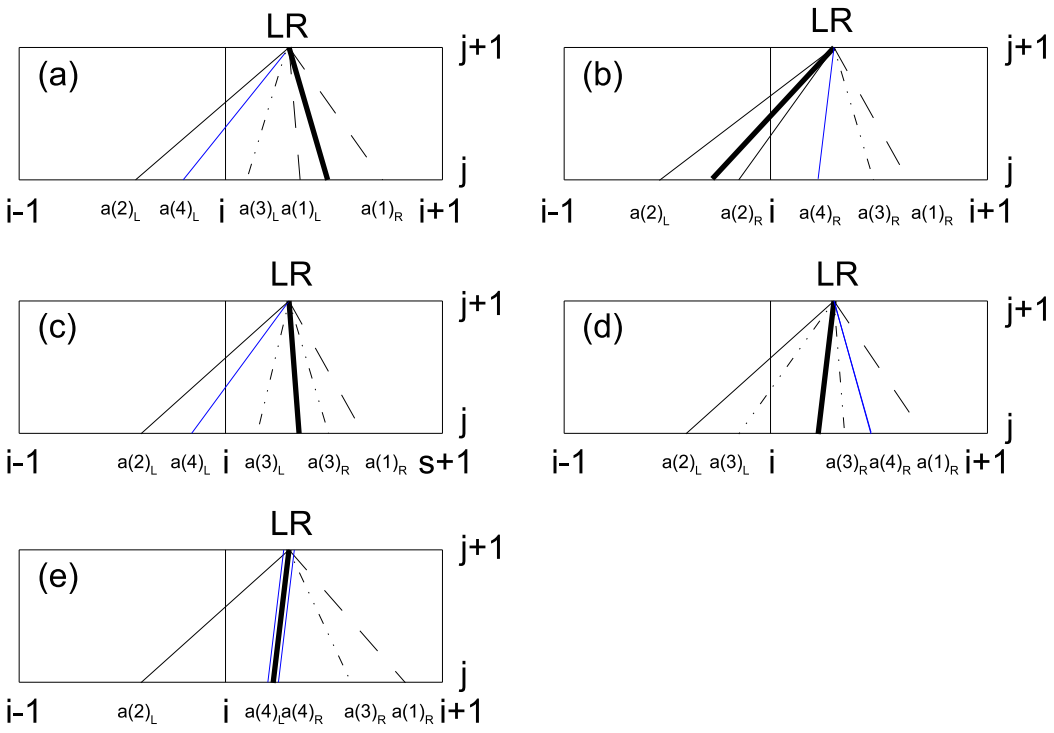

Figure 4.4: Configuration of characteristics in the $x-t$ plane for $\lambda_{1,2,3,4}$ shocks in combined load system. (a): λ_1 shock; (b): λ_2 shock; (c): λ_3 shock when $u_L > 0$; (d) λ_3 shock when $u_R < 0$ and (e): λ_4 contact wave when $u_L = u_R > 0$. The shock path is shown by the thick line whereas λ_1, λ_2, λ_3 and λ_4 characteristics are represented by dashed, thinner solid, dot-dashed and blue solid lines, respectively.

Similarly, for a λ_2 shock, as $\lambda_4 < \lambda_2$, so that $\lambda_{4R} < W$ and there are four characteristics on the right side of the shock, see Figure 4.4(b). The four variables on

the right side are solved from four Riemann equations along the four characteristics on this side. The other five variables are solved by one Riemann equation along λ_{2L} and four shock conditions.

λ_3 shock

For a λ_3 shock, the characteristic λ_4 on both sides of the shock could be greater or smaller than W. When $u_L \geq 0$ and $h_L > 0$, $W \leq \lambda_{3L} \leq \lambda_{4L}$, so that the λ_4 characteristic is located on the left side of the shock, see Figure 4.4(c). There are three Riemann equations on the left side and two on the right side. Conversely, when $u_R < 0$ and $h_R > 0$, $W > \lambda_{3R} > \lambda_{4R}$, then λ_4 characteristic is located on the right side of the shock and there are three Riemann equations on the right side and two on the left side, see Figure 4.4(d). Therefore for a λ_3 shock there are three Riemann equations on one side and two on the other side. Together with the four shock conditions, this system has nine equations and nine unknowns (h_L, u_L, B_L, c_L, h_R, u_R, B_R, c_R and W), and the shock can be solved by solving these nine nonlinear equations.

λ_4 shock

As the λ_4 characteristic field here is linearly degenerate, the discontinuity solution associated with λ_4 is a contact wave. Across the λ_4 contact wave, if $u_L = u_R = W \neq 0$, then h, u and B are continuous from the shock conditions (2.56), (2.57) and (2.88), and c is discontinuous. When $u_L = u_R > 0$, there are two characteristics on the left side (λ_{2L} and λ_{4L}) and three on the right side

(λ_{1R}, λ_{3R} and λ_{4R}) of the λ_4 contact wave, see Figure 4.4(e). Conversely, when $u_L = u_R < 0$, there are three characteristics on the left (λ_{2L}, λ_{3L} and λ_{4L}) and two on the right (λ_{1R} and λ_{4R}) of the λ_4 contact wave (not shown). Therefore, the nine unknowns can be solved by the five Riemann equations and four shock conditions.

If $u_L = u_R = W = 0$, from the shock conditions, u is continuous, B and c are discontinuous, and h could be continuous or discontinuous. In this case, the shock condition for mass (2.56) is consequently satisfied and cannot be used to solve the contact wave. Note that $\lambda_{3L} = W = \lambda_{3R}$, therefore there are three characteristics on the left side (λ_{2L}, λ_{3L} and λ_{4L}) and three on the right side (λ_{1R}, λ_{3R} and λ_{4R}) of the contact wave. Thus, for the λ_4 contact wave with $u_L = u_R = W = 0$, there are six Riemann equations and together with the three shock conditions, the wave can be solved.

The steps to proceed with the shock solutions under the STI MOC scheme for the combined load system are similar to those for the bed-load-only system and not presented here.

4.4 Boundary conditions implementation under STI MOC scheme

4.4.1 Upstream (seaward) boundary

As the position of the seaward boundary in all swash simulations in this work is assumed to be fixed during the computation time, the mesh at the seaward

boundary remains the same. The variables at the seaward boundary are calculated based on the assumptions of the seaward boundary conditions in each individual swash simulation.

Here we illustrate the seaward boundary treatment in the combined load system as an example. The grid and characteristic configuration at the seaward boundary with shoreward velocity is shown in Figure 4.5, in which grid (1) represents the seaward boundary. When the water velocity at the seaward boundary is seaward, the λ_3 and λ_4 characteristics are located between the grids (1) and (2) in Figure 4.5; the characteristic configuration under this case is not shown. The values of variables at $a(2)$, $a(3)$ and $a(4)$ are extrapolated from

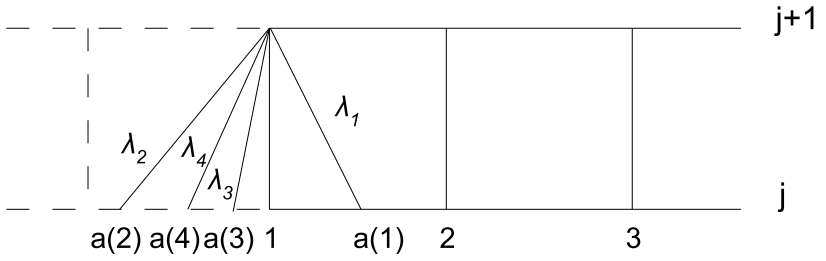

Figure 4.5: Grid and characteristic configuration at the seaward boundary in the combined load system.

those at the grids (1) and (2) at the (j) time step. Then, the values of variables at grid (1) at the $(j+1)$ time step can be solved by the four Riemann equations along the four characteristics. The procedure we refer to § 4.2.

4.4.2 Downstream (shoreward) boundary

From the shock conditions for the case in which one side of the shock is dry bed with zero velocity in Appendix A, it is deduced that the water depth at the tip is 0 and the shock speed is identical to the particle velocity u_s, where the subscript s indicates the shoreline position. The bed level at the tip is obtained from the shock condition corresponding to the sediment conservation equation. In the combined load system, from (2.71), at the shoreline ($h_s = 0$), $c_s = c_{eq} = u_s^2 - u_{crs}^2$. In the bed-load-only system, from (2.30), for formulae $q = q(u)$, in which $q_h = 0$, if $h = 0$, $\lambda_1 = u/2 - \sqrt{u^2/4 + \sigma q_u}$, $\lambda_2 = u/2 + \sqrt{u^2/4 + \sigma q_u}$, and $\lambda_3 = u$. When $u_s \neq 0$, $q_u > 0$, so that $\lambda_1 < u_s$ and $\lambda_2 > u_s$, and the λ_2 characteristic extends from the flow interior to the shoreline and the λ_3 characteristic is identical to the shoreline path, see Figure 4.6. Therefore, the Riemann equations along the

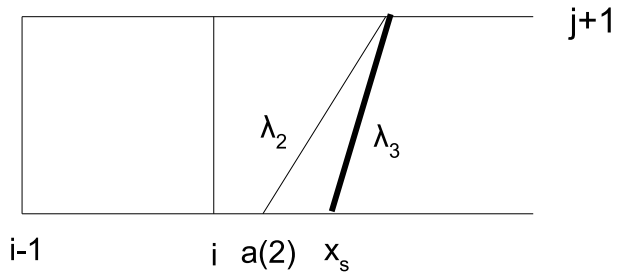

Figure 4.6: Grid and characteristic configuration at the shoreline in the bed-load-only system.

λ_2 and λ_3 characteristics can be used to solve the bed level on the left side of the shoreline (B_s). Note that the Riemann equation along λ_3 is essentially $\dfrac{dx_s}{dt} = u_s$. As previously mentioned, a sediment bore forms at the shoreline for $q = q(u)$, and there is a shock relation between the bed levels on both sides of the sedi-

ment bore. In the uprush, as the bed level on the right side of the sediment bore is known, the shock relation for bed levels can be used to solve the variables at the shoreline. Thus for the bed-load-only system with $q = q(u)$, we have three equations for three unknowns (u_s, B_s and x_s) at the tip. Similarly, there are four equations (three Riemann equations along λ_2, λ_3 and λ_4 and one shock relation) for the combined load system with four unknowns (u_s, B_s, c_s and x_s). Note that the Riemann equation along λ_4 at the shoreline gives $c_s = c_{eq} = u_s^2 - u_{crs}^2$. The variables at the shoreline for both systems in the uprush with $q = q(u)$ can be obtained by solving these equations. The procedure to solve these variables is similar to that for a moving shock and is not presented here.

However, in the backwash, as the bed level on the right side of the sediment bore at the tip is unknown, the shock relation between bed levels is not used directly to determine dependent variables of the flow region; instead extrapolation is used to obtain u_s and B_s in the backwash. The shock relation between bed levels is used to obtain the bed level on the dry beach as the shoreline retreats.

For formulae $q = q(h, u)$, from Appendix B, there is an analytical solution for the shoreline movement in the uprush over a sloping erodible beach. In the numerical code, however, we do not use the analytical solution, and extrapolation is used to solve the wet-dry boundary both in uprush and backwash.

As the shoreline is moving, the last node in the research domain keeps changing, and the number of total nodes could be incremented or decremented by one during each time step. The procedure of tracking the moving shoreline and

calculating the variables at the wave tip by extrapolation under the STI MOC scheme is as follows:

1. Estimate the approximate location of the shoreline at time step $(j+1)$, i.e., x_s^{j+1}, using the variables at the previous time step (j), i.e., $x_s^{j+1^{(1)}} = x_s^j + u_s^j \Delta t$.

2. The velocities at the two adjacent nodes to the left of the shoreline at time step $(j+1)$, are utilised to calculate u_s^{j+1} by linear / quadratic extrapolation. When the number of total nodes remains the same as that at the previous time step (Figure 4.7(a)) or is incremented by one (Figure 4.7(b)), the two adjacent nodes are $(i-1)$ and (i); while when the number is decremented by one (Figure 4.7(c)) , the two adjacent nodes are $(i-2)$ and $(i-1)$.

3. Calculate the new position of the shoreline by $x_s^{j+1^{(2)}} = x_s^j + \frac{1}{2}(u_s^j + u_s^{j+1})\Delta t$.

4. Check if the new calculated shoreline position $x_s^{j+1^{(2)}}$ and the previously calculated one $x_s^{j+1^{(1)}}$ agree with each other within the desired accuracy (10^{-12}). If the required accuracy (10^{-12}) is achieved, the shoreline position is found and $x_s^{j+1} = x_s^{j+1^{(2)}}$; if not, set $x_s^{j+1^{(1)}} = x_s^{j+1^{(2)}}$, and Steps 2-4 are repeated to calculate the new $x_s^{j+1^{(2)}}$ until the two values $x_s^{j+1^{(1)}}$ and $x_s^{j+1^{(2)}}$ agree with each other within a specified error limit.

5. The water depth at the shoreline is set to 0. The shock relation between bed levels on both sides of the sediment bore is used to calculate the bed level on one side if the bed level on the other side is known. When the shoreline is moving shorewards $(u_s^{j+1} \geq 0)$, the bed level on the right side

is known, and bed level on the left side can be obtained. If the wave tip is moving seawards ($u_s^{j+1} < 0$), the bed level on the right side is unknown, and in this case the bed level on the left side is extrapolated by the variables at the two neighbouring points at time step $(j+1)$, and the bed level on the right side is therefore obtained from the shock condition. In the combined load system, the suspended sediment is in the equilibrium state due to the zero water depth at the shoreline, thus $c_s^{j+1} = (u_s^{j+1})^2 - u_{crs}^2$.

6. If the new shoreline position x_s^{j+1} is on the right side of node (i), and the horizontal distance between these two positions is greater than Δx, a new fixed node $(i+1)$ is introduced, and the number of total nodes is incremented by one, see Figure 4.7(b).

7. If the new shoreline position is on the left side of node (i), node (i) has become dry domain and disappears, the number of total nodes is decremented by one, see Figure 4.7(c).

8. If the number of total nodes is incremented by one, the dependent variables at the new fixed node $(i+1)$ at time step $(j+1)$ are interpolated by variables at the fixed node (i) and those at the shoreline boundary.

4.5 Numerical implementation

The sizes of the spatial interval Δx and time interval Δt are important parameters in the numerical model. In this section, the sizes of Δx and Δt are varied to test to what extent the results of the swash simulation are changed.

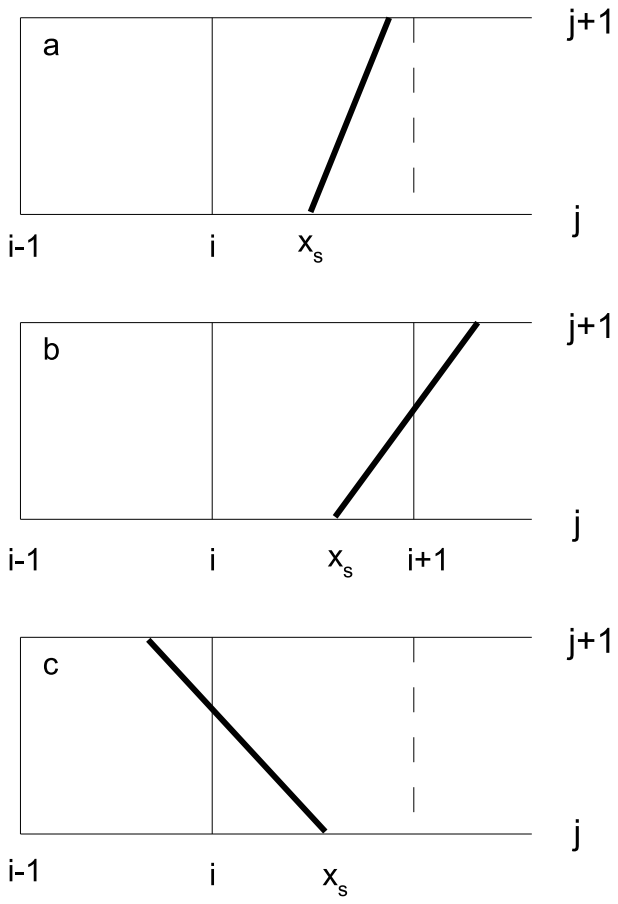

Figure 4.7: Schematic diagram for shoreline movement under STI MOC solver. Thick solid line: shoreline path. (a): Same number of total nodes; (b): one incremented number of total nodes and (c) one decremented number of total nodes in two consecutive time steps.

Here we simulate the PW01 swash event morphodynamically by the bed-load-only model ($q = u^3$) with five sets of Δx and Δt parameters, which are shown in Table 4.1, to show the convergence of the results.

The comparisons of different sets of Δx and Δt for $\sigma = 0.01$ and $\sigma = 0.0654$ are shown in Figure 4.8 and 4.9. The comparison for both σ shows that the results are converged, and it is illustrated that the accuracy obtained by any further

Parameter set	Δx	Δt
Set 1	2×10^{-2}	4×10^{-3}
Set 2	1×10^{-2}	2×10^{-3}
Set 3	5×10^{-3}	1×10^{-3}
Set 4	2×10^{-3}	4×10^{-4}
Set 5	1×10^{-3}	2×10^{-4}

Table 4.1: Δx and Δt sets for testing result convergence.

reduction in mesh spacing from Set 2 is very small. Therefore the values of Δx and Δt in Set 2 are used in the simulations over mobile bed in this work.

However, it should be noted that the results are sensitive to σ, and the smaller σ is, the more refined grids are required. Therefore, when $\sigma = 1 \times 10^{-7}$, finer interval values are used for verification against the equivalent hydrodynamic solutions, see Appendix C. This is due to the highly singular characteristic behaviour near the shoreline for $\sigma \to 0$.

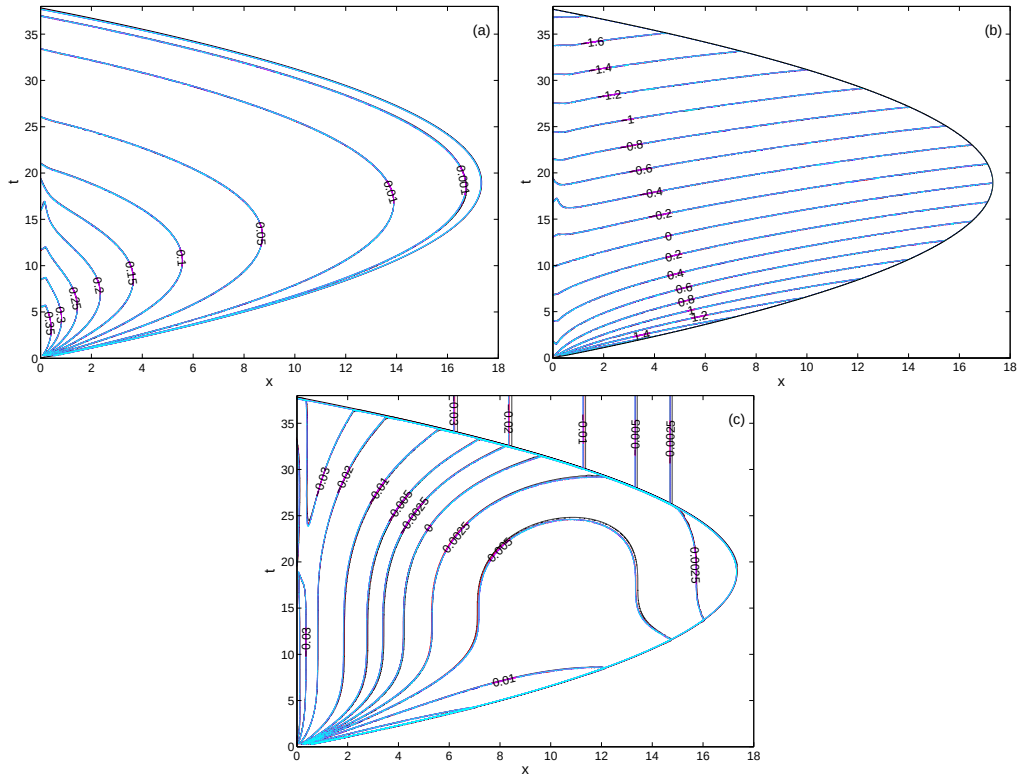

Figure 4.8: Comparison of results of convergence for PW01 swash event with $\sigma = 0.01$. (a) h; (b) u and (c) ΔB. Black: Set 1; red: Set 2; blue: Set 3; magenta: Set 4 and cyan: Set 5.

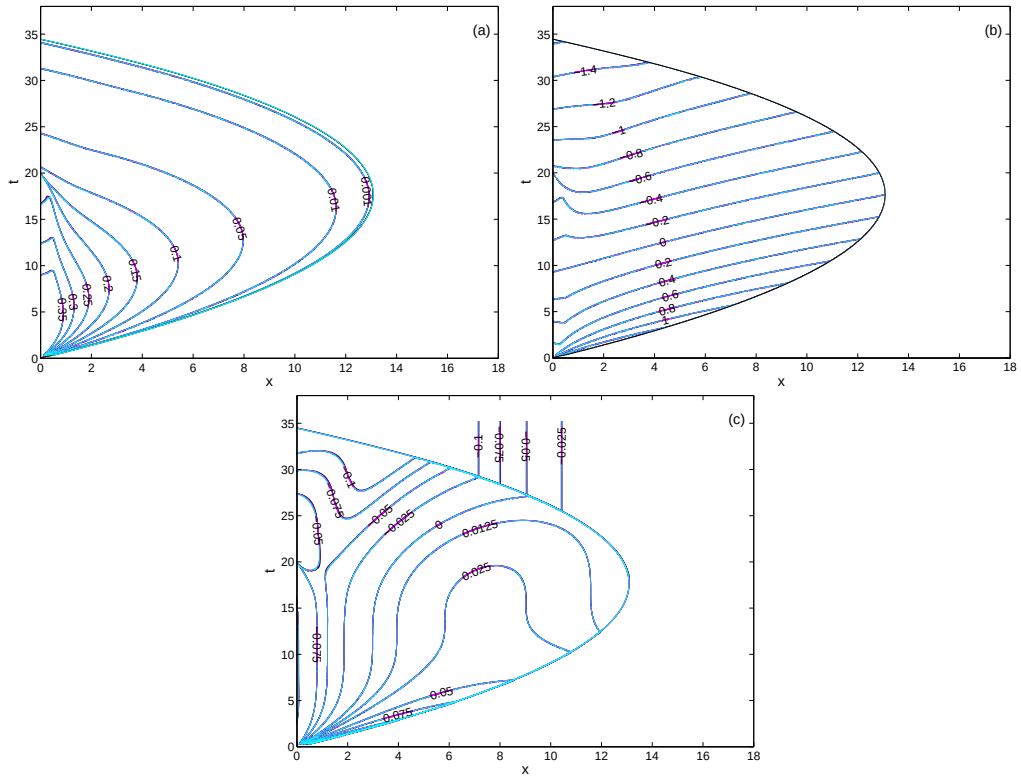

Figure 4.9: Comparison of results of convergence for PW01 swash event with $\sigma = 0.0654$. (a) h; (b) u and (c) ΔB. Black: Set 1; red: Set 2; blue: Set 3; magenta: Set 4 and cyan: Set 5.

CHAPTER 5

Fully coupled bed-load-only simulation for PW01 swash under different sediment transport formulae

A range of sediment transport formulae for bed load or suspended load in equilibrium state are examined using the fully coupled bed-load-only model under one PW01 swash cycle on an erodible beach. Simulations are normalised via the same net sediment flux at the initial shoreline position after one single swash event, to examine the distribution of sediment deposition / erosion in the swash zone, and also the differences between fully coupled and the equivalent uncoupled simulations (PH05). Furthermore, bed shear stress described by the Chezy law is then included in fully coupled simulations to examine effects of bed shear stress on the net beach change.

5.1 Different sediment transport formulae

Six of the more commonly used bed-load formulae are considered: $\widehat{q} = A\widehat{u}^3$, the Grass formula (Grass, 1981; Soulsby, 1997; Pritchard and Hogg, 2005; Kelly and Dodd, 2009); the Bagnold formula (see Soulsby, 1997; Yalin, 1977); the Meyer-Peter Müller formula (see Soulsby, 1997); the Van Rijn formula (see Soulsby, 1997); the Bailard formula (e.g. PH05) and $\widehat{q} = \bar{A}\widehat{h}\widehat{u}^3$, which was considered by PH05, and which we refer to as the PH formula. Note that some of these formulae (Van Rijn and Bailard) have been slightly modified (thresholds have been excluded) for the purpose of examining the effects of different powers of u on sediment transport; the names of formulae, however, are not changed. These give rise to six models for the swash zone simulations. The expressions of dimensional and dimensionless q and the corresponding variables of different sediment transport formulae are summarized in Table 5.1, wherein it should be noted that the six different formulae have been numbered I to VI, with the different dimensional coefficients also numbered correspondingly.

It should be noted that for the Bagnold and Meyer-Peter Müller formulae, if $|u| < u_{crb}$, then $q = 0$, thus $q_h = 0$ and $q_u = 0$. Note also that there is a discontinuity in q_u for the Bagnold formula at $|u| = u_{crb}$. When $|u| < u_{crb}$, as $q_h = 0$ and $q_u = 0$, it is found that one of the roots of the polynomial (2.30) is 0, and the other two are identical to the hydrodynamic characteristics.

	(I) Grass	(II) Bagnold	(III) Meyer-Peter Müller
$\widehat{q}$	$A_1\widehat{u}^3$	$A_2\widehat{u}(\widehat{u}^2-\widehat{u}_{crb}^2)$	$A_3(\widehat{u}^2-\widehat{u}_{crb}^2)^{3/2}$
q	u^3	$u(u^2-u_{crb}^2)$	$(u^2-u_{crb}^2)^{3/2}$
q_0	$A_1(gh_0)^{3/2}$	$A_2(gh_0)^{3/2}$	$A_3(gh_0)^{3/2}$
q_h	0	0	0
q_u	$3u^2$	$3u^2-u_{crb}^2$	$3\|u\|(u^2-u_{crb}^2)^{1/2}$
σ	$\xi A_1 g$	$\xi A_2 g$	$\xi A_3 g$
	(IV) Van Rijn	**(V) Bailard**	**(VI) $\widehat{q}=\widehat{A}\widehat{h}\widehat{u}^3$ (PH)**
$\widehat{q}$	$A_4\widehat{u}\|\widehat{u}\|^{2.4}$	$A_5\widehat{u}\|\widehat{u}\|^3$	$A_6\widehat{h}\widehat{u}^3$
q	$u\|u\|^{2.4}$	$u\|u\|^3$	hu^3
q_0	$A_4(gh_0)^{1.7}$	$A_5(gh_0)^2$	$A_6h_0(gh_0)^{3/2}$
q_h	0	0	u^3
q_u	$3.4\|u\|^{2.4}$	$4\|u\|^3$	$3hu^2$
σ	$\xi A_4 g^{1.2}h_0^{0.2}$	$\xi A_5 g^{3/2}h_0^{1/2}$	$\xi A_6 g h_0$

Table 5.1: Expressions for six sediment transport formulae and corresponding variables.

5.2 Initial and boundary conditions

5.2.1 Initial conditions

The initial conditions are shown in Figure 5.1. The beach is of a uniform slope $\alpha = 0.1$, so the bed elevation $B = \alpha x$. The dam is situated at $x = 0$, with water on the left side but none on the right. The water depth and velocity on the left side of the dam is $h(x < 0, t = 0) = 1$ and $u(x < 0, t = 0) = 0$, and the initial

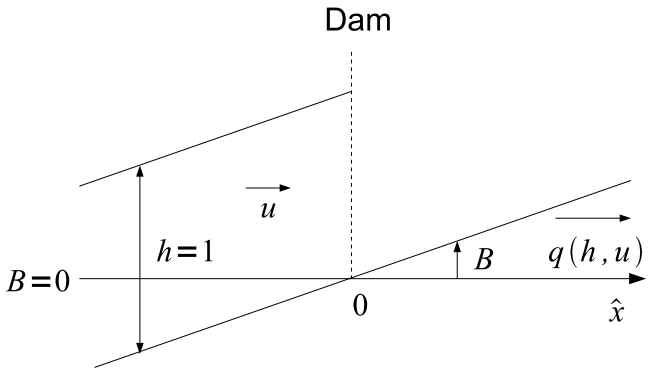

Figure 5.1: Initial conditions for the PW01 swash.

water velocity is 0. The dam is assumed to collapse at $t = 0$.

In this wet-dry dam-break problem, the discontinuity of velocity at the tip in time, i.e. between the initial conditions and the solution just after collapse (i.e., for $0 < t = t^* << 1$), prohibits the use of the initial conditions in the MOC STI solver (KD10); instead, the corresponding Riemann wave solution on a flat mobile bed at a finite time $t = t^*$ such that $0 < t^* \ll 1$ has been used for the initial data (see Kelly and Dodd, 2009, 2010). Theoretically, the smaller t^*, the more accurate is the simulation; however, note that as $t^* \to 0$ the required spatial resolution increases, so that $\Delta x \to 0$ to ensure a Courant number < 1. Therefore, computational time may increase rapidly.

However, each sediment transport formula in general corresponds to a Riemann solution, the derivation of which can be complicated. Therefore, it is desirable instead to use the (analytical) PW01 solution (here at $t = t^* = 0.01$; KD10 found that $t^* = 0.1$ was sufficient in the Riemann problem) $\Rightarrow B(x, t^*) = B(x, t = 0) = \alpha x$. Comparisons of solutions using this approach and that obtained using the flat-mobile-bed Riemann wave initial data for the Grass for-

mula (I) and Van Rijn formula (IV) reveal very close agreement: see Appendix C.3. Therefore, the PW01 solution is used as initial data for all formulae examined here.

5.2.2 Boundary conditions

In the present swash simulation, the seaward boundary is chosen at a point far enough away to ensure that the flow is uninfluenced by the reflected wave from the land so that the water depth h and bed level B at that point remain unchanged through the computation time. However, as the flow is dominated by gravity, u at that point decreases as time increases. Here, the seaward boundary is chosen at $x = -250$, where $h(x = -250, t) = 1$ and $B(x = -250, t) = -250\alpha$. As $u(x = -250, 0) = 0$, then $u(x = -250, t) = u(x = -250, 0) - \alpha t = -\alpha t$.

The landward boundary when $t > 0$ is the wet-dry boundary. In the uprush for formulae I–V, we solve the variables at the shoreline by the Riemann equations along λ_2 and λ_3 characteristics and the shock relation between bed levels on both sides of the sediment bore at the tip, see § 4.4.2; instead extrapolation is used to obtain u_s and B_s in the backwash, with the shock relation used to obtain B on the dry beach as the shoreline retreats. For formula VI, extrapolation is used to solve the variables at the shoreline both in uprush and backwash.

5.3 Determination of the dimensionless bed mobility parameter

Because of the differing dimensions of A_i (and the different dependencies of q on u and h) choosing a single σ value for all formulae yields very different amounts of sediment movement (dimensional and dimensionless), so in principle each formula ought to be calibrated to measured data. Here we choose σ for formula I roughly based on the previously calibrated value from KD10, and then calculate all other values by normalising simulations for the other formulae such that we obtain the same net sediment flux under the PW01 event at $x = 0$ (see Table 5.2). Note that other normalisations are possible, e.g. identical bed change at $x = 0$, but yield a similar overall picture. Note also that we take $\sigma = 0.01$ for formula I, which is lower than that of KD10 ($\sigma = 0.0654$); this is to ensure the "equivalent" σ for VI does not lead to unrealistically large local bed changes for the large resulting bed mobilities. The value of u_{crb} in formulae II and III is set to 0.45, which is higher than the range of values in Soulsby (1997), to examine the effect of the sediment motion threshold.

5.4 Beachface evolution

For all six simulations, at the moment of dam collapse there is a sudden acceleration in water velocity at the tip. After the collapse, the flow is dominated by gravity, and the velocity gradually decreases in time for all x. Maximum inundation (and run-up) is achieved where $u_s = 0$, and in the backwash the tip

	(I) Grass	(II) Bagnold	(III) Meyer-Peter Müller	(IV) Van Rijn	(V) Bailard	(VI) PH
σ	0.0100	0.01176	0.0126	0.00888	0.00693	0.6200
Net sediment flux at $x = 0$	0.4457	0.4461	0.4457	0.4458	0.4460	0.4460
ΔB at $x = 0$	-0.0601	-0.0604	-0.0615	-0.0639	-0.0707	-0.1984
Max. inundation	17.33	17.13	17.06	17.12	16.96	26.34

Table 5.2: Normalisation based on identical net sediment flux at $x = 0$ for different sediment formulae. Values of σ, sediment loss at $x = 0$, bed change at $x = 0$, and maximum inundation are illustrated.

subsequently recedes and offshore velocity increases. The sediment is moved onshore during run-up and offshore during backwash, with associated bed deformation. This leads to a convergence of λ_3 characteristics in the lower swash, resulting in a λ_3 shock in all six simulations.

Overall, the flow is qualitatively similar for all simulations; it is shown (in scaled form) for I only in Figure 5.2(a) and (b). Additionally, we show h and u for VI in Figure 5.3, which is particularly useful also for comparison with equivalent simulations including bed shear stress; see § 5.8. Bed change is similar for I-V. Therefore, we show the bed change ΔB for I and VI only, in Figure 5.2(c) and (d). The most striking difference between (c) and (d) is the much larger inundation for formula VI (see Table 5.2), which results from a larger onshore

maximum velocity for that formula at the moment of dam collapse (for VI about 1.47 times that for I). It is also found that the magnitude of instantaneous sediment deposition / erosion in the upper swash for VI is considerably smaller than that for I-V, which is because the water depth h in the upper swash for VI is considerably reduced, see Figure 5.3.

For all formulae sediment is initially moved onshore, causing deposition in the upper swash in the uprush with sediment coming from the base of the swash, only for the backwash subsequently to transport that and more sediment offshore. This is the result of the asymmetry in the PW01 swash velocity (see PH05).

Also shown (Figure 5.2(e) and (f)) are dimensionless bed change (ΔB) contours in the equivalent uncoupled simulations for I and VI. The pattern of erosion and deposition for formula I is very similar in coupled and uncoupled simulations (cf. Figure 5.2(c) and (e)); uncoupled and coupled ΔB also show some similarities for VI (cf. Figure 5.2(d) and (f)). Only at the base of the swash ($x \approx 0$) do we see substantial differences, in part due to dam collapse and the aforementioned backwash bore formation in both coupled simulations.

The shoreline trajectories of all formulae (I-VI) in fully coupled simulations, as well as the uncoupled one, are shown in Figure 5.4. The significantly increased inundation and swash period for the formula VI (also with respect to the PW01 solution) are apparent in Figure 5.4. However, those for $q = q(u)$ (I-V) are very close to each other and considerably reduced from the PW01 solution. This is consistent with the formation of a sediment bore at the shoreline for I-V, which

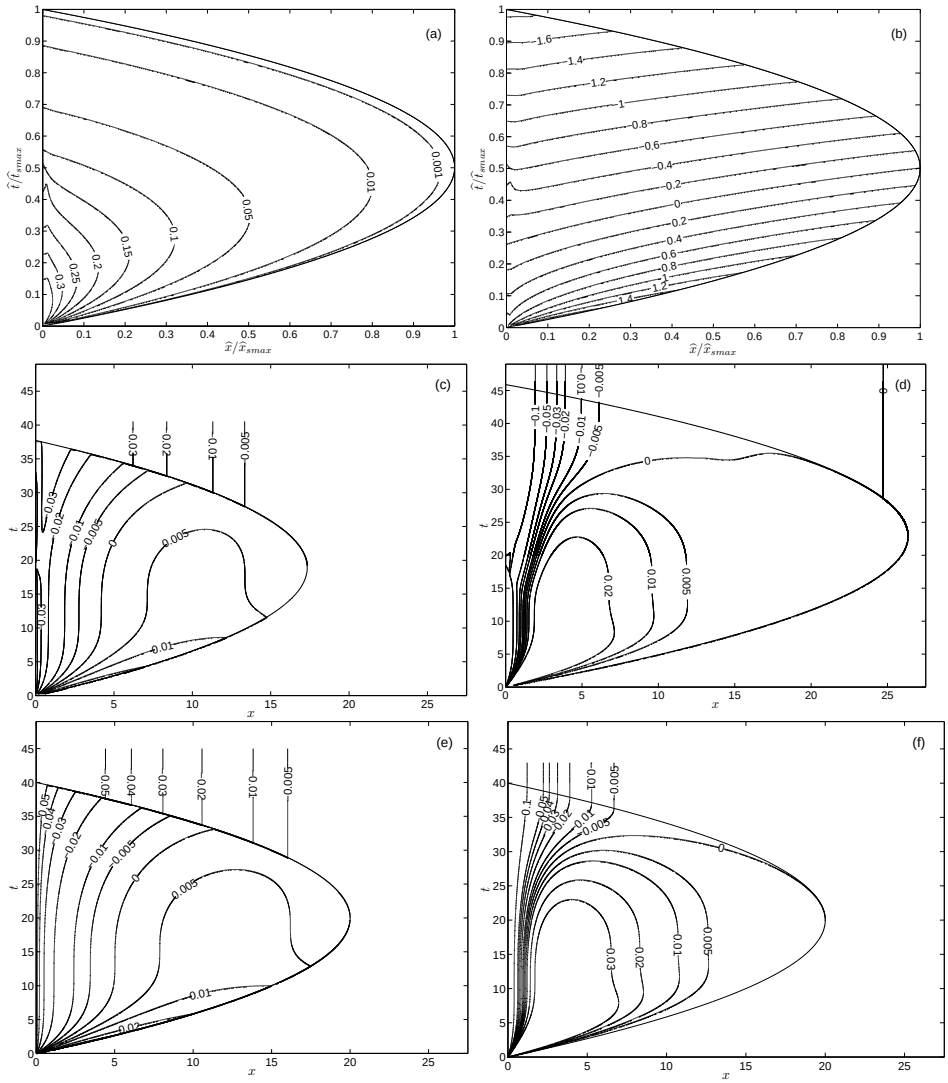

Figure 5.2: Contour plots of flow and bed change for bed-load-only simulations with formulae I ($q = u^3$) ($\sigma = 0.01$) and VI ($q = hu^3$) ($\sigma = 0.62$) under a single PW01 swash. (a) h for I; (b) u for I. Note that space and time axes are normalised by maximum inundation and swash period respectively. (c) ΔB for I; (d) ΔB for VI; (e) ΔB for I (uncoupled); (f) ΔB for VI (uncoupled).

does not occur for VI. This bore transports a large amount of sediment, even though $h \to 0$ there, and this is one of the main objections to use of formulae I-V for making engineering predictions in vanishing water depth. The existence

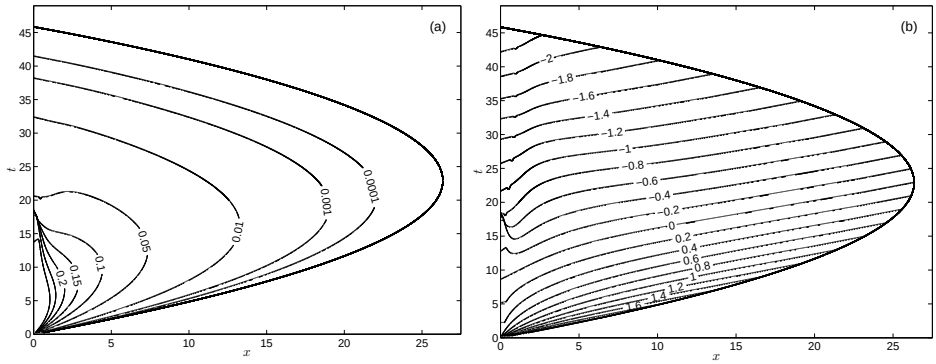

Figure 5.3: Contour plots of flow for bed-load-only simulations with formula VI ($q = hu^3$) ($\sigma = 0.62$) under a single PW01 swash. (a) h; (b) u.

(non-existence) of the bore can also be seen in Figure 5.2(c) and (d) in the discontinuity (continuity) in bed contours when moving from wet to dry regions.

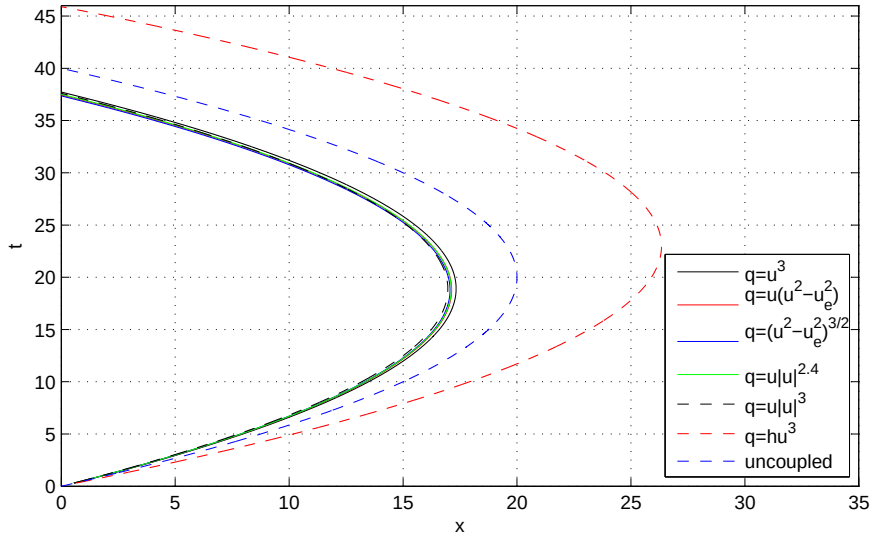

Figure 5.4: Shoreline trajectories for formulae (I-VI) along with that for PW01 (i.e. uncoupled). Colours indicate formula–see legend.

The sediment bore at the tip for I-V increases the beach slope in the uprush, see Figure 5.5, and therefore reduces the maximum inundation compared to

the fixed bed case. For formula VI, a large hump of sediment immediately the shoreline decreases the beach slope, and the maximum inundation is considerably enhanced compared to the fixed bed case.

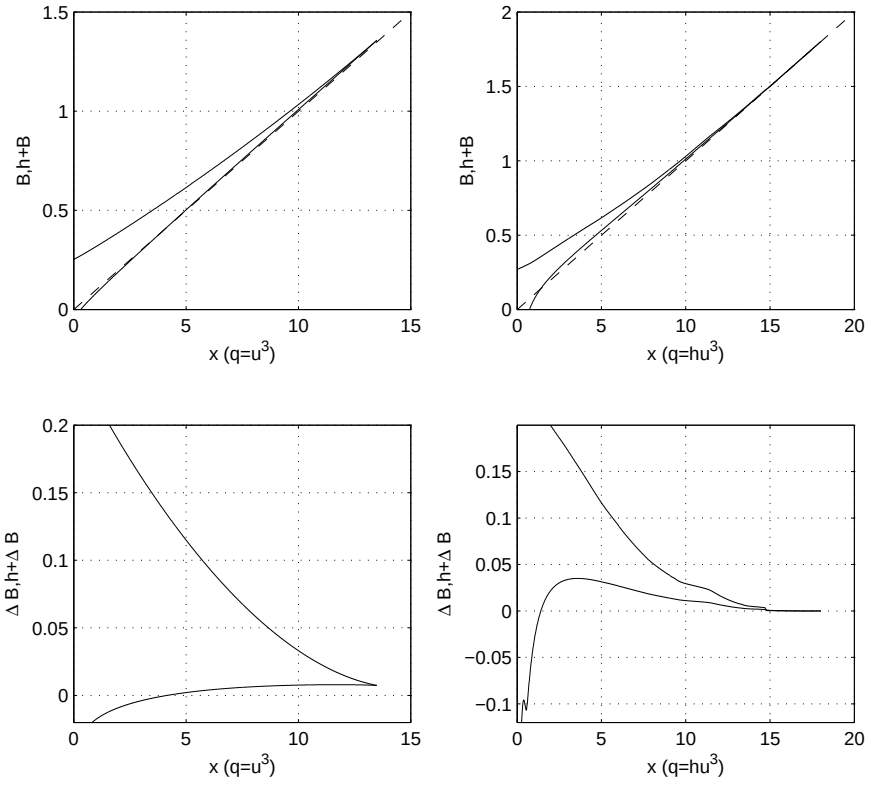

Figure 5.5: Beach and beach change profiles for formula I ($q = u^3$) and VI ($q = hu^3$) at $t = 10$. Dashed line represents the initial beach.

5.5 Final beach change

The final bed changes when the shoreline has receded back to the initial shoreline position after one single PW01 swash event are shown in Figure 5.6 for all formulae. The bed changes of the equivalent uncoupled simulations are also shown.

Final profiles for all $q = q(u)$ formulae indicate net offshore sediment flux, consistent with PH05 with, generally, net erosion increasing offshore, but also with less net erosion than for uncoupled simulations (Figure 5.6) (see KD10) over the whole swash. The highest power of u yields the largest (smallest) erosion in the lower (upper) swash and smallest maximum inundation, as can be observed from the coloured squares indicating the maximum run-up of each coupled simulation. This is because the velocity in the lower swash is generally larger than that in the upper swash, therefore an increase in the power of u gives an increase (decrease) in the sediment transport in the lower (upper) swash, which results in more (less) erosion in the lower (upper) swash. Profiles are generally similar, however.

Note that this switch between upper and lower swash can be observed in both coupled and uncoupled simulations, indicating that only at the base of the swash, where the dam collapses and bores are formed, are the basic morphodynamics changed by full coupling. This implies that some success may be obtained with uncoupled or quasi-coupled (see Postacchini et al., 2012) models of beach change, as long as probable inaccuracies are understood.

For both formulae II and III (those with thresholds) there is a region in which the bed level does not change (when $|u| < u_{crb}$), and the width of this region under the PW01 swash event is $u_{crb}^2/(2\alpha) = 1$. The presence of u_{crb} reduces the sediment movement (thus Bagnold (II) and Meyer-Peter Müller (III) formulae have a correspondingly larger σ than the Grass formula (I) to ensure the same sediment flux). However, the profiles differ little from that for I.

For formula VI ($q = hu^3$), as expected there is relatively little bed change in the upper swash, with significantly more (net erosion) in the lower swash, where h increases. Note that for VI more erosion is predicted in the mid- to lower swash by the fully coupled simulation than by the uncoupled one: see Figure 5.6.

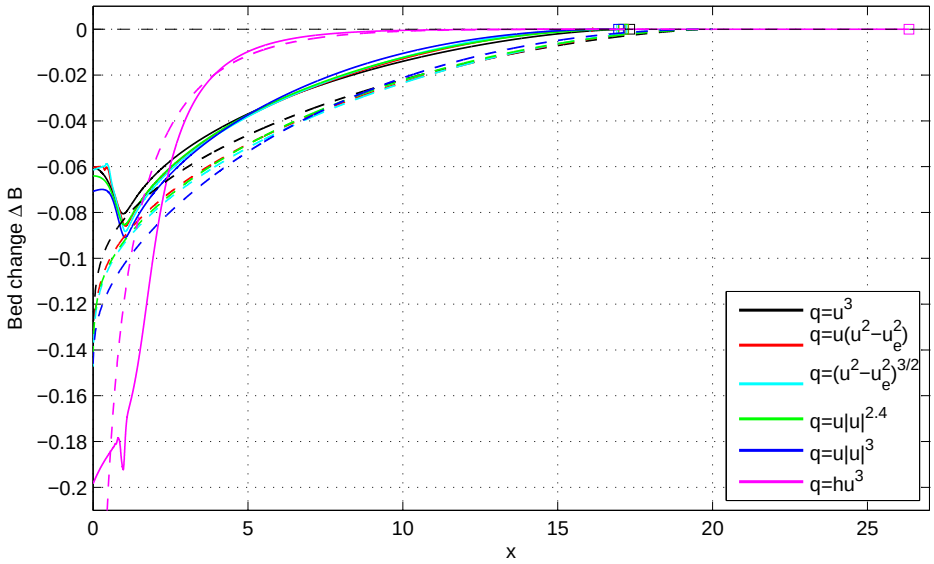

Figure 5.6: Dimensionless change in bed level relative to the initially plane beach after one single PW01 swash. Solid lines: fully coupled simulations. Dashed line: uncoupled simulations. □ indicates position of maximum inundation for the coupled events (for the PW01 (uncoupled) event it is at $x = 20$). Colours indicate formula–see legend.

5.6 Net erosion and deposition: Influence of power of u and h

The zero contour in the dry bed region near the maximum inundation in Figure 5.2(d) seems to indicate that net deposition occurs in the extreme upper swash using VI. However, these extremely small deposition could be caused by numerical errors. In fact, since fluid transport is proportional to h^1, and the net flux of water is 0 in the swash zone, a bed load formula with h^1, e.g. $q = hu^3$, seems to be roughly the border between net-erosive and net-depositional behaviour in the upper swash.

It is therefore instructive to examine the dependence of q on h. We do so in Figure 5.7, in which equivalent final profiles for normalised simulations for another three formulae, $q = h^{0.8}u^3$, $q = h^{1.2}u^3$, and $q = h^{1.3}u^3$, as well as those for a selection of powers of u (i.e. those without thresholds) are shown. In general, the relative deposition (erosion) in the upper (lower) swash increases as the power of either h or u increases; of these two factors h is the dominant one. Importantly, a power of $h > 1$ results in net deposition in the upper swash, and, in fact, the development of a small berm or swash bar there. Note that this berm is a feature of the upper swash and is not connected with the formation of a backwash bore, as found for the more generic backwash bore bars by Zhu et al. (2012). It looks qualitatively similar to the pattern of implied deposition obtained by PH05 when a settling lag was introduced.

It can be seen that (Figure 5.7) the formulae $q(h, u)$ predict significantly more

erosion than $q(u)$ in the lower swash based on the same net flux normalisation. This is due to the much larger σ values we imposed on these formulae in order to achieve the same net flux.

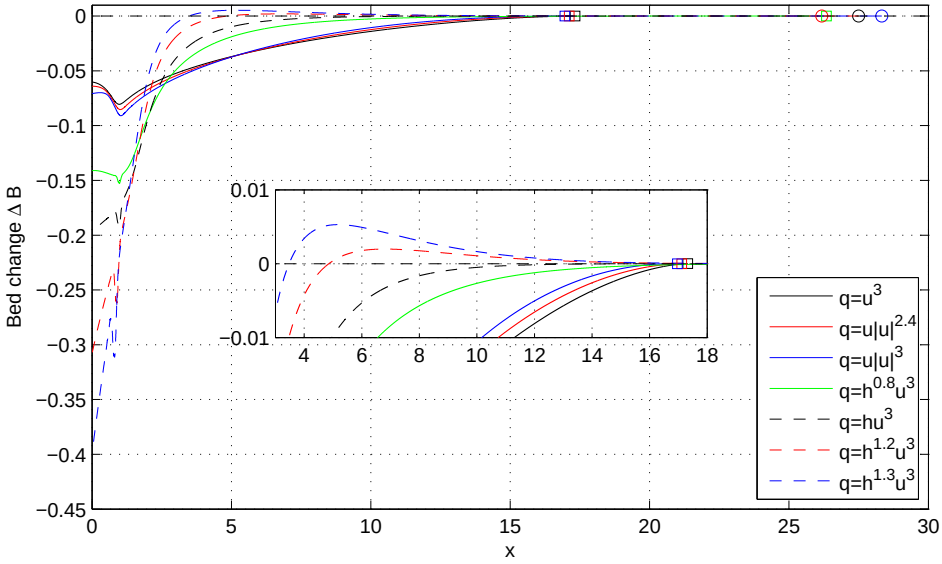

Figure 5.7: Dimensionless change in bed level relative to the initially plane beach after one single PW01 swash for different powers of h and u. □ and ◯ indicate positions of maximum inundations. Colours indicate formula– see legend.

5.7 Uncoupled and coupled modelling

In Figure 5.8 following PH05 we illustrate differences in instantaneous sediment transport (q) between coupled (in black) and uncoupled (in red) approaches for I and VI. For I (left panel) differences are apparent even for small times, due to the different speeds of the uprush tip (related to different maximum inundation). Note, however, two points: (i) Instantaneous q values for coupled and un-

coupled calculations are similar where both are non-zero; the major discrepancies are the times of inundation (t_i) and denudation (t_d), and the discrepancy in t_d is particularly large. (ii) In the backwash q in the coupled simulations shows slightly less offshore transport than its uncoupled equivalent. What this tells us is that the velocity, from which q is derived, is similar, but that the smaller initial velocity, which can be obtained by the Riemann solution for the wet-dry dam-break problem over a flat mobile bed (Kelly and Dodd, 2009), results in a less exaggerated net erosion. For VI there is no such clear correspondence.

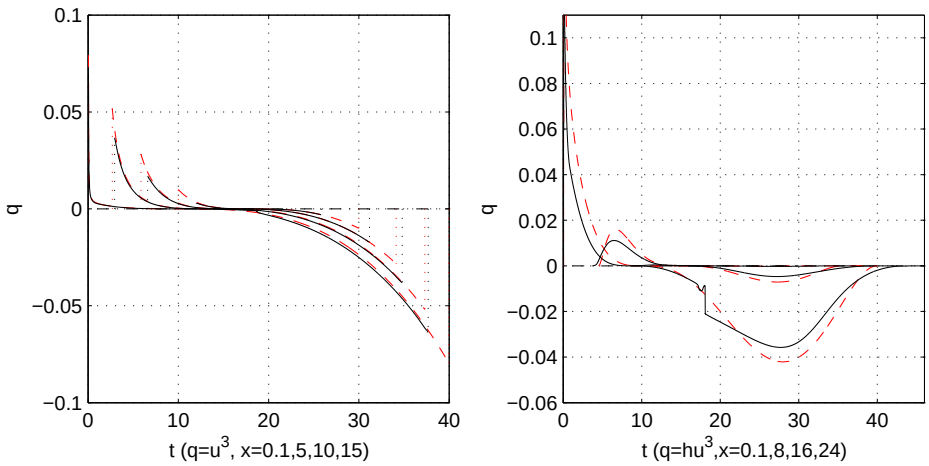

Figure 5.8: Dimensionless instantaneous $q(x)$ at a number of locations in the PW01 swash. Present simulations (black) and uncoupled (PW01) ones (red). (Left: I. Right: VI)

In Figure 5.9, also following PH05, we plot the aforementioned net sediment flux ($Q(x) = \int_{t_i}^{t_d} \sigma q(x,t)\, dt$) in the uprush, backwash, and over the whole event, comparing it to that obtained from the uncoupled approach. For I (indicative of I-V recall) differences between the approaches do appear to accumulate over the swash event, with relatively little discrepancy in the uprush, but signifi-

cant disagreement in the backwash, which results in the main differences, see also the bottom panel in Fig. 5.9, in which the difference in net sediment flux between coupled and uncoupled approaches is shown. For VI significant differences exist over all phases of the swash.

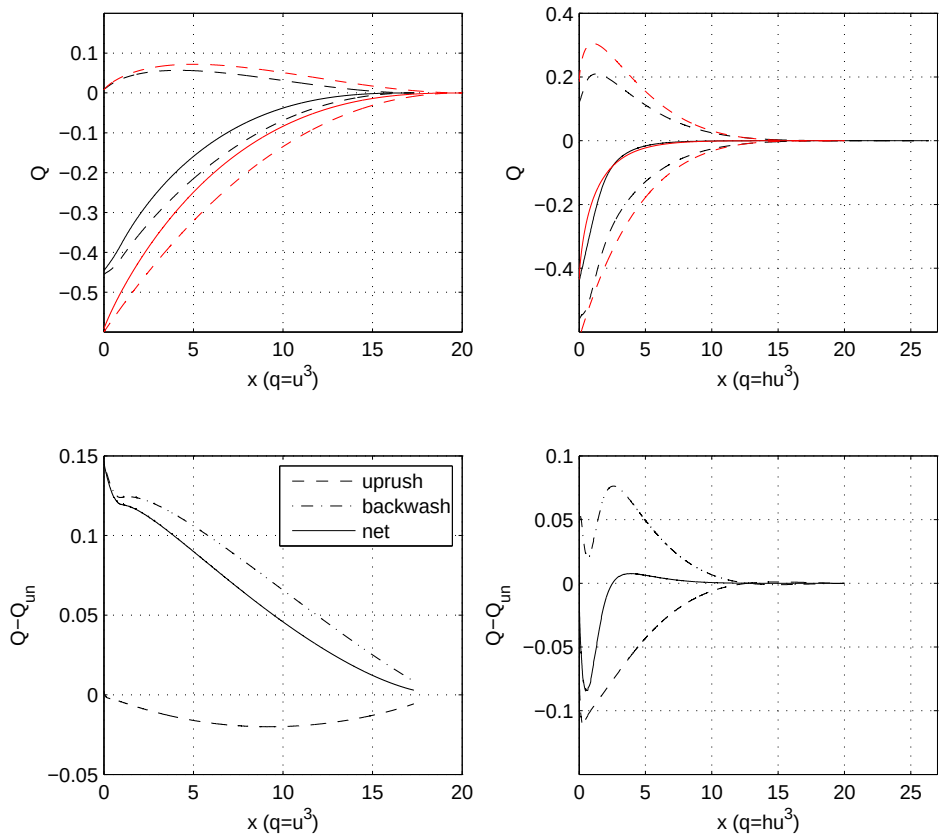

Figure 5.9: Top: Dimensionless $Q(x)$ (net sediment flux) for uprush and backwash (dashed lines) and the whole swash event (solid lines) for present simulations (black) and uncoupled (PW01) ones (red). Note that the uprush (backwash) here is defined as the duration until (after) maximum inundation is achieved. Bottom: difference between Q from present simulations and that from uncoupled approach. (Left: I. Right: VI)

5.8 Simulations with bed shear stress

We describe the bed shear stress by the Chezy law $\tau = C_D u^2$ (Soulsby, 1997). When bed shear stress is included, the momentum equation (2.27) is changed and it becomes:

$$u_t + uu_x + h_x + B_x = -\frac{C_D|u|u}{h}; \tag{5.1}$$

(2.26) and (2.28) remain the same. Consequently, the Riemann equations (2.45) become:

$$\Re^{(k)} = \lambda_k \frac{du}{dt} + \frac{\lambda_k + \sigma q_h}{\lambda_k - u}\frac{dh}{dt} + \frac{dB}{dt} = -\lambda_k \frac{C_D|u|u}{h},\ k = 1, 2, 3, \tag{5.2}$$

where λ_k is obtained from (2.30).

The swash flow is computed by solving (5.2) numerically (Kelly and Dodd, 2009). Note that the term $-\frac{C_D|u|u}{h}$ in (5.1) $\to -\infty$ at the shoreline, i.e., as $h \to 0$, in the uprush. In the flat fixed bed dam-break solution with bed shear stress (Dressler, 1952; Whitham, 1955), this term is balanced by h_x, which implies that $h_x \to -\infty$ at the wave tip. For the uprush of swash flow over a sloping beach, this balance is also appropriate (see also Antuono et al., 2012). However, in the backwash $-\frac{C_D|u|u}{h}$ cannot be balanced by h_x, as $-\frac{C_D|u|u}{h} \to \infty$ when u is negative, while h_x cannot $\to \infty$. Therefore u must be 0 such that (5.1) also holds at the shoreline in the backwash. This implies that there is no receding shoreline (see Antuono et al., 2012, for a detailed asymptotic analysis).

Due to these considerations the numerical implementations for the shoreline solution in the uprush and backwash are different. Extrapolation is employed to solve the tip in the uprush, and according to the analysis of the shoreline in

the backwash, $u_s = 0$ is imposed in the numerical solution.

Note that the shock conditions for the system with bed shear stress are identical to those without shear stress (KD10, Zhu et al., 2012).

Fully coupled simulations with sediment transport formulae I ($q = u^3$) and VI ($q = hu^3$), representing $q(u)$ and $q(h, u)$ respectively, are considered with bed shear stress included. The numerical simulations and comparisons confirm the analysis in the uprush $h_x \to -\infty$ near the shoreline, causing the swash flow in the uprush much deeper than those with no bed shear stress. The backwash flow becomes very thin and slow due to the resistance of bed shear stress, which results in much less offshore sediment transport, especially for $q = hu^3$.

The bed changes at $t = 40$ with different C_D values for formulae I ($\sigma = 0.01$) and VI ($\sigma = 0.62$) are shown in Figure 5.10. Note that the bed is still wet at $t = 40$ as the shoreline does not recede seawards ($u_s = 0$) in the backwash. Note also that we retain σ values from Table 5.2 here. In reality C_D and σ will be related, but as we do not know the relation it is appropriate to test different C_D values for the given (normalised) σ.

It is seen that the maximum inundations for both formulae are much reduced from those with no shear stress, i.e. $C_D = 0$; as C_D increases, the maximum inundation decreases. Note that for VI, the maximum inundation is significantly reduced when bed shear stress is included even with a small C_D: from $x = 26.34$ (off scale on figure) for $C_D = 0$ to $x = 14.61$ for $C_D = 2 \times 10^{-4}$. One important feature of the non-frictional simulation with VI is the wide and thin swash flow behind the shoreline, see Figure 5.3(a), while the simulation with

bed shear stress yields much deeper tip flow. The bed shear stress confines the wide and thin tip flow to a narrower region, and therefore the flow is much deeper and the maximum inundation is greatly reduced.

The net sediment flux at $x = 0$ is still offshore for both formulae for all tested non-zero C_D values, however, the magnitude of net erosion is considerably reduced. For formula I, net erosion is predicted all over the swash zone to a reduced extent for $C_D = 0, 2 \times 10^{-4}, 1 \times 10^{-3}$ and 1×10^{-2}, see Figure 5.10. How-

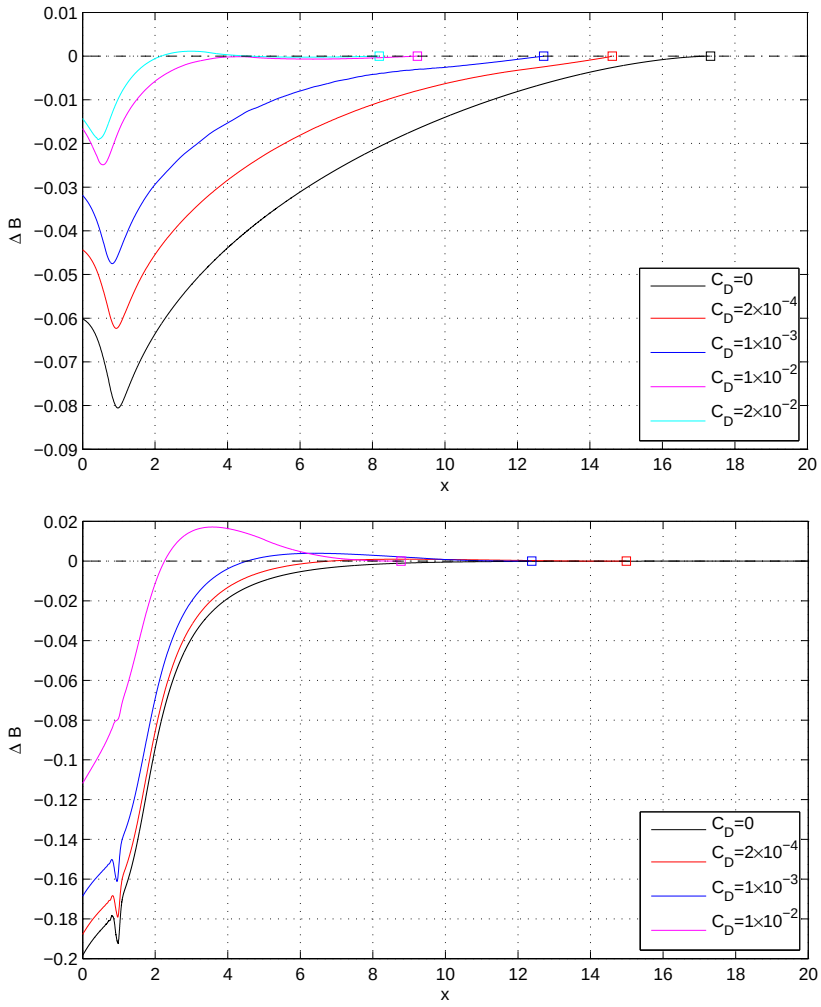

Figure 5.10: Bed change for formulae I ($q = u^3$) and VI ($q = hu^3$) with bed shear stress under the PW01 swash event at $t = 40$. Top: I and bottom: VI.

ever, net erosion in the upper swash is becoming closer to 0 as C_D increases and net deposition is predicted in the region around $x = 3$ for $C_D = 2 \times 10^{-2}$. Bed shear stress reduces the velocity in the uprush and backwash, and reduces correspondingly the onshore and offshore sediment transport; the sediment transport reduced in the backwash is to a greater extent such that deposition occurs for large C_D values.

Note that deposition occurs in the upper swash for formula VI for all tested C_D values. The sediment flux in this formula is dependent on h and u, and the greatly reduced h and u in the upper swash during the backwash period result in significantly less offshore sediment transport in this region. The combined effect of reduced onshore and offshore sediment transport is net deposition in the upper swash and erosion in the lower swash for VI, and the deposition in the upper swash is much more than that which occured in the simulation with formula I.

CHAPTER 6

Fully coupled bed-load-only simulation for HP79 swash and a solitary wave

In this chapter, we examine the HP79 swash event, in which a uniform bore advances into still water, collapses at the initial shoreline position and then climbs up the beach, over an erodible beach by the bed-load-only model. Note that $q = u^3$ is used to describe the transport of bed load in the fully coupled simulation. The development of the backwash bore observed by Hibberd and Peregrine (1979) over a fixed bed is investigated over erodible beaches of different bed mobilities. The resulting beach changes and bed steps (discontinuities in bed level) associated with the backwash bore are also examined. Moreover, a swash event created by a solitary wave travelling over an initially flat, erodible bed and then climbing up a sloping beach is also examined. To get further understanding of the bed step development, bed shear stress is included in the

bed-load-only simulation for a solitary wave. The bed step development in HP79 and solitary wave simulations is compared.

6.1 HP79 swash simulation

6.1.1 Initial and boundary conditions

Initial conditions

The initial conditions are shown in Figure 6.1. In the region $x \leq -10$ the bed is flat while for $x \geq -10$ the beach is of a uniform slope, with the beach slope $\alpha = 0.1$. The bore height is 0.6, and at $t = 0$ the uniform bore is assumed to be located at $x = -10$. There is therefore a discontinuity in h, u and B at $x = -10$, with h_L, u_L and B_L on the left side and h_R, u_R and B_R on the right side. The velocity of the bore is W.

For $x \geq -10$, $h(x, t = 0) = 1 - \alpha(x + 10)$, $u(x, t = 0) = 0$ and $B(x, t = 0) = \alpha(x + 10)$ ($u_R(t = 0) = 0$, $h_R(t = 0) = 1$, and $B_R(t = 0) = 0$). At $t = 0$, $x \leq -10$ is a constant region such that $h(x, t = 0) = h_L(t = 0)$, $u(x, t = 0) = u_L(t = 0)$ and $B(x, t = 0) = B_L(t = 0)$, where $h_L(t = 0) = 1.6$ and such that $u_L(t = 0)$, $B_L(t = 0)$ and also the shock speed $W(t = 0)$ are determined by shock relations (2.56)-(2.58) as $h_R(t = 0)$, $u_R(t = 0)$ and $B_R(t = 0)$ are known. The initial shoreline position is at $x = 0$.

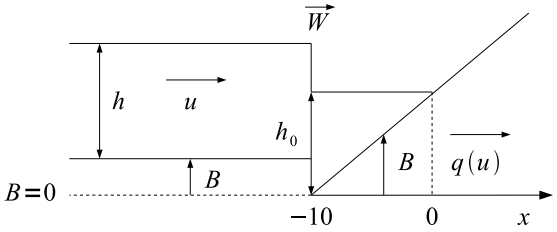

Figure 6.1: Initial conditions for the HP79 swash over an erodible beach.

Boundary conditions

The seaward boundary is chosen so as to be far enough away from the shore that h, u and B at that point are uninfluenced by the wave reflected from the shore throughout the computation time. Here the seaward boundary is at $x = -100$, and $h(x = -100, t) = h(x = -100, t = 0)$, $u(x = -100, t) = u(x = -100, t = 0)$ and $B(x = -100, t) = B(x = -100, t = 0)$. The landward boundary is a wet-dry boundary.

6.1.2 Flow structure

The complete solution (for $\sigma = 0.0654$) for a uniform bore climbing over an erodible bed is shown in Figure 6.2. When the uniform bore climbs up the beach, the bore height decreases and the velocity of the water behind the bore increases, and sediment is moved shorewards as bed load. However, the speed of the bore decreases and then increases.

When the bore collapses at the initial shoreline position, the water at the shoreline reaches its maximum shoreward velocity, and runs up the beach. As there is water continuously coming in from the seaward boundary, the water in the

upper swash is much deeper than that of PW01 swash over an equally mobile bed (see KD10). The value of the velocity at the bore collapsing point is bigger than the KD10 solution, consequently the maximum inundation is bigger. However, the inundation is significantly reduced compared to that observed by HP79, consistent with the results of KD10.

When the backwash starts, gravity dominated backwash flow retreats back rapidly; however, it is retarded by the continuously incoming water. Therefore, a backwash bore gradually develops, due to the convergence of λ_3 characteristics (HP79). This backwash bore develops at $(x, t) \approx (13.57, 47.09)$. At the late stage of the backwash, the shoreline gradually catches up with the backwash bore, and as there is also a sediment bore at the shoreline, it is addressed as a problem of the collision of two shocks. This shock-shock collision ultimately results in a bed step (or berm or swash bar) and a new shoreline with a finite water depth being created on the beach. This problem is solved as a Riemann problem (see § 6.1.3), which is a dam-break problem over a bed with a discontinuous bed step at the foot of the dam and probably with an initial water velocity. Then the new shoreline keeps still and then moves slowly seawards and then shorewards, and gradually settles down.

The water moves the sediment shorewards and causes deposition in the run-up stage. While in the backwash, sediment is moved offshore, but as the velocity is not symmetric and the onshore movement is dominant, the overall sediment flux at $x = 0$ is onshore. The event results in deposition from $x \approx 4.57$ almost to $x_{s_{max}}$ (maximum inundation).

Note, in particular, the velocities (Figure 6.2(b)). In the uprush the maximum velocity for the mobile bed case ≈ 0.76 times that for the fixed bed. The peak velocity in the backwash ≈ 0.58 times the fixed bed equivalent. This discrepancy results from the smaller inundation and the reduced slope for the backwash (because of the deposition: see Figure 6.2(c)). This results in a weaker shock that forms later in the swash event, and reduced flow velocities at the tip compared with those in the equivalent fixed bed case.

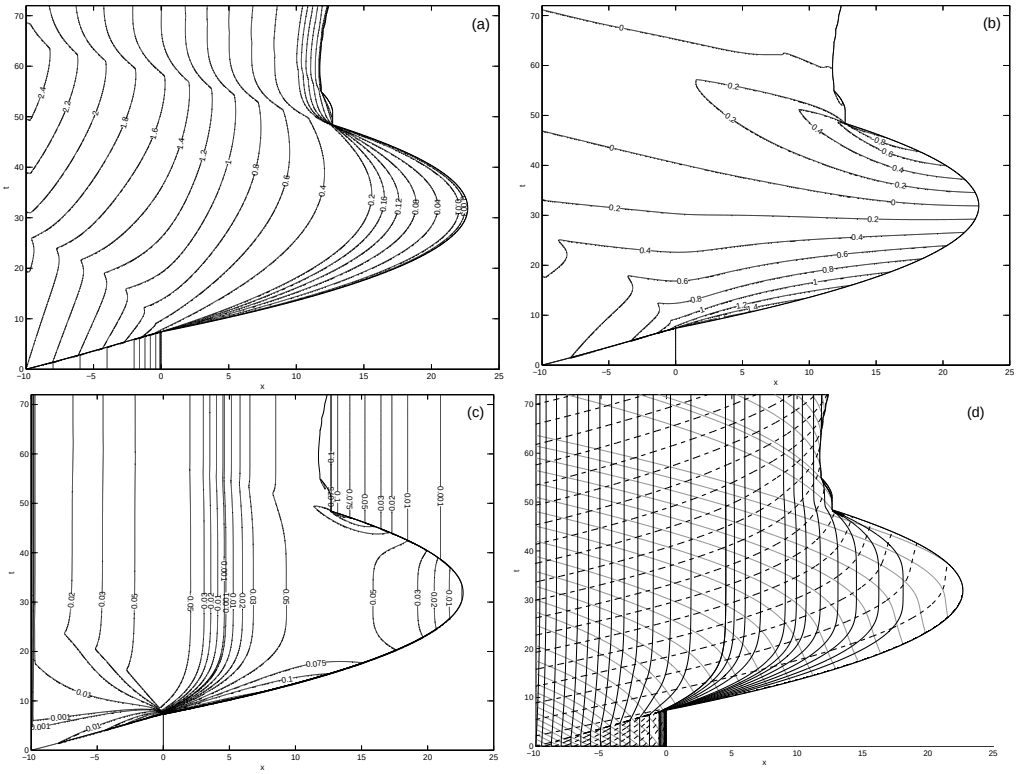

Figure 6.2: Contour plots for the bed-load-only HP79 simulation over an erodible beach ($\sigma = 0.0654$). (a) h; (b) u; (c) ΔB; (d) characteristics diagram.

6.1.3 Analysis when the shoreline catches up with the backwash bore

In the simulation, the shoreline eventually catches up with the backwash bore. This is essentially a problem of shock-shock collision. In this problem, there are three regions; here we may call them respectively the left, middle and right region, see Figure 6.3. Accordingly, variables in the left, middle and right regions are denoted by the subscripts Lc, Mc and Rc. As the two shocks come closer, the middle region gradually tends to vanish, and in the limiting case this region converges to one point. Therefore, at the moment of the two shocks colliding, the middle region is assumed to disappear and the flow has only one discontinuity; however, the shock conditions are usually not satisfied at this discontinuity, and this discontinuity is not stable and usually collapses. The regions on the left and right side of the discontinuity after collision, are not constant states with constant h, u and B values, which therefore is not a Riemann problem; however, we assume that the solution for the idealised Riemann problem with constant states on the two sides could be used as an approximation for wave structure in a sufficiently small time interval after the shock collision. Therefore, the immediate wave structure after collision is obtained by solving the idealised Riemann problem.

Generally, the resulting Riemann problem is a wet-wet dam-break problem, and this Riemann solution is given in § 3.5. However, in the case of the shoreline approaching the backwash bore in the present swash simulation, we have $h_{Rc} = 0$ and $u_{Rc} = 0$; the corresponding Riemann problem is a wet-dry dam-break

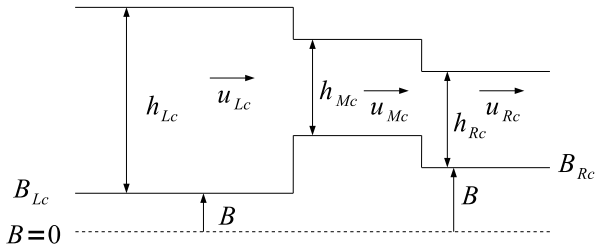

Figure 6.3: Schematic diagram for two shock collision.

problem with a bed step; the Riemann solution is given in § 3.4. The backwash bore is thought to be the shock on the left in Figure 6.3, and the sediment bore at the shoreline is the right shock. As the shoreline approaches the backwash bore, the middle region width $\rightarrow 0$ and it finally becomes dry, with $h_{Mc} = 0$ and $u_{Mc} = \dfrac{dx_s}{dt}$. When the two shocks are close within a grid cell of each other, the numerical solution is only an approximation for the case of zero middle region width. The analytical solution for the shock, of which one side is nearly dry bed but the water is of a finite velocity, in Appendix A is utilised to obtain the limit flow structure right before the shock collision.

From Appendix A, when the shoreline approaches the backwash bore, the bed difference associated with the backwash bore $B_R - B_L \rightarrow h_L - h_R \rightarrow h_L$. At the moment of collision of the shoreline and the backwash bore, $B_R - B_L = h_L$. Therefore, we have $B_{Mc} - B_{Lc} = B_R - B_L = h_L$. From the shock relation for the sediment bore at the tip, $B_{Rc} = B_{Mc} - \sigma u_{Mc}^2$. The resulting bed step height is $B_{Rc} - B_{Lc} = B_R - B_L - \sigma u_{Mc}^2 = h_L - \sigma u_s^2$. This shows that the bed step height is slightly lower than the water depth on the seaward side h_L, which forms a wet-dry dam-break problem with a bed step. The water on the seaward side of the bed step may overtop the bed step, depending on the velocity and also

bed mobility. In the present simulation, the water is of a seaward velocity, and it cannot overtop the bed step.

6.1.4 Maximum inundation and backwash bore development

As aforementioned, the maximum inundation is reduced in the mobile swash event compared with the hydrodynamic event. Although there is a backwash bore formed in the swash events with different σ values, the shock development and shock strength ($\lambda_L - \lambda_R$) for different swash events vary considerably. The shoreline motion and backwash bore development are shown in Figure 6.4.

The maximum inundation decreases rapidly as σ increases, and the maximum inundation when $\sigma = 0.0654$ is only 71% of that when $\sigma = 1 \times 10^{-7}$. From Figure 6.4 and 6.5, it is found that the backwash bore forms at a later stage and the duration is much shorter for a bigger σ. Moreover, the shock strength weakens as bed mobility increases, see Figure 6.5.

6.1.5 Final beach profile

The resulting final beach changes for various σ values are shown in Figure 6.6. Deposition is found throughout most of the final bed profiles for all σ values, and the magnitude of deposition increases as σ increases. However, near the maximum inundation there is slight erosion for all σ values except $\sigma = 0.0654$. There is a discontinuous bed step, which is associated with the backwash bore, in all the final bed profiles.

The relationship between bed step and σ, bed-step crest elevation and σ is

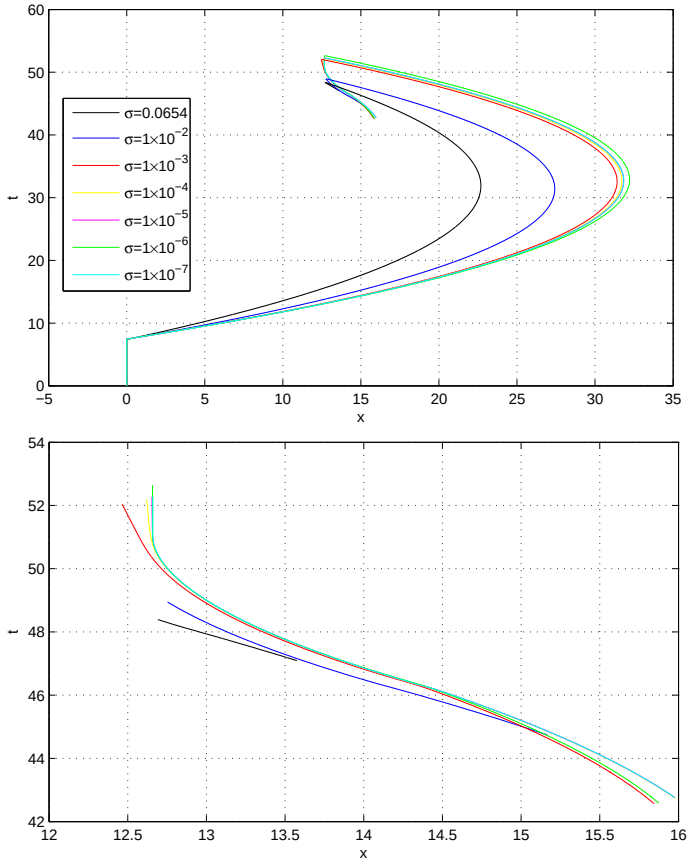

Figure 6.4: Dimensionless backwash bore position and shoreline position (top); and blow-up of backwash bore position (bottom). All for various σ values for mobile bed HP79 event.

shown in Figure 6.7. Note that the bed step is referred to the bed elevation difference at a discontinuous point, and that the bed-step crest elevation here refers to the vertical distance from the top of the bed step in the final profile to the original bed level at that location. The magnitude of the bed step is determined by the shock strength and the bed mobility: it increases as shock strength and bed mobility increase. However, the shock strength itself is also related to bed mobility: it weakens as bed mobility increases, see Figure 6.5. Therefore the height of the bed step first increases as σ increases, but after a

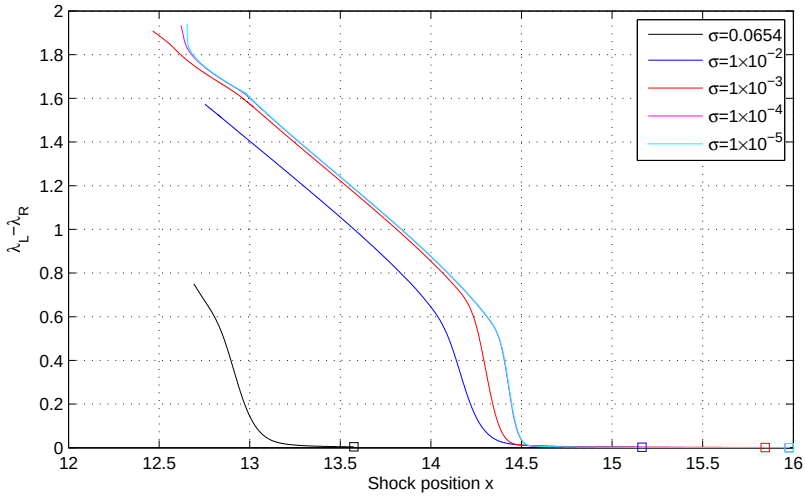

Figure 6.5: Dimensionless shock strength as a function of shock position for various σ for mobile bed HP79 event. □ indicates point of shock inception.

certain value it decreases (see Figure 6.6 and 6.7). The bed-step crest elevation, however, increases with mobility as more sediment is deposited in the swash (due to increased mobility).

It is the flow velocity at the tip that determines how much sediment is stripped from the beach as the shoreline recedes. As mentioned in § 6.1.2, flow velocity is reduced when σ increases. Therefore, although increased bed mobility favours a larger bed step in principle, the weaker shock strength and lower velocity lead eventually to a decreasing bed step (although a larger overall bed elevation with respect to the initial bed level): see Figure 6.6 and 6.7. As $\sigma \to \infty$ there is more deposition overall.

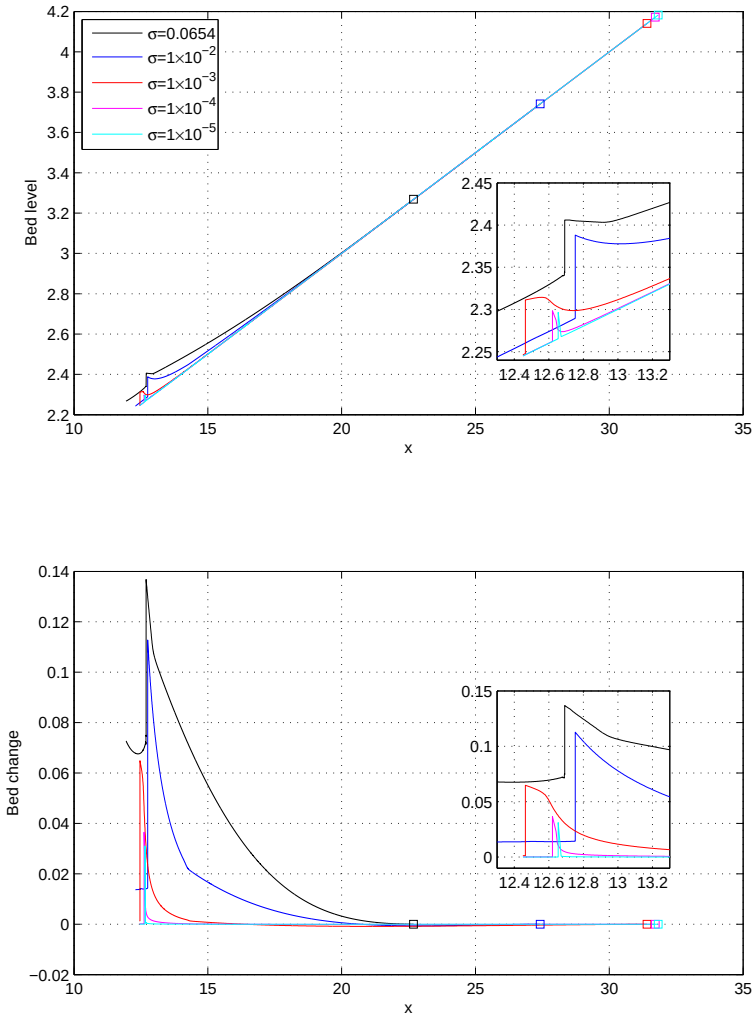

Figure 6.6: Dimensionless final beach profile (top) and bed change (bottom) for various σ for mobile bed HP79 event. □ indicates position of maximum inundation.

6.2 Solitary wave simulation

6.2.1 Initial and boundary conditions

Initial conditions

The solitary wave is a solution to the Korteweg-De Vries (KDV) equation with a single crest whose amplitude diminishing to 0 at inifinity from the wave crest

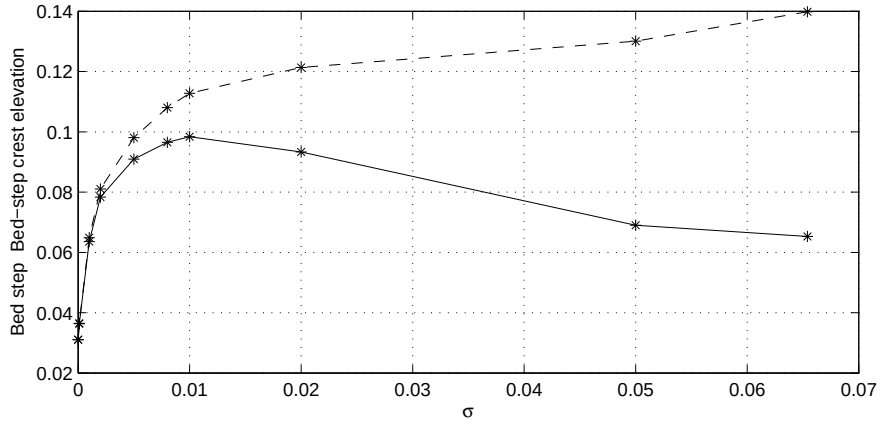

Figure 6.7: Dimensionless bed step height and bed-step crest elevation for various σ for mobile bed HP79 event. Black solid line: bed step height; black dashed line: bed-step crest elevation.

(Mei, 1990, p. 540-543); the KDV equation is derived from the Boussinesq equations. We consider a solitary wave of height $h_w = 0.6$ on a still water depth of $h_{st} = 1$, with crest initially located at $x = -22$ when $t = 0$, see Figure 6.8. For $x \geq -10$, $h(x, t = 0) = 1 - \alpha(x + 10)$, $u(x, t = 0) = 0$ and $B(x, t = 0) = \alpha(x + 10)$. In the region $x \leq -10$ the bed is flat while for $x \geq -10$ the beach is of a uniform slope, with the beach slope $\alpha = 0.1$. For $x < -10$, the water depth is $h(x < -10, t = 0) = h_w \text{sech}^2 \left(\left(\frac{3h_w}{4h_{st}^3} \right)^{1/2} (x - 22) \right)$ (Mei, 1990, p. 540-543). From Synolakis (1987), when $h_w/h_{st} > 0.055$ the wave breaks in the uprush, and it breaks in the backwash when $h_w/h_{st} > 0.044$. Thus, the solitary wave considered will break in both the uprush and the backwash. The water velocity is determined by the Riemann invariant along the backward characteristic: $u(x < -10, t = 0) = 2(\sqrt{h(x, t = 0)} - 1)$. The bed level is adjusted to the water flow with $B(x < -10, t = 0) = \sigma \frac{(u(x,t))^3}{\sqrt{h(x,t)}}$. However, the water flow is assumed

not to be affected by the bed change at the initial time.

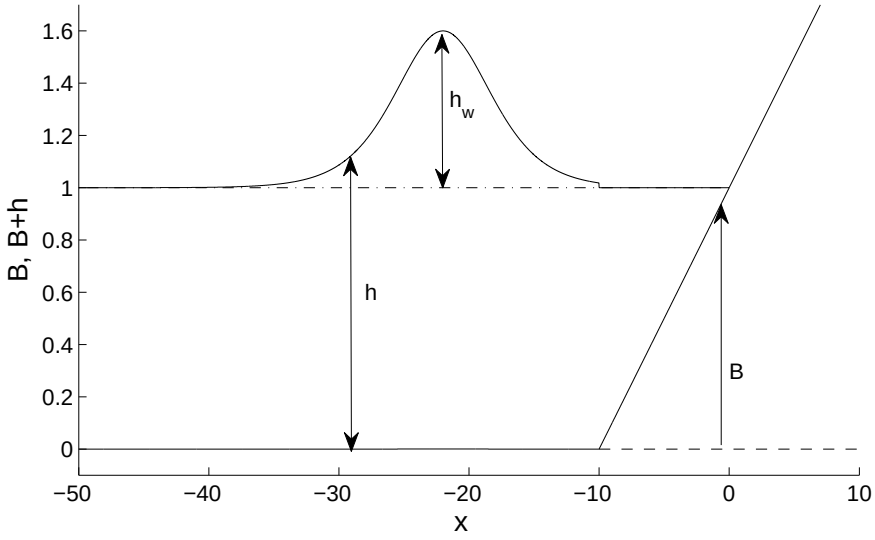

Figure 6.8: Initial conditions for a solitary wave.

Boundary conditions

The seaward boundary is chosen so as to be far enough away from the shore that h, u and B at that point are uninfluenced by the wave reflected from the shore throughout the computation time. Here the seaward boundary is at $x = -150$, and $h(x = -150, t) = 1$, $u(x = -150, t) = 0$ and $B(x = -150, t) = 0$. The landward boundary is a wet-dry boundary.

6.2.2 Swash simulation without bed shear stress

As the solitary wave approaches the shore, it breaks and forms a shock (bore) travelling to the shore, and the shock then reaches the shoreline position and collapses. After the bore collapses, the water climbs up the dry beach. The flow

is very asymmetric, with deeper flow in the uprush, see Figure 6.9. During the backwash, a backwash bore develops, and the shock strength gradually increases, with increasing differences in h, u and B on the two sides of the shock. The shoreline eventually catches up with the backwash bore, leading to a bed step on the beach, see Figure 6.10.

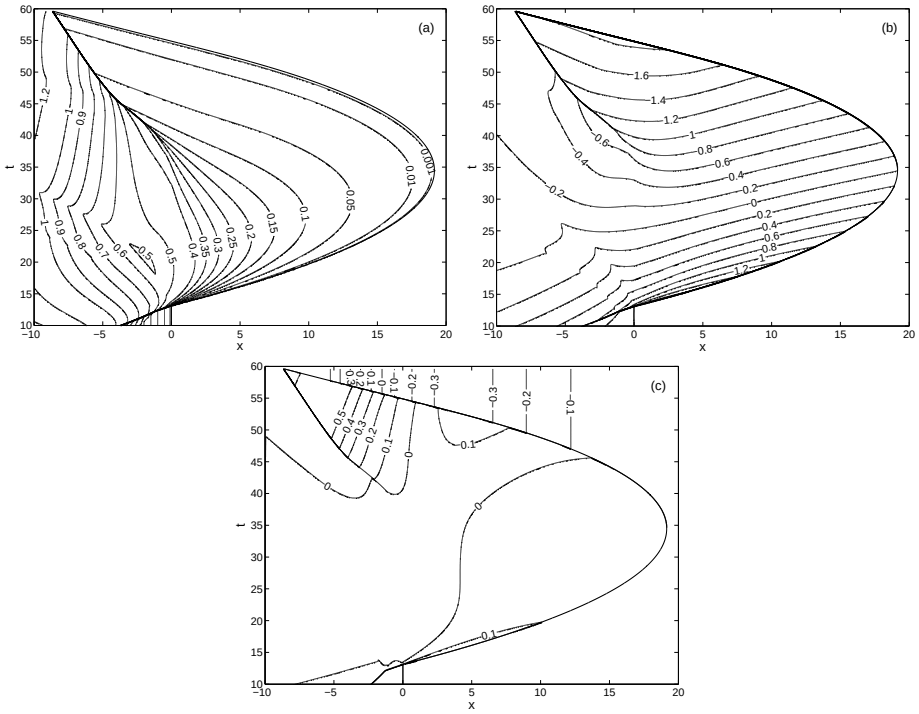

Figure 6.9: Contour plots for bed-load-only solitary wave simulation over an erodible beach ($\sigma = 0.0654$). (a) h; (b) u; (c) ΔB.

The beach profiles and changes of three bed mobilities when the shoreline catches up with the backwash bore are shown in Figure 6.10. For all the three σ values, a bed step forms, and the height decreases as σ decreases. The position of the bed step is further onshore when σ decreases. It seems that the bed step height is closely related to the position. The bed step heights are much larger than those in the HP79 simulations in § 6.1.5. Net erosion is predicted in most of

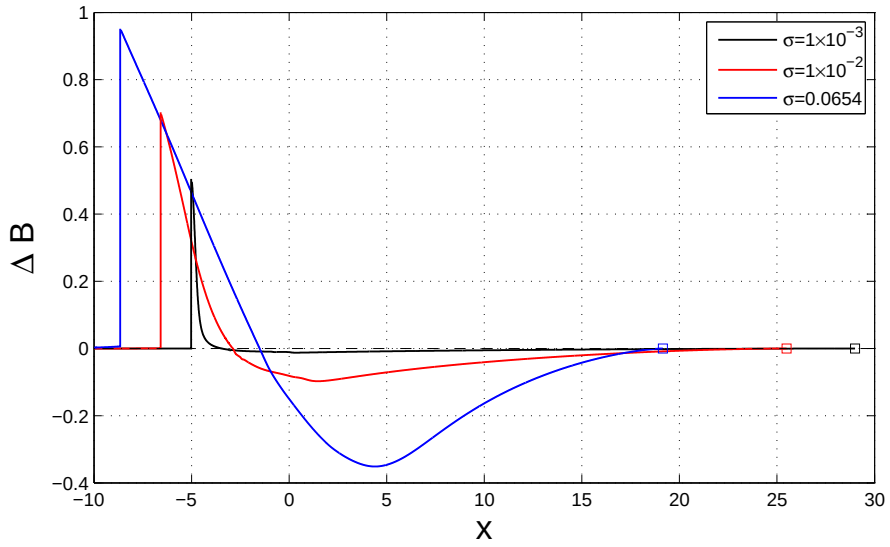

Figure 6.10: Beach changes for mobile bed solitary wave simulations without bed shear stress ($\sigma = 0.0654$).

the swash zone while deposition is predicted near the bed step. The erosion / deposition decreases as σ decreases.

6.2.3 Swash simulation with bed shear stress

To get further understanding of the bed step development, bed shear stress described by the Chezy law, is further included in the solitary wave simulation. The contours of h, u and ΔB in the equivalent simulation with bed shear stress with $C_D = 2 \times 10^{-3}$ are shown in Figure 6.11. The comparison in Figure 6.9 and 6.11 shows that the maximum inundation is considerably reduced when bed shear stress is included, and the uprush flow is deeper. The no receding shoreline is clearly shown in Figure 6.11. The backwash flow is thin and much slower due to bed shear stress, and the shock is therefore less pronounced. The

bed change is also reduced from that without bed shear stress, see Figure 6.9(c); however, the bed difference associated with the backwash bore is still of considerable magnitude.

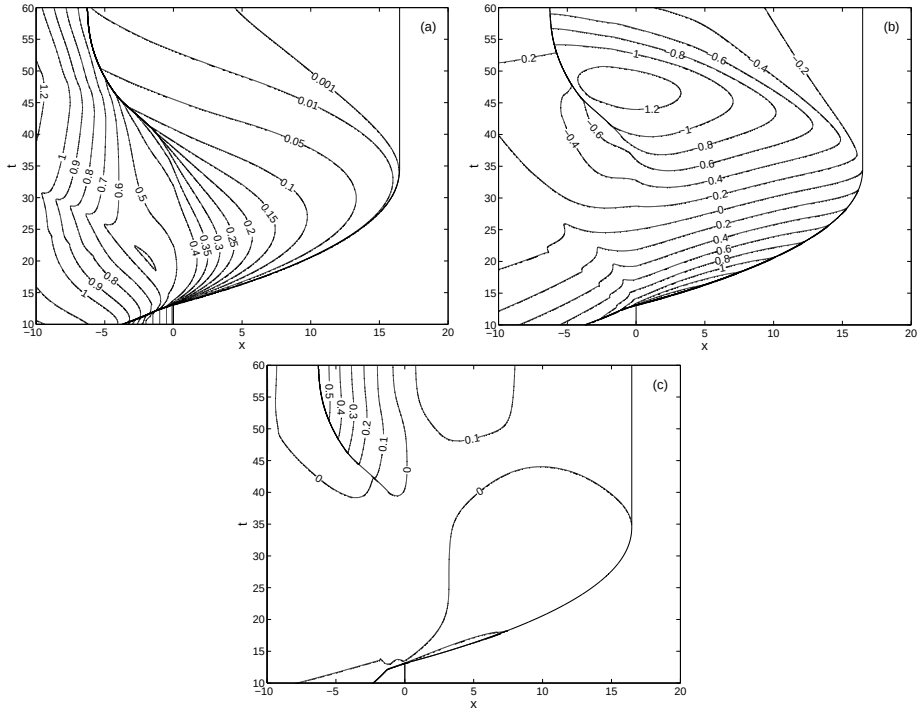

Figure 6.11: Contour plots for bed-load-only solitary wave simulation with bed shear stress over an erodible beach ($\sigma = 0.0654$ and $C_D = 2 \times 10^{-3}$). (a) h; (b) u; (c) ΔB.

Note that the shoreline will not catch up with the backwash bore when bed shear stress is included; however, the resulting bed change at $t = 60$ is qualitatively similar to that without bed shear stress, see Figure 6.12. Less erosion is predicted, and the bed step height is reduced with further onshore position.

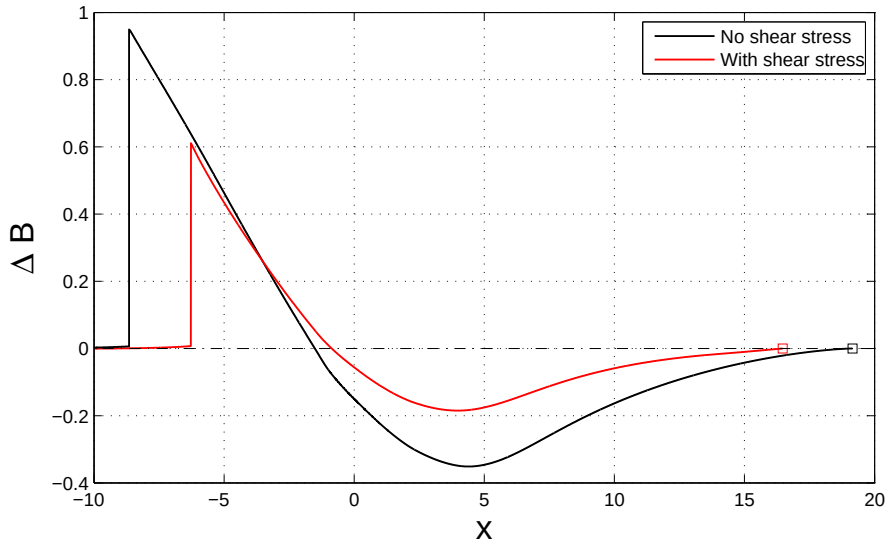

Figure 6.12: Beach changes for mobile bed solitary wave simulations without and with bed shear stress ($\sigma = 0.0654$).

6.3 Comparison of the bed step development in HP79 and solitary wave simulations

We show the final beach profiles and bed changes for the HP79 swash and a solitary wave when the shoreline catches up with the backwash bore, in Figure 6.13. It is shown that much more erosion occurs under a solitary wave. The bed step height in the solitary wave case is much larger and the position is further offshore. From the analysis in § 6.1.3, the bed step height largely depends on the water depth on the seaward side.

The water depth on the seaward side in the solitary wave case is much larger than that in the HP79 case and so is the bed step. The water depth is closely related to the swash events and also the position of the bed step. From Figure 6.6, it is seen that the relation between bed step heights for different bed mobilities

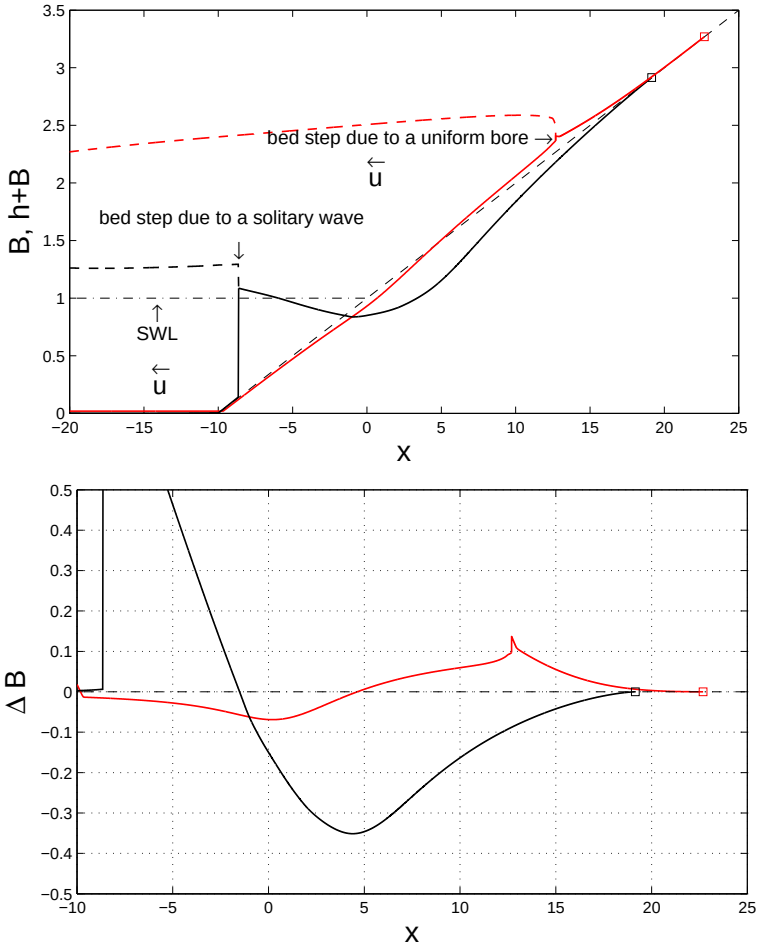

Figure 6.13: Beach profiles (top) and changes (bottom) under a solitary wave (black) at $t = 48.390$ and the HP79 swash (red) at $t = 59.614$.

and the bed step positions is not apparent, while Figure 6.10 and 6.12, the bed step heights in the solitary wave case are closely related to the position.

It should be noted that the water elevation on the seaward side of the bed step in the solitary wave case is very close to the mean water level, and the bed level is lower than the mean water level. The water depth on the seaward side of the step as well as the bed step height are thus closely related to the bed step position.In contrast, in the HP79 swash, the water and bed level at the bed step are higher than the mean water level, (see Figure 6.6). With a lower bed level than the mean water level at the seaward side of the bed step, it could result in a large water depth with a corresponding large bed step, as the water level is close to the mean water level. This explains the fact of the much larger bed step and the dependence of bed step height on the step position under a solitary wave.

However, from Appendix A, for $q = hu^3$, there is no bed step on the beach profile when the shoreline catches up with the backwash bore. This indicates great significance of sediment transport formula for the bed step development. Additionally, the present simulation does not consider downslope effect and suspended load. Furthermore, swash interactions, which are important for bed step, are not considered in the simulation. They might reduce the bed step height as there is not enough time for the backwash bore to develop, or the bed step may be flattened or disappear due to shock collision caused by swash interactions.

CHAPTER 7

Fully coupled combined load simulation for PW01 and HP79 swash events

In this chapter, the combined load model is used to simulate the PW01 and HP79 swash events. Firstly, the effects of suspended load on the swash flow and beachface evolution are identified by suspended-load-only simulations for the PW01 swash. Then, the HP79 swash event is simulated by the combined load model. The sediment entrainment and transport of suspended load as a uniform bore advances into still water and then climbs up over an erodible beach are illustrated. Different pre-suspended sediment concentrations are imposed to examine the role of pre-suspended load. Note that in the absence of field data, the values for σ, m_e and w_s are chosen for the purpose of comparison between bed- and suspended load, and that sediment motion thresholds $u_{crb} = 0$ and $u_{crs} = 0$ are assumed for simplification.

7.1 Physical interpretation

When $\sigma = 0$ in (2.70), we have $B_t = m_e(c - u^2)$. When m_e increases, if u and c are not greatly changed, the effect of entrainment ($m_e u^2$) and also settlement ($m_e c$) increases. The net change in B, i.e., $|B_t|$, increases as m_e increases. However, from (2.71), if w_s is fixed, c remains the same, which is because c is the scaled form of suspended sediment concentration in the water column. As there is more entrainment when m_e is increased, the non-scaled concentration $\widehat{c} = c_0 c = \frac{\widehat{m}_e}{\widehat{w}_s} c = \frac{m_e}{\xi w_s} c$ is proportional to m_e. This also explains the fact that with the same settling velocity w_s, the amount of settlement increases as m_e increases.

When m_e is fixed (the amount of entrainment remains unchanged), if w_s is increased, the sediment settles out more quickly, and from (2.71) c decreases also more quickly. Accordingly, the settlement is confined to a narrower region from the initial entrainment position. This shows that w_s controls not only the magnitude of erosion / deposition (because of different settlement although with the same entrainment) but also the position of erosion / deposition. This is very important for pre-suspended sediment. For instance, with a larger w_s, pre-suspended sediment is more likely to settle out in the lower swash. In the limit $w_s \to \infty$, the sediment entrained is deposited instantaneously, resulting the steady-state sediment transport in PH05, which could also be interpreted as bed load transport.

When bed load is included, from (2.70) and (2.71), the variations of B_t caused by suspended load and c against the change in m_e or w_s remain similar to those in the suspended-load-only simulations. Furthermore, if the inclusion of sus-

pended load has little effect on the velocity magnitude and also the velocity distribution, e.g., u_x, then the bed change caused by bed load in the combined load simulation remains similar to that in the equivalent bed-load-only simulation.

7.2 Suspended-load-only simulation for the PW01 swash

Suspended-load-only simulation can be achieved by setting the bed mobility parameter for bed load $\sigma = 0$ in the combined load model. The initial conditions are shown in Figure 5.1, and it is assumed that there is no pre-suspended sediment in the water column behind the dam.

The final bed changes of various m_e with $\sigma = 0$, $w_s = 0.001$ and $w_s = 0.03$ after one single PW01 swash event are shown in Figure 7.1. It is shown that suspended load results in net deposition in the upper swash near the maximum inundation and net erosion in the lower and middle swash, consistently with the equivalent uncoupled simulations by PH05. The bed changes of various m_e but the same w_s, have very similar patterns, and the erosion / deposition increases as m_e increases for both examined w_s values.

The final bed changes for various w_s with $m_e = 1 \times 10^{-4}$ after one single PW01 swash are shown in Figure 7.2. It is shown that the magnitude of erosion/ deposition decreases as w_s increases, and the position of the maximum deposition for a larger w_s is further offshore. It is consistent with the previous analysis that

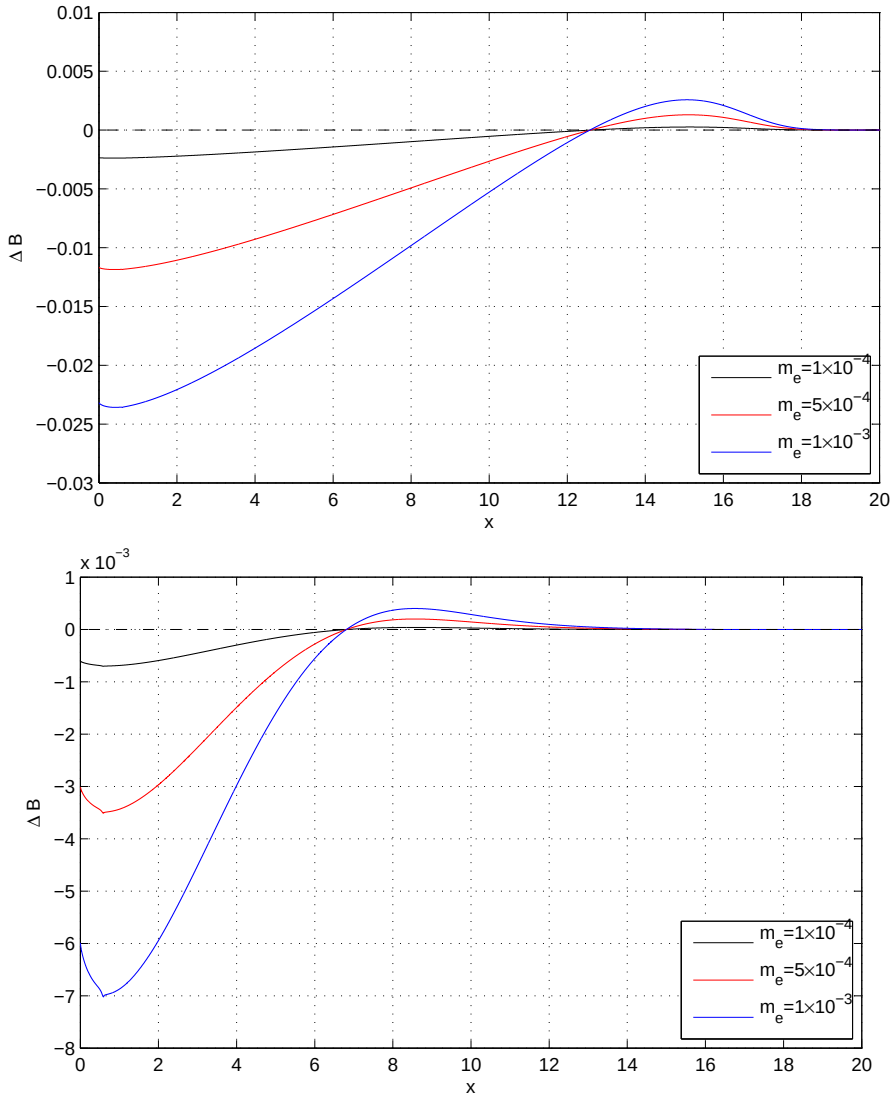

Figure 7.1: Bed changes for suspended-load-only simulations with various m_e values after a single PW01 swash. Top: $w_s = 0.001$ and bottom: $w_s = 0.03$.

w_s controls the amount of erosion / deposition and also sediment distribution. In order to investigate the effects of suspended load on the swash flow, we show the comparison of contours of h and u in the suspended-load-only simulation ($\sigma = 0$, $m_e = 0.001$ / 0.005 and $w_s = 0.001$) with the equivalent fixed bed case ($\sigma = 0$ and $m_e = 0$), i.e., PW01 solution, in Figure 7.3. It is shown that the flow

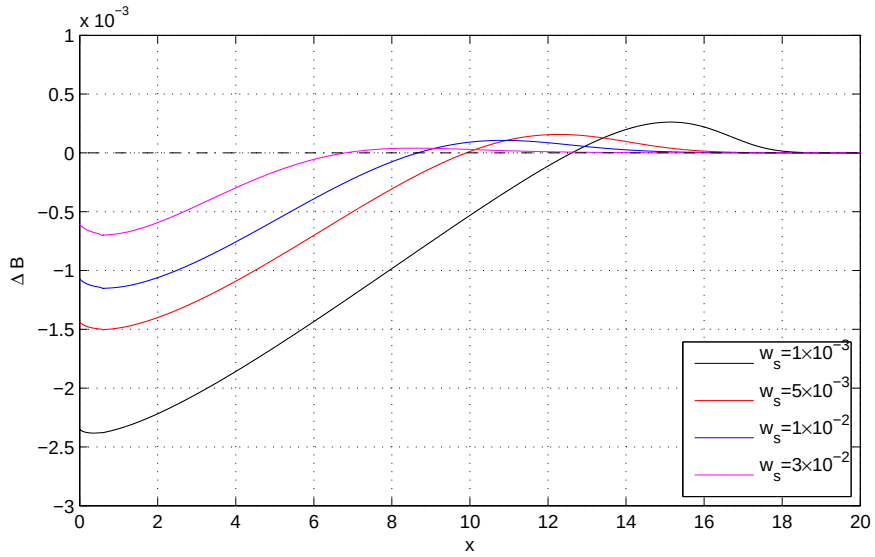

Figure 7.2: Bed changes for suspended-load-only simulations with various w_s values and $m_e = 1 \times 10^{-4}$ after a single PW01 swash.

structure of the suspended-load-only simulation with $m_e = 0.001$ is very close to the PW01 solution, although the bed profile is changed to a certain extent (the maximum net beach change ≈ 0.023). For $m_e = 0.005$, the flow is changed to a greater extent due to the larger bed change (the maximum net beach change ≈ 0.11); however, the maximum inundation is changed little from that in the PW01 solution. Note that although the final bed change is of considerable magnitude for $m_e = 0.005$, the swash flow is changed to a smaller extent than it is by bed load (KD10), see also § 5. The smaller effect of suspended load on the swash flow indicates the smaller importance of fully coupling for suspended-load-only simulation.

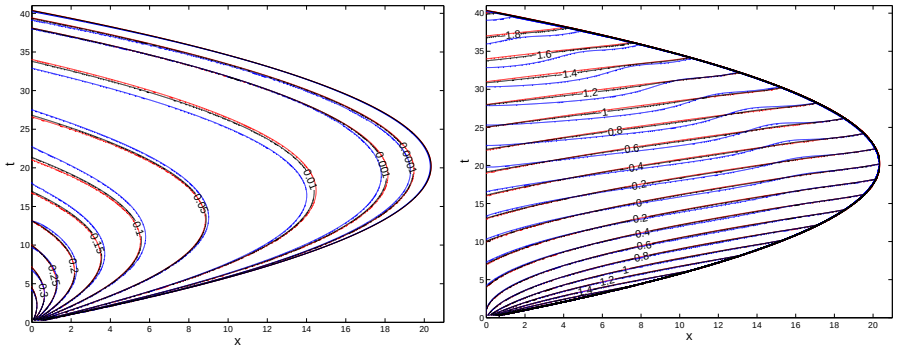

Figure 7.3: Comparison between suspended-load-only simulations and the PW01 solution under one single PW01 swash. (a):h; (b): u. Black: suspended-load-only ($m_e = 0.001$); blue: suspended-load-only ($m_e = 0.005$) and red: the PW01 solution.

7.3 HP79 swash simulation

7.3.1 Initial and boundary conditions

Initial conditions

The initial conditions are as shown in Figure 6.1. The initial shoreline position is at $x = 0$. There is a discontinuity in h, u and B at $x = -10$ at $t = 0$. The initial conditions for h, u and B we refer to § 6.2.1.

However, suspended sediment is included in this simulation, and there might be pre-suspended sediment in the water column. As the water on the right side is motionless, we assume that for $x \geq -10$ the initial suspended sediment concentration $c(x \geq -10, t = 0) = 0$. The water on the left side of the bore ($x < -10$) is of a finite velocity, and the initial pre-suspended sediment concentration is $c(x < -10, t = 0) = c_{in}$, where c_{in} is a finite value and could be 0. Due to

the linearly degenerate characteristic field associated with suspended sediment transport, there is no discontinuity in the suspended sediment concentration c at the incoming bore. As $u_L < W$ and $u_R > W$, therefore $c_L(t = 0) = c_R(t = 0) = 0$.

Boundary conditions

The seaward boundary is chosen so as to be far enough away from the shore that h, u, B and c at that point are uninfluenced by the wave reflected from the shore throughout the computation time; there is therefore a certain region of constant h, u, B and c. The seaward boundary is chosen at $x = -100$, and h and u are assumed to be unchanged with $h(x = -100, t) = h(x = -100, t = 0)$ and $u(x = -100, t) = u(x = -100, t = 0)$ during the simulation time. However, B and c could vary with time, depending on the pre-suspended sediment concentration c_{in} and the equilibrium concentration c_{eq}. When $c_{in} > c_{eq}$, the pre-suspended sediment will settle down and c will decrease with time to c_{eq} and B will consequently increase; while when $c_{in} < c_{eq}$, sediment will be entrained off the bed and into suspension and therefore B will decrease and c will increase. In the combined load simulations, it is assumed that $c_{in} = c_{eq}$ unless specified. The variables at the seaward boundary are obtained by solving the Riemann equations, see § 4.4.1.

The landward boundary is a wet-dry boundary and the solution we refer to § 4.4.2.

7.3.2 Flow structure

The flow structure for a uniform bore climbing over an erodible beach simulated by the combined load model with $\sigma = 0.01$, $m_e = 0.001$ and $w_s = 0.01$ is shown in Figure 7.4.

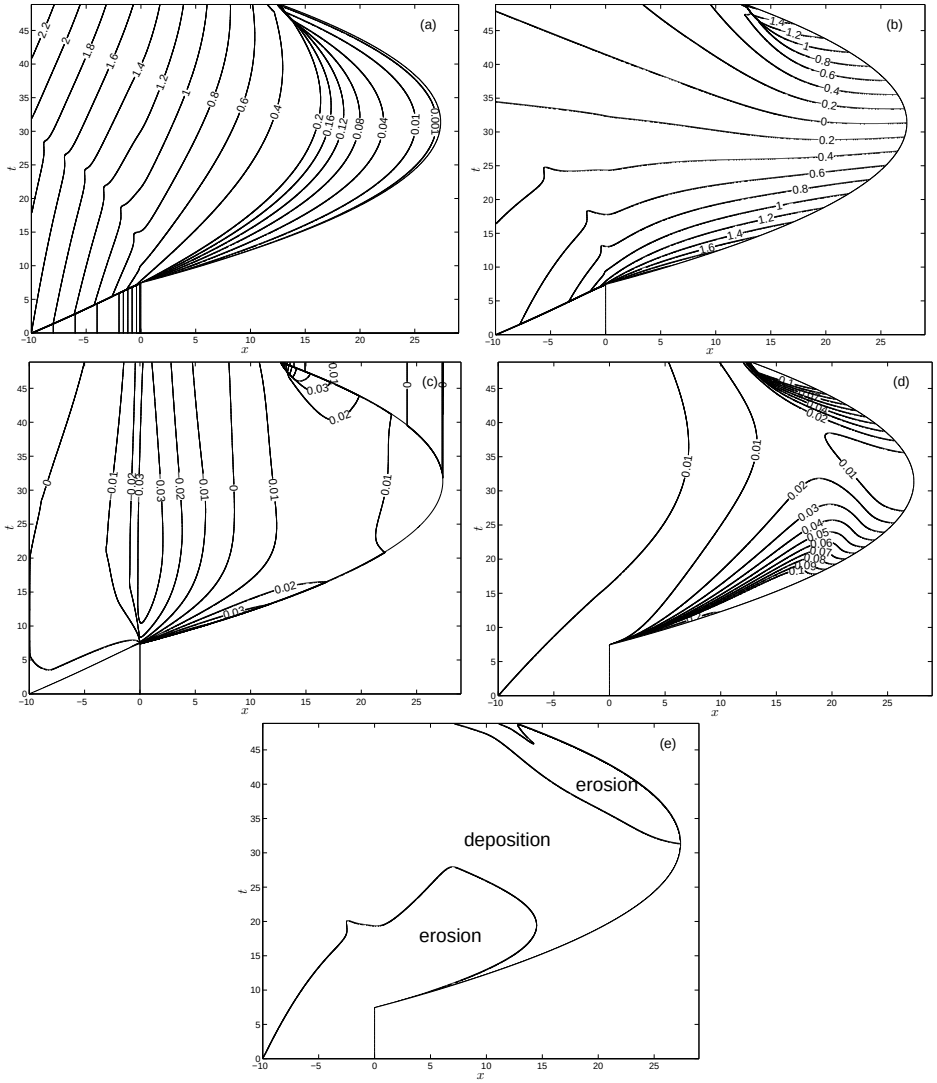

Figure 7.4: Contour plots for the combined load HP79 simulation with $\sigma = 0.01$, $m_e = 0.001$ and $w_s = 0.01$. (a): h; (b): u; (c): ΔB; (d): non-scaled concentration $\widehat{c}$ and (e): instantaneous deposition / erosion distribution due to suspended load.

When the bore advances into still water, the velocity of the water behind the bore is smaller than the speed of the bore. As the pre-suspended load is transported along the flow, there is therefore a region immediately behind the bore, in which the suspended sediment is from the local entrainment and that pre-suspended in the water in front of the bore. Due to the zero concentration of suspended sediment in the still water in front of the bore, the concentration of suspended sediment immediately behind the bore $\widehat{c}$ is relatively low ($< 0.01\,\mathrm{m}^3/\mathrm{m}^3$) even though the water is of a high velocity; the concentration is rapidly raised when the water depth approaches 0, see Figure 7.4. Note that the initial concentration behind the bore is $c_{in} = c_{eq} = 0.293 \Rightarrow \widehat{c}_{in} = 0.0176\,\mathrm{m}^3/\mathrm{m}^3$. However, the pre-suspended sediment gradually moves shorewards during the uprush.

The bore then collapses at the initial shoreline position, and when the bore collapses, the water velocity reaches its maximum. It therefore causes considerable sediment entrainment into the water column which is then moved onshore, and there is consequently erosion caused near the initial shoreline position, see Figure 7.4(c).

The flow begins to decelerate when the flow climbs up the dry beach. In the uprush, sediment is moved shorewards as bed load and also suspended load. It should be noted that a sediment bore, which is associated with bed load, still forms at the shoreline in the combined load simulation. From Figure 7.4(e), it is seen that sediment in the lower swash is entrained into the water column when the concentration is lower than the equilibrium one in the early uprush,

and transported to the upper swash along the flow. In the late stage of the uprush, the suspended sediment concentration becomes larger than the equilibrium one in the upper swash, and the suspended sediment begins to settle down. The region of sediment settlement extends to the lower swash at the end of the uprush. Note that the sediment concentration at the shoreline is always equal to the equilibrium concentration $c_{eq} = u_s^2$, and at the maximum inundation is 0. The concentration gradually decreases in the uprush due to the decelerating flow.

During the backwash, the suspended sediment concentration in the upper swash is lower than the equilibrium one because sediment has settled out, and sediment is entrained into water column and moved seawards. Instantaneous erosion is caused by suspended load in the upper swash during the backwash, see Figure 7.4(e). In contrast, in the lower and middle swash, sediment is deposited onto the bed.

The combined bed change caused by bed- and suspended load near the maximum inundation is net erosion but values are extremely small, see Figure 7.4(c). Deposition is predicted in the region $7.5 \lessapprox x \lessapprox 24$ (Figure 7.4(c)). It should be noted that in the equivalent bed-load-only simulation there is also erosion near the maximum inundation.

From Figure 7.4(b), it is seen that the backwash flow is rapid, and there is also incoming water, resulting in a backwash bore, which is also observed in the equivalent hydrodynamic and bed-load-only simulations. A bed step forms associated with bed load. There is more erosion on the right side of the bore

than that on the left side caused by suspended load due to the larger velocity on the right side. Suspended sediment is moved from the right side of the backwash bore to the left side, and settles on the left side.

7.3.3 Final beach change caused by combined load

The final beach change and also changes caused by bed load and suspended load when the receding shoreline catches up with the backwash bore in the swash event with $\sigma = 0.01$, $w_s = 0.01$ and $m_e = 0.001$ are shown in Figure 7.5. It is found that bed load causes deposition in the middle swash and erosion in the lower and upper swash. However, the values of erosion in the upper swash are extremely small. In contrast to bed load, suspended load causes deposition in the upper swash and erosion in the lower swash. Note that the overall magnitude of beach change caused by suspended load is smaller than that caused by bed load, thus the bed change pattern caused by combined (bed and suspended) load with these parameters is similar to that caused by bed load. It should be noted that net erosion, though with a extremely small value, predominates under the combined effect of both loads near the maximum inundation, see also Figure 7.4(c).

It is shown that the overall beach change caused by bed load is larger than that caused by suspended load in Figure 7.5. However, bed load does not always dominate, and field measurements have shown that suspended load could be the dominant form of sediment transport in the swash zone (Jackson et al., 2004; Masselink et al., 2005; Blenkinsopp et al., 2011; Pritchard and Hogg,

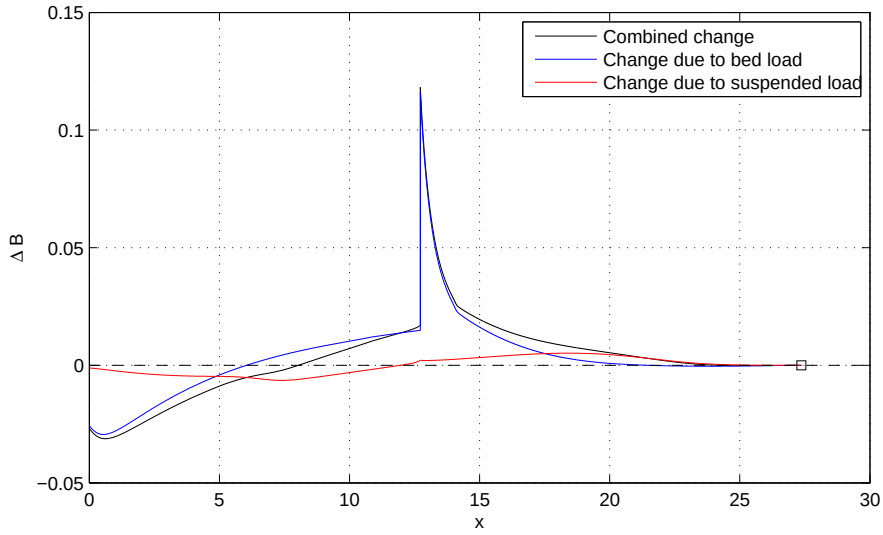

Figure 7.5: Bed changes for combined load simulation with $\sigma = 0.01$, $m_e = 0.001$ and $w_s = 0.01$.

2005). Therefore we reduce σ to 0.001, and the corresponding beach changes are shown in Figure 7.6. The bed change profile caused by combined load is greatly changed from that caused by bed load, with much more deposition in the upper swash and erosion in the lower swash. However, the bed change near the bed step is still very close to that caused by bed load, which implies the great dependence of the beach change around shocks on that caused by bed load.

7.3.4 Final bed changes caused by suspended load for various m_e / w_s in combined load simulations

The bed changes caused by suspended load in the combined load simulations with various m_e values ($\sigma = 0.01$ and $w_s = 0.01$) are shown in Figure 7.7. The bed change patterns caused by suspended load are very similar; more deposi-

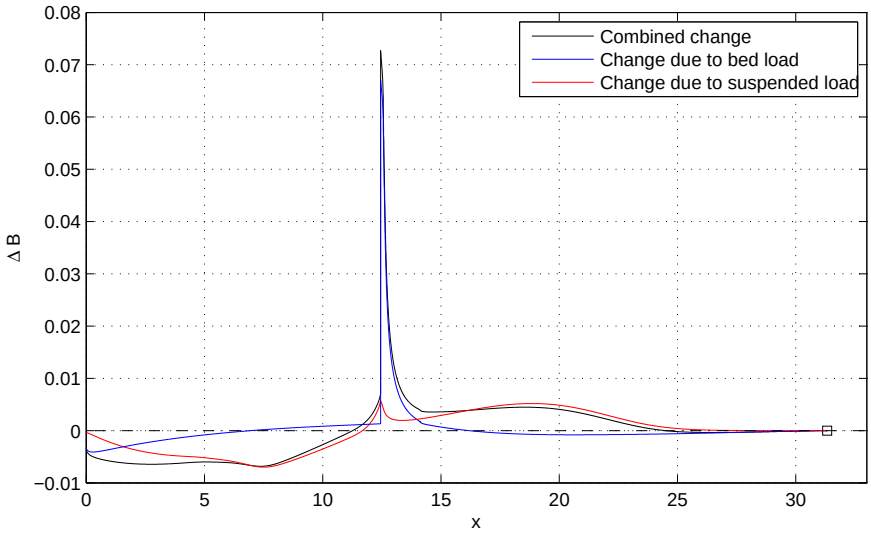

Figure 7.6: Bed changes for combined load simulations with $\sigma = 0.001$, $m_e = 0.001$ and $w_s = 0.01$.

tion in the upper swash and erosion in the lower swash is found when m_e is increased, consistent with the suspended-load-only PW01 simulations in § 7.2. However, if a different pre-suspended sediment concentration c_{in} is imposed, the pattern of bed change caused by suspended load could be altered.

The bed changes caused by suspended load in the combined load simulations with various w_s values ($\sigma = 0.01$ and $m_e = 0.001$) are shown in Figure 7.8. The bed change patterns are very different, with more erosion for a smaller w_s value in the lower and middle swash. More sediment is deposited in the upper swash for a smaller w_s.

7.3.5 Bed step development

From (2.88), it is shown that the bed difference of the bed levels on the two sides of a shock is not directly determined by suspended load. However, suspended

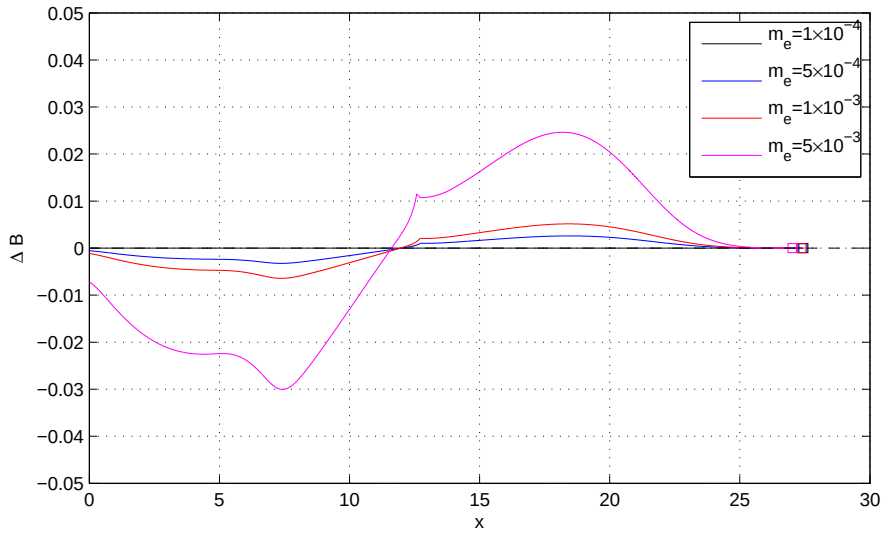

Figure 7.7: Bed changes caused by suspended load in the combined load HP79 simulations with various m_e values ($\sigma = 0.01$ and $w_s = 0.01$).

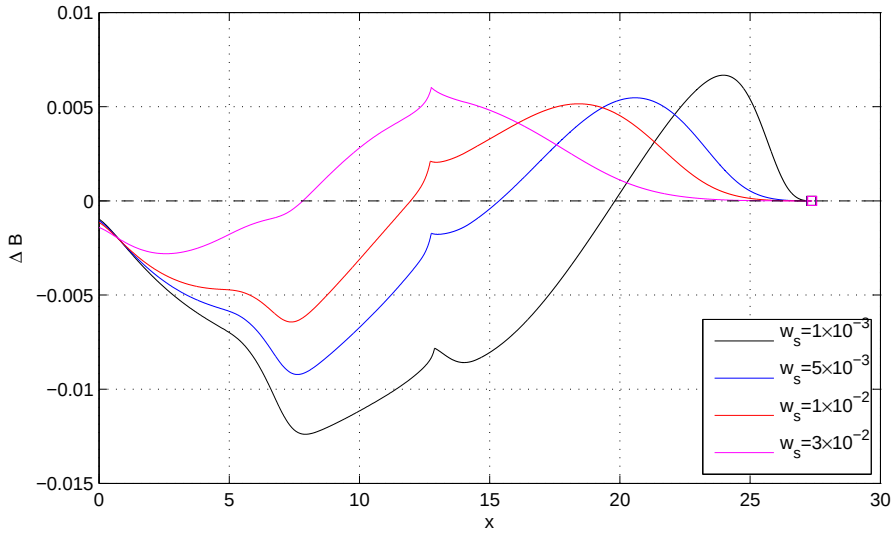

Figure 7.8: Bed changes caused by suspended load in the combined load HP79 simulations with various w_s values ($\sigma = 0.01$ and $m_e = 0.001$).

load can affect the bed step height by modifying the hydrodynamics, e.g., the velocities on the two sides of the bore. The bed difference in the combined load simulation with $\sigma = 0.01$, $m_e = 0.001$ and $w_s = 0.01$ and that in the equivalent bed-load-only simulation are shown in Figure 7.9. The development of the bed step is slightly altered when suspended load is included; however, the overall patterns are generally similar, which suggests that the bed step is affected little by suspended load due to little changed hydrodynamics.

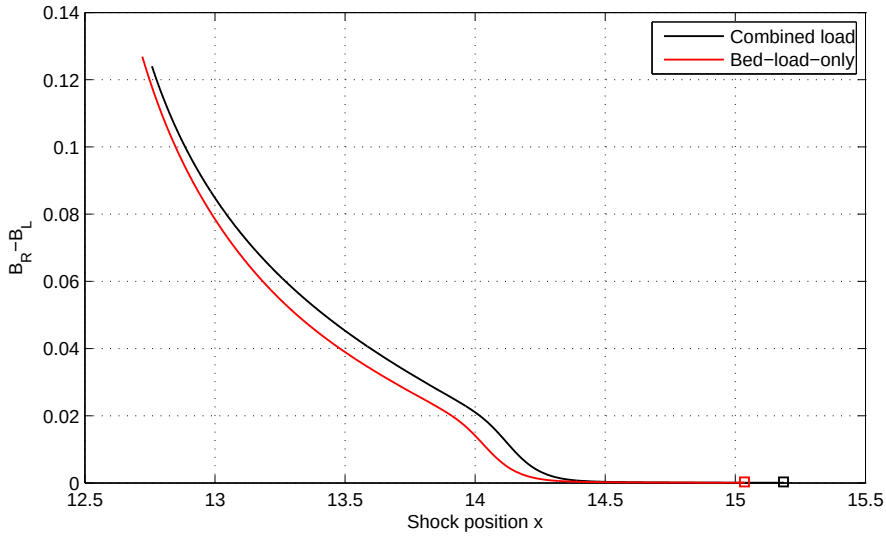

Figure 7.9: Bed step height as a function of shock position in the combined load and equivalent bed-load-only simulations for the HP79 swash ($\sigma = 0.01$, $m_e = 0.001$ and $w_s = 0.01$). □ indicates point of shock inception.

7.3.6 Effects of pre-suspended sediment

The bed changes in the combined load HP79 swash simulations with $\sigma = 0.01$, $m_e = 0.001$ and $w_s = 0.01$ but different initial pre-suspended concentrations c_{in} are shown in Figure 7.10. Note that $c_{eq} = 0.293$ in all simulations with $\sigma = 0.01$.

It is shown that the bed changes in the region $x \lessapprox 7.5$ are closely related to c_{in}, and the larger c_{in} the more relative deposition in the region. However, the bed changes in the upper swash with different c_{in} values are very close. The region in which the bed change varies with c_{in} is that into which the pre-suspended sediment can be advected.

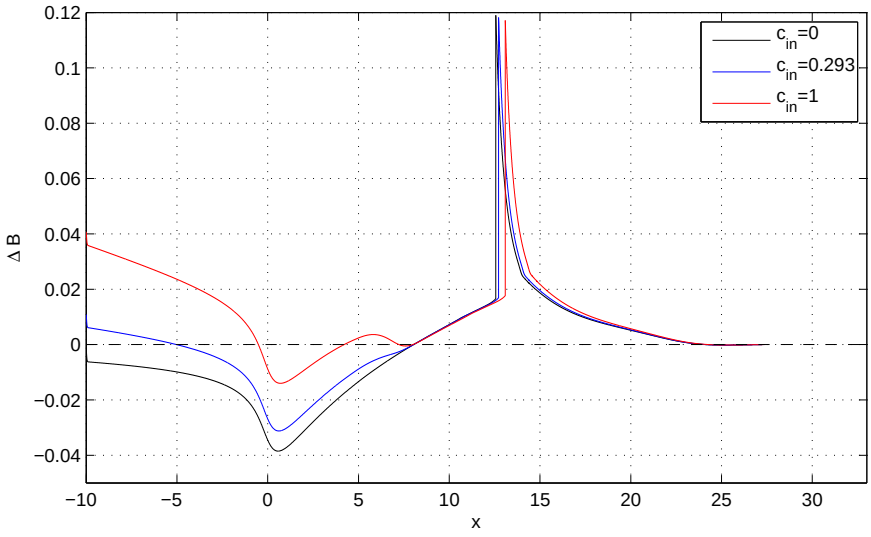

Figure 7.10: Bed changes in the combined load HP79 simulations ($\sigma = 0.01$, $m_e = 0.001$ and $w_s = 0.01$) with different pre-suspended sediment concentrations (c_{in}).

The results of suspended-load-only PW01 simulations and combined load HP79 ones show that suspended load causes deposition in the upper swash and erosion in the lower swash. However, whether suspended load causes erosion or deposition in the lower swash also depends on the concentration of pre-suspended sediment (c_{in}). For instance, deposition may occur in the lower swash if a large c_{in} is imposed. The bed changes caused by suspended load with different c_{in} values are therefore shown in Figure 7.11. It is clearly seen

that when the pre-suspended sediment is of a high concentration, e.g., $c_{in} = 1$, the bed change caused by suspended load in the lower swash is deposition instead of erosion as shown in Figure 7.11. However, net erosion still occurs in a certain region in the middle swash even with a large c_{in} value.

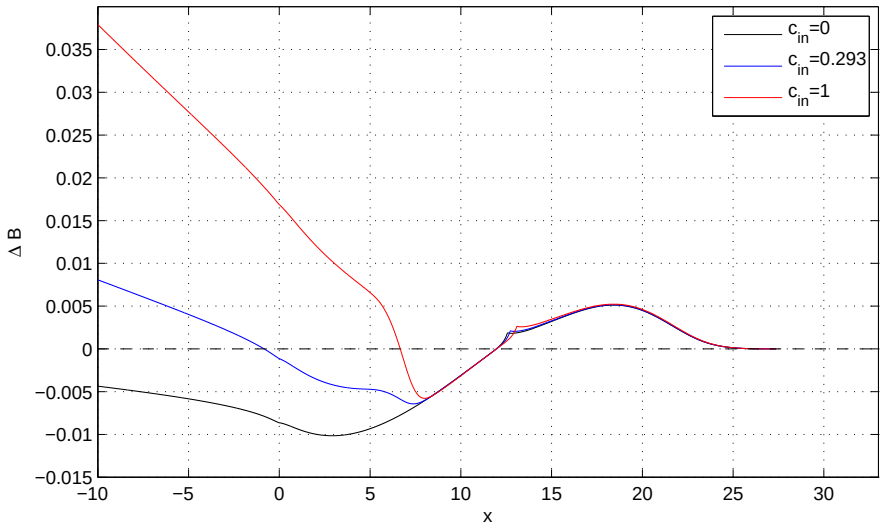

Figure 7.11: Bed changes caused by suspended load in the combined load HP79 simulations ($\sigma = 0.01$, $m_e = 0.001$ and $w_s = 0.01$) with different pre-suspended sediment concentrations (c_{in}).

CHAPTER 8

Conclusions and recommendations

8.1 Review and conclusions

The present work has focused on simulating and understanding the flow and beachface evolution in the swash zone during one single swash event using fully coupled simulations. The fully coupled models are formulated by coupling the 1D NSWEs with a bed evolution (sediment conservation) equation. The beachface evolution is caused by the sediment transport in the form of bed- and suspended load, and therefore the fully coupled models developed include a bed-load-only model and a combined load model.

The beachface evolution during a single PW01 swash is examined by the fully coupled bed-load-only model with a series of sediment transport formulae. The results are consistent with PH05 in that bed-load-only simulation under the PW01 swash yields net erosion over the whole swash zone[1]. Consistent with

[1]The suspended sediment flux in the steady state in PH05 is essentially a total load or bed load description.

KD10, however, full coupling yields significantly less erosion for all the examined $q = q(u)$ formulae compared to the equivalent uncoupled ones. This is primarily because the smaller initial swash tip velocity (for sediment transport formulae $q = q(u)$) results in a smaller swash period and therefore a less exaggerated velocity asymmetry. Inclusion of a threshold of movement or differing powers of u makes little difference to this. However, inclusion of water depth in the expression for sediment transport, thought to be appropriate in very small water depths, leads to correspondingly small sediment transport and therefore also to small beach change in the upper swash. Because for $q = q(h, u)$ the water depth is now a controlling factor, and the PW01 swash asymmetry in h yields larger depths in the uprush, the resulting net bed change in the upper swash depends on two competing factors, h and u asymmetry in the PW01 event (both of which are diminished in importance in the upper swash). The result is little net change in the upper swash. Further, if we examine this h dependence by taking $q \propto h^n$ for $n > 1$, the result is net deposition in this region. The shoreline motion in the simulations with formula $q \propto h^n$ ($n > 0$) over a plane mobile beach is ballistic in the uprush.

The equivalent simulations with bed shear stress, which becomes more effective in the flow with shallow depth, can yield qualitatively different net bed change. Bed shear stress greatly reduces the velocity, especially that in the backwash, resulting generally in less sediment transport and particularly less offshore sediment transport. Although the net sediment flux at $x = 0$ is still offshore, the beach change profile inside the swash zone is considerably changed for both

formulae $q = u^3$ and $q = hu^3$. Deposition occurs for $q = hu^3$ for all tested non-zero C_D values in the upper swash, and deposition occurs for $q = u^3$ in the middle swash only when a relative large C_D value is imposed. The implication is that bed shear stress must be included not just to obtain correct quantitative beach change, but also to obtain correct qualitative beach behaviour.

The HP79 uniform bore is examined on a mobile bed by the bed-load-only simulation with $q = u^3$. In contrast to the net erosion over the whole swash under the PW01 swash event, considerable deposition occurs in the swash zone under the HP79 swash, due to the different swash hydrodynamics. Similarly to the fixed bed simulation of HP79, a backwash bore is formed, which is, however, less pronounced and forms later in the backwash. However, on an erodible beach the backwash bore is associated with the formation of a beach step (or swash bar). The process during which the shoreline catches up with the backwash bore is essentially a shock-shock collision problem. Right before the collision, it is shown that the bed difference associated with the backwash bore, is equal to the water depth on the seaward side of the backwash bore. As the sediment bore at the shoreline strips away sediment, the bed step height is lower than the water depth on the seaward side after the collision. The wave structure after the collision is obtained by the Riemann solution for wet-dry dam-break problems with a bed step in § 3.

A bed step also forms under the swash event driven by a solitary wave. The bed step heights for different bed mobilities are much larger than those in the HP79 simulation. When bed shear stress is included in the solitary wave sim-

ulation, the bed step height is reduced but is still of considerable magnitude. The results show that the bed step height depends largely on the position of the step. This is because the bed step height is closely related to the water depth on the left side, and the water depth depends on the swash event and the position of the step, and therefore swash period and ensuing event. This also explains the much larger bed step height under a solitary wave than that in the HP79 swash simulation. Note that the bed step development is closely related to the sediment transport formula q. It is shown that if q is dependent on h, there is no bed step in the bed profile when the shoreline catches up with the backwash bore. Furthermore, the downslope effect and swash interactions, which might have great effect on the bed step development, are not considered in the simulation.

Finally, the fully coupled combined load model, which includes bed- and suspended load, is used to simulate the PW01 and HP79 swash events. The combined load PW01 simulations show that suspended load results in deposition in the upper swash and erosion in the lower swash. The sediment entrainment parameter m_e controls the amount of erosion / deposition, and the settling velocity of suspended sediment w_s controls the amount and distribution of erosion / deposition. The combined load HP79 simulation confirms that inclusion of suspended load results in deposition in the upper swash near the maximum inundation and erosion in the lower swash. However, a large pre-suspended sediment concentration may result in deposition instead of erosion in the lower swash. It is shown that suspended load has much less effect on the maximum

inundation and swash hydrodynamics than bed load. Furthermore, bed load results in the formation of a bed step, and bed load dominates the beach change near the bed step even when suspended load is dominant in the overall beach change.

8.2 Recommendations

The combined load model in the present work, although it considers bed- and suspended load, is still limited and idealised in the assumption of shallow water and the exclusion of some physical factors, such as infiltration / exfiltration and bed shear stress. Furthermore, the numerical code is designed for swash flows with no more than two shocks and no shock interactions. Thus there remains considerable work to be done for better understanding and simulating of swash zone morphodynamics.

Firstly, the Riemann wave structure regarding the parallel rarefaction shock for the wet-dry dam-break problem over a discontinuous mobile bed in § 3.4 is not obtained by the numerical solution. This could be because that the hypothesis of the parallel rarefaction shock is not correct, or that the numerical method used to solve the governing equations for the shock cannot find all the possible solutions for the system. In the latter case, an appropriate numerical method is required. More testing should be carried out to obtain the correct Rieamnn solution for such dam-break problems.

Secondly, the sediment transport formula for bed load has a great effect on the beach face evolution including the bed step development. The water veloc-

ity (and depth) power-law-based formulae have deficiencies (see also Kelly, 2009), and may account for problems in the simulation for beachface evolution. The $q(u)$ formula could overestimate the sediment transport near the shoreline where depths are small. The depth and velocity power-law-based formulae $q(h, u)$ are limited to only small water depths for which the sediment mobility is restricted by depth. Therefore, a new formula which describes the transport of bed load by $q(u)$ in the region of relatively deep water, and $q(h, u)$ in the very shallow region is desirable.

Thirdly, bed shear stress is important for swash flow especially for the flow near the shoreline, since bed shear stress becomes significant near the shoreline due to the very shallow water depth. Inclusion of bed shear stress therefore also reduces the amount of sediment transport. Bed shear stress, simply described by the Chezy approach, has been introduced in the fully coupled bed-load-only model in an attempt to examine the effects of bed shear stress on the swash flow and beachface evolution. The great effect of bed shear stress on swash simulation with $q = hu^3$, which can be interpreted as the flux of suspended load in equilibrium state, indicates possibly also a great effect on simulations with unsteady suspended sediment transport, e.g., combined load simulations in the swash zone. Therefore, the inclusion of bed shear stress in the combined load system is a logical next step. The boundary layer approach (Barnes et al., 2009; Briganti et al., 2011), which is more realistic, could be introduced to calculate bed shear stress more accurately; it would be interesting to see how the results of simulations with bed shear stress by the boundary layer approach differ from

those including the Chezy law.

Additionally, no downslope effect is considered, therefore the bed step associated with the backwash bore is vertical. Swash interactions, which are important for the bed step development, are also not simulated. Swash interactions might reduce the bed step height as there is not enough time for the backwash bore to develop, or the bed step may be flattened or disappear due to shock collision. It would be very interesting to see the bed step development when the two physical processes are included.

Lastly, the numerical scheme of STI MOC can resolve shocks very accurately; however, when there are several shocks in the computed area at the same time, the simulation becomes very complicated. Comparison with a state-of-art finite volume code (Zhu et al., 2012), indicates very close agreement everywhere except near shocks, indicating that the characteristics method approach is highly beneficial in this regard. Moreover, when shocks interact with each other, e.g., shock collision, the present numerical code cannot automatically proceed. Thus more flexible and powerful numerical solvers would enable the models to simulate more than one swash cycle, and also be more applicable for swash simulation.

APPENDIX A

Shock relation when one side of the shock is a dry bed for both bed-load-only and combined load systems

One special case occurs when one side of the shock is a dry bed. In order to utilise the shock conditions, we here consider a limit case of $h_R \to 0$ to look at the shock with a dry bed, but for simplicity, we write it as $h_R = 0$ hereafter in this section. This kind of shock, in which $h_R = 0$, can be further subdivided into two cases: $u_R = 0$ and $u_R \neq 0$ (a finite value).

i) Shock with $h_R = 0$ and $u_R = 0$

A shock with $h_R = 0$ and $u_R = 0$ is usually the shock at the tip / shoreline.

From (2.56), we have

$$h_L(u_L - W) = 0 \tag{A.1}$$

Thus, $h_L = 0$ and / or $W = u_L$.

- a) $W = u_L$, $h_L \neq 0$

  From (2.57),

$$\begin{aligned} & Wu_Lh_L - h_Lu_L^2 - \frac{h_L^2}{2} - \frac{1}{2}(B_L - B_R)h_L &= 0 \\ \Rightarrow \quad & h_Lu_L^2 - h_Lu_L^2 - \frac{h_L^2}{2} - \frac{1}{2}(B_L - B_R)h_L &= 0 \\ \Rightarrow \quad & h_L\left(-\frac{h_L}{2} - \frac{1}{2}(B_L - B_R)\right) &= 0 \end{aligned} \tag{A.2}$$

  As $h_L \neq 0$ by assumption,

$$h_L = -B_L + B_R \Rightarrow B_L - B_R = -h_L < 0 \tag{A.3}$$

  From (2.58), for $q = h^n|u|^{m-1}u$ ($n \geq 0$ and $m > 1$) we have:

$$\begin{aligned} & (B_L - B_R)W - \sigma h_L^n|u_L|^{m-1}u_L + \sigma h_R^n|u_R|^{m-1}u_R = 0 \\ & \Rightarrow B_L - B_R = \frac{\sigma h_L^n|u_L|^{m-1}u_L}{W} = \sigma h_L^n|u_L|^{m-1} \geq 0 \end{aligned} \tag{A.4}$$

  which contradicts (A.3). Therefore $W = u_L, h_L \neq 0$ is not a solution to this shock

- b) $h_L = 0$

  When $h_L = 0$, (2.56) and (2.57) are satisfied. The wave solution for a wet-dry dam-break problem with $q = u^3$ over a mobile bed presented by Kelly and Dodd (2009) shows that at the wave tip ($h = 0$),

a λ_3 sediment bore forms, and the water depth on the left side of the sediment bore $h_L = 0$. It was also pointed out by Kelly and Dodd (2009) that at the wave tip λ_3 is identically u, the sediment bore is moving along the λ_3 characteristic and the speed is identical to the particle velocity. Additionally, evidence from the Riemann wave solution for a wet-wet dam-break problem over a mobile bed in §3.5 with $q = u^3$ also shows that when one side of the dam is nearly dry bed, i.e., $h_R \to 0$, for the shock adjacent to the dry bed $h_L \to 0$ and $W \to u_L$. Furthermore, the work of Dodd et al. (2008), which uses the same set of equations solved via a Riemann-type scheme, also suggests that the water depth at the wave tip tends to 0. By analogy, $h_L = 0$ and $W = u_L$ is the solution for the shock with $q = h^n|u|^{m-1}u$ ($n \geq 0$ and $m > 1$), the right side of which is dry bed, i.e., $h_R = 0$ and $u_R = 0$.

From (A.4),

$$B_L = B_R + \frac{\sigma h_L^n |u_L|^{m-1} u_L}{W} = B_R + \sigma h_L^n |u_L|^{m-1}. \tag{A.5}$$

Note that when $n = 0$, from (A.5) $B_L - B_R > 0$ if $u_L \neq 0$, and we could say that there is a sediment bore at the tip. However, when $n > 0$, $B_L = B_R$, e.g., $q = hu^3$, and the bed level at the shoreline is continuous and there is no sediment bore at the tip.

ii) Shock with $h_R = 0$ and $u_R \neq 0$

From (2.56), we also have $h_L = 0$ or $u_L = W$. We discuss these two solutions below.

- a) $W = u_L$ and $h_L \neq 0$

  From (2.57), $B_L - B_R = -h_L < 0$ is obtained. From (2.58),

$$\begin{aligned} B_L - B_R &= \frac{\sigma h_L^n |u_L|^{m-1} u_L - \sigma h_R^n |u_R|^{m-1} u_R}{W} \\ &= \frac{\sigma h_L^n |u_L|^{m-1} u_L - \sigma h_R^n |u_R|^{m-1} u_R}{u_L} \end{aligned} \tag{A.6}$$

  When $n = 0$, as $u_R \neq 0$, it is possible for $B_L - B_R = \sigma(|u_L|^{m-1}u_L - |u_R|^{m-1}u_R)/u_L < 0$, and it depends on the shock itself. Therefore, $W = u_L, h_L \neq 0$ could be a solution to this shock with $q = |u|^{m-1}u$ ($m > 1$).

  However, when $n > 0$, $B_L - B_R = \sigma h_L^n |u_L|^{m-1} \geq 0$, which is inconsistent with $B_L - B_R = -h_L < 0$. Therefore $W = u_L$ and $h_L \neq 0$ is not a solution to this shock with $q = h^n|u|^{m-1}u$ ($n > 0$ and $m > 1$).

- b) $h_L = 0$

  When $h_L = 0$, (2.56) and (2.57) are satisfied. From (2.58),

$$B_L = B_R + \frac{\sigma h_L^n |u_L|^{m-1} u_L - \sigma h_R^n |u_R|^{m-1} u_R}{W} \tag{A.7}$$

  Therefore $h_L = 0$ is also a possible solution of this shock with a bed load transport formula $q = h^n|u|^{m-1}u$ ($n > 0$ and $m > 1$).

Which solution, solution a) or solution b), is the physical solution to the shock with $h_R = 0$ and $u_R \neq 0$, depends on the conditions of the specific shock.

Here the backwash bore in the HP79 simulation in § 6, in which $q = u^3$, is investigated to illustrate how to determine which solution is physical.

For the backwash bore, $u_R < u_L < 0$, $W < 0$ and $B_L - B_R < 0$. From (2.57),

$$(W - u_R)h_R u_R - (W - u_L)h_L u_L - \frac{1}{2}(h_R + B_R - h_L - B_L)(h_L + h_R) = 0 \tag{A.8}$$

From (2.56), $(W - u_R)h_R = (W - u_L)h_L = -m_s$, therefore (A.8) becomes:

$$-m_s(u_R - u_L) = \frac{1}{2}(h_R + B_R - h_L - B_L)(h_L + h_R) \tag{A.9}$$

For the backwash bore in § 6, $m_s \leq 0$ and $u_R - u_L < 0$, therefore it requires $(h_R + B_R - h_L - B_L)(h_L + h_R) \leq 0$. Note that the equal sign is only valid in the limit of $m_s = 0$, i.e., $h_R = 0$, which determines that $h_R + B_R < h_L + B_L$, essentially $h_L > h_R + B_R - B_L > 0$, when $m_s \to 0$. Therefore, in the limit $m_s = 0$, $h_L = h_R + B_R - B_L = B_R - B_L$ and $h_L + h_R > 0$. To conclude, solution a) is the physical solution to the backwash bore in the HP79 simulation in the present work.

We here also investigate the solution to the backwash bore when $u_R < u_L < 0$, $W < 0$ if $q = hu^3$ is used to describe the sediment transport in the simulation. From (A.9), we also have $h_R + B_R \leq h_L + B_L \Rightarrow h_L \geq B_R - B_L = 0$ during the backwash. Therefore, in the limit $m_s = 0 \Rightarrow h_L = 0$. Therefore the solution to the backwash bore, in which $u_R < u_L < 0$ and $W < 0$, with $q = hu^3$ is $h_L = 0$. Note that for $q = hu^3$, no bed step forms when the shoreline catches up with the backwash bore.

APPENDIX B

Riemann equations at $u = 0$ or $h = 0$ for formulae $q = h^n|u|^{m-1}u$ ($n \geq 0$ and $m > 1$)

A generalised sediment transport formula for bed load:

$$q = h^n|u|^{m-1}u\,, \quad \text{for } n \geq 0 \text{ and } m > 1, \tag{B.1}$$

is assumed to examine the Riemann equation (2.45) when $u = 0$ or $h = 0$.

B.1 Riemann equation (2.45) at $u = 0$

When $u = 0$, $\lambda_3 = 0$ and $\lambda_{1,2} \neq 0$. As $u \to 0$, $\lambda_3 - u \to 0$, and $\dfrac{\lambda_3 + \sigma q_h}{\lambda_3 - u}$ in (2.45) might $\to \infty$. Here we investigate the term $\dfrac{\lambda_3 + \sigma q_h}{\lambda_3 - u}$ as $u \to 0$.

For the formula $q = h^n|u|^{m-1}u$, we have $q_h = nh^{n-1}|u|^{m-1}u$ and $q_u = mh^n|u|^{m-1}$.

From equation (2.30), we have

$$\frac{\sigma(uq_u - hq_h)}{\lambda_3} = -(\lambda_3^3 - 2u\lambda_3^2 + (u^2 - \sigma q_u - h))$$
$$\frac{\sigma(m-n)h^n|u|^{m-1}u}{\lambda_3} = -(\lambda_3^3 - 2u\lambda_3^2 + (u^2 - \sigma m h^n|u|^{m-1} - h)). \tag{B.2}$$

In the limit $u \to 0$, from (B.2), we have $\frac{\sigma(m-n)h^n|u|^{m-1}u}{\lambda_3} \to h \Rightarrow \frac{\lambda_3}{u} \to \sigma(m-n)h^{n-1}|u|^{m-1}$. Note that $m = n$ is very special case as $q \propto$ water discharge, and is not considered in this section. Also that $h \neq 0$ is assumed and the case $h = 0$ will be analysed in Appendix B.2. As $m > 1$, therefore $\frac{\lambda_3}{u} \to 0$, and

$$\frac{\lambda_3 + \sigma q_h}{\lambda_3 - u} = \frac{\lambda_3/u + \sigma q_h/u}{\lambda_3/u - 1} \to 0 \tag{B.3}$$

Thus, when $u = 0$, the Riemann equation (2.45) along the $\lambda_3 = 0$ characteristic becomes $\frac{dB}{dt} = 0$, which essentially indicates that the bed level does not change when the water is motionless.

B.2 Analytical shoreline motion for $q = h^n|u|^{m-1}u$ ($n > 0$ and $m > 1$)

It is well known that the shoreline motion of the PW01 swash event is ballistic, i.e. it is dependent only on the initial velocity imparted at the point of bore collapse and the beach slope. The work of KD10 indicates that shoreline motion in the uprush with $q = u^3$ is close to ballistic, but with a reduced restoring force, due to the bed mobility which leads to a sediment bore at the uprush tip. It is instructive to examine the shoreline motion for the generalised formula (B.1). For formula (B.1), the shoreline travels along the λ_3 characteristic with $\lambda_3 = u$.

The Riemann equation (2.45) applies along the shoreline characteristic (λ_3), and we have:

$$\lambda_3 \frac{du}{dt} + \frac{\lambda_3 + \sigma q_h}{\lambda_3 - u} \frac{dh}{dt} + \frac{dB}{dt} = 0. \tag{B.4}$$

If at the shore

$$\frac{\lambda_3 + \sigma q_h}{\lambda_3 - u} \frac{dh}{dt} = K_0 \text{ (a constant)}, \tag{B.5}$$

then (B.4) can be rewritten as

$$udu + dB = -K_0 dt \tag{B.6}$$

$$\Rightarrow \quad u_s^2 = u_0^2 - 2(B_s - B_0) - K_0(t - t_0), \tag{B.7}$$

where B_s is the bed level at the tip.

In fact it can be shown (see Appendix B.3) that for the general formula $q = h^n|u|^{m-1}u$ ($n > 0$ and $m > 1$)

$$\frac{\lambda_3 + \sigma q_h}{\lambda_3 - u} \frac{dh}{dt} = 0 \tag{B.8}$$

at the shoreline, so that u_s is a function of B_s (or vice versa). If u_0 and B_0 are known then u_s at different bed levels B_s can be calculated from (B.7). In particular, at maximum run-up $B_s(x_s = x_{s_{max}}) - B_0 = u_0^2/2$, where x_s is the shoreline position and $x_{s_{max}}$ is the shoreline position at maximum run-up. Therefore, (B.7) can be used to predict B_s or u_s, if one of them is known. In the uprush this means that for $q = h^n|u|^{m-1}u$ ($n > 0$ and $m > 1$) we have:

$$u_s^2 = u_0^2 - 2(B_s - B_0), \tag{B.9}$$

where $B_s = B(x, 0)$ as there is no sediment bore at the tip. Thus, the tip motion is solely determined by the existing beach slope, and will be ballistic if $B(x, 0) = \alpha x$, with α a constant beach slope.

However, as the bed level at the tip during the backwash is not known as an analytical expression, the analytical expressions for u_s and x_s cannot in general be derived during this phase. In general, backwash will not have been ballistic if there is bed change in the final bed profile.

When $n = 0$, no proof is found for $\frac{\lambda_3 + \sigma q_h}{\lambda_3 - u}\frac{dh}{dt} = K_0$, therefore no analytical shoreline motion is found for $q = |u|^{m-1}u$ ($m > 1$).

B.3 Term $\frac{\lambda_3 + \sigma q_h}{\lambda_3 - u}\frac{dh}{dt}$ at the shoreline

From equation (2.30) and also that $\lambda_3 = u$ at the shoreline,

$$\begin{aligned}
\lambda_3 - u &= \pm\sqrt{(\sigma q_u \lambda_3 + h\lambda_3 - \sigma q_u u + \sigma h q_h)/\lambda_3} \\
&= \pm\sqrt{(\sigma m h^n |u|^{m-1}\lambda_3 + h\lambda_3 - \sigma m h^n |u|^{m-1}u + \sigma n h^n |u|^{m-1}u)/\lambda_3} \\
&= \pm\sqrt{h + \sigma n h^n |u|^{m-1} + O(h^n)}. \qquad \text{(B.10)}
\end{aligned}$$

- For $n > 1$, in the limit $h \to 0$,

$$\frac{\lambda_3 + \sigma q_h}{\lambda_3 - u}\frac{dh}{dt} \sim \pm\frac{1}{\sqrt{n\sigma h^{n-1}|u|^{m-1} + 1}}$$
$$\left[2u\frac{d\left(h^{1/2}\right)}{dt} + \frac{2n\sigma|u|^{m-1}u}{2n-1}\frac{d\left(h^{n-1/2}\right)}{dt}\right] \to 0. \qquad \text{(B.11)}$$

- For $n = 1$, in the limit $h \to 0$, $\frac{\lambda_3 + \sigma q_h}{\lambda_3 - u}\frac{dh}{dt} \sim \pm 2u\sqrt{\sigma|u|^{m-1} + 1}\frac{d\left(h^{1/2}\right)}{dt} \to 0$.

- For $0 < n < 1$ in the same limit we have:

$$\frac{\lambda_3 + \sigma q_h}{\lambda_3 - u}\frac{dh}{dt} \sim \pm\frac{1}{\sqrt{h^{1-n} + n\sigma|u|^{m-1}}}$$
$$\left[\frac{2u}{2-n}\frac{d\left(h^{1-n/2}\right)}{dt} + 2\sigma|u|^{m-1}u\frac{d\left(h^{n/2}\right)}{dt}\right] \to 0. \qquad \text{(B.12)}$$

To conclude, $\frac{\lambda_3 + \sigma q_h}{\lambda_3 - u}\frac{dh}{dt} = 0$ at the shoreline for $q = h^n|u|^{m-1}u$ ($n > 0$ and $m > 1$), both in uprush and backwash.

APPENDIX C

Model verification

C.1 Bed-load-only model

Four comparisons are made to verify the bed-load-only model, and the formula $q = u^3$ is used in the verification simulations for the bed-load-only model. First, we compare with the PW01 analytical solution, which shows the accuracy of the model. Note that PW01 is a non-erodible bed solution; we approximate it here by putting $\sigma = 1 \times 10^{-7}$, and the results are compared with the analytical solutions in Peregrine and Williams (2001). We then compare with the original HP79 swash event (again with $\sigma = 1 \times 10^{-7}$), and results are compared with those presented by Hibberd and Peregrine (1979). Of particular importance here is the correct formation of the backwash bore. We then compare with the PW01 swash event over a mobile bed ($\sigma = 0.0654$), namely the numerical solution of KD10. This allows confirmation that the model works correctly morphodynamically. Finally, we again examine the mobile bed HP79 swash ($\sigma = 0.0654$), but this time compare with results from a state-of-the-art

finite volume model (Briganti et al., 2012, 2011) in order to illustrate the level of agreement that can be expected when verifying against the mobile bed HP79 solution that we provide.

It should be noted that in all the following comparison figures, the contours of black colour represent the present numerical results and those of red colour represent analytical solutions or other numerical data for verification.

C.1.1 PW01 swash event ($\sigma = 1 \times 10^{-7}$)

We use $\Delta x = 2.5 \times 10^{-3}$ and $\Delta t = 4 \times 10^{-4}$, and the CFL stability criterion is satisfied. The contour comparison is shown in Figure C.1. The contours of h and u are in very close agreement, except at the shoreline. The numerical scheme slightly overpredicts the maximum inundation, and it shows a discrepancy of 0.57%.

C.1.2 HP79 swash event ($\sigma = 1 \times 10^{-7}$)

For this simulation, $\Delta x = 5 \times 10^{-3}$ and $\Delta t = 2 \times 10^{-3}$ are used, and also the CFL stability criterion is satisfied. The comparison between the morphodynamic simulation with $\sigma = 1 \times 10^{-7}$ and the results in Hibberd and Peregrine (1979) is shown in Figure C.2. The maximum run-up predicted by the model is slightly larger than that of HP79: see Figure C.2. A possible reason for this is that $h(x = x_s) \equiv 0$ in our model, while that in HP79 is 1×10^{-4}; note that the contour $h = 1 \times 10^{-4}$ in Figure C.2(a) is quite close to the shoreline of HP79. The largest discrepancies are in h, particularly around the point where the shoreline

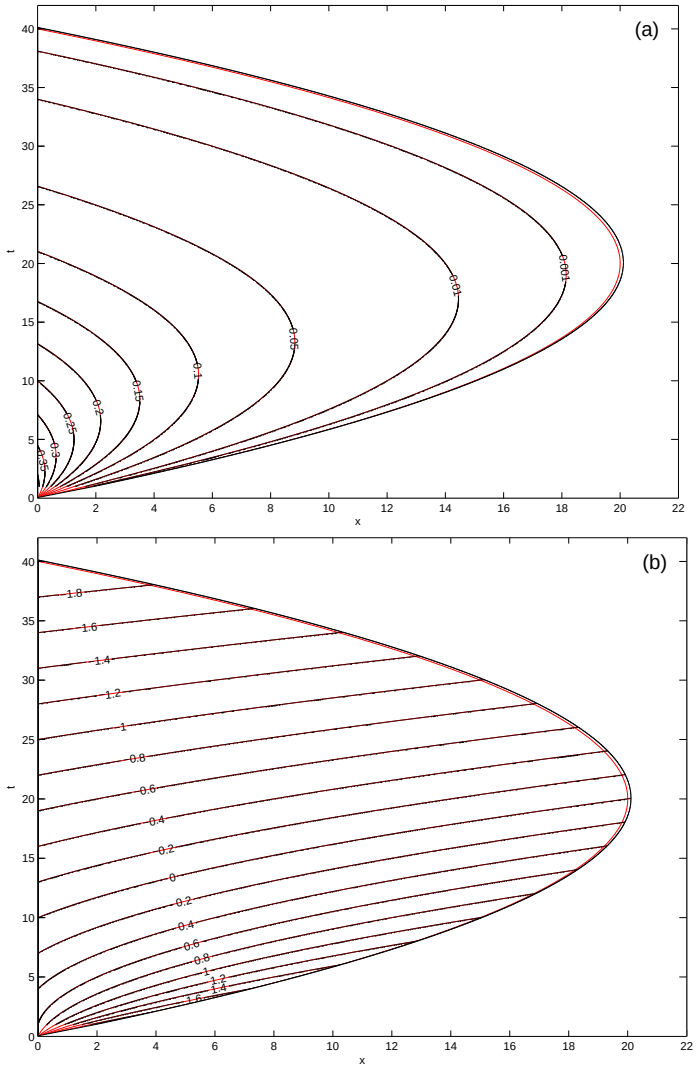

Figure C.1: Contour comparison with PW01 solution ($\sigma = 1 \times 10^{-7}$). (a) h; (b) u.

catches up with the backwash bore. Even with a quite small σ, the hydrodynamic shock and morphodynamic shock behave differently, especially when the shock strength is extremely large. Lastly, it should be borne in mind that the results from HP79 were here transcribed for comparison purposes by scanning the original figure into a CAD package and then manually adding contour points and then converted to (x, t) coordinates.

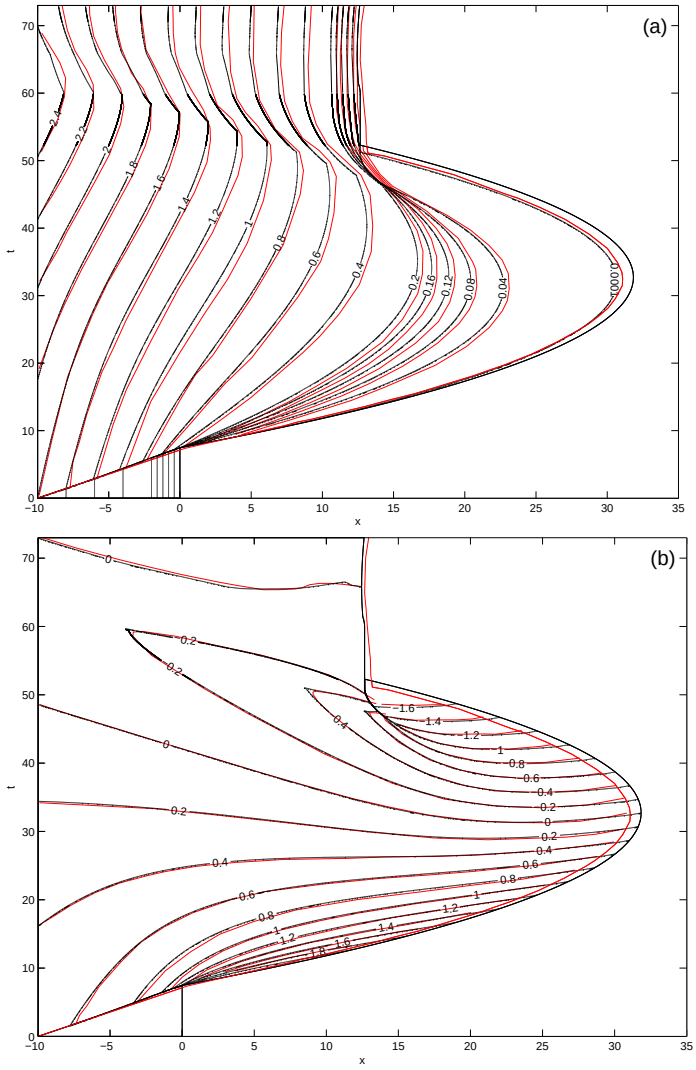

Figure C.2: Contour comparison with HP79 solution ($\sigma = 1 \times 10^{-7}$). (a) h; (b) u.

C.1.3 KD10 swash event ($\sigma = 0.0654$)

The comparison is shown in Figure C.3. Only small discrepancies are found in contours for h and u, while there are some discrepancies in that for ΔB. The possible reason for this is that second order interpolation in space is utilized to get the values at the characteristic intersection points ($a(1)$, $a(2)$ and $a(3)$ in Figure 4.1), while linear interpolation was used in KD10.

C.1.4 HP79 swash event ($\sigma = 0.0654$)

The HP79 mobile bed swash event is also considered but comparison is made with the results simulated by the finite volume model of Briganti et al. (2012): see Figure C.4. There is one backwash bore in the simulation with the STI MOC method, while no bore occurs when using the finite volume method, and it is clearly seen that there are some disagreements around where the shoreline meets the backwash bore in the STI MOC model. However, these two sets of results are in rather good agreement, and the discrepancy is to some degree, inevitable, determined by the nature of these two numerical methods.

These four comparisons show that the STI MOC numerical solution is of high accuracy, and can be generally be used for different types of swash events, and also with different bed mobility.

C.2 Combined load model

The verification of the combined load model is achieved by simulating the PW01 swash event and the results are compared with the uncoupled suspended load only simulations in Pritchard and Hogg (2005) and also Pritchard and Hogg (2006) (hereafter PH06). In the combined load model, $\sigma = 1 \times 10^{-7}$ and $m_e = 1 \times 10^{-8}$ are used to model the nearly fixed bed, and the results for $w_s = 0.001$ and $w_s = 0.03$ are compared with the equivalent uncoupled simulations in PH06. Note that different non-dimensionalisations are used in the present model and that in PH05, the equivalent values for m_e and t are of one

magnitude difference in the two models.

The comparisons for $w_s = 0.001$ and $w_s = 0.03$ are shown in Figures C.5 and C.6, respectively. Both comparisons show very close agreement, which suggest that the combined load model can be used to simulate swash events.

C.3 PW01 simulation with different initial data

The initial data used to initialise the fully coupled simulation under the PW01 swash event in KD10 are from the Riemann solution of the equivalent wet-dry dam-break problem over a flat mobile bed (Kelly and Dodd, 2009). However, the Riemann solution of a wet-dry dam-break problem over a sloping fixed bed, i.e. PW01 solution, could also be used to initialise the fully coupled PW01 swash simulations with different sediment transport formulae. We here compare the results of swash simulations initialised by the two sets of initial data from the wet-dry dam-break problem over a flat mobile bed and PW01 solution. Comparison of the results for the Grass formula (I) and Van Rijn formula (IV) when using the PW01 solution as initial data with those obtained using the Riemann solution over a flat mobile bed is shown in Figure C.7. Both comparisons show very close agreement, therefore the PW01 solution at a finite time can be generally used for fully coupled PW01 swash simulation over a mobile bed.

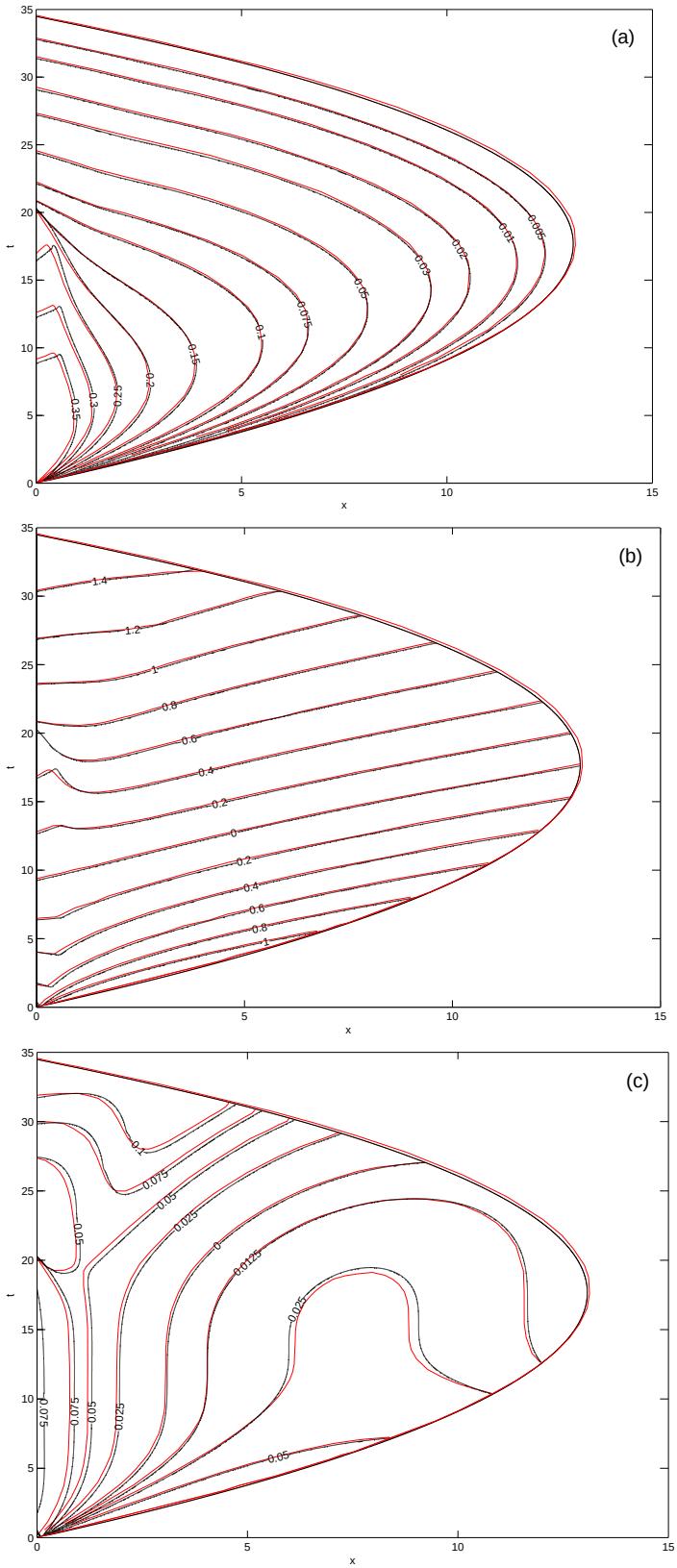

Figure C.3: Contour comparison with KD10 solution ($\sigma = 0.0654$). (a) h; (b) u; (c) ΔB.

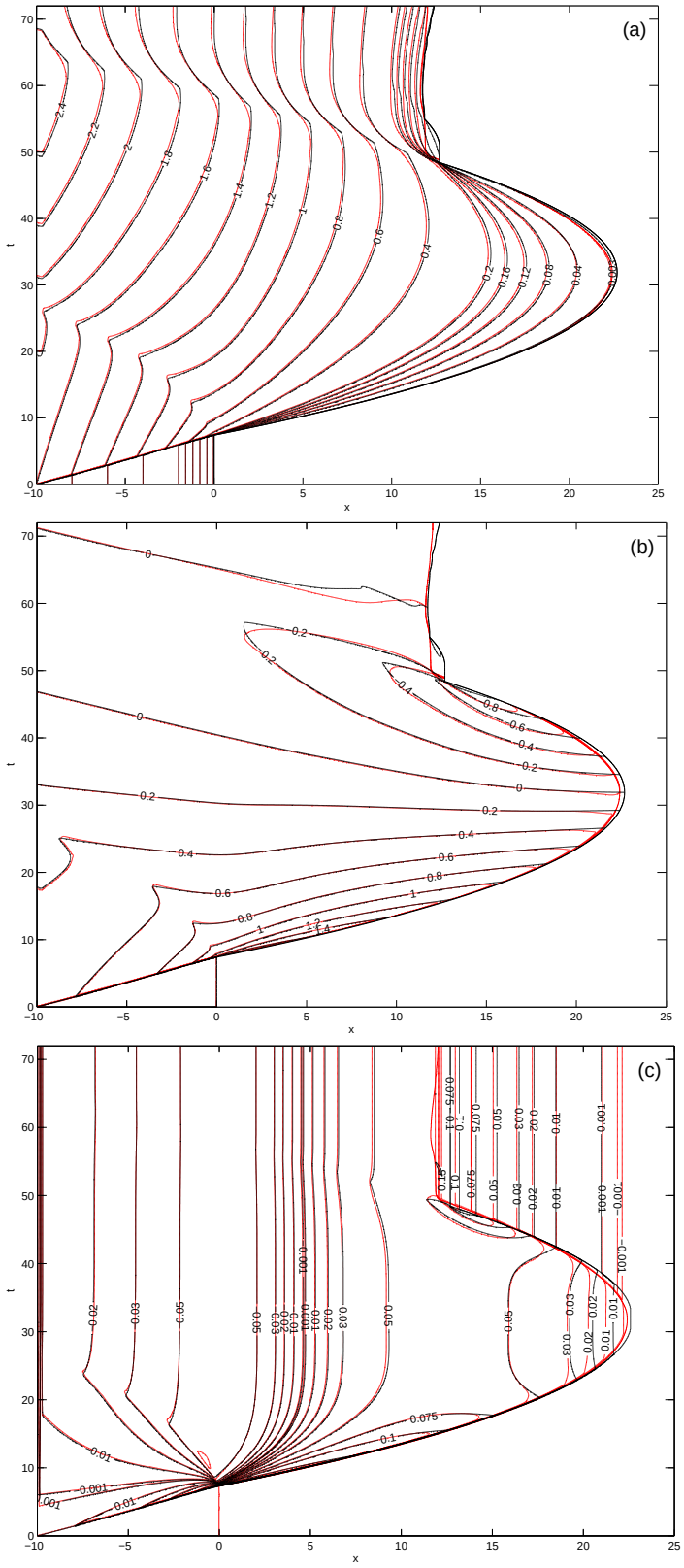

Figure C.4: Comparison using mobile bed HP79 event ($\sigma = 0.0654$) with Briganti et al. (2012). (a) h; (b) u; (c) ΔB.

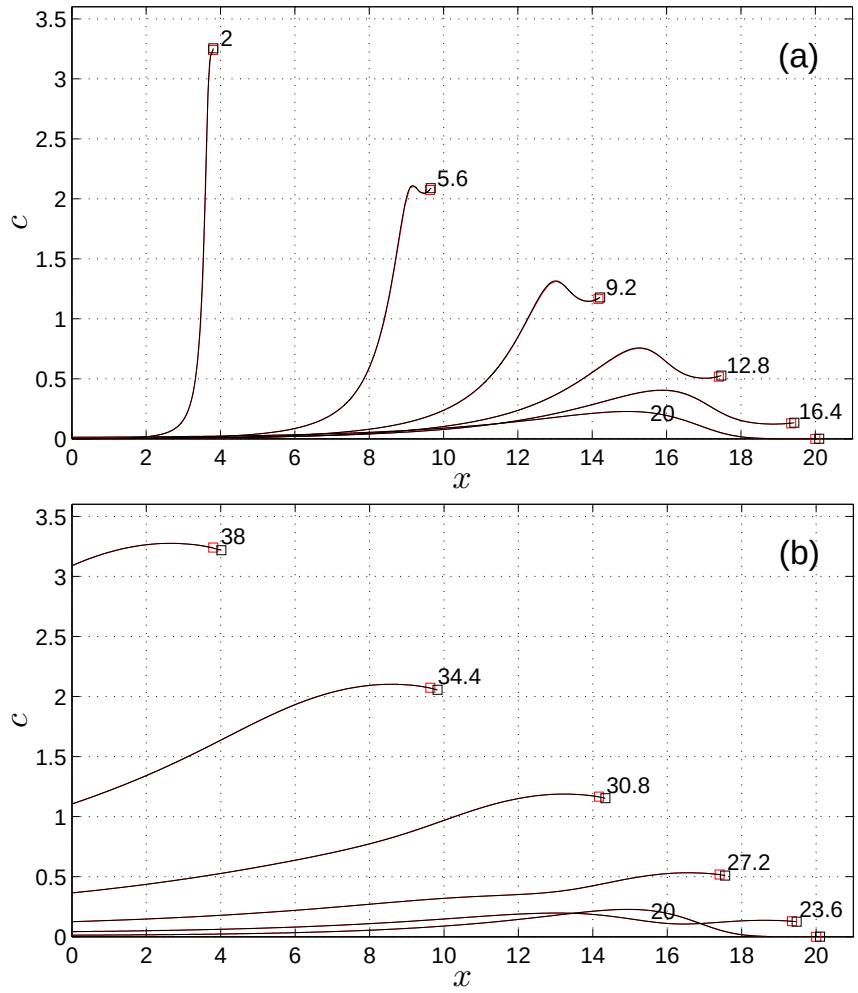

Figure C.5: Comparison of sediment concentration in the water column under the PW01 swash event with those in PH06 simulation with $w_s = 0.001$. (a): $t = 0-20$ (uprush); (b) $t = 20-40$ (backwash). Black line: present combined load model; red line: PH06 solution. Labels indicate the value of t and □ indicates shoreline position. (PH06 solution reproduced courtesy of Dr. D. Pritchard)

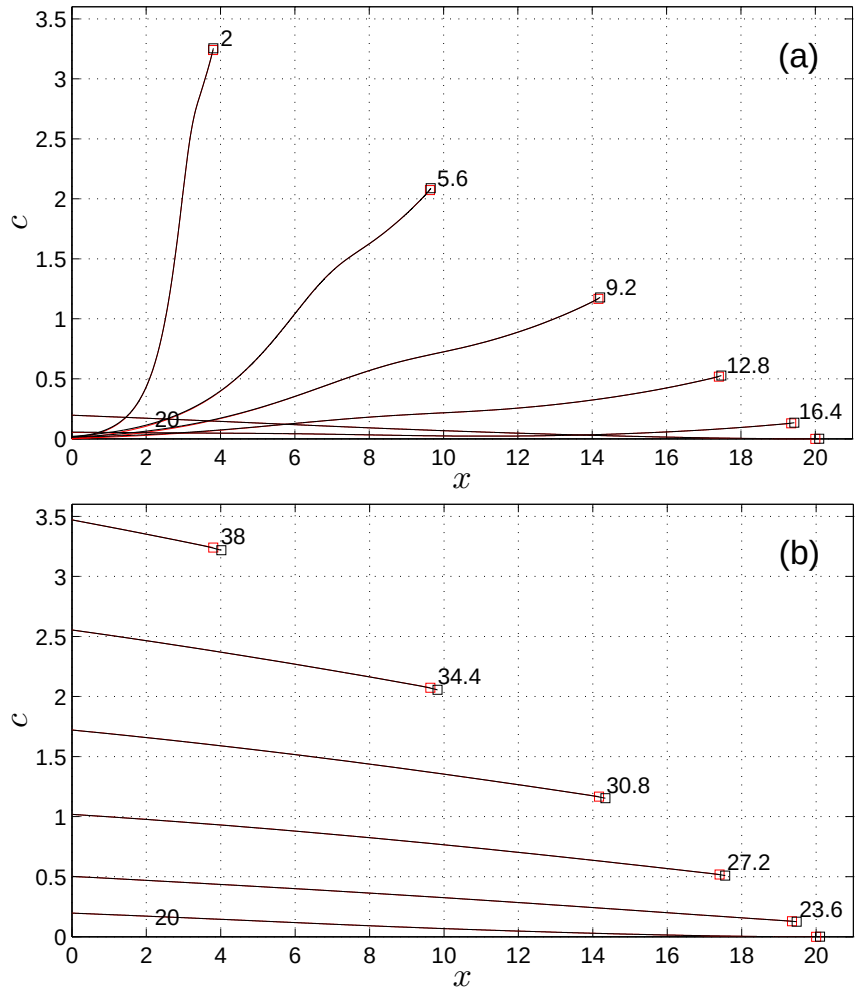

Figure C.6: Comparison of sediment concentration in the water column under the PW01 swash event with those in PH06 simulation with $w_s = 0.03$. (a): $t = 0 - 20$ (uprush); (b) $t = 20 - 40$ (backwash). Black line: present combined load model; red line: PH06 solution. Labels indicate the values of t and □ indicates shoreline position. (PH06 solution reproduced courtesy of Dr. D. Pritchard)

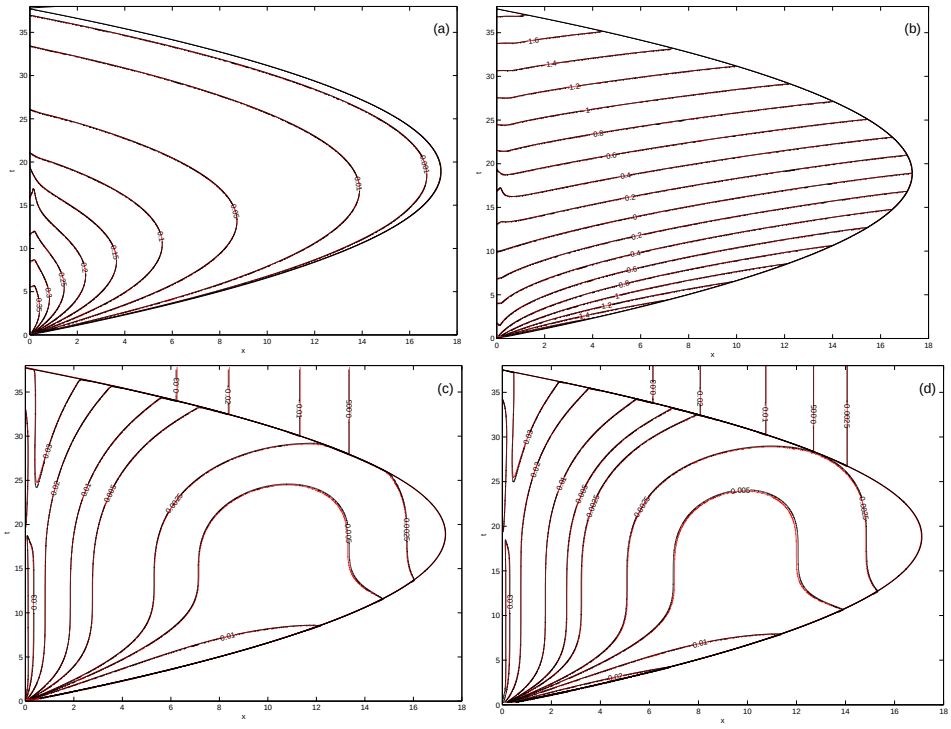

Figure C.7: Comparison of fully coupled PW01 simulations using PW01 solution as initial data (black) and those using Riemann solution over flat mobile bed (red) for formula I ($q = u^3$) ($\sigma = 0.01$) and IV ($q = u|u|^{2.4}$) ($\sigma = 0.00888$). (a) h, (b) u, (c) ΔB, all for I; (d) ΔB for IV.

References

Antuono, M. (2010). A shock solution for the nonlinear shallow water equations. *J. Fluid Mech.*, 658:166–187.

Antuono, M., Soldini, L., and Brocchini, M. (2012). On the role of the Chezy frictional term near the shoreline. *Theor. Comput. Fluid Dyn.*, 26:105–116.

Bailard, J. and Inman, D. (1981). An energetics bedload model for a plane sloping beach: local transport. *J. Geophys. Res.*, 86:2035–2043.

Barnes, M. P., O'Donoghue, T., Alsina, J. M., and Baldock, T. E. (2009). Direct bed shear stress measurements in bore-driven swash. *Coastal Eng.*, 56:853–867.

Bernetti, R., Titarev, V. A., and Toro, E. F. (2008). Exact solution of the Riemann problem for the shallow water equations with discontinuous bottom geometry. *J. Comput. Phys.*, 227:3212–3243.

Blenkinsopp, C. E., Turner, I. L., Masselink, G., and Russell, P. E. (2011). Swash zone sediment fluxes: field observations. *Coastal Eng.*, 58:28–44.

Briganti, R. and Dodd, N. (2009). Shoreline motion in nonlinear shallow water coastal models. *Coastal Eng.*, 56(5-6):495–505.

Briganti, R., Dodd, N., Kelly, D. M., and Pokrajac, D. (2012). An efficient and flexible solver for the simulation of the morphodynamics of fast evolving flows on coarse sediment beaches. *Int. J. Numerical Meth. Fluids*, 69(4):859–877.

Briganti, R., Dodd, N., Pokrajac, D., and O'Donoghue, T. (2011). Nonlinear shallow water modelling of bore-driven swash: description of the bottom boundary layer. *Coastal Eng.*, 58(6):463–477.

Brocchini, M. and Dodd, N. (2008). Nonlinear shallow water equation modeling for coastal engineering. *ASCE J. Water. Port Coast. Ocean Eng.*, 134:104–120.

Capart, H. and Young, D. L. (1998). Formation of a jump by the dam-break wave over a granular bed. *J. Fluid Mech.*, 372:165–187.

Carrier, G. F. and Greenspan, H. P. (1958). Water waves of finite amplitude on a sloping beach. *J. Fluid Mech.*, 4:97–109.

Chisnell, R. F. (1957). The motion of a shock wave in a channel, with applications to cylindrical and spherical shock waves. *J. Fluid Mech.*, 2725.

Di Giacinto, M. and Valorani, M. (1989). Shock detection and discontinuity tracking for unsteady flows. *Computers and Fluids*, 17:61–84.

Dodd, N., Stoker, A., Calvete, D., and Sriariyawat, A. (2008). On the evolution of beach cusps. *J. Fluid Mech.*, 597:145–169.

Dressler, R. F. (1952). Hydraulic resistance effect upon the dam-break functions. *Journal of Research of the National Bureau of Standards*, 49(2):217–225.

Elfrink, B. and Baldock, T. (2002). Hydrodynamics and sediment transport in the swash zone: a review and perspectives. *Coastal Eng.*, 45:149–167.

Erikson, L., Larson, M., and Hanson, H. (2005). Prediction of swash motion and run-up including the effects of swash interaction. *Coastal Eng.*, 52:285–302.

Fraccarollo, L. and Capart, H. (2002). Riemann wave descriptions of erosional dam break flows. *J. Fluid Mech.*, 461:183–228.

Grass, A. (1981). Sediment transport by waves and currents. Report FL29, Ma. Tecnol., SERC London Cent.

Guard, P. A. and Baldock, T. E. (2007). The influence of seaward boundary conditions on swash zone hyrdodynamics. *Coastal Eng.*, 54:321–331.

Hibberd, S. and Peregrine, D. H. (1979). Surf and run-up on a beach: A uniform bore. *J. Fluid Mech.*, 95:323–345.

Ho, D. V. and Meyer, R. E. (1962). Climb of a bore on a beach. Part 1. Uniform beach slope. *J. Fluid Mech.*, 14:305–318.

Hogg, A. J. and Pritchard, D. (2004). The effects of hydraulic resistance on dam-break and other shallow inertial flows. *J. Fluid Mech.*, 501(DOI: 10.1017/S0022112003007468):179–212.

Horn, D. P. and Mason, T. (1994). Swash zone sediment transport modes. *Mar. Geol.*, 120:309–325.

Jackson, N. L., Masselink, G., and Nordstrom, K. F. (2004). The role of bore collapse and local shear stresses on the spatial distribution of sediment load in the uprush of an intermediate-state beach. *Marine Geology*, 203:109–118.

Jeffrey, A. (1976). *Quasilinear hyperbolic systems and waves*. Pitman.

Keller, H., Levine, D. A., and Whitham, G. B. (1960). Motion of a bore over a sloping beach. *J. Fluid Mech.*, 7(2):302–316.

Kelly, D. M. (2009). *Bore-driven swash on a mobile beach*. PhD thesis, School of Civil Engineering, University of Nottingham, Nottingham, UK.

Kelly, D. M. and Dodd, N. (2009). Floating grid characteristics method for unsteady flow over a mobile bed. *Computers and Fluids*, 38:899–909.

Kelly, D. M. and Dodd, N. (2010). Beach-face evolution in the swash zone. *J. Fluid Mech.*, 661.

Kobayashi, N. and Johnson, B. D. (2001). Sand suspension, storage, advection and settling in surf and swash zones. *J. Geophys. Res.*, 106(C5):9363–9376.

Lax, P. D. (1957). *Hyperbolic systems of conservation laws and the mathematical theory of shock waves*. CBMS Regional Conf. Ser. Appl. Math.

LeVeque, R. J. (1992). *Numerical methods for conservation laws*. Lectures in mathematics. Birkhäuser Verlag, Basel, 2nd edition.

Masselink, G., Evans, D., Hughes, M. G., and Russell, P. (2005). Suspended sediment transport in the swash zone of a dissipative beach. *Mar. Geol.*, 216:169–189.

Masselink, G. and Hughes, M. G. (2003). *Introduction to Coastal Processes & Geomorphology*. Hodder Arnold, London, UK.

Masselink, G., Russell, P., Turner, I., and Blenkinsopp, C. (2009). Net sedimnet transport and morphological change in the swash zone of a high-energy sandy beach from swash event to tidal cycle time scales. *Mar. Geol.*, 267:18–35.

Mei, C. C. (1990). *The Applied Dynamics of Ocean Surface Waves*, volume 1 of *Advanced Series on Ocean Engineering*. World Scientific, Singapore, second edition.

Moeckel, W. E. (1952). Interaction of oblique shock waves with regions of variable pressure, entropy and energy. *Nat. Adv. Comm Aero, Washington*.

Moretti, G. (1971). Complicated one-dimensional flows. Technical Report Pibal 71–25, Polytechnic Inst. of Brooklyn, Dept of Aerospace Engineering and Applied Mechanics.

Moretti, G. (1987). Computation of flows with shocks. *Ann. Rev. Fluid Mech.*, 19:313–337.

Moretti, G. (2002). Thirty-six years of shock fitting. *Computers and Fluids*, 31:719–723.

Needham, D. J. and Hey, R. D. (1991). On nonlinear simple waves in alluvial river flows: a theory for sediment bores. *Phil. Trans. Roy. Soc. Lond. A*, 334:25–53.

Peregrine, D. and Williams, S. M. (2001). Swash overtopping a truncated beach. *J. Fluid Mech.*, 440:391–399.

Postacchini, M., Brocchini, M., Mancinelli, A., and Landon, M. (2012). A multi-purpose, intra-wave, shallow water hydro-morphodynamic solver. *Adv. Water Resources*, 38:13–26.

Pritchard, D. (2009). Sediment transport under a swash event: the effect of boundary conditions. *Coastal Eng.*, 56:970–981.

Pritchard, D., Guard, P. A., and Baldock, T. E. (2008). An analytical model for bore-driven run-up. *J. Fluid Mech.*, 610:183–193.

Pritchard, D. and Hogg, A. J. (2002). On sediment transport under dam-break flow. *J. Fluid Mech.*, 473:265–274.

Pritchard, D. and Hogg, A. J. (2003). Cross-shore sediment transport and the equilibrium morphology of mudflats under tidal currents. *J. Geophys. Res.*, 108(C10):3313, doi:10.1029/2002JC001570.

Pritchard, D. and Hogg, A. J. (2005). On the transport of suspended sediment by a swash event on a plane beach. *Coastal Eng.*, 52:1–23.

Pritchard, D. and Hogg, A. J. (2006). Reply to discussion of "On the transport of suspended sediment by a swash event on a plane beach". *Coastal Eng.*, 53:115–118.

Ritter, A. (1892). Die Fortpflanzung der Wasserwellen. *Vereine Deutscher Ingenieure Zeitschrift*, 36:947–954.

Shen, M. C. and Meyer, R. E. (1963a). Climb of a bore on a beach. Part 2. Non-uniform beach slope. *J. Fluid Mech.*, 16:108–112.

Shen, M. C. and Meyer, R. E. (1963b). Climb of a bore on a beach. Part 3. Run-up. *J. Fluid Mech.*, 16:113–125.

Soulsby, R. L. (1997). *Dynamics of Marine Sands*. Thomas Telford, London.

Stoker, J. (1957). *Water Waves*. Interscience, New York, N.Y.

Synolakis, C. (1987). The run-up of solitary waves. *J. Fluid Mech.*, 185:523–545.

Toro, E. F. (1997). *Riemann solvers and numerical methods for fluid dynamics*. Springer, Berlin.

Toro, E. F. (2001). *Shock-capturing methods for free-surface shallow flows*. Wiley, New York, NY.

Toro, E. F. (2009). *Riemann solvers and numerical methods for fluid dynamics*. Springer, Berlin, 3nd edition.

Van Rijn, L. C. (2007a). Unified view of sediment transport by currents and waves. i: Initiation of motion, bed roughness, and bed-load transport. *ASCE J. Hydraulic Eng.*, 133:649–667.

Van Rijn, L. C. (2007b). Unified view of sediment transport by currents and waves. ii: Suspended transport. *ASCE J. Hydraulic Eng.*, 133:649–667.

Watson, G., Peregrine, D. H., and Toro, E. (1992). Numerical solution of the

shallow water equations on a beach using the weighted average flux method. In Hirsch, C., editor, *Computational Fluid Dynamics*, volume 1. Elsevier.

Whitham, G. (1955). The effects of hydraulic resistance in the dam-break problem. *Proc. Roy. Soc. London A.*, 227(1170):399–407.

Whitham, G. (1958). On the propagation of shock waves through regions of non-uniform area or flow. *J. Fluid Mech.*, 4(4):337–360.

Yalin, M. (1977). *Mechanics of Sediment Transport*. Pergamon.

Zhu, F., Dodd, N., and Briganti, R. (2012). Impact of a uniform bore on an erodible beach. *Coastal Eng.*, 60:326–333.